Summer 2007

Shaken Baby Syndrome: Retinal Hemorrhaging. A Biomechanical Approach to Understanding the Mechanism of Causation

Steven Alex Hans
Old Dominion University

Shaken Baby Syndrome: Retinal Hemorrhaging - a Biomechanical Approach to Understanding the Mechanism of Causation

By

Steven Alex Hans

A Dissertation Submitted to the Faculty of
Old Dominion University in Partial Fulfillment of the
Requirement for the Degree of

Doctor of Philosophy

Mechanical Engineering

OLD DOMINION UNIVERSITY
August 2007

Approved by:

Sebastian Bawab (Director)

Ayodeji Demuren (Member)

Gene Hou (Member)

Michael Woodhouse (Member)

ABSTRACT

Shaken Baby Syndrome: Retinal Hemorrhaging - a Biomechanical Approach to Understanding the Mechanism of Causation

Steven Alex Hans
Old Dominion University, 2007
Director: Sebastian Y. Bawab

Shaken Baby Syndrome (SBS) is a form of abuse where typically an infant, age six months or less, is held and shaken. There may or may not be direct impact associated with this action. Further, there is very little agreement on the actual mechanism of SBS. Clinical studies are limited in showing the exact mechanism of injury and only offer postulations and qualitative descriptions. SBS has received much attention in the media, has resulted in a great deal of litigation and can be the source of unfounded accusations. Therefore, it is necessary to try to quantify the forces that may cause injury due to SBS.

The physiology of infants makes injury due to SBS more likely. Infants have relatively large heads supported by weak necks that simply act as tethers (Prange et al., 2003). Therefore, there is minimal resistance to shaking. In addition, the cerebrospinal fluid (CSF) layer surrounding the infant's brain is up to 10 mm thick as opposed to 1 – 2 mm in older children and adults (Morison, 2002). This thick layer reduces the resistance in rotation of the brain and can cause shearing injuries to the brain tissue. In addition, retinal hemorrhaging has been reported in SBS. The infant's eyes have a vitreous that is typically more gelatinous and with a higher viscosity than in adult eyes. In addition, this vitreous is firmly attached to the retina and is difficult to remove (Levin, 2000).

A preliminary parametric model of an infant eye will be presented so that resultant nodal retinal force of the posterior retina can be investigated and compared with a documented shaking frequency and a documented impact pulse. Retinal forces are then compared with various studies that investigate retinal detachment or adhesive strength. This eye model is built using a variety of material properties that have been reported for the sclero-cornea shell, choroids, retina, vitreous, aqueous, lens, ciliary, optic nerve, tendons, extra ocular muscles, optic nerve, and orbital fatty tissue. The geometry of the eye has been

carefully optimized for this parametric model based on scaling to an infant from an adult using idealized eye globe geometry and transverse slice tracings of "The Visible Human Project."

This model shows promise in investigating the forces and kinematics of the infant eye exposed to harmonic shaking and further bolsters some of the few biomechanical studies investigating SBS. However, improvements are necessary to complete the eye model presented. Specifically, improvements on the mechanical properties for the components of the eye and especially the infant eye are needed. There is currently a deficit of biomechanical studies of the materials needed for the infant eye that is specifically geared for use in an explicit finite element code package. Conversions and adaptations of available materials are used in this first version of the infant eye model presented here and are in fair agreement with some of the clinical studies concerning SBS.

This dissertation is dedicated to my wife Christina Hans

ACKNOWLEDGMENTS

I am grateful for my wife during my several years as a graduate student. During the course of my study, she has been extremely supportive and nurturing, allowing me to focus on my work. She has sacrificed her needs and wants during this process and I am indebted to her for that.

I would also like to express my gratitude to my advisor, Sebastian Bawab. During my time as a graduate student, Dr. Bawab provided a stimulating environment with care and compassion equal to his demand for quality and excellence. During my research process, Dr. Bawab would frequently calm me when something was not going as planned and refocus my efforts. I have gotten to know Dr. Bawab over the course of almost 10 years now and not only is Dr. Bawab my mentor, he is a true friend—family really.

I would also like to acknowledge Michael Woodhouse. Dr. Woodhouse actually is responsible for my interest in biomechanics and helped me narrow my topic of study. Dr. Woodhouse is the definition of a true southern gentleman, and I enjoy working with him.

I would also like to thank each of the committee members: Dr. Demuren and Dr. Hou. I have gotten to know these professors over the years and enjoy working on projects with them.

Lastly, I would like to thank the mechanical engineering department for making my graduate student experience a positive one.

TABLE OF CONTENTS

Page

LIST OF TABLES

LIST OF FIGURES

CHAPTER I

INTRODUCTION

Shaken baby syndrome is a controversial issue as the very diagnosis places accusations of criminal action on caregivers. Unfortunately, clinical observations, albeit intuitive, are sometimes not enough to define the actual causation of shaken baby syndrome. On the other hand, malignant behavior is easily down played or lied about: the baby fell on the floor. Over the years, however, research in clinical analysis, and now biomechanical modeling, has helped define the actual causation of injury. Specifically, research has compelled the study of both impact and pure shaking scenarios. Most clinical observations support the notion that shaken baby syndrome carries unique pathology (Levin, 2000) that cannot be reproduced through accident alone. Where these clinical studies fall short is the certainty that shaking alone can cause injuries; this is where the biomechanical modeling can help.

Although a very new area, most of the focus of biomechanical investigations is concerned with brain injury (Prange & Margulies, 2001; Morison, 2002). This proposed research will also carry over into the retinal hemorrhaging aspects by considering a full-featured finite element eye model and ocular region based on materials and geometry from all genres of research. Although the investigative model presented does support clinical observations and compliments the work of Morison, the work remains an investigation and further enhancements are needed.

Aims and Objectives

The objective of this research is to build a preliminary computer eye model that compares the resultant nodal retinal forces from a pure shaking motion to an impact pulse representive of a fall. This computer model will be a coupling of rigid body dynamics and finite element analysis with material properties from various references. This model is a complex endeavor and will contain several components of the eye, and surrounding area. Retinal hemorrhaging mostly occurs in the posterior region of the eye and this is where the focus of the modeling is. In order to model the kinematics, the entire eye complex with orbit, muscles, optic nerve, fatty tissue, and eyelid are modeled.

The secondary objective of this work is to perform a parametric study of the vitreous materials currently available from the literature. The vitreous body occupies $4/5^{ths}$ of the volume of the eye globe (Hogan, Alvarado, & Weddell, 1971) and is a critical component to eye. The vitreous interaction with the retinal wall is of particular interest as Levin (2000) suggests that the viscous vitreous shears the retinal blood vessels due to vitreous shaking. As presented in chapter 7, the material compliancy varies greatly from study to study. Unfortunately, no vitreous testing has been reported for human infants. Only information regarding the qualitative nature of the vitreous is given for infants (Hogan, Alvarado, & Weddell, 1971; Zimmerman, 1980; Sebag, 1998; Levin, 2000). Currently, no such study exists that compares published vitreous materials in a dynamic saccadic movement with all of the considered components of the eye and surrounding tissues for adult or infant.

Thesis Overview

Chapter 2 of this thesis contains the literature review section that is split into several categories. Clinical background on shaken baby syndrome (SBS) will be discussed followed by retinal hemoraging related studies. The following reviews will cover mathematical eye models with emphasis on the cornea and sclera materials. A review of the optic nerve and related clinical, histological, and biomechanical studies is presented. A review is presented regarding the brain biomechanical studies, which includes studies of the infant brain. The vitreous body review contains histological and material property determinations. The retina and choroid are grouped together as most of the studies that will be presented discuss both of these delicate membranes.

Included in the retina and choroid review are studies concerned with retinal adhesion and detachment. Muscle model studies regarding finite element models and analytical models are reviewed followed by fatty tissue and skin studies. Finally, the literature review is concluded with mention of some of the eye structures that are simplied in the current work such as the lens and ciliary body.

Chapter 3 discusses the influences that go into determining the geometry of the eye and ocular cavity. Details of eye dimensioning are given as well as build-up geometries from the Visible Human Project. Details are discussed that did not make the final presented model, and scaling methods to infant dimensions are provided.

Chapter 4 goes into extreme detail on meshing the eye and fatty tissue. Included in this section are various techniques that are utilized to build the eye mesh.

In particular, the fatty tissue, vitreous, and aqueous proved to be extremely challenging.

The next three chapters break the eye into three primary sections: the ocular shell layers, the structures that encase and tether the eye, and the interior vitreous material. Chapter 5 examines the cornea, sclera, choroid, and retina in detail and considers possible constitutive material fits that could be used in finite element analysis. Also discussed in this chapter are the retinal adhesive and peeling studies. Chapter 6 goes into the analytical muscle modeling and the optic nerve studies. Included in this study is the fatty tissue model comparison. Included also are separate investigative models into the optic nerve response and muscle activation dynamics with calibration to previous muscle model studies for horizontal eye motion.

Chapter 7 provides a critical comparison and analysis of possible candidate vitreous materials in a saccadic eye movement. In this section a detailed description of the eye model is provided with a look into the shear strain at the posterior pole. This chapter not only compares the materials from different studies, but also examines different constitutive models using these materials. Also included is the parameterization of the optic nerve and eye mesh density to investigate the sensitivity on the shear strain.

Chapter 8 presents an investigative study using a possible vitreous material candidate from chapter 7 for shaken baby syndrome. Specifically, the harmonic shaking sequence is used from past research and compared to an impact simulation. A comparison of the posterior retinal forces is given to study the differences between the two types of motion. Also considered in this chapter is the possibility of

modeling retinal detachment. Parameterization of the fatty tissue and optic nerve is also investigated in the chapter.

Finally, chapter 9 provides concluding remarks with final opinions and ideas for future work in the area of infant eye models.

Eye and Surrounding Tissue Anatomy

In order for the reader to have a perspective on the relevant ocular and extra-ocular components in this work, a description of anatomy is presented. The gross anatomy of the eye (Figure 1.0) contains three fundamental membrane layers starting outward with the cornea and sclera shell. The second layer inward is the choroid layer, which interfaces the retina. The interior of the eye is divided into two chambers by the lens and ciliary body. The anterior chamber is the aqueous humor and is enclosed between the cornea, lens and ciliary body. The posterior chamber is the vitreous body and interfaces the entire retinal membrane.

Connecting this eye globe is the optic nerve located at the posterior-medial area interfacing the sclera shell. The optic nerve is essentially an extension of the brain (Hogan, Alvarado, & Weddell, 1971) with a dura sheath followed by a pia and arachnoid layer. There is also cerebral fluid encasing the optic nerve tissue matter with more of a concentration of fluid just posterior to the eye globe attachment (Hayreh, 1984).

Attached to the eye are six extra-ocular muscles (Figure 1.1) that control eye movement. Of these muscles, four are the rectii (medial, lateral, superior, and

inferior). There are also two oblique muscles (superior and inferior). All the muscles, with the exception of the inferior oblique, originate from the apex of the ocular cavity. The superior oblique also goes through a boney loop known as the trochlea pulley before attaching to the eye globe, while the rectii and inferior oblique are directly attached to the eye. The inferior oblique muscle is attached to the base of the ocular cavity directly below the eye globe. Encasing the eyeball, optic nerve, and muscles is the ocular fat tissue.

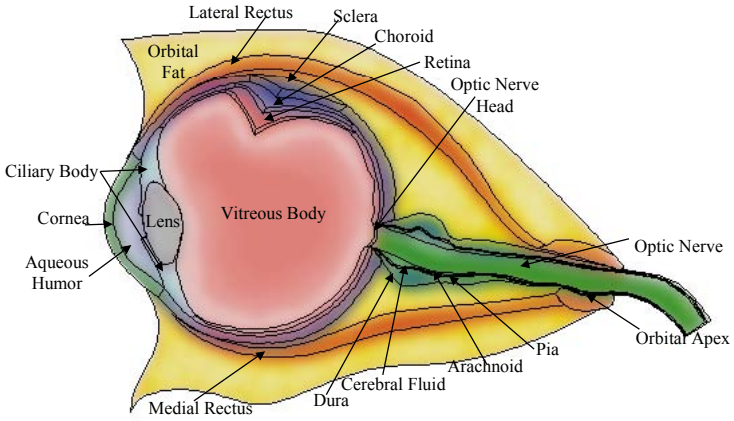

Figure 1.0: Superior view of the eye and surrounding tissues.

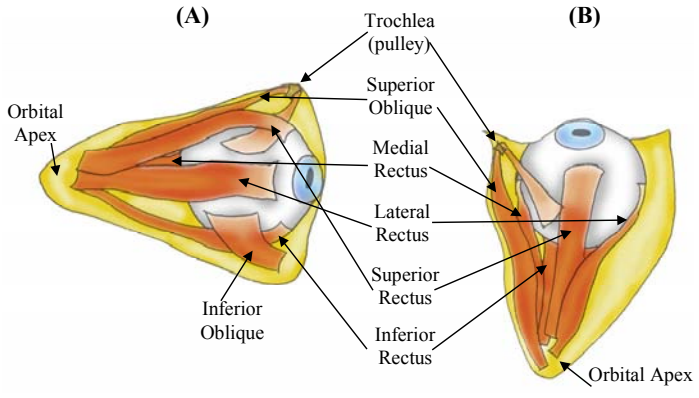

Figure 1.1: Extra-ocular muscle locations showing a (A) lateral and (B) superior view.

CHAPTER II

LITERATURE REVIEW

Introduction

The literature is broken into several sections. The first two sections deal with the clinical aspects of shaken baby syndrome (SBS) and retina hemorrhaging as a result of shaking. The SBS section highlights historical information and also describes the diagnosis and associated injuries. In addition, a critical argument is posed that discusses the necessity of impact in combination with shaking or shaking alone that is sufficient to cause injury. Retinal Hemorrhaging (bilateral) is one indication in the diagnosis of SBS. This section will cover the specific definition of retinal hemorrhaging and the locations in the eye that have been reported in abuse studies. In addition, other injuries will be discussed that may cause retinal hemorrhaging that is different than injuries from SBS. Finally, this section will discuss the physiological differences of infant eyes compared to the adult that predisposes infants to injury as a result of SBS.

In order to build a biomechanical eye model to help explain the input forces required to cause retinal hemorrhaging, a look at previous eye models is considered. In the biomechanical eye models section, finite element eye models are compared. Most of these eye models deal with impact trauma to the cornea and sclera shell and are therefore optimized for this loading condition. Most of the emphasis on modeling impacts to the eye globe involves the consideration of the cornea and sclera materials.

Other studies considering the cornea and sclera are included in the biomechanical eye section.

Hemorrhaging has been reported in the optic nerve in SBS; therefore, a comprehensive look into optic nerve biomechanical, clinical, and anatomical studies is presented. Very few groups have built models of the optic nerve, and those that have focus on the optic nerve head (part of the optic nerve that interfaces with the posterior sclera shell) in glaucoma investigations. Briefly, glaucoma is the second leading cause of adult blindness that results from intraocular pressures that are too much for the nerve to withstand. While most of these studies are concerned with glaucoma, they can still provide insight into this biomechanical eye model. This work considers the optic nerve as a tether and so an attempt is made to adapt the comprehensive works in the optic nerve section into the eye model.

The optic nerve is an extension of the brain so that the next logical literature review covers biomechanical models and material studies of the brain for humans (adult and infant) and other species. Included in this section is some research on the compliant infant skull. The brain is not modeled in this work; however, the influence of these presented studies is important to point out. The most important discussion is the work done by Morison (2002) that modeled SBS and effects on the bridging veins. The other studies mentioned have been used to gather knowledge on viscoelastic properties of the brain and some of the modeling methods that are considered.

The vitreous body, a semi-fluid substance, occupies most of the eye globe volume and offers mechanical support and energy absorption properties. Some of the

studies considered here discuss material testing of the vitreous body. And as will be considered, there are variations in the final material parameters that can be used in the finite element model due to testing and sample preparation protocol. The composition and histology of the vitreous body are also detailed.

Next, literature concerned with the retina and choroid is presented. Material determinations of both the choroid and retina are considered here in addition to the studies of retinal detachment/adhesion to the choroid. Most of these studies determine the linear elastic modulus based on simple axial tension tests, although the authors of these studies maintain that the retina and choroid are more hyperelastic. The detachment studies discussed have two methods of testing the retinal adhesive force. The first method proposes pealing the retina off the choroid and the second method induces bubbles (called blebs) in the retina and calculates the force needed to remove the retina from the pigment epithelium.

The extra-ocular muscles are considered next in the biomechanical model. Most of the work done on muscles utilizes an analytical phenomenologic model called the Hill-type muscle. This method of muscle modeling is able to model complex motions with various control algorithms. In addition to the Hill-type muscle properties, finite element muscles are also discussed. An interesting investigation into the modeling of the extraocular muscles is the determination of the plant properties. The plant is the eyeball in these studies and has the unique feature to have the dynamic effects of the optic nerve tested by isolating the contribution of the muscle attachments. This is important as most of the optic nerve papers discussed propose experimental properties mostly from other tissue studies under the

assumption that the optic nerve is composed of the same material. In the analytical muscle models, the plant parameters are directly measured from a patient (Collins, Scott & O'Meara 1969).

Finally, a review of the fatty tissue and skin research is considered. Most of the biomechanical eyes discussed do not include the fatty tissue or do not consider the eyelid. However, exclusion may or may not be valid. In this study the infant eye must have this feature as the rotational motion applied justifies it. The eye can be considered a spherical joint (mostly) and the fatty tissue would represent the other portion of this joint. In addition, the fatty tissue plays an important role in impact studies as it offers energy absorption capabilities. This section highlights properties of skin from various studies and also discusses various fatty tissue studies. As will be shown, fatty tissue has been considered from all over the human body (buttocks, foot pad, and breast tissue).

Shaken Baby Syndrome

Clinical observations and diagnosis of SBS started when Caffey (1972, 1974) coined the phrase *Whiplash Shaken Infant Syndrome*. In the following years this diagnosis would simply be called Shaken Baby Syndrome. The actual mechanism of injury is debatable, but the injuries associated with SBS are subdural hematomas (SDH) (Duhaime et al., 1996), diffuse axonal injury (DAI) (Margulies & Thibault, 1992; Jafari et al., 1997; Bain & Meaney, 2000; Prange & Margulies, 2001), and retinal hemorrhaging (Lambert, Johnson, & Hoyt, 1986; Gilliland, Luckenbach, &

Chenier, 1994; Betz et al., 1996; Gilliland, Luckenbach, & Chenier, 1994; Kapoor et al., 1997). There appears to be evidence that bilateral SDH and retinal hemorrhaging would indicate abuse while unilateral injuries would be associated with accidental impacts or falls (Duhaime et al., 1996). This also leads to the belief that to get bilateral SDH and retinal hemorrhaging the infant would have been shaken vigorously about the sagittal plane (Gilliland & Folberg, 1996; Levin, 2000). Further, Levin defines SBS as aform of child abuse "in which the perpetrator violently shakes an infant resulting in brain, skeletal and/ or retinal haemorrages" (p. 151). However, the force required to cause SBS associated injury is not agreed upon and is a source of controversy. As Caffey defines SBS it appears that only severe shaking of the head is needed. In addition, arguments have been made regarding the frequency of shakes. Is it one or several? What are the manners of these shakes? It appears that there needs to be an extreme amount of shaking according to a postmortem study with perpetrator confessions (Betz, Püschel, Miltner, Lignitz, & Eisenmenger, 1996).

In addition, accidental injuries have typically not shown similar patterns of retinal hemorrhaging or SDH as those attributed to SBS (Elder, Taylor, & Klug, 1991; Johnson & Braun, 1993; Reiber, 1993; Duhaime et al., 1996). Concerning fall accidents, Chadwick et al. concludes that falls of less than four feet that are reported to cause fatalities are inconclusive and falls from buildings and the like are more accurate to look at when studying injuries due to falls (1355). Deaths from falls four feet or less are suspicious. At the same time, diagnosis of abuse can be wrong (Kirschner & Stein, 1985; Weissgold et al., 1995). Careful examination is needed to avoid false accusations of abuse.

There are two camps of belief with regards to SBS. Duhaime et al. concluded that shaking alone could not generate enough force to cause subdural haematoma. Supporting their findings were lifelike dolls with accelerometers affixed to their heads. These dolls were then shaken violently and then shaken followed with an impact to the head. Comparing the mean head acceleration to known tolerance criteria led to the conclusion that shaking alone was not the cause of acute subdural haematoma.

However, this study has been under scrutiny. Specifically, the dolls used are not representative of the infant. Morison (2002) built a model that included the cerebrospinal fluid layer (CSF) that surrounds the brain. This CSF layer can be up to 10 mm thick as compared to 1-2 mm thick in adults. Morison's model showed that the brain in the CSF could not resist the shearing forces imposed on it. Looking at the bridging vein response showed that failure occurred when simple harmonic oscillations were applied. Morison assumed a position where the baby is held by the torso and is shaken back and forth. Morison concluded based on the breached stretch ratio of the bridging veins that indeed "shaking can be just as dangerous as hard impacts, and considerably more dangerous than soft impacts" (p. 106).

Retinal Hemorrhaging

The assertion is made that "retinal hemorrhage is perhaps no more specific as fracture and one surely would not suggest that all fractures are the same in terms of pathogenesis or aetiology" (Levin, p. 157). Further retinal hemorrhages can be

described by the location and severity. Kapoor, Shiffman, Tang, Kiang, and Woodward (1997) describe the mapping of the hemorrhages in the different layers of the retina (e.g. preretinal, intraretinal, subretinal). Lancon, Haines, and Parent (1998); Betz et al. describe the distribution of hemorrhages. Lambert, Johnson, and Hoyt (1986) examined optic nerve sheath hemorrhages. Optic nerve sheath hemorrhaging is perhaps attributed to the slack in the nerve sheath combined with the passive response of the ocular muscle attachments (Levin). Green et al. (1996) concludes that hemorrhages were most likely to occur in the posterior pole in a study including 16 children who had died from SBS. Gilliland, Lieberman, Milroy, and Parsons (1996) claim that these peripheral retinal hemorrhages are from acceleration-deceleration injury with a few cases involving direct head trauma. Levin concludes, "The findings of massive hemorrhages throughout the retinal surface at all layers reflects a shaking aetiology [(i.e., the study of cause)] unless proven otherwise. Traumatic retinoschisis [(i.e., splitting of the retina)] has only been reported in SBS" (p. 161). Hadley, Sonntag, Rekate, and Murphy (1989) report a 100% incidence of retinal hemorrhaging from children who died from SBS. However, in another study this rate has been reported as low as 49%-57% (Gilliland & Folberg, 1996). In yet another study with 16 children, 81% had ocular abnormalities (Green et al., 1996). Studies conflict saying that vitreous hemorrhaging is not common, 27% occurrence (Pounder, 1997), and then another study claims 100% occurrence (S. G. Elner, V. M. Elner, Arnall, & Albert, 1990) in postmortem studies. Also, postmortem studies indicate the distribution of the hemorrhage to be mostly posterior but also mention that it can extend anteriorly as far as ora serrata (Green et al.; Betz et al., 1996). The

pathophysiology of retinal hemorrhages is unknown in SBS (Levin). However, Green et al. explains that the force based on statistics is relatively small to create intraretinal, subhyaloid (i.e., canal located in the vitreous body that supplies nutrients to the anterior eye), or optic nerve sheath hemorrhage than for retinoschisis, choroidal (layer between the retina and sclera), or vitreous hemorrhages.

Extending the pathophysiology of retinal hemorrhages, Terson syndrome is compared to SBS (Levin). A characteristic of Terson syndrome is the optic nerve sheath hemorrhage (Betz et al.; Levin). Terson syndrome has been used to describe SBS postmortem studies. However, Terson syndrome can happen without the optic nerve sheath hemorrhage (Levin). Further, Bedell (1955) explains that SBS can occur with subdural optic nerve sheath hemorrhage without intracranial hemorrhage. Brinker et al. (1997) argue blood located in the optic nerve sheath results from intracranial pressure. However, Paton (1924) and Levin contradict this. Levin believes that the mechanism is due to orbital shaking causing direct trauma to the optic nerve. Further, Levin explains for this to be a fluid problem, blood would have to be found along the entire length of the optic nerve, and this is not considered in the postmortem studies carried out by Green et al. Therefore, Terson syndrome may resemble SBS but arguments show that there is no relation. Levin concludes that an overwhelming majority of SBS victims with retinal hemorrhages do have intracranial bleeding despite the exceptions.

The vitreous in an infant is well attached to the retina in the posterior pole, peripheral retina all the way to the ora serrata (Hogan, 1963). In addition, the vitreous is more viscous in infants than children and adults (Matthews & Das, 1996;

Ferrone & de Juan, 1994). As a result, the retina of a child is more resistant to mechanical stress (Feldman, Brewer, & Shaw, 1995). When an infant is shaken, the vitreous causes shear stresses at the points of attachment (Sebag, 1991). The posterior retina can be sheared in any of the layers (Levin). Tongue (1991) mentions that one cannot be certain that the retinal folds are a causation of child abuse. However, Levin; Weinberg and Tunnessen (1996); Andrews (1996); Betz et al.; Bedell; Spaide, Swengel, Scharre, and Mein (1990) disagree; retinal folds are caused by SBS. Further head trauma is not needed to cause retinoschisis (Massicotte et al., 1991). The vitreous is also well attached to the superficial retinal blood vessels (Levin). Therefore, at detachment, these blood vessels can rupture due to shearing (Andrews).

As mentioned before, the optic nerve has slack that allows movement of the eye. This may also allow the eyeball to shake when the child is shaken. The eye is tethered via the muscle attachments and may explain the findings in optic nerve sheath hemorrhages (Budenz et al., 1994). Further, this would imply that the problem is not a fluid mechanics issue (Green et al.). Interestingly, all infants involved in SBS in Budenz et al. had intradural hemorrhages of the optic nerve sheath. Clearly, there are conflicting accounts of the injury mechanism of retinal hemorrhaging. Studies try to compare the retinal hemorrhaging in SBS with other symptoms. Current research on the magnitude and type of force are still inconclusive. Further, the word 'retinal hemorrhage' is used loosely as it may describe the overall phenomenon of hemorrhaging in the eye. Clinical studies have shown hemorrhaging in just about any portion of the posterior pole with a few cases describing hemorrhaging towards the

anterior. In addition, the physiological make up of the eye in the infant is different from a child or adult (e.g., the vitreous being more viscous and firmly attached to the retina).

Biomechanical Eye Models

Several Eye models exist to examine blunt trauma or intraocular pressure (Kobayashi, Woo, Lawrence, & Schlegel, 1971; Woo, Kobayashi, Lawrence, & Schlegel, 1972a; Woo, Kobayashi, Schlegel, & Lawrence, 1927b; Vito & Carnell, 1992; Uchio, Ohno, Kudoh, Aoki, & Kisielewicz, 1999; Power et al., 2002; Stitzel, Duma, Cormier, & Herring, 2002). Woo et al. (1972a & b); Kobayashi et al.; Vito and Carnell modeled the cornea-scleral shell with two-dimensional finite element analysis utilizing symmetry. These computer models were used to investigate intraocular pressure (IOP). Both the Kobayashi et al. and Vito and Carnell models considered an elastic modulus for the material properties. And both studies considered incompressible material as well (i.e., Poisson's ratio is 0.49). However, Woo et al. (1972a & b) approximated the moduli of the sclera, cornea to be exponential. Further, a Poisson's ratio of 0.49 was assumed for nearly incompressible tissue.

Uchio et al. (1999) furthered the modeling to include a full eye geometry including a rigid body lens and attachment to the cornea representing the ciliary body. The cornea and sclera were modeled using shell elements and the aqueous humor and vitreous body were modeled using solid elements. The actual material properties are unclear for the aqueous and vitreous as the only mention of material properties is that

it is modeled with a hydrostatic pressure of 20 mm Hg. The Uchio et al. geometry of the cornea-sclera shell varies in thickness in anterior to posterior and is denoted in a midsagittal view of the eye. In addition, Uchio et al. determined the stress-strain relationship of the cornea and sclera to be nonlinear and did strip tests to measure this. In addition, Poisson's ratio was calculated from the strip tests and did not equal 0.49 as assumed in the previous two-dimensional model studies. Uchio et al. built this eye model to investigate the behavior (i.e. stress-strain and failure) of the eye response to impacts with a blunt object to determine the threshold of penetrating ocular injury. Later studies utilizing the Uchio et al. eye model studied the effects of air-bag impacts (Uchio, Kadonosono, Matsuoka, & Goto, 2004) and airbags with photorefractive keratectomy (Uchio, Watanabe, Kadonosono, Matsuoka, & Goto, 2003). A major limitation in the Uchio et al. eye model highlighted by Power (2001) is that the boundary conditions of the eye are not modeled. The eye is supported to the posterior pole to the socket of a rigid body skull.

Power and Power et al. considered several components of the eye while using geometry and material properties from previous literature. The Power model considers the cornea and sclera with material properties from Uchio et al., and geometric properties described by Woo et al. (1972a & b). The lens and ciliary body, like Uchio et al., are considered. The lens is rigid while the ciliary body is a tension only elastic muscle with an initial guess on the material properties. Similarly, the six ocular muscles that tether the eye use this same guessed muscle model. The aqueous humor and vitreous body are also guessed quantities based on the properties of fatty tissue (Todd & Thacker, 1994). The geometrical properties of the lens are based on

visual anatomy sources. This eye complex is then inserted into a rigid body socket with the muscle tethers attached. The socket void is then filled with fatty tissue from Todd and Thacker. This fatty tissue is modeled as linear elastic material with Poisson's ratio of 0.49. The parametric study concluded with the head complex affixed to a Hybrid III 50 percentile dummy model and tested. Power et al., did mention a validation of the eye model using (Scott, Lloyd, Benedict, & Meredith, 2000; Vinger, Duma, & Crandall, 1999). In the Scott et al. study, projectiles of various sizes are impacted into porcine eye samples to study the kinetic energy and visualize ocular failure. In the Vinger et al. study, unembalmed cadaver eyes are mounted into a fixture and impacted with baseballs to investigate injury levels.

The Stitzel et al., eye model is designed for high deformation rates. Further, the material properties use an orthotropic material with nonlinear stress-strain in plane and a nonlinear shear modulus. Additionally, a separate constant is used for the compressive modulus. Like the Power and Power et al. model, Stitzel et al. utilizes the material properties from Uchio et al. The geometric detail of the lens and ciliary body is enhanced compared to the Power model. However, the muscles of the ciliary body are adapted from the Power material properties, which were based on an initial guess. The aqueous and vitreous are modeled using the Eulerian approach to model fluid in contrast to the Power model. Testing similar to the approach in Vinger et al. is done and compared to the simulation model. However, unlike the Power model, the validation process is more rigorous with experimental-simulation comparisons with a spherical ball (i.e., a BB pellet), a foam cylinder modeled after foam in a typical car interior, and a baseball.

Optic Nerve and Related Studies in Pia-mater and Axonal Materials

The modeling of the optic nerve head and optic nerve sheath remain underdeveloped as compared to the cornea-sclera models mentioned above. This is actually quite surprising as this area of the eye is of interest in the study of glaucoma (Morrison, 1995; Quigley, 1995; Anderson, 1995). However, mostly histological studies cover the lamina cribrosa and the scleral tissue anterior to it in response to intraocular pressure (IOP) (Bellezza et al., 2003; Jonas, Berenshtein, & Holbach, 2003; Jonas, Gusek, Holzmann, & Naumann, 1988; Jonas, Maradin, Schrehardt, & Naumann, 1991; Jonas & Buddle, 2000; Quigley, 1981; Quigley, Flower, Addicks, & McLeod, 1980; Swindale, Stjepanovic, Chin, & Mikelberg, 2000; Britton, Drance, Schulzer, Douglas, & Mawson, 1987; Caprioli & Miller, 1988; Ethier et al., 1999; Levy & Crapps, 1984; Rohrschneider, Burk, & Völcker, 1993; Yan, Flanagan, Farra, Trope, & Ethier, 1998; Hernandez, 2000). These studies are useful but incomplete for building a computer model. Dimensional properties and boundary conditions can be gathered from these histological studies however.

Dongqi and Zeqin (1999) and Edwards and Good (2001) both propose a mathematical model to predict behavior due to IOP on the lamina cribrosa. Both studies examine the lamina as a circular plate and base the calculation on elastic stress-strain theory. This study assumes isotropy; however, the lamina cribrosa is reported to be porous (Morrison, 1995). Comparing the theoretical values with experimental data, Dongqi and Zeqin show a good prediction on a displacement versus IOP plot. Edwards and Good make similar assumptions as Dongqi and Zeqin but adjust the Young's modulus to fit experimental data of displacements. The

predictability of this model is examined by plotting displacement versus radial position and shows to be within a reasonable range. However, the displacement versus IOP appears to have an "approximate agreement" (Edwards and Good, p. 218).

Two other studies are conducted that use finite element modeling to examine and predict optic nerve head (ONH) behavior (Bellezza, Hart, & Burgoyne, 2000; Sigal et al.). Bellezza et al. considered a half, idealized (i.e. perfectly spherical and of uniform thickness) sclera shell of solid elements. This sclera shell is built with two layers except at the posterior end where there is only a single layer of elements representing the ONH. The scleral material is adapted from Kobayashi et al. An interesting suggestion in Bellezza et al. is to model within the ONH the axonal bundles. The axonal modulus is an initial guess based on the modulus from Kobayashi et al. to be two magnitudes of order less. Bellezza et al. justify this to be appropriate because "the axons are likely to be compliant and unlikely to bear significant load" (p. 2994). The study tests the sensitivity of geometry features with imposed IOP. There is not a validation and Bellezza et al. conclude that more work needs to be done and stress that this is an initial investigative study.

Sigal et al. stress the importance of geometry and expose the mathematical models previously presented (Dongqi and Zeqin; Edwards and Good). In addition, Sigal et al. highlight the differences from the Bellezza et al. model and include biofidelic geometry in a progression of models. The mesh data is extremely refined and includes varying sclera thickness at the posterior region. In addition, a portion of the optic nerve is considered and composed of the pia mater, CRA (central retinal artery), scleral tissue, lamina cribrosa, and neural tissue. These values are based on

previous literature and are all elastic and isotropic. The mesh utilizes a shell element labeled as a 2-D 8-Node Structural Solid (Ansys, 2005). Therefore, the model is only a cross-sectional view with a slice along the equator. Sigal et al. determine that the CRA does not contribute to the ONH biomechanics. However, this may be due to the simplification of the CRA and the boundary conditions of the CRA wall assumed to be attached to the neural tissue. Sigal et al. decided to investigate another model in a parametric study that neglected the CRA. Despite the biomechanical materials used, Sigal et al. stress that very little is known about the CRA and pia mater and so values are adapted to these structures. There is a comparison with tomography images with IOP induced. However, Sigal et al. are careful not to conclude a validation and mention, "this finding implies that scanning laser tomography has limited ability to estimate lamina cribrosa deformation" (p. 4378). In addition, Sigal et al. stress, "biomechanical effects … depend strongly on scleral properties" (p. 4378).

Concerning the vascular physiology Sigal et al. is the only study to consider the CRA. Further details of the vascular physiology are considered by Bill (1993) in regards to glaucoma but are only a clinical study. Gundiah, Ratcliffe, and Pruitt (2007) determine the strain energy function for arterial elastin utilizing thoracic aortas from adult porcine. The mechanical testing apparatus employed a biaxial stretcher (similar to that used by Rivlin and Thomas in one of the experiments of material determination of rubber). The study concluded with mention that the Mooney-Rivlin data did not adequately fit and a neo-Hookean model is able to model the arterial elastin much better (coefficients given are 162.57 kPa for the autoclaved sample and 76.94 kPa for the alkali extracted sample). However, it is not clear if these

mechanical properties for the arterial elastin would be appropriate to use to model the CRA in the optic nerve.

Also furthering the biomechanical work presented by Bellezza et al., Downs et al. (2003)[1] present a study that fits the peripapillary sclera (i.e. ONH area) with a linear viscoelastic equation. Sclera tissue is extracted from rabbit and monkey eyes. Several samples are taken at different orientations using a cutting die to get precise sample dimensions. However, the thickness measured under a microscope was averaged for each sample over the area. Ultimately, the study determines the long and short-term moduli (i.e. E_0 and E_∞). In addition, the short and long term time constants are determined. A comparison is made between the rabbit and monkey stress relaxation curves. The monkey sclera is determined to be stiffer and exhibits a slower relaxation. The limitations presented by Downs et al. are the constant thickness of the samples and the impossibility of removing the episclera. In addition, orientation is considered when excising the sclera samples, all but radial orientation. Downs et al. mention that the fibril orientation in this direction may demonstrate a stiffer response, and further, the anisotropy of material cannot be determined from tensile tests performed in this study.

Burgoyne, Downs, Bellezza, Suh, and Hart (2005) elaborate on the model from Bellezza et al. utilizing material properties determined from Downs et al. A technique of continuum finite element models is used where each continuum element represents a model of a micro-finite element structure. The continuum element will be the boundary conditions for the micro-finite element structure and the material

[1] Downs et al. (2003) and later mentioned Burgoyne et al. (2004) are continuations and refinements from the original Bellezza et al. (2000) study.

orientation of the continuum will be based on the micro-finite element structure. Downs et al. mentions that this provides an optimal computation of the ONH. Downs et al. reports that the initial results from the micro-finite element structure produced von Mises stresses many times higher than the continuum element. This mapping of stresses from continuum element to substructure is an interesting approach, and Downs et al. plan to extend the study to include astrocytes (Ellis, McKinney, Willoughby, Liang, & Povlishock, 1995; Lamb, Harper, McKinney, Rzigalinski, & Ellis, 1997) and retinal ganglion cell axons (Triyoso and Good, 1999; Jafari, Maxwell, Neilson, & Graham, 1997; Bain & Meaney, 2000).

Hayreh examines the optic nerve sheath of rhesus monkeys, humans, and rabbits (1984). Of particular interest is the description of the nerve sheath just posterior the sclera attachment is described to be rather bulbous with a larger space between the optic nerve and dura. Observations in cadavers showed wrinkling in this area that became bulbous with injection. These wrinkles are non-existent posterior the nerve. Dissection of the sheath from the nerve was achieved with little resistance. Despite this particular paper being a purely clinical and pathological review, it highlights important features of the optic nerve and also agrees with the bulbous area of the optic nerve from the transverse slices of the Visible Human Project. Other research related to the optic nerve is the various microanatomy studies on axonal nerves in guinea pigs. Guy et al. examine axon and Fiber diameter of guinea pig optic nerves in detail and they report a mean diameter of 1.18 micrometers (1989). Thresholds of axonal damage reported for the optic nerve in adult male guinea pigs is a strain of 0.21 (Bain & Meaney, 2000). This is considered to be the optimal strain at

which false negatives and false positives are prevented. However, it is not clear if these can be translated to humans. Observations of the fiber alignment of the sclera shell and optic nerve sheath are made and compared. These histological comparisons show that the sclera and dura collagen are large and non-uniform as opposed to the optic nerve sheath, which is smaller and uniform (Raspanti et al., 1992). This would indicate that both these structures would respond to mechanical loading differently.

Human spinal cord pia mater biomechanical properties are investigated (Mazuchowski & Thibault, 2003). In this study, the stretch ratio is determined to be 1.1 at which plastic deformation started. This pia mater is considered, as it is one of the substructures of the optic nerve. Further, this study concludes with an average elastic modulus of 1.4 MPa. While this sample was tested in vitro, another group (Chang, Hung, & Feng, 1988) did an in-vivo study of the viscoelastic properties of the spinal cord of cats. The test determined the viscoelastic response of the spinal cord under a uniaxial experiment. A comparison of gray and white matter of rabbit spinal cord is investigated and the moduli are determined (Ozawa et al., 2001). The value reported by Ozawa et al. is averaged to be 3.3 kPa. Mechanical tests on cadaver spinal cords reveal nonlinear stress-strain response with relaxation observed over one minute (Bilston & Thibault, 1996). The data is fitted to both hyperelastic and viscoelastic models.

Optic nerve sheath diameter measurements are studied using sonographic measurements in normal adults (Ballantyne et al., 2002). Three measurements are made of each eye in the sample pool and within a narrow variation. The mean optic nerve sheath diameter is reported to be 3.2 mm. This value is within the same range

observed in the Visible Human Project transverse slices. Mean nerve diameters are reported to be 3.2 ±0.4 mm anteriorly to 2.6 ±0.4 mm posteriorly (Lam, Glasier, & Feuer, 1997). In addition, the sheath diameter is reported to be 5.2 ±0.9 mm anteriorly to 3.9 ±0.4 mm posteriorly by Lam & Feuer. Ultrasound measurements of the optic nerve sheath diameter of children age 10 days to 13 years old are examined (Newman et al., 2002). Also noted in this clinical study are indications of whether the optic disc appears normal or has some abnormalities. This study is particularly useful in comparing the scaled infant to clinical observations.

Infant Brain Studies/Infant Skull Studies/Adult Brain Studies

Morison (2002) created a biomechanical model of the brain and bridging veins to model SBS. The literature review of this SBS is divided in two parts: in support of pure shaking and shaken impact syndrome. The latter group is fairly sparse with Duhaime et al. (1987) being the main proponent of shaken impact syndrome. There appears to be overwhelming support for pure shaking. Further review of brain scaling methods along with describing the importance of the rotational component in head injury is reviewed. Possible candidates for bridging veins and brain materials are examined. In addition, physical testing on a small sample of infant bridging veins is conducted with the ultimate conclusion being that testing these fragile veins is difficult and suffers from breakage.

The sample pool of bridging veins was relatively small and the spread of failure due to stretch varied. A vein could very likely break at 15% strain. Despite

this, there was good repeatability at low strain rates that allowed the usage of the force-displacement of a typical sample in the biomechanical model. This was done by specifying spring elements between nodes of the brain (nine in total) and applying this force-displacement curve in a non-linear spring formulation. This allowed the complex model to display very simple results that could allow for definitive answers on bridging vein stretch. Morison also mentions that the current quoted ultimate stretch of 1.5 may be significantly overestimated and failure can occur, as seen in the testing, at rates lower than this. Essentially, any maximum stretch ratio seen in this biomechanical model should be considered a possibility for failure.

The brain materials considered in this work are tabulated showing the bulk, short and long term modulus, and decay constant. Morison makes particular distinction between the studies that include the cerebrospinal fluid layers (CSF) or the lack of this layer. Either previous works disregard this important layer by fixing nodes of the skull to the brain, model with friction (frictionless) contacts, or create a "soft solid" layer between the skull and brain. One of the key features in this biomechanical model is the CSF layer that is modeled as a fluid using a coupling between the Lagrangian mesh to a Eulerian mesh by an Arbitrary Lagrange Euler (ALE) coupling algorithm. This allows the fluid to be modeled without concern to extreme deformation of the Lagrange solid elements that would be considered in a "soft solid" layer. Modeling this fluid layer is particularly important in infants as the CSF is up to 10 mm in thickness as opposed to 1-2 mm in adults. Ultimately, the properties of Zhou et al. (1996) are chosen as they provide several data points of the

complex shear modulus and a method of conversion to the short and long term modulus and the beta constant.

The motion of brain model is made to be simple harmonic rotation by specifying the moment arm of the neck to the head assuming that the perpetrator of the shaking would more likely grab the torso. The frequency of the shake is 4 Hz and is documented in Duhaime et al. (1987) in a plot showing the acceleration trace of four peaks with the distance from the start of the first peak to the end of the last peak equal to 500 msec. In addition, this was determined to be the limit that an adult could possibly shake an infant. The amplitude of this harmonic motion is made to be ±60 degrees and represents the limits of motion of the system.

The positional information is then converted to rotational and translational velocity and applied to the rigid body skull that encases the brain model. The positioning at the start of the simulation is located at –60 degrees and represents the head location close to the torso. The simulation is run for four cycles, and it is noted that the first peak of the stretch ratio is the highest. This observation is explained to be caused by subsequent oscillations having the brain compressed. At the start of the simulation the brain is centered in the skull and would have more travel causing a higher stretch ratio. Morison concludes that the first shake could still be the worst however.

Ultimately, this work provides valuable insight on bridging vein failure under documented motions from previous motions of SBS. Morison varies the frequency and amplitude of the shakes conducting parameter studies and also compares to impacts with soft and hard surfaces. Comparison of the 4Hz, ±60 degree shakes with

the hard and soft impact shows stretch ratios greater than 1.2 for the hard surface and shake. The shake is actually a little worse with regard to the stretch ratio than for the hard surface. The soft surface impact shows the stretch ratio between 1.1 and 1.15. Morison mentions that future work would include improvements to the brain model, parameter studies on different height/weights, more motion studies, and inclusion of eye components to investigate retinal hemorrhaging.

The Morison study made the assumption that the skull is rigid when compared to the brain dynamics. Typically, this assumption has been made for investigative studies looking at brain damage and axonal injury (Brands, 2002; Brands, Bovendeerd, & Wismans, 2002; Prange & Margulies, 2001; Zhou, Khalil, & King, 1996). One study investigates (Lapeer & Prager, 2001) the biomechanics of the fetal skull subject to uterine pressures under birth. The skull is modeled using laser-scanning techniques to create a detailed final mesh with separate fetal skull bones connected by fontanelles and sutures using a Mooney-Rivlin model with $C_1 = 1.18$ MPa and $C_2 = 0.295$ MPa (Rivlin & Thomas). These values are used from previous studies of fetal dura mater. The cranial bone of the infant is thin and yielding uses an orthotropic material formulation with $E_1 = 3.86$ GPa, $E_2 = 0.965$ GPa, $\nu_{12} = 0.22$ and, $\nu_{21} = 0.055$. Lapeer & Prager conclude that the deformation of the fetal skull is in good agreement with clinical experimental data. Marguiles and Thibault (2000) also investigate the infant skull and suture properties. Measuring infant cranial bone and porcine cranial bone showed similarities between the two allowing further investigation into the infant porcine suture properties as well. An idealized skull mesh with the sutures was created for finite element analysis. A brain mesh using

linear viscoelastic solid properties ($G_\infty = 2.32x10^{-3}$ MPa, G_0= 5.99x10-3 MPa and $\beta = 0.09248\ s^{-1}$) is modeled and shares the same nodes as the skull cap modeling no slip at the interface. Impacts determined by Duhaime et al. (1987) are used for loading conditions, and the results conclude that the cranial suture is not capable of absorbing shock in the infant. This shock absorption increases with age and while the pliant skull and sutures are important for newborns, this does leave them vulnerable to injury.

Considering axonal injury in infant brains, Prange and Margulies (2001) examined 3-5 day-old piglet brains subjected to non-impact rotations. The locations of injury in the white matter of the axons were documented, and a finite element brain using material properties based on Ogden hyperelastic and viscoelastic material is made. The mesh, tetrahedral, contained 49565 elements encased in a rigid skull. Angular velocity is applied and the locations of axon injury previously determined in the white matter are compared to the equivalent element locations. The results yielded show to be greater than adult guinea pig axonal threshold strain at 21%. Metz, McElhaney, and Ommaya (1970) make a comparison between elasticity of live, dead, and fixed brain tissue. The experiment involved insertion of a cylinder into the brain tissue that was encased in a rubber membrane, which was expanded with fluid. This tube was inserted in anesthetized adult Rhesus monkeys and then again in another location after sacrificed. The experiment is repeated again after perfusing fluid into the heart. The modulus[2], E, is determined by (2.0) and plotted versus inflation. It is observed that the modulus increases after death and fixation and that

[2] Terms and nomenclature are with respect to the sourced documents. In this case Poisson's ratio is labeled as μ where typically it is referred to as ν in other texts.

the elastic modulus increases concavely upward with strain varying between $1x10^5$ and $3.5x10^5$ dyn/cm^2.

$$\delta = \frac{P_1 r_1}{E}\left[\frac{r_2^2 + r_1^2}{r_2^2 - r_1^2} + \mu\right] \qquad (2.0)$$

Where P_1 = internal pressure, r_1 = internal radius, r_2 = external radius, E = elastic modulus, μ = Poisson's ratio, and δ = radial deformation.

Margulies and Thibault (1992) propose a criterion to use for diffuse axonal injury (DAI) in place of the current HIC[3] (head injury criteria). In this research they consider animal studies, analytical model experiments, and physical models. Animal studies consisted of inducing comas in baboons by moving the head suddenly in rotation without impact. The brains are then excised and examined. The threshold of injury is compared to the load time history. The analytical models utilize a viscoelastic solid material for the human and baboon brain simulations. The physical models involved filling human and baboon skulls with a transparent material representative of the brain. Deformations of an orthogonal grid inserted into this material are recorded, and the shear strain is noted. Compiling all of these techniques concludes the critical strain ranged from 0.05 to 0.10 for moderate to severe DAI in areas of interest.

Ellis et al. (1995) created a model to characterize the stretch-induced injury of cells of brain origin. This involved using rat cortical astrocytes by creating a cell culture on a silastic membrane and inducing controlled stretch by applying a pressure pulse. Ellis et al. record the membrane deformation versus pressure. The

[3] The head injury criterion (HIC) is an injury index for the head defined by the U.S. government (MADYMO, 2004).

morphologic examination of the astrocytes did not detach from the membrane. Some of the cells did show swelling when exposed quickly to a deformation. The test is developed to provide a simple, reproducible in vitro method of studying the mechanical injury to cells.

Zhou, Khalil, and King (1996) built a three-dimensional model of the human head with rigid body skull and viscoelastic brain material. Morison (2002) uses the viscoelastic materials from Zhou, Khalil, and King (1996). Deducing the complex modulus from Shuck, Haynes, & Fogle (1970) the short and long term shear modulus and beta constant is determined using the empirical inter-conversion equation from Christensen (1982). The study differentiated between the white and gray matter assigning different short and long-term shear moduli but keeping the same beta constant. From Zhou, Khalil, and King (1996) the $G_0 = 41$ kPa, $G_\infty = 7.6$ kPa, and $\beta = 700\ s^{-1}$ for white matter. $G_0 = 34$ kPa, $G_\infty = 6.3$ kPa, and $\beta = 700\ s^{-1}$ for gray matter. The original study (Shuck, Haynes, & Fogle, 1970) determined the complex shear moduli by testing specimens from human and monkey brains. Further, Zhou, Khalil, and King (1996) scaled impact test results using Holbourn's scaling law as a basis to scale from rhesus monkey brain to human. Not only did they do mass scaling, but they considered time scaling as well. They conducted parametric studies and showed that material properties of the brain have influence over the stretch of the parasagittal bridging veins.

An investigation of the pressure-volume relationship of the CSF space has been done (Sahay & Kothiyal, 1984). From this, a qualitative study discusses a new modeling technique using a hyperelastic spherical model. Comparing to an actual

CSF pressure-volume curve shows a similarity when using this model. One of the deficiencies in this model is that the hyperelastic model does not take into account the history-dependence of soft biological materials. Sahay and Kothiyal highlight the fact that, while more accurate, viscoelastic modeling would involve more complexity than the current proposed model using two constants.

Miller (1999) determined the mechanical properties of the brain using a combined hyperelastic and viscoelastic formulation. Porcine brain was used in this study and procedure compressed the sample in unconfined compression. Using these results and varying the loading velocity so as to determine time constants, a total of four parameters are left to be determined. This formulation agreed very well with finite element analysis and has the benefit of modeling large deformations and requiring fewer parameters than in non-linear modeling.

Lippert, Rang and, Grimm (2004) determine the material properties of the brain at frequencies greater than 400 Hz. The argument is made that the simulation range includes higher frequencies and therefore material testing should be done in higher frequencies as well. The testing approach involved separating a lamb brain into white and gray matter with no regard to maintaining cell structure. Intentionally disturbing the fine structure allowed for the brain material to become homogenized. In addition, a sample from more than one lamb is used with the understanding that the study is to consider the average material properties. The testing method employed involved stuffing the brain matter into test tubes and sending a pressure wave through the material. Referred to as the “wave-in-a-tube” (Lippert, Rang, & Grimm, 2004) method, the pressure wave undergoes partial mode conversion and is turned to a shear

wave. Once at the other end the wave is converted back to a pressure wave. The difference in the wave can be used to determine the elastic material properties as long as the material is homogenous (explaining the reasoning behind mixing up the brain matter). This method is used to determine the complex material properties but is unable to determine the components of those properties. Thus the complex shear can be determined, but the G' and G" cannot be found (2.1).

$$G^* = G'(\omega) + iG''(\omega) \qquad (2.1)$$

Where G* is the complex shear modulus, G' is the storage shear modulus, G" is the loss modulus.

This study calculates the complex bulk modulus while other researchers base their values on observations. Typically, the standard value for Poisson's ratio is 0.5 for brain matter. This is a valid assumption based on observations that the material is incompressible. This study reports a range within 0.3140 to 0.4715 for Poisson's ratio and is expected, as the moduli determination at the higher frequencies is much larger. The study investigates pressure waves all the way to the 10 MHz range.

Brands (2002) built a model containing a non-linear viscoelastic formulation for use in predicting brain injury in head impact simulations. In this work, numerical accuracy is discussed. Wave propagation inside brain tissue should be considered, and the rule of thumb of 24 elements per wavelength is suggested for accurate modeling. In addition, FE codes using explicit time integration methods such as MADYMO (2004) should use a time step such that speed of the fastest wavelength multiplied by the time step is smaller than the smallest element size in a given mesh. A highlight of this work is the work on non-linear viscoelastic material development.

Oscillatory strain loading is applied to determine linear viscoelastic properties, and the stress relaxation test is used to determine the non-linear portion of the viscoelastic properties. The bulk modulus is determined from ultrasonic experiments and is equal to the dilatation wave speed through the material squared multiplied by the density of the material. Solid brick elements are used with reduced integration to prevent mesh locking. Simple shear experiments are performed on a rotational viscometer using porcine, gelatin, and silicone gel. The latter two have been used to mimic brain material. A three-dimensional model is studied containing the skull, meningeal layers and CSF, and brain tissue. The model is composed of solid brick elements and is used to investigate the effects of shear softening and to compare different modeling parameters.

Molloy et al. (1990) determine the force needed to traverse a small metal sphere through brain material using in vitro canine specimens. This group concluded the force needed to move a three-millimeter sphere to be 0.07 ±0.3 N. The purpose of the work is to investigate the possibility of moving a thermal-seed through the brain material for use in eradication of brain tumors. Unlike the work of Weber and Landwehr (1982) and Lee, Litt, and Buchsbaum (1992), which use manipulation of metallic spheres for mechanical property determination, no information is provided on the displacement-force characteristics that would be suitable for use in biomechanical modeling. Continuing a review of magnetic manipulation instrumentation, Gillies et al. (1994) provide a comprehensive overview of the technological advances of this method.

Vitreous Body

The importance of the vitreous in SBS is considered (Levin; Andrews). Unlike the Power and Power et al. model, the vitreous is a viscoelastic gel-like substance (Wolter, 1961) and should not be considered linear elastic. Tokita, Fujiya, and Hikichi (1984) measured the viscoelastic properties of a bovine vitreous to determine the complex shear modulus[4]. The storage and loss shear moduli are plotted versus frequency. The test apparatus employs a torsion pendulum.

Bettelheim and Wang (1976) used bovine eyes as well to determine the complex modulus. The testing in Bettelheim and Wang involved the placement of chucks in directions running laterally, along the Cloquet's canal, and obliquely. Careful cuts are made and the chucks are placed. From this setup, the storage and loss moduli are examined at different frequencies for different samples. There are small differences, but Bettelheim and Wang explain that these differences are consistent and probably are due to the collagen fibers running parallel to the Cloquet's canal. Bettelheim and Wang test the viscoelastic properties of the vitreous using an in vivo method while Tokita et al. employ an in vitro procedure.

The concern with the shearing of the in vitro procedure can cause the collagen fibers to be compromised (Weber & Landwehr, 1982). Therefore, the vitreous would appear to be weaker than it actually is. Weber and Landwehr test the vitreous by inserting a small steel sphere in the vitreous in an attempt to leave the vitreous with the collagen fiber network intact. Assuming a Voigt-Kelvin model (Flügge, 1967; Drozdov 1998), an equation of motion is assumed for this system given the mass of

[4] Measured in the frequency domain, the complex modulus takes the form: $G^*_\alpha(i\omega) = G'_\alpha(\omega)+iG''_\alpha(\omega)$ where G' is referred to as the storage modulus and G" is the loss modulus (Christensen, 1982)

the small sphere and force amplitude applied sinusoidally. In order to achieve this model, Weber and Landwehr place coiled magnets laterally on either side of the eye. Periodic excitement of the sphere is achieved by energizing these magnets alternately. Plotting this information, the damping and spring constant can be determined which describe the vitreous material. This approach is similar to a viscoelastic material with a spring and damper in parallel (Flügge, 1967).

In an extended study, Weber, Landwehr, Kilp, and Neubauer (1982) examine a larger sample of pig eyes and include the examination of human eyes. Results of the testing determined that the vitreous response of human and pig eyes are similar. Analytical and numerical solutions of the vitreous humor under saccadic movements have been performed (David et al., 1998). This study considers retinal detachment due to tears or holes are more susceptible in myopic eyes. This time dependent shear motion is modeled using material properties fitting a Maxwell-Voigt model from parameters determined from Lee, Litt, and Buchsbaum (1992). The work shows the analytical and numerical solutions to be in good agreement with results showing the motion of vitreous to be dominated by circumferential velocity following the motion of the eye wall.

The rheological properties of the human vitreous are measured (Lee, Litt, & Buchsbaum, 1992) using a microrheometer. Unlike some rotational rheometers, this test leaves the delicate structures of the collagen fibers intack. A four-parameter model is considered when testing the creep response of the viscoelastic vitreous. From a sample of twenty eyes, each is sectioned into three parts, anterior, central, and

posterior. The four-parameter model gives six parameters that are used in comparing the three areas of the vitreous of the human:

μ_m = unrecoverable viscosity in units dyne-sec/cm^2

μ_k = internal viscosity in units dyne-sec/cm^2

τ_m = relaxation time in seconds

τ_k = retardation time in seconds

J_m = instantaneous elastic compliance in units cm^2/dyne

G_k = internal elastic modulus in units dyne/cm^2

The tabulated results are compared and show the unrecoverable viscosity to be almost 3.5 times greater in the posterior region of the eye as compared to the anterior region. The internal elastic modulus is twice as large in the anterior region of the eye as compared to the posterior region. There are differences in all the variables but these appear to be the greatest.

In a second study a comparison is made between the bovine and porcine vitreous and the human (Lee, Litt, & Buchsbaum, 1994). The same methodology is considered when measuring these samples comparing the six parameters of the species together. The unrecoverable viscosity is the greatest in the bovine increasing from anterior to posterior with posterior magnitude of 250. The porcine is considerably lower in magnitude (125) with the anterior and posterior portions showing similar values as opposed to the central, which is extremely small (18). The lowest values are from the human, but like the bovine values increase anterior to posterior with the posterior magnitude of (50).

A similar trend in relative proportions is examined with the internal viscosity parameter as the unrecoverable viscosity. The posterior magnitude of the bovine (20) is four times that of the human posterior region and almost double the porcine.

The compliance parameter in the bovine appears to be uniform in all three sections with the anterior being the greatest (0.06). The porcine samples show the anterior region to be the greatest of all regions from all three species with a value approaching 0.08. The central portion of the vitreous for the porcine is low by four times the anterior region and the magnitude climbs back up in the posterior region to 0.05. The human has the lowest compliance of all with the anterior region being extremely low by three times the central and posterior portions, which are about equal.

The internal elastic modulus for the bovine increases from anterior to posterior with the posterior magnitude over 25. The porcine is about 10 and is fairly uniform through the three sample areas. The human anterior internal elastic modulus magnitude is comparable to the bovine posterior while a sharp decrease in value is indicated in the central and posterior to levels just greater than the porcine (porcine is around 10 and human anterior and posterior is around 12).

The relaxation time is relatively the same in the bovine with the posterior having a higher value greater than 10. Comparably, the porcine anterior and posterior (a little lower for the posterior) are in the 8-9 ranges. However, the central portion of the porcine has an extremely low value of just greater than 2. The human relaxation time is extremely low compared to the bovine and porcine with anterior and central

values approximately ¼ magnitude. The posterior of the human has a relaxation time approaching 2.

The last parameter in the Lee, Litt and, Buchsbaum study compares the retardation time between the three species. The bovine samples decrease going anterior to posterior with anterior magnitude close to one and the posterior around 0.7. As seen in other parameters (unrecoverable viscosity, internal viscosity, elastic compliance, and relaxation time), the porcine retardation time for the anterior and posterior is significantly greater than the central portion with values around 0.8 for the anterior and posterior and ½ that for the central. The human as in the other parameters is lower than the bovine and porcine. The values increase going anterior to posterior unlike the bovine, which decreases in this manner. The magnitude of the retardation time for the human is around 0.3 anterior increasing to around 0.4 posterior.

As can be seen in this study (Lee, Litt, & Buchsbaum, 1994), the vitreous is extremely non-homogenous throughout the sample. In addition, adapting mechanical properties from other species needs scrutiny as the values of the measured parameters show great variation between them. Supplementing this work, Lee, Litt and, Buchsbaum (1994) also look at the concentration of electrolytes, collagen, and hyaluronic acid in each of the three species for each sample divided into anterior, central, and posterior sections. This study also showed considerable differences between the species. The vitreous of the eye (for porcine) is made up of hyaluronan forming a gel and is supported by a fine collagen mesh of type II and IX fibers (Noulas et al., 2002). The hyaluronan (HA) concentrations, in human eyes, increase

going anterior to posterior while the viscosity decreases in this order (Bettelheim & Zigler, 2004).

Vitreous obtained from an autopsy of an infant (9-month-old) is almost entirely gel and retains it shape when placed on a surgical towel exposed to air (Sebag, 1991). Changes in the physical properties are noted when the vitreous is introduced to temperature changes (Kawano, Honda, & Negi, 1982). The viscosity is reduced as the vitreous is heated, while freezing was observed to have less of an effect. Tensile tests have been conducted on vitreous membranes by embedding silk sutures in rabbit eyes (Numata, Constable, & Whitney, 1975). After two weeks the rabbits are killed, and the membrane is prepared for tensile testing. Separate plots for elongation and force in milligrams is reported. Type I membranes broke with 2 to 16 grams of force and with a corresponding elongation of 127- 200%. Type II membranes broke with 200 milligrams to 2 grams of force and the elongation was 51-152% before breaking. The last, type III, broke with 200 milligrams to 5.5 grams of force and elongated to 53-186% before breaking.

The acoustic parameters are determined for human and pig eyes and compared (Thijssen, Mol, & Timmer, 1985). The sound velocity is measured for the cornea, vitreous humor, lens, retina, choroids, and sclera. The vitreous humor of the porcine is measured to be 1497 ± 2 ms^{-1} compared to the human with value 1506 ± 3 ms^{-1}.

Buchsbaum et al. (1984) model the vitreous humor as a homogenous viscoelastic sphere. This study employs the moduli from Zimmerman (1980). Zimmerman (1980) determined the elastic shear modulus to be ½ dyn/cm^2 based on methods where the subject tracks light scattering patterns caused by inducing motion

in the vitreous humor. Zimmerman determined from this study that the vitreous humor is over-damped. Buchsbaum et al. mentions that the Zimmerman method deviates from their in vitro values of porcine vitreous and also from Bettelheim and Wang (1976) for the bovine concluding that there is probably significant differences in human gel properties.

The mechanical properties of hyaluronic acid are investigated (Gibbs, Merrill, & Smith, 1968). The viscoelastic response is measured in an oscillating Couette rheometer. It is observed that the moduli of the hyaluronic acid are a function of concentration, temperature, pH, and ionic strength. However, the vitreous properties are expected to differ as the collagen network has a great influence on the viscosity (Weber & Landwehr, 1982).

Nickerson et al. (2005) creates a cleated rheometry tool for use in testing the mechanical properties of the vitreous humor. This tool proved valuable in preventing slip and thus provides viscoelastic properties that are higher than previously published. The vitreous humor of the eye is described to be a network of collagen type II fibrils with coils of hyaluronan filling the spaces between the fibrils. The G' and G" are reported for bovine vitreous to be 30 Pa and 16 Pa respectively. The G' and G" for the porcine vitreous is considerably lower than the reported bovine vitreous G' and G" with values equal to 9.5 Pa and 3.6 Pa respectively. In addition, the steady state values for bovine are reported to be 6.5 Pa for G' and 2.0 Pa for G". For porcine, the steady state values are 2.6 Pa for G' and 0.65 Pa for G". Nickerson et al. notes that the initial moduli may be closer to the in vivo case while the steady state moduli represents a minimum value (five times lower than the in vivo moduli).

A small puddle of liquid is left behind over a period of time explaining the lower moduli values of the steady state. However, Nickerson et al. maintain that these values are greater than the current viscoelastic properties published.

On the replacement of the vitreous, Chirila et al. (1998) and Dalton et al. (1995) consider various polymers. Dalton et al. provide a comprehensive review of previous mechanical modeling of the vitreous (influenced by the viscoelastic studies and not the work of Weber and Landwehr (1982)). They consider potential substitutes that would have similar magnitudes as previous viscoelastic studies (ten years before the Nickerson et al. study). Of particular importance is the selection of a material that could be injected through a needle and still maintain the proper G' G" moduli.

Retina Properties/ Choroid Properties/ Retinal Adhesion/ Detachment Studies

Mechanical properties of the retina in simple elongation have been performed (Wu, Peters, & Hammer, 1987; Jones, Warner, & Stevens, 1992; Stevens et al., 1992). Wu, Peters and, Hammer explain that there are several studies that investigate the sclera strength and disregard the retina and choroids since these structures are several magnitudes weaker and can be neglected. In this work retina specimens are prepared from bovine eyes. The isolated retina is then sectioned into 13 mm x 5 mm strips. The thickness measurement is not attempted in this study; however, a figure showing the varying thickness in the human eye is illustrated. Three locations are selected for the specimens (meridional with meridional vessel, meridional without

visible vessel and, equatorial). The strips are fastened to the testing apparatus using an adhesive (super glue) and then soaked in a physiological saline solution during the testing process. Applying three loading cycles preconditions the strip samples. It appears that this was done to remove the hysteresis effects as observed in the force versus normalized displacement curves. The effects of strain rate are examined and the retina is shown to be sensitive to strain rate. Failure of these samples is noted with loading of 0.2 grams to 0.33 grams with an extension ratio 1.7 to 1.95. Comparing the tensile strength with the adhesive strength of the retina, it is noted that the tensile is "roughly twice the adhesive strength" (Wu, Peters, & Hammer, p. 67) and is compared with deGuillebon and Zauberman (1972). Concluding with the elastic modulus, it is compared to that of choroidal strips to be an order of magnitude less. The tangent modulus is 0.46-0.58 x 10^4 Pa at a middle stress level of 1.2 x 10^3 Pa.

A mathematical model is developed by Jones, Warner and, Stevens (1992). In this study the retina is regarded as an elastic membrane or sheet. The thickness for this study is assumed to be 0.1 mm and the Poisson's ratio is set to 0.5 for incompressibility. The experimental portion of this study involves excising fresh bovine retina and stretching the sample onto a metal washer with known inner and outer diameter. To maintain a non-slip boundary on the washer butylacrylate cement is applied to the retina. The sample is then placed in a humid environment to prevent the sample from drying out. Then a suture is made with the center of the retina and drop of glue runs down the thread. Measurements of the height and traction force are made. Finally, utilizing the mathematical model by a simple Hooke's law

relationship, the calculated force predicted by the model is compared to the experiment giving a seven percent difference in the forces. From this, the elastic modulus is determined to be $2x10^4$ Pa and is comparable to the work of Wu, Peters, and, Hammer (1987).

Graebel and van Alphen (1977) performed uniaxial measurements on choroids and sclera samples from humans and determined the stress-strain behavior of the scleral strips follow an exponential trend while the choroidal strips follow a power law. Specimens are attached to a loading machine with grips made of sand paper glued to the samples. Strain rate is rather slow with the displacement rate set at about one mm/min. The thickness of the samples is assumed to be 0.16 mm for the choroids and 0.85 mm for the sclera samples. The elastic modulus is determined to be $9.68x10^4$ Pa (this is noted to be the tangent modulus). Graebel and van Alphen emphasize that these samples are taken post mortem, same as Moses (1985), causing the blood in the veins to have drained, which could cause variations from the actual living choroidal elastic modulus.

Moses (1985) determines the modulus using an assumed thickness of 0.002 cm for strip samples 1 cm by 1 cm. The values are tabulated in two sections (meridional strips and equatorial strips) and organized by age. The Young's modulus for the meridional strips on average seems to be larger than the equatorial strips. Averaging the values for the initial test, the Young's modulus for the meridional strips is 3.16×10^4 Gm/cm^2 and 1.28×10^4 Gm/cm^2 for the equatorial strips. The elongation versus grams for eye number seven is plotted and shows the hysteresis

loops during the repeated stress-relaxation cycles indicating the very non-linear nature of this material.

Friberg and Lace (1988) conducted simple tension experiments of choroids and sclera strips from the human eye bank. Testing is done in different locations and orientations of the eye (anterior strips, posterior strips and, radial strips proximal the equator). The average modulus for the choroidal strips is $2.2x10^5$ Pa for the anterior, $7.5x10^5$ Pa for the posterior, and $8.2x10^5$ Pa for the radial strips. The average failure stress is $3.3x10^5$ Pa.

Coleman and Lizzi (1979) determine the in vivo choroidal thickness using radio frequencies. This method allows for measurements to be taken from the living state and the accuracy is better than 20 μm. The retinal thickness is also displaced so that it can be subtracted from the thickness of the retina-choroid. This retina thickness is derived spectrally and is 170 μm in the location of the signal. The choroidal thickness is greatest in the posterior pole and is determined to be 420 μm. This is larger than any previously reported values.

Zauberman and deGuillebon (1972) investigate traction force in rabbits by anesthetizing the rabbits and inserting a glass capillary tube into the eye. Cyanoacrylate adhesive is then inserted into the tube so as to attach the glass tube to the retina. The tube is then pulled inducing retinal detachment in vivo in the living rabbit. The detachment diameter in the living rabbit was observed to be between 0.6 and 0.9 mm. As the tube is elevated, the retina began to tear at a height range of 0.2 to 0.3 mm. The tip of the tube broke away at a height of 0.7 to 1.1 mm. The rabbets are then killed and after a time lapse similar experiments are performed. The

diameter of detachment is noted to be 3 to 8 times larger than in the living rabbit. Tears in the postmortem test are observed when the glass pipe is elevated 0.2 to 0.4 mm in height and total break away occurs at an elevation of 1.8 to 2.4 mm.

In another study, Zauberman and deGuillebon (1972) performed tests on owl monkey and albino rabbit eyes. In this experiment the traction speed is varied and a force transducer is added to the instrumentation. The study quantified low rates of traction to be between 0.2 and 0.8 mm/min, medium traction rates to be 8.5 and 21.5 mm/min and high rates to be 42.5, 85.0, and 425.0 mm/min. Low traction rates resulted in higher retinal detachments and larger areas of detachments. Increasing the detachment rates resulted in lower and smaller retinal detachments. The force versus detachment is shown for the traction rate of 8.5 mm/min. From start of detachment to the start of the tear the slope is roughly 150 mg/mm.

Retinal traction is determined in vivo by Kain (1984) who investigates the retinal adhesion between the retina and pigment epithelium. The method involves inserting micropipette into the retina pigment epithelium layer and injecting Ringer's solution. A second pipette is located on the surface of the bleb (retinal bubble) and attached to a pressure transducer. The pressure versus time is recorded. This test is performed in vitro.

DeGuillebon and Zauberman (1972) measure the force and elongation associated with retinal pealing of retina sample strips 6.5 mm wide by 7 mm in length. The test setup involves placing the sample strip on a suction platform inclined at 23 degrees. The end of the retina is glued to a metallic rod that contains a transducer to measure force. The suction platform is then moved at various rates (8.5,

42, and 210 mm/min). It is observed at pealing rates 2 and 8.5 mm/min the retina pealed smoothly from the pigment epithelium. At the rate of 42 mm/min the choroid would detach from the sclera initially. At the rate of 210 mm/min the retina pealed away erratically and choroids would partially become detached as well. Plots of the force versus pealing rate and percent elongation versus pealing rate are displaced. Cross plotting these two graphs would yield force versus percent elongation and would be suitable for finite element software.

Marmor, Abdul-Rahim and, Cohen (1980) also performed strip testing similar to deGuillebon and Zauberman (1972). Dutch rabbit samples are taken and the strips are placed in a water bath to prevent dehydration. The force versus time of the pealing is displaced. The experimental setup used the same 23-degree orientation as deGuillebon and Zuaberman (1972) in order to minimize tissue drag in the bath medium. Initially, the force spikes past 100 mg and drops down sharply to a relatively constant value of 20 mg for approximately 25 seconds. Next, the study induced local detachments in vivo by injecting fluid to create blebs in the retinal surface. Then the time for resorption of the retina is recorded in a plot that graphs resorption time in minutes to bleb area in mm^2. Visually, the median resorption time is about 150 minutes for a bleb area of 2.5 mm^2. Other studies would follow that would vary the parameters by studying the resorption in cats (Negi & Marmor, 1986).

It is also noted that retinal adhesion deteriorates rapidly after enucleation (Endo, Yao, & Marmor, 1988) and a streamlined method is developed for in vitro testing of retinal adhesiveness in rabbits. This study ranked the pigment adherence based on a visual scale and plotted versus pealing rate. Another study investigated

the retinal adhesiveness in monkey retina and plotted the percent retinal pigment to enucleation time and incubation time (Endo, Yao, & Marmor, 1988). It is noted that the adhesiveness is sensitive to temperature, pH, and concentrations of calcium and magnesium.

Kita et al. (1989) and Kita et al. (1990) determined the adhesive force in Dutch rabbits to be $1.8x10^2$ dyne/cm from a sample of 84 and 87 respectively. A small dome-shaped retinal detachment (referred to as a bleb) is made in the posterior pole of the retina. This bleb is considered as an idealized sphere and the subretinal and intravitreal pressures are measured along with the radius of the bleb. Then (2.2) is used to determine the retinal force.

$$P_S - P_V = 2T / R \qquad (2.2)$$

Where P_S is the subretinal pressure, P_V is the intravitreal pressure, T is the tension, and R is the radius of the sphere (bleb).

Kita and Marmor (1992) would later conduct a similar study comparing rabbit, cat, and monkey eyes. The retinal adhesive force for them is noted to be 1.0, 1.8, and $1.4x10^2$ dyne/cm. There appears to be a decrease in the rabbit eyes from both Kita et al. studies. Other variations related to bleb creation and adhesive force investigates the effects of calcium concentrations (Kita, Negi, & Marmor, 1992) and other agents used to induce bleb creation (Kita & Marmor, 1992).

Muscle Modeling Studies

Six extra-ocular muscles control the eye. Interestingly, the eye represents a simple joint (Robinson, 1981). Each pair of muscles controls a plane of motion and the eye center becomes the joint. In most of the studies considered, muscles measured in length are converted to degrees or radians by using the globe radius. Muscle modeling in general is comprehensive and describes the phenomenological properties using the Hill type description (Hill, 1950). The muscle is composed of a passive element in parallel with a series and contractile element in serial (Maxwell model) (Hatze, 1977). However, the muscle can also be modeled as a Voigt model with the passive and contractile element in parallel which is in series with the series element (Winters, 1985). Zajac (1989) details muscle-modeling fundamentals using the Hill type formulation. The MADYMO software models the muscle using a Voigt model. The original work from Hill considered the heat of shorting of a muscle and (2.3) that resulted is used to determine the contractile force-velocity relationship.

$$v = \frac{b(P_0 - P)}{(P + a)} \qquad (2.3)$$

Where P is the force exerted by the contractile element, v is the velocity at that force P, P0 is the isometric tension, and a and b are constants. These constants are properties of the muscles and determine the shape of the force-velocity relationship curve.

Winters (1985) and Winters and Stark (1985 and 1988) tabulate various muscle properties using the force-velocity relationship from the classic Hill equation in a modified form in order to streamline the usage of the shape parameters. Using a dimensionless Hill parameter (called A_f in Winters and Stark 1988), the peak

unloaded shortening velocity can be determined based on the rest length of the muscle and the fraction of fast fibers in the muscle.

The dimensionless Hill parameter, fast fiber ratio, and muscle lengths are tabulated for elbow flexion, knee flexion, ankle dorsal flexion, ankle plantar flexion, wrist flexion, wrist extension, and, eye rotation. The eye rotation parameters, which are of particular interest, are for horizontal motion as elaborated in Winters (1985). Parameters in this study are also given to determine the series elastic and passive elastic properties. Last, the excitation and activation time constants are given. Winters and Stark (1985) list parameters as well and perform sensitivity analysis. There are some slight variations in the tabulated values given from Winters and Stark (1988).

Lehman and Stark (1983) utilized mathematical muscle modeling in perturbation analysis of the eye, head, and arm movements. Each movement is originated from a second order differential equation with a force function. The plant parameters (inertial, viscous, and elastic) for the eye are given. A unique property of the eye is that these values can be determined by isolating the muscle. Concerning the rotational properties of the eye, the measurements are taken during strabismus surgery. Collins, Scott and O'Meara (1969) provided these values by isolating the contributions from the muscle. Lehman and Stark (1979) investigate saccades in eye movement using non-linear and linear models based on the Hill force-velocity equation. Also, Winters, Nam, and Stark (1984) investigate saccadic eye movements and the slower eye movements using the mathematical modeling. Stark et al. (1980) create a helmet apparatus to measure movements of the head and eye saccades.

Rath (2005) studies the effects of extraocular muscles on the sclera tabulating the width, length, physiologic cross sectional area, and the maximum force. The force equation uses a constant of 30 N/cm2 and is the same value used in Winters and Stark (1988).

Van der Horst (2002) models the human neck response in accident collisions using the Hill type muscle model with varying levels of activation. This work is of particular interest as the MADYMO software is utilized and provides insight into the methodology of determining and inserting the necessary parameters unique to this software package. The passive muscle behavior is examined and follows a similar methodology as Deng and Goldsmith (1987). Also highlighted, is the process of muscle activation. Two first order differential equations are solved. The first concerns the neural excitation and the second is the active state dynamics. The time constants from Winters and Stark are used to determine the time signals. Interestingly, Winters (1985) exhaustively tested the response of the eye muscles for horizontal motion by applying various neural step functions.

Other systems are utilizing these hill type muscles. Delp et al. (1990) and Delp (1990) consider the lower extremity modeling using mathematical muscles. Biomechanical modeling during gait of the ankle is considered (Buchanan et al., 2005) using the Hill muscles. Crandall et al. (1996) investigate the biomechanics of the lower extremities testing the passive and active responses. He (1988) models the cat hind limb using the Hill type muscles. Woittiez, Huijing, and Rozendal (1983) investigate the twitch forces in rats and diagram the active length-force characteristics. Durfee and Palmer (1994) use the Hill type muscles doing

experiments on hind-limb muscles in cats to determine the parameters rather than acquire them from literature.

Finite element analysis has also been employed in modeling muscles and tendons, although not as comprehensively as the Hill type. Power (2001) models the passive behavior of the extraocular muscles using membrane tria-elements with a linear elastic modulus based on the tensile strength of collagen from rat-tails. Zobitz, Luo, and An (2001) determine the compressive material properties of supraspinatus tendon using a hyperelastic formation (Ogden model). The material parameters are modified till the finite element model gives the same response as the experimental compression tests on cadaver specimens. Hirokawa and Tsuruno (2000) model the anterior cruciate ligament using finite element analysis with material properties using Mooney-Rivlin parameters. The material parameters are compiled from previous works. The work provides insight into the shape changing effects having an influence on the stress- something that analytical models cannot do.

Meshing muscles can be an extremely difficult task; Fernandez et al. (2004) describe meshing techniques using volumetric datasets from the Visible Human Project. Dong et al. (2002) also develop methods to model the muscle geometry, deformation, and texture in various visual simulations. This work is more appropriate for visualization studies and not biomechanical modeling; however, the group uses the visible human dataset and does provide interesting details on building the muscles.

Johansson, Meier, and Blickhan (2000) investigate muscle modeling using finite element analysis but include the Hill type muscle formulation into the

continuum mechanics. The work is verified using a simple model of a squid tentacle and compares the response to the experimental results. The advantages of this modeling method are the ability to model the muscle behavior in three-dimensional space. The disadvantage is the computational cost.

Sarma et al. (2003) investigate the material properties of a smooth tracheal muscle tissue using a hyperelastic formulation. An experiment using canine tracheal smooth muscles is used in an electrical stimulation test. The resulting stiffness and length are recorded and the stress-strain behavior is obtained. The hyperelastic studies involved tried more than one formulation for comparison. Material models used include Ogden, Mooney-Rivlin, and Yeoh. It is determined that the Ogden model fit the experimental data the best, so that is what is used in the study. A finite element model of the smooth tracheal muscle is created and compares well with the experimental data.

On the importance of tissue preparation and freezing effects on vocal fold tissue, Chan and Titze (2003) measure the viscoelastic properties from adult dogs ten minutes postmortem and at various freezing rates. The groups of tissue samples are divided into slow and fast freezing. The elastic shear modulus and dynamic viscosity is compared between the three groups (ten minutes postmortem, slow freezing, and fast freezing) revealing that the slow freezing method has the adverse effect of lowering the elasticity and viscosity of the sample. The fast freezing method showed little difference from the postmortem samples.

Skin and Fatty Tissue Material Studies

Chabanas, Luboz, and Payan (2003) investigate patient specific finite element meshes of the facial soft tissues and muscles. Essentially, the study uses hexahedral meshes to model the soft skin tissue and underlying muscles around the orbicularis oris. The study mentions that hexahedral elements are preferred to tetrahedral for their convergence, error estimation, and time. This study considers the practicality in maxillofacial surgery by acquiring CT scans from various patients and transforming the hexahedral mesh to each of the skull surfaces. The benefit of the semi-automatic method is that the time consuming meshing is prevented. However, examination of the mesh is still required to remove or modify some of the hexahedral meshes that may have adversely changed shape due to the transformation. The study relies on the mechanical properties from Duck (1990) for the skin and muscle tissue. These materials are linear elastic. The skin tissue is assigned a value of 15 kPa for the modulus and the Poisson's ratio is set to 0.49 for incompressibility. The muscle stiffness is given linear orthotropic values for the modulus. From Duck (1990), the modulus of the fibers at rest is 6.2 kPa and the modulus of the fibers at full activation is set to 110 kPa. The study mentions the modulus across the fibers remains constant but does not specify the value. In addition, it is not explained how the modulus of the fibers at rest and at full activation are introduced into the model, nor is the Possion's ratio mentioned for the muscle material (assuming it is 0.49 as the skin tissue). The boundary conditions with the skull can be rather complex; the study currently fixes the tissue to the bones so there is no sliding. The nodes around the cheek and lip are free to move however. The validation of this work relies heavily on the clinical

application. However, this method is useful for clinical applications as a tool to estimate errors between surgical procedures and the planning.

Shergold, Fleck, and Radford (2004) examine the stress-strain of pigskin using uniaxial testing at low and high strain rates. This study uses as a comparison silicone rubber. The study mentions that uniaxial tensile tests on human tendons and rat tendons show that the collagen fibers can be considered elastic-plastic; however, skin cannot be expressed using these properties alone. The constitutive model employed is an Ogden model (the Mooney-Rivlin material model is shown to be inappropriate despite its use in other studies) using two coefficients. The study does emphasize that an orthotropic formulation may be more appropriate; however, this would require more variables and be inapplicable to many of the finite element packages. The experiment involves circular cylindrical specimens of silicone rubber (specimen diameter of 7.7 mm and thickness 2.0 mm) and pigskin (specimen diameter of 7.0 mm and thickness 2.3 mm). Impact testing is employed at various rates, and the results are plotted. Further axial tension tests are performed on the rubber sample using a dog-bone shaped specimen. The axial tensile test is not performed on the pigskin; however, information is gathered from previous studies. Pigskin is chosen, as it is comparable to human skin and also to avoid the ethical and immunological issues with testing human skin.

Strain rate is considered with the Ogden hyperelastic constitutive model plotting the absolute stress versus stretch ratio. The Ogden is able to fit the data extremely well as opposed to the Mooney-Rivlin fit, which is only able to give an accurate description at low rates of strain hardening. The experiment shows that

strain hardening is strong at high compressive strains for the silicone rubber and pig skin and these samples are sensitive to strain rate. The Ogden model is able to capture the effects of the strain hardening versus the Mooney-Rivlin model. In addition, it is revealed that the strain rate sensitivity is described by an increase in the shear modulus with increasing strain rate without change to the strain-hardening exponent.

Todd and Thacker (1994) develop a method to determine the elastic modulus of the buttocks in vivo from male and female volunteers. The objective of this study is to show the applicability of using finite element analysis in the design of seat cushions. The geometry of the volunteers is gathered from magnetic resonance imaging (MRI). A two-dimensional map with one-millimeter resolution of the transverse sections of the abdomen is taken. After digitizing the images, the finite element model is created using hexahedral elements. The finite element model contains the bone, tissue, and cushion properties. The cushion and buttocks share the same node in order to prevent complex contact gap interface from needing to be modeled. The force-displacement of the subjects is measured using a contour gage consisting of a steeper motor attached to a threaded shaft with a strain gage to measure axial compression. As the contour gage progressed, the axial force is measured. Data acquisition methods transform the information into a force-deflection curve and follow the form (2.4).

$$F = -0.112 + 0.967x + 10^{(-0.908+0.0704x)} \qquad (2.4)$$

Where F is the axial force and x is the displacement. From this information, the modulus information is tabulated for the seated and supine positions for each of the

male and female and are as follows: female seated is 47.5 kPa, female supine is 11.9 kPa, male seated is 64.8 kPa, and male supine is 15.2 kPa. Power (2001) uses the value of 47 kPa in the fatty tissue for the eye globe, which is the elastic modulus of the female in the seated positioning.

Luboz et al. (2004) investigated the prediction of tissue compression in orbital surgery. The study includes a finite element model and a two dimensional mathematical model. The study obtains the CT scans of the ocular cavity, muscles, optic nerve, and eye globe geometry from a patient with exophthalmia. The study is of interest to help surgical procedures in pre-operative diagnosis and analysis. The eye globe is considered rigid in this case with the fatty tissue being composed of solid hexahedral elements in the finite element model. The material of the fatty tissue is assigned an elastic modulus of 20 kPa influenced from previous published values. The Poisson ratio is set to 0.1 to model the poroelastic properties of the fatty tissue. This study explains that the fat tissue is a combination of fat fibers (mostly collagen) and pockets of physiological fluid; hence, the assignment of 0.1 for the Poisson ratio.

Exophthalmia corrections require the surgeon to apply pressure to the eye globe in order to compress the fatty tissue and force it out towards the sinus cavity. This is a very delicate procedure and special care must be taken to prevent damage to the eye globe or optic nerve. The force of this pressure is measured using a custom sensor and is 12 N in magnitude. The boundary conditions at the orbital wall involve fixing the nodes of the fatty tissue except where incisions are made. The study concludes that the mathematical model is able to predict globe displacement to within 3% of the clinical results while the finite element model under-predicts by 36%.

Explanations of this under prediction are due to the selected parameters of the fatty material (despite the parameters being tuned to the data). Further work needs be done to include the muscles and properties need to be determined from a large base of patients. However, no mention of the contribution of under prediction is attributed to the fixing of the fatty tissue to the ocular cavity or that the globe is a deformable body and the stress contour would surely be different if the globe was not considered rigid.

Miller-Young, Duncan, and Baroud (2002) conducted axial compression tests at varying strain rates on cylindrical fatty heal pads excised from cadaver heels. A total of ten samples are used and a strict criteria of rejecting the sample is employed if the sample is loaded in the test unevenly (slip occurrence) or if the mass measurements before and after indicate shrinkage of the sample. The constitutive equations used a hyperelastic formulation by way of the Mooney-Rivlin equation. In addition, the constants of the Mooney-Rivlin equation are modified to account for the viscoelastic parameters. The time constants for the viscoelastic properties are determined from the stress-relaxation data of the loading test. The quasi-static loading determines the strain energy density. Then a comparison of the experimental results is compared with the constitutive equation showing a good correlation of 0.9. The study mentions that these parameters can easily be introduced into finite element packages; however, it is unclear how this would be used in MADYMO software, as the coefficients for the Moony-Rivlin material cannot be variables dependent on the viscoelastic properties. Finally, mention of further validation is necessary by creating a simple finite element model and comparing it to the experimental data.

Verver (2004) creates a full-featured finite element buttocks model with skin and bone structures modeled using triangular elements. The rest of the soft tissue has been lumped together to form a homogenized tetrahedral tissue mesh. The model contains 158,310 elements and 29,661 nodes with an element size set to ten millimeters. Of interest, the soft tissue is modeled as Moony-Rivlin material with the two coefficients set to 1.65 kPa and 3.35 kPa. The Poisson ratio is assumed to be 0.49 for incompressibility. Unfortunately, no material testing is performed and the influence of the parameters is based on values that are within ranges of other published values.

Samani et al. (2001) present a method of modeling the human breast using MRI Data. Emphasis on this research is given to mesh generation. The favorable choice of element is the hexahedral as the tetrahedral element is claimed to have slow convergence with mesh refinement, and also exhibit over-stiffening with volumetric locking possible with incompressible material. The logical choice then would be to use hexahedral elements in conjunction with voxel-based mesh generation, transfinite interpolation mesh generation, and manual mesh generation. The breast skin is modeled as linear elastic material with Young's modulus of 10.0 kPa and thickness of one millimeter. The fatty tissue is acquired from experimental data in another work. The data is curve fitted to a hyperelastic Neo-Hookean model. This study did not conduct a validation and proposed to material test in another study that will be presented next.

Samani and Plewes (2004) determine the hyperelastic parameters of breast tissue samples (ex vivo) gathered from breast reduction surgery. Axial compression

tests are performed on samples sized to 15 x 15 x 10 mm^3. The specimens are visually identified as adipose or fibroglandular tissue. The tissue samples are preconditioned with 25 cycle sinusoidal indentations; then 5 cycles are used for the force-displacement data. Using this experimental force-displacement data, finite element models representing the performed experiment are created and the material parameters are set using hyperelastic parameters (Mooney-Rivlin model). The parameters in the finite element model are modified until they converge to the same force-deflection curve determined from the compression tests. This optimization technique performed a minimization of the least squares of the force-displacement and is referred to as the data inversion technique in this study.

Conclusion

A review of some of the relevant studies investing shaken baby syndrome have been given. A comparison is given highlighting the argument for and against injury induced by pure shaking. In addition, a description and definition of retinal hemorrhaging is provided, highlighting the need for this biomechanical eye model. The sections to follow discuss the studies (biomechanical and clinical) that influence the current eye model.

What is not discussed are some of the structures of the eye that have little biomechanical research or can be simplified via assumptions in the modeling process. The hyaloid is an artery traversing the vitreous body providing nutrients to the lens and anterior section during development in the embryonic stages. By birth this artery

has usually regressed (Jack, 1972; Elliott & Elliott, 1973; Ruiz-Moreno & Perez-Santonja, 1998; Torii et al., 2001). Very little biomechanical information is available and most of the vitreous studies leave this out; therefore, it is left out of the proposed model.

The anterior portion of the eye contains a complex structure detailing the ciliary body and zonular processes attached to the lens. These structures are important, but in this first model, most of the clinical studies with retinal hemorrhaging are concerned with the posterior region. These structures are modeled but are simplified and based on the work of Power (2002) rather than doing a complete and extensive literature review. However, information concerning lens accommodation and compliance are quite involved and interrelated with the ciliary body (Fisher, 1986; Fisher, 1987; Quigley et al., 1990; Schachar, Huang, & Huang, 1993; Burd, Judge, & Flavell, 1999; Heickell et al., 2001; Schachar & Bax, 2001; Burd, Judge, & Cross, 2002; Judge & Burd, 2002; Krag & Andreassen, 2003).

CHAPTER III

GEOMETRY OF EYE AND OCULAR REGION

Introduction

A biomechanical model of an infant eye is developed using finite element method and rigid body analysis. The computational software used is MADYMO (2004) version 6.2 and the preprocessing consisted of using Easicrash (2007) and other meshing and modeling techniques that are highlighted in chapter four. The eye model consists of the extraocular muscles modeled using a Hill-type (Hill, 1950) muscle for the contractile and passive parts attached to the tendon (series elastic) composed of membrane elements. The cornea and sclera are modeled as a non-uniform thickness globe with the choroid, retina, ciliary body, lens, vitreous, and aqueous inside of this globe. Posterior to the eye globe, the optic nerve is modeled to mainly act as a tether as postulated in Levin (2000). The fatty tissue is also modeled encasing the globe and conforming to the eye socket geometry. The fatty tissue completely encases the eye globe and at the surface (most anterior) the skin is modeled using membrane elements. This entire eye complex is attached to a rigid body representing the head center of gravity (C.G.). In addition, for visualization, the skull is modeled using shell elements and fixed to the head C.G. completely.

In order to build the eye model, the geometry needs to be developed and meshed. This proved to be rather time consuming, as the desire was to create

geometry that was true to reality. The geometry resources describe the dimensions for an adult eye, as very little detailed information exists for an infant eye. There are some sources that are used to verify the scaling to an infant, and those will be discussed in this chapter (Hogan, Alvarado, & Weddell, 1971; Newman et al., 2002).

Eye Geometry

The non-uniform geometry of the cornea and sclera is used from Woo et al. (1972) as is used in Power (2001) and Stitzel et al. (2002). The eye is composed of spherical shells with two radii with centers separated 5 mm apart. The posterior radius is 12 mm and the anterior radius is 7.8 mm (Figure 3.0). The thickness of the eye is non-uniform as well being thickest in the posterior region at 1 mm decreasing in thickness in the equatorial area to 0.55 mm and increasing anteriorly to 0.8 just posterior the limbus, which is 0.66 mm in thickness. The most anterior eye thickness is 0.52 mm in the area of the cornea.

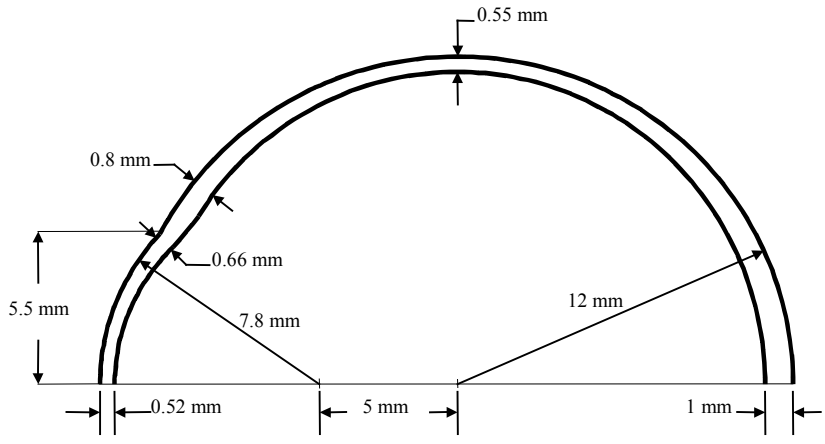

Figure 3.0: Geometry of the idealized cornea-sclero shell from Woo et al. (1972)

The inside of the eye contains two main chambers (aqueous and vitreous) separated mainly by the lens and ciliary body (Figure 3.1). The geometrical locations of the lens and ciliary body are gathered from the work of Power (2001). Comparing this work to the geometrical considerations of the Visible Human Project, the eye geometry is about the same size. The eye globe geometry is also in agreement with the histological average provided in Hogan, Alvarado, & Weddell (1971), which details the gross anatomy of the eye showing the cornea to be 11.7 mm in diameter looking from the frontal projection. The cornea radius is 7.8 mm and the sclera radius is 11.5 mm (Figure 3.2). The average eye diameter from this histological study is 24 mm in the anteroposterior, transverse and vertical directions.

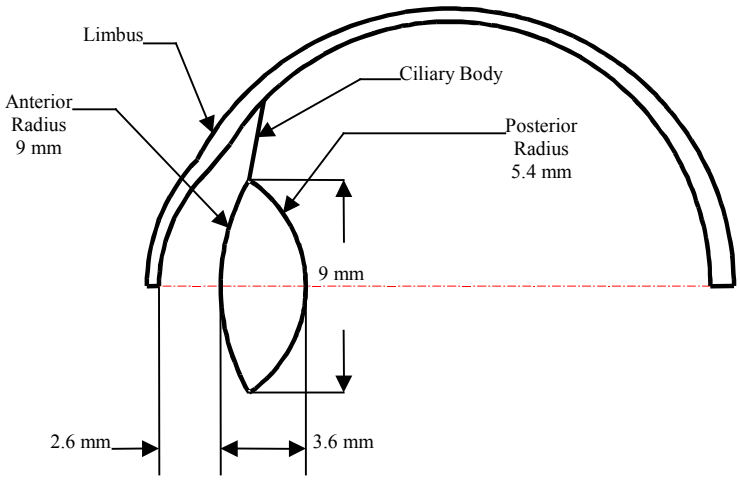

Figure 3.1: Location and dimensions of the lens from Power (2001)

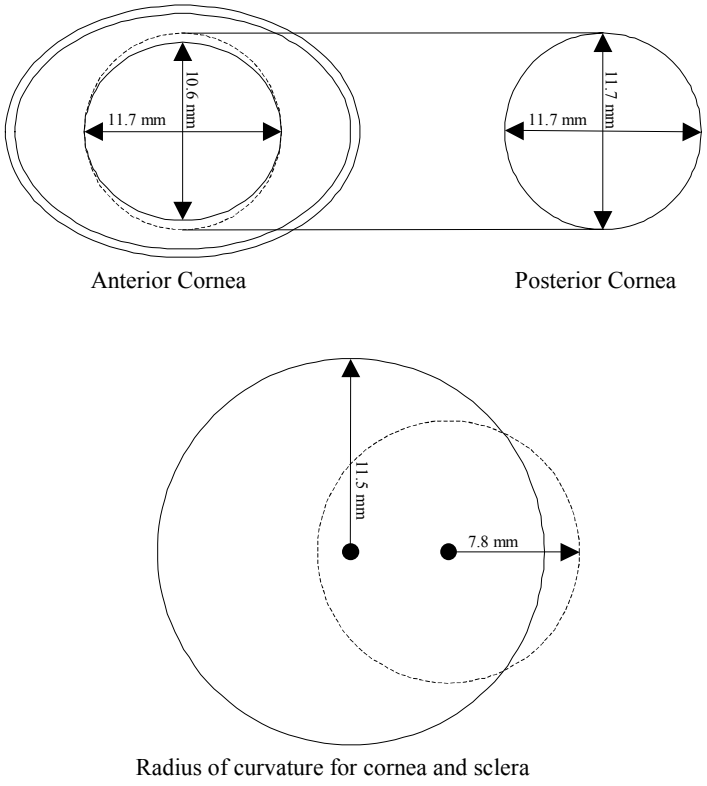

Figure 3.2: Diagram outlining cornea and sclera dimension from Hogan, Alvarado, & Weddell (1971)

The overall geometry of the eye socket in relation to the muscles, eye, and optic nerve is considered. Rather than solely gathering this information based on descriptive histological studies and diagrams alone, an attempt is made to build the geometry of these structures and then add the idealized geometry of the eye. The geometry of these other structures is derived from transverse slices scanned in at 1 mm increments (Visible Human Project, 2007). The slices of interest around the eye socket are used (Figure 3.3). A typical slice trace is shown in Figure 3.4 with the final slice layers represented as spline curves shown in Figure 3.5. The geometry of the eye socket, optic nerve, eyeball, and muscles for each slice is created with spline curves traced on each image dataslice. Once all of the spline curves are created for

the slice layers of interest, each is then offset by 1 mm. The geometry is then surfaced and ultimately meshed (a very tedious process). Finally, the dimensions are checked against histological studies to verify that the curve data (Figure 3.5) agrees. Ultimately, the muscles (Figure 3.6) are made analytical since there is really no suitable finite element property available as compared to the verified analytical Hill-type muscles. In addition, the ultimate locations of the muscles are modified to coincide with Hogan, Alvarado, & Weddell (1971) (Figure 3.7). Interestingly, the optic nerve sheath that is built from the transverse slices matches the description provided by Hayreh (1984). The most anterior section of the nerve is rather bulbous (Figure 3.8). The final location of the optic nerve head is changed to a new location based on Hogan, Alvarado, & Weddell as this represents more of an average location.

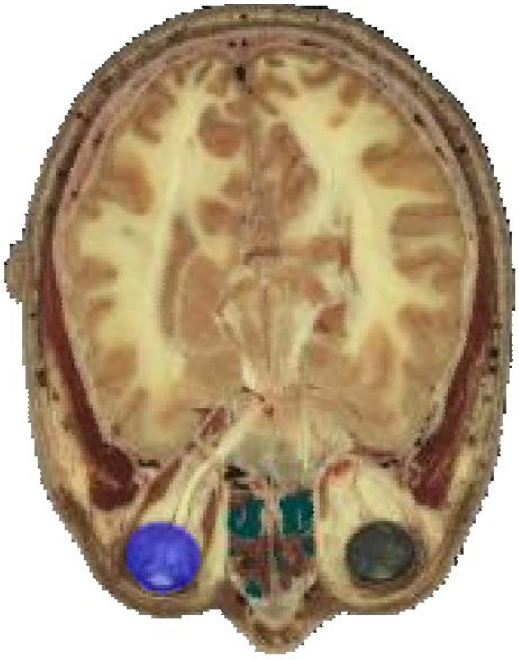

Figure 3.3: Transverse slice number 104 detailing the eye and optic nerve (Visible Human Project, 2007)

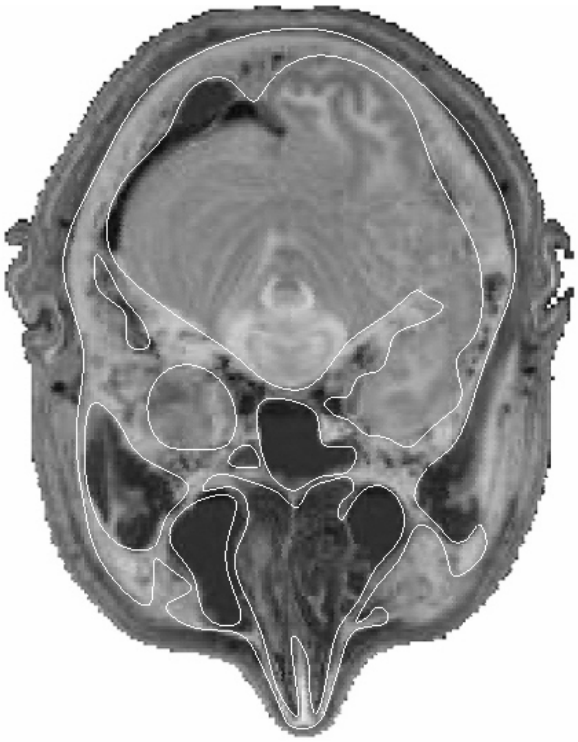

Figure 3.4: A typical spline curve tracing of a transverse slice (Visible Human Project, 2007)

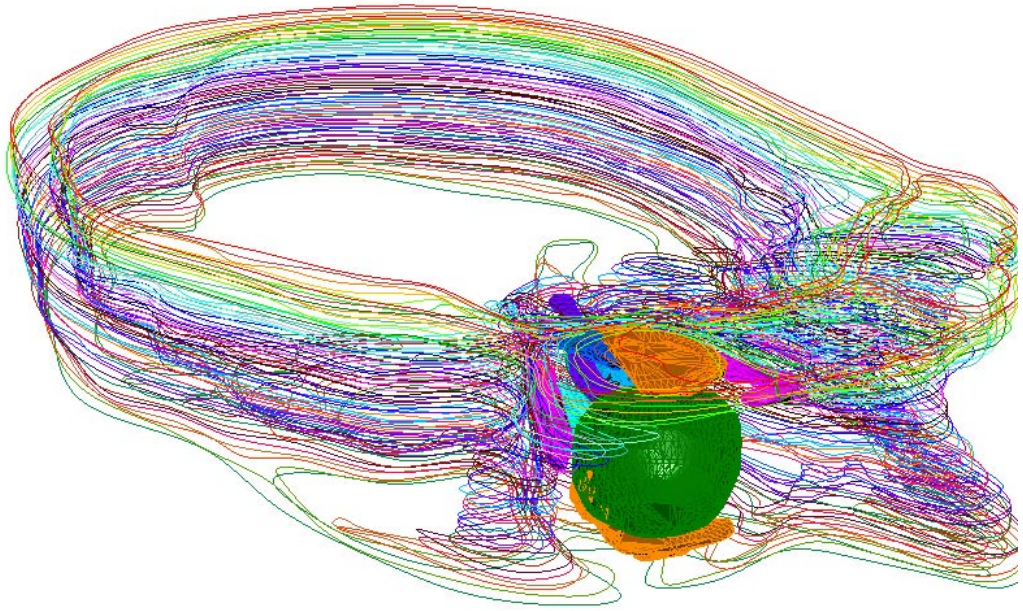

Figure 3.5: Complete build up of spline curves offset 1 mm based on Visible Human Slices

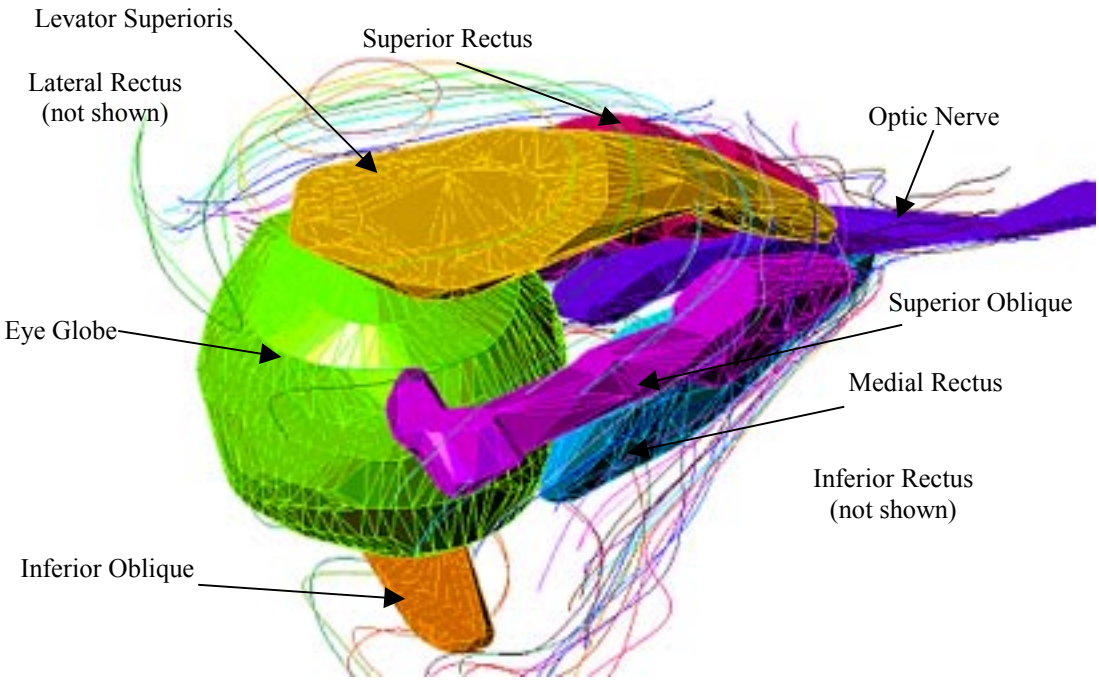

Figure 3.6: Using transverse slices to create muscle geometry

In the Power (2001) model, the orbital opening is based on Sauerland and Grant (1994) as simplified pyramids (Figure 3.9). This assumption is probably appropriate, except that the fatty tissue is neglected anterior the cornea (including eyelid). This is probably done to create a worst-case scenario as this Power study is concerned with ocular injuries from night vision goggles. In the current eye model, the non-uniform pyramid is created based on the transverse slices and totally encases the eye (Figure 3.10).

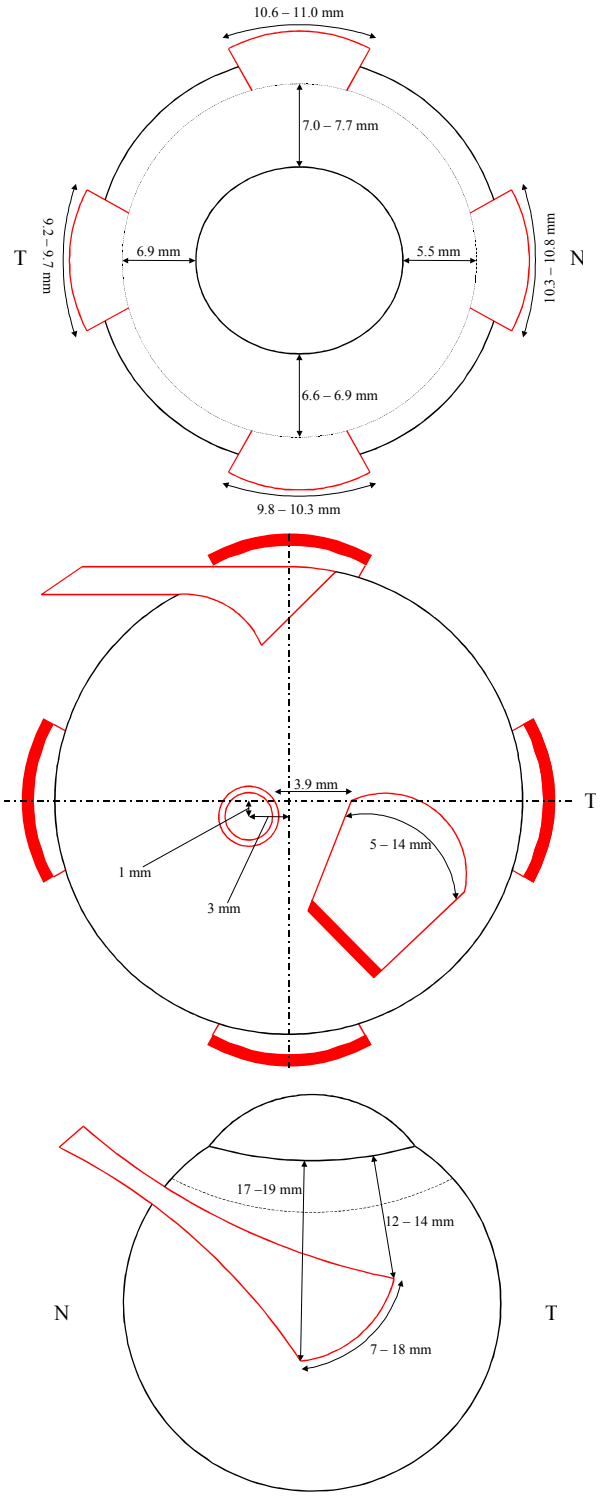

Figure 3.7: Muscle locations from Hogan, Alvarado, & Weddell (1971)

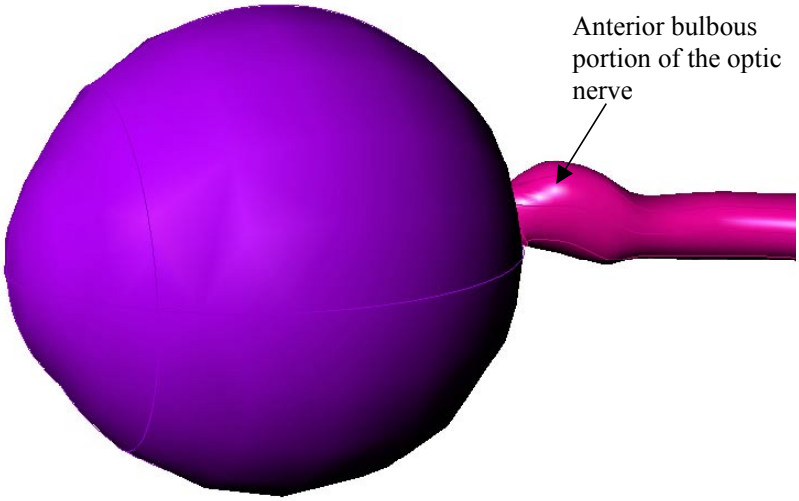

Figure 3.8: Bulbous portion of the nerve is shown which is built from the transverse slice information

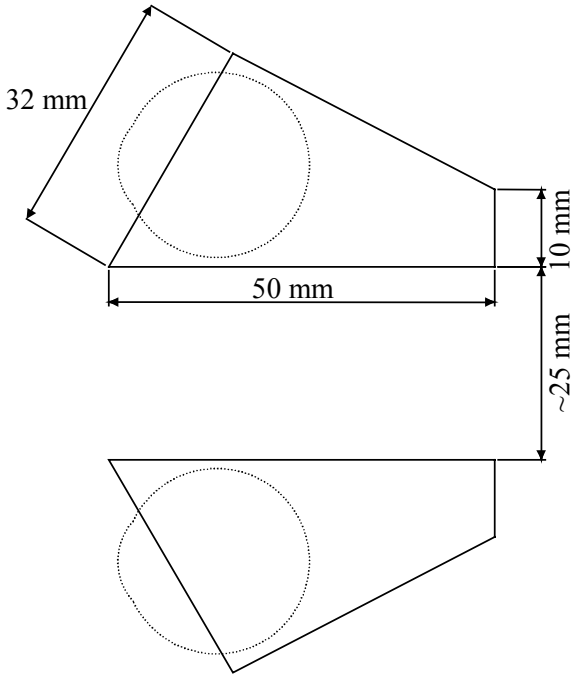

Figure 3.9: Bony orbit as used in the Power (2001) model

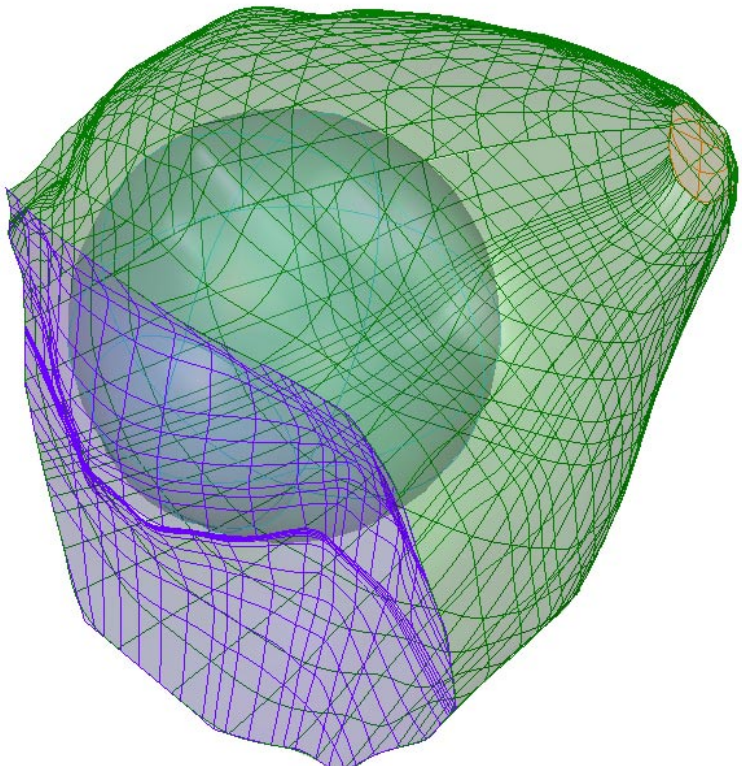

Figure 3.10: Fatty tissue modeled from transverse slice data

Figure 3.10 describes the boundary of the ocular socket with the anterior section covering the eye considered as well. The MADYMO finite element human model influences the anterior portion that resembles the eyelid boundary.

The lid information is originally based on this information and at one time included the eye opening as shown in Figure 3.11. However, during the initial tests unrealistic contact interactions resulted as the eyelid edge interfacing the eye globe caused the eyeball to squish into the lid opening. Therefore, the eyelid opening is removed to simplify the contact algorithm. In addition, this removal of the eyelid is justified as the fatty tissue interface for this study serves to encase the eyeglobe only. The inside of the fatty tissue contains a void area large enough for the eye globe to fit

into totally encasing the eye. Modeling the fatty tissue in this way allows the eye to rotate within this void as a kind of spherical joint.

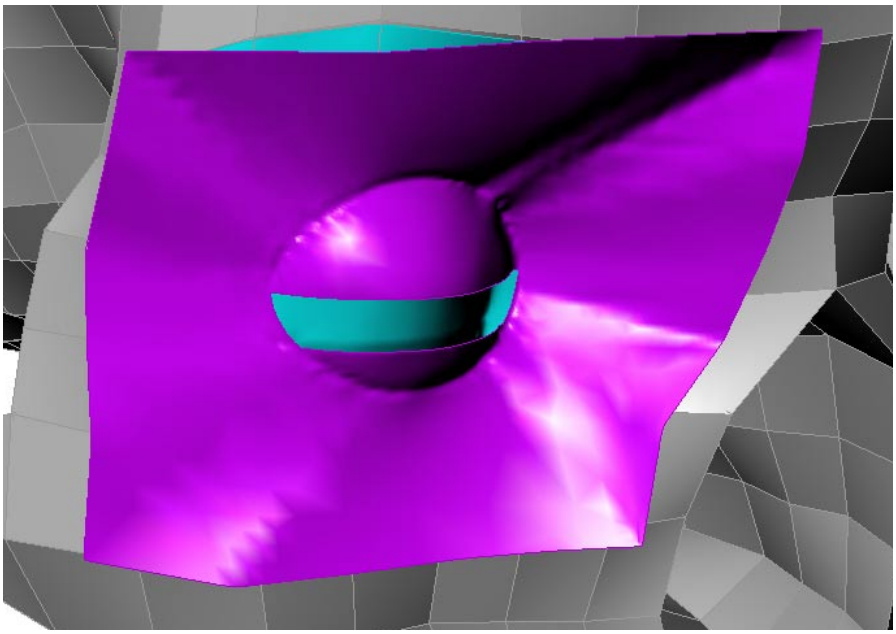

Figure 3.11: First version of fatty tissue displaying eyelid opening.

Scaling to infant dimensions

At birth the eye diameter is 16 to 17 mm in diameter and is used in this study as the main scaling factor (Hogan, Alvarado, & Weddell 1971). Comparing the diameter at birth to the diameter of an adult gives a scale factor of 0.645. Therefore, all structures after modeling are ultimately scaled by 64.5%. There is not much information concerning infant size structures in the eye; however, there is a study that measured the optic nerve sheath diameters (Newman et al., 2002). A comparison is made between this study and the optic nerve dimensions after scaling. The scaled

optic nerve, using the 64.5% reduction factor, measures to be 2.4 mm inferior to superior and 3.0 mm medial to lateral at the optic nerve head (ONH). The study tabulates the clinical details of the patient and for an infant aged ten days, with normal optic disc appearance noted, the right optic nerve sheath diameter is 1.9 mm and the left optic nerve sheath diameter is 2.6 mm. Another patient, 18 months of age with normal optic disc appearance noted, has a right optic nerve sheath diameter of 2.5 mm and the left optic nerve sheath diameter of 2.9 mm. Therefore, using this study as a check, it would appear that basing the scaling on the eye globe anteroposterior diameter would be an appropriate approximation to acquiring the eye complex geometry for an infant. Further, this scaling reduction is used later in the reduction of muscle properties for the analytical Hill-type muscles and of the stiffness and damping characteristic of the eye response.

Conclusion

This chapter highlights some of the modeling that goes into creating the geometry for the eye structure. Modeling the geometry of the eye is a rather complex endeavor. As will be illustrated in later chapters, meshing is not an easier process either. Initially, the geometry is modeled in the most detailed manner to capture all possible information. As the early biomechanical models advanced, some of the complexity is taken out to streamline and stabilize the simulation where appropriate.

CHAPTER IV

MESHING OF THE EYE AND FATTY TISSUE

Introduction

This chapter highlights some of the meshing techniques that are involved in creating the complex geometry of the eye and fatty tissue. Essentially, the hardest components to mesh are the fatty tissue and eye globe with interior structures. The techniques in this study utilized tetrameshing, manual meshing, automeshing, volume dividing for hexahedral meshing, and hexahedral dominant algorithms (Joe 2006). Another technique involves a bottom up approach when meshing volumetric datasets (Zhang and Bajaj, 2004). This technique creates hexahedral elements and then refines the mesh near the surface boundary. This technique has not been used in this work. However, opposing this is the technique provided by Geompack++ (Joe 2006). Essentially this software is able to create hexahedral dominant meshes by taking the surface quadrilateral mesh and building hexahedral elements inwards. The term hexahedral dominant comes into play when the algorithm can no longer fit hexahedral elements and starts filling voids with tetrahedral elements, pyramids, and wedges. The pyramids and wedges are degraded hexahedral elements in the MADYMO software and it is advised to avoid their use if possible. In addition, this method also ends up creating some elements with off aspect ratios and extremely small edges that can adversely affect the time step in MADYMO.

When deciding the mesh, one must consider the meshing density, element size (for Courant time step), the type of mesh, the type of material model that will be used, contact gaps, and interfacing other structures. All these items are considered when meshing the eye and fatty tissue and will be discussed. The order will start with the eye globe and inner structures and then the fatty tissue.

Eye Meshing

The eye geometry considered in this model contains the cornea-scleral shell, aqueous humor, vitreous body, cilliary body, lens, and interface to the optic nerve. The muscle attachments are directly attached to the sclera shell using locations from Hogan, Alvarado, and Weddell (1971) as mentioned in chapter 3. The muscles and optic nerve will be discussed in more detail in chapter 5. The cornea and sclera, from Figure 3.0, have a non-uniform thickness going anterior to posterior. Consideration has been given to capture this thickness variation in the mesh model. This geometry is initially modeled as a solid layer as shown in Figure 4.0.

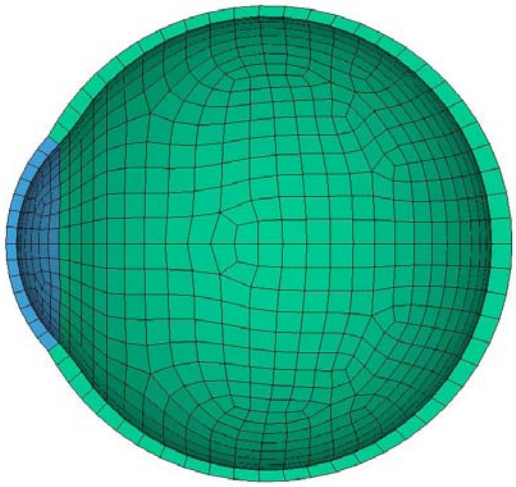

Figure 4.0: Sagittal view of cornea and sclera elements

Figure 4.0 shows the mesh of the cornea and sclera about the perimeter as one layer of hexahedral elements. In the Power (2001) model[5], the shell of the eye is modeled as 3 node membrane elements that only account for in-plane stress. Bending cannot be resisted and is consistent with previous literature that considers the sclera and cornea as a membrane (Woo et al., 1972). The mesh used in the Power model is rather course with a typical element edge length around 1.5-4 mm (Figure 4.1).

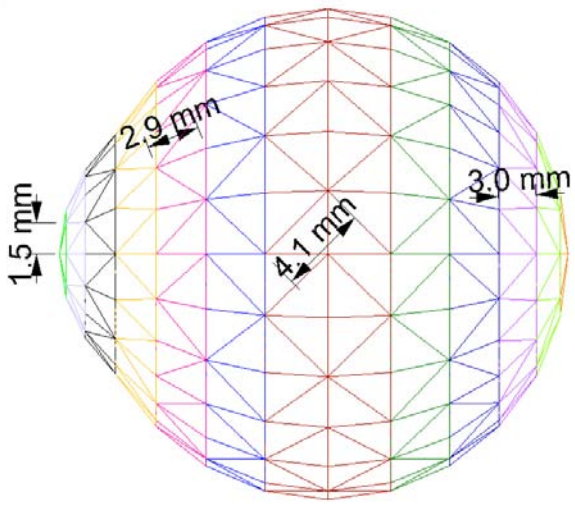

Figure 4.1: Mesh size of the Power (2001) eye globe geometry

This edge length is based on a reproduction of the eye model based on the Power (2001) figures and increases towards the equator with the smallest elements near the posterior and anterior poles. The Stitzel et al. (2002) eye shell used quadrilateral

[5] Appendix C details the reconstruction of the Power (2001) eye model including testing as indicated in Power et al. (2002).

membrane elements with a mesh density 4 to 11 times greater as mentioned in Stitzel et al. The meshing of the eye is done in circumferential rings, as done with Power (2001), except that the thickness is specified at each node. In the Power (2001) model, the thickness is only specified per element and is a limitation of the software. This will result in discrete steps in the thickness of the shell.

In this model, it was originally thought to keep the cornea and sclera as solid elements in order to maintain the transitional thickness along the globe (anterior to posterior). However, there are only a handful of material models that can be used in conjunction with the hexahedral elements and all of these material properties would resist bending. In order to consider the cornea and sclera as membranes, shell elements had be used with a suitable material model able to provide in plane stress resistance only. Unfortunately, this method will cause stepping in the thickness gradiant as only the thickness can be specified for the element. The MADYMO software does offer a honeycomb type material that allows one to specify the 3 triaxial material properties. However, the next approach is taken and, as with Power, membrane elements are used. In this model, the cornea and sclera are modeled using quadrilateral membrane elements.

In order to capture the thickness information a script is developed to convert the solid element to a two-dimensional quad element located at the mid-plane of the solid element (Figure 4.2) with specified thickness noted. This script creates a property for each element with a different thickness. This allowed for non-circumferential meshes to have varying thickness from element to element. There is still a discrete difference from one element to the next, but it is a much smaller step

due to the smaller mesh size. The early meshes (Figure 4.19) did not mesh the cornea and sclera in perfect circumferential rings as the Power and Stitzel et al. model did. However, the mesh refinement initially is 1 mm for each element edge.

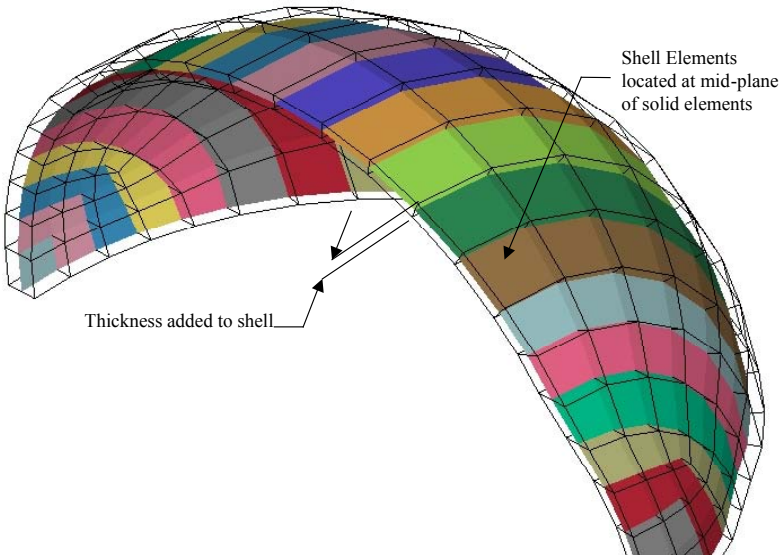

Figure 4.2: Conversion of solid cornea and sclera elements to shell elements

The eye model process involved several remeshings, and this edge length still stayed in the 1-2 mm length for all meshes. The posterior and anterior region mesh size is typically smaller due to the meshing algorithms that are utilized.

Inside the eye globe the vitreous and aqueous meshes are considered and are partitioned by the lens and ciliary body mesh. When creating the eye model, the actual surface information that encases the vitreous and aqueous are considered; then the solid meshing is created. The vitreous is considered as a sphere and is thus divided up into seven parts (Figure 4.3) in order to proceed with a manual meshing

scheme that involved meshing the inner cube and then sweeping the surface mesh to each of the six surfaces to create a hexahedral meshed vitreous.

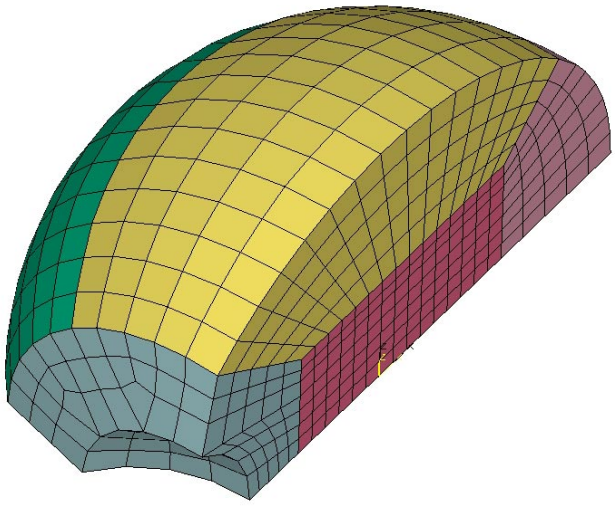

Figure 4.3: Manual Partitioning of the vitreous for hexahedral meshing (one quarter shown)

The aqueous is meshed using hexahedral elements as well but there was some difficulty in creating the mesh as the boundary of the ciliary body to the sclera shell posterior the limbus was making it difficult to sweep (Figure 4.4). Ultimately, manual and sweep meshing is employed to create the mesh of the aqueous. First, a sweeping is done except for the outermost perimeter of the aqueous that is wedged in between the ciliary body and sclera (Figure 4.4). Second, the outermost solid element is manually meshed using the three points that lie on the sclera and ciliary body and the node between the two elements of the aqueous created from the sweep (node is highlighted in Figure 4.4). The four element pairs that are selected create an ill-formed 8-node solid brick element. Lastly, the mid-node of the two outermost elements from this sweep is moved inward towards the center of the eye, correcting

the shape of the element (Figure 4.4 second image). This process is repeated to form the outermost solid elements of the aqueous. Finally, smoothing algorithms are then run in order to optimize the vitreous and aqueous mesh.

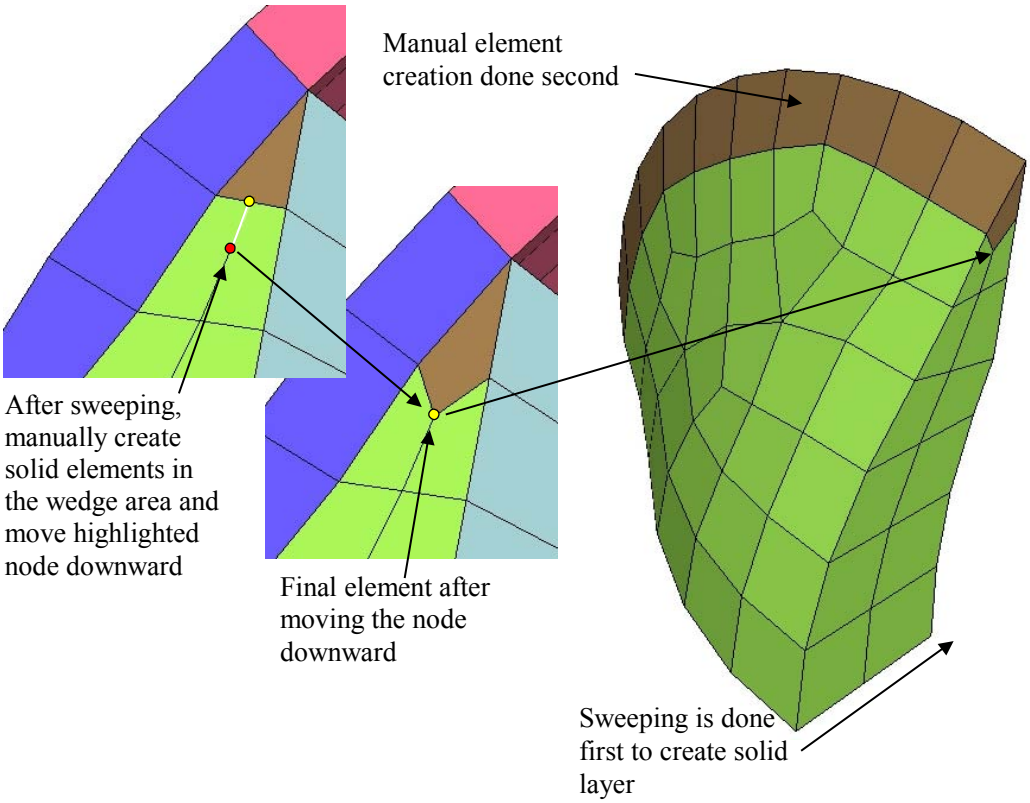

Figure 4.4: Manual meshing process of the aqueous humor

The lens and ciliary body mesh are trivial to create as they are based on the surface mesh of the vitreous and aqueous. The retina and choroid mesh are also trivial to make, as they are duplicates of the sclera shell posterior the ciliary body.

An early attempt is tried to build the eye mesh manually, and keep the average edge length of the cornea and sclera around 1 mm by projecting the sclera and cornea mesh to the vitreous cube. This is a desirable technique because the cornea and sclera

shell is an involved process to convert from a solid to a shell with a different thickness for each element. This method would allow the cornea and sclera shell to remain the same. However, this did not produce the desired cubic shapes needed for the hexahedral elements. Instead, a separate mesh of the cornea and sclera is made capturing the thickness locations. Then, a new eye globe is built from the vitreous cube out, and the final surface mesh (after converting from solid to shell using a thickness script) is then projected to the separate cornea and sclera mesh originally created. This provided the desired results as seen in Figure 4.5 and ensured the final globe surface geometry would remain true.

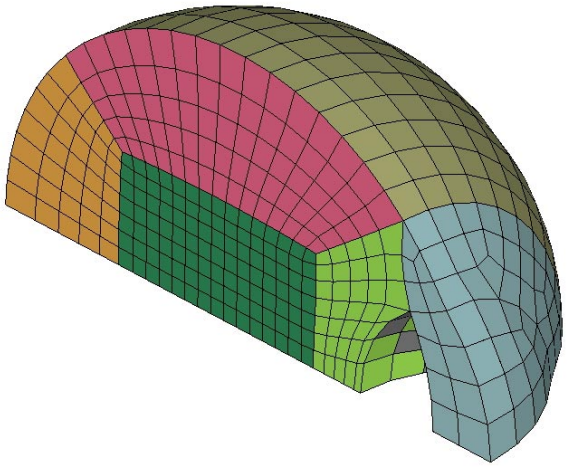

Figure 4.5: Final meshed eye after smoothing solid elements (one quarter shown)

However, this manual meshing was rather slow and changes to the mesh required complete overhaul of the model. Therefore, tetrameshing was attempted. The tetramesh would use the cornea and sclera shell (Figure 4.6) and fill the volume with tetrameshing. This proved be a trivial process and allowed the complex

information of the vitreous and aqueous to be modeled quickly. However, the vitreous would not exhibit shearing despite having a low shear modulus specified.

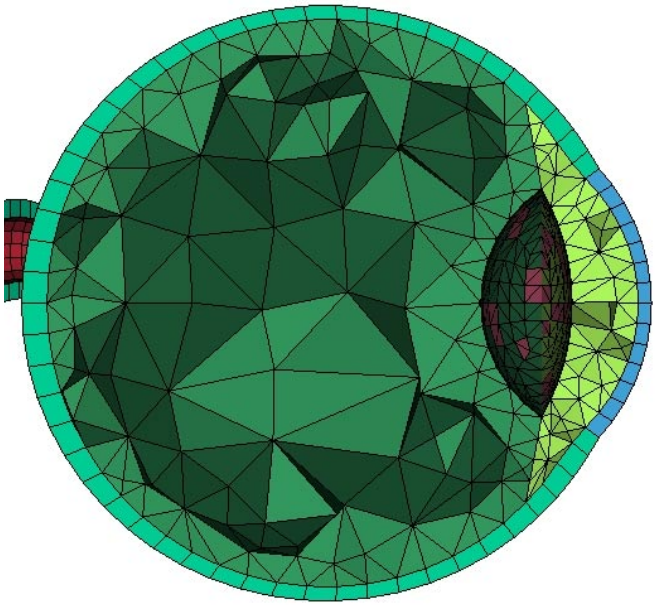

Figure 4.6: Tetra-meshing of vitreous and aqueous (sagittal plane section)

Unfortunately, for viscoelastic materials with Poisson's ratio 0.5 mesh locking is displayed (Samani et al., 2001). Samani et al. explain that the tetrahedral elements "exhibit over-stiffening and volumetric locking especially with incompressible material" (p. 271). Mesh locking is also mentioned in Brands (2002). In this case, hexahedral elements have been observed to perform as a rigid structure when the full integration method is used. Therefore, it is important to use reduced order integration, which uses a single point in each solid element as opposed to all eight points. Manzini and Putti (2007) further discuss mesh locking and proposed methods

to overcome and provide accurate results. In the MADYMO software, an hourglass parameter can be specified to help suppress the zero-energy hourglass modes as a result of using the reduced integration method (MADYMO 2004). Gopalakrishnan (2002) examines these zero-energy modes in detail concerning meshlocking of Lagrangian fluid modeling.

The second idea would be to use the Geompack++ algorithm (Joe, 2006) to facilitate the aqueous and vitreous meshes. One of the features of this software is to create a hexahedral-dominant mesh based on a surface mesh. This would be optimal, as the steps of creating the surface would be minimized. Several scripts had to be created to convert the MADYMO surface mesh file to a mesh and curve file suitable for the Geompack++ software. Then a script is created to convert the output mesh file from Geompack++ software back into a MADYMO syntax mesh file. Once the groundwork is complete, the process is as simple as tetrameshing. This technique is utilized for the aqueous (Figure 4.7), vitreous (Figure 4.8), and the fatty tissue (Figures 4.9 and 4.10). Immediately apparent are the small tetrahedral and degraded 8-node solid elements located near the center of the aqueous and vitreous (Figures 4.7 and 4.8). The vitreous solid elements are rather good and share the same node as the shell boundary for the cornea and sclera. However, after traversing about four elements into the center, the element size and shape are fitted with degenerated hexahedral (pyramid and wedge) and tetrahedral elements. These elements also have a much smaller element edge and required an Euler time step of the order $1x10^{-9}$ to compile. The current eye model is to be used in simulation run times of the order of several 100 milliseconds, so this method had to be abandoned. However, it cannot be

stressed enough that this technique is truly pioneering and is very close to allowing one to automesh using hexahedral elements the same as if they are tetrahedral.

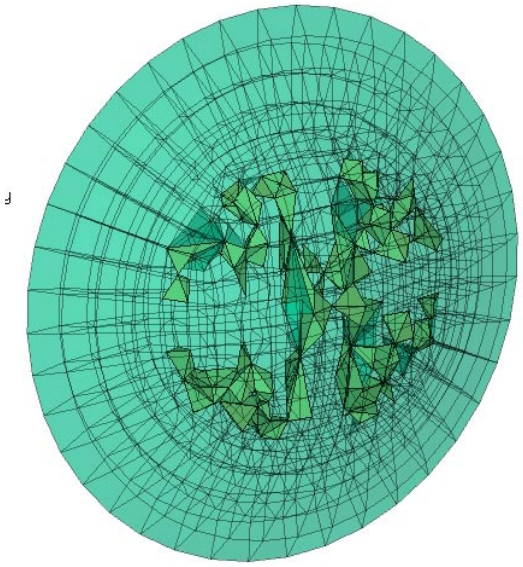

Figure 4.7: Hexahedral dominant meshing of the aqueous humor tetra-mesh shaded

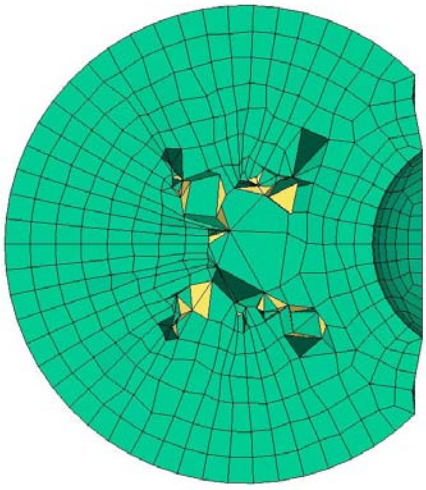

Figure 4.8: Hexahedral dominant meshing of the vitreous body (sagittal plane section)

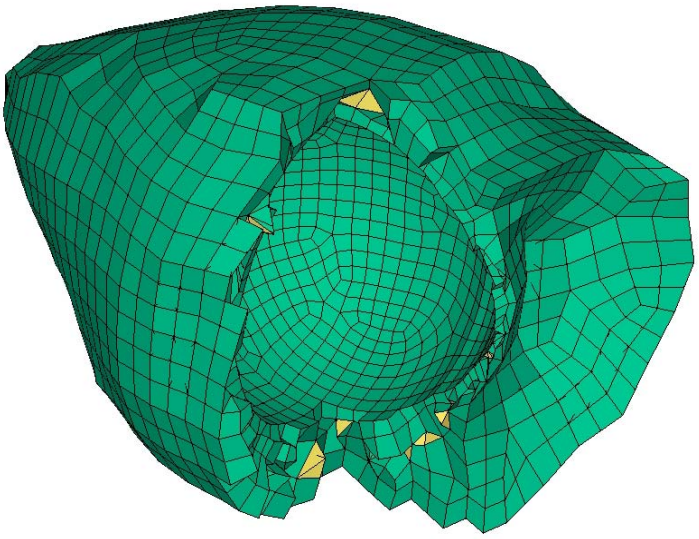

Figure 4.9: Hexahedral dominant meshing of the fatty tissue (cut away to show interior of globe region)

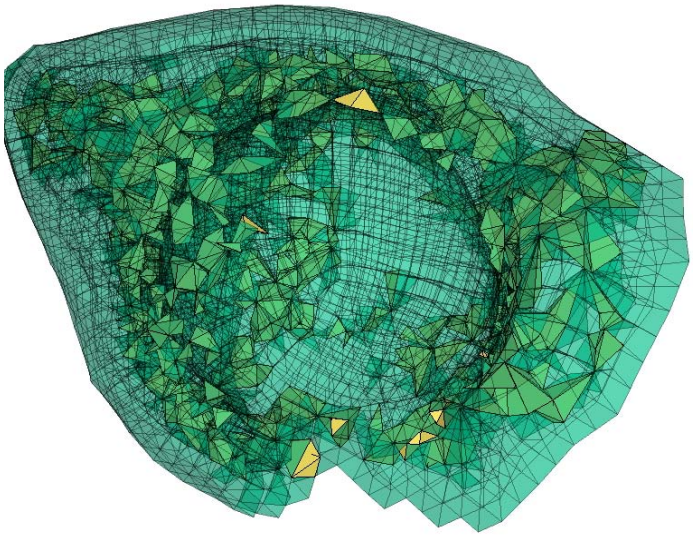

Figure 4.10: Hexahedral dominant meshing of the fatty tissue (made transparent to show the solid tetra-mesh)

The last method involves using Cubit software, a full-featured software, allowing generation of two- and three- dimensional finite element meshes and geometry preparation. The Cubit software is particularly good at hexahedral meshing

by portioning the desired geometry. In addition, modifying the entire mesh density is simple and automatic once the geometry is portioned and each of the volumes contains a mesh algorithm assigned (such as sweeping, mapping, multi-sweeping, or other). First, the geometry profile from Woo et al. (1972) and Power (2001) is imported into the CUBIT software (Figure 4.11).

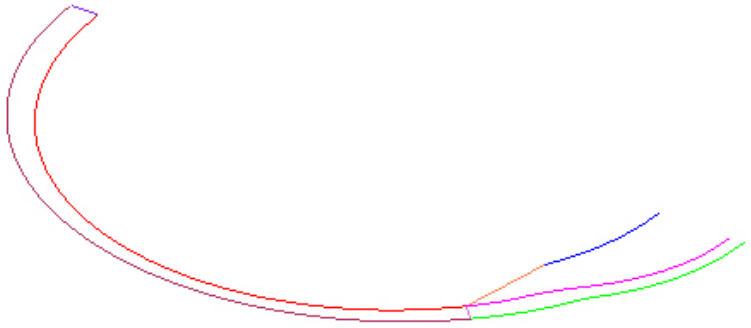

Figure 4.11: Curve profile information of the eye geometry

After the importation of the curves, the solid geometry is created for one quarter of an eye by sweeping the upper and lower bounds for the sclera and cornea (this layer will be created as a solid 8-node element layer one element layer thick) about the x-axis (axis traversing from the posterior to anterior pole). Next the vitreous and aqueous quarter geometries are created in the same way (Figure 4.12). The cornea portion of the eye does not exist yet. The information from Figure 3.2 is used concerning the cornea diameter of 11.7 mm when viewed from the frontal plane. The actual cornea, as seen in Figure 3.2, is really elliptical in shape. In order to create the cornea, and divide up the quarter eye for meshing, a cylinder with diameter 11.7 mm is created along the x-axis (Figure 4.13 and 4.14).

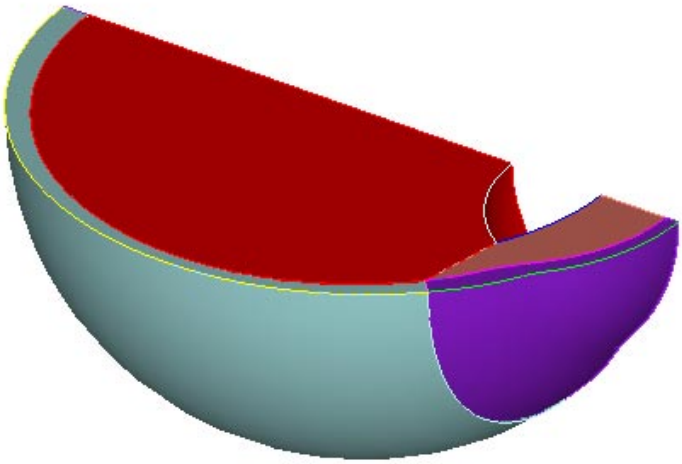

Figure 4.12: Solid volume creation of quarter eye by sweeping curves about the x-axis

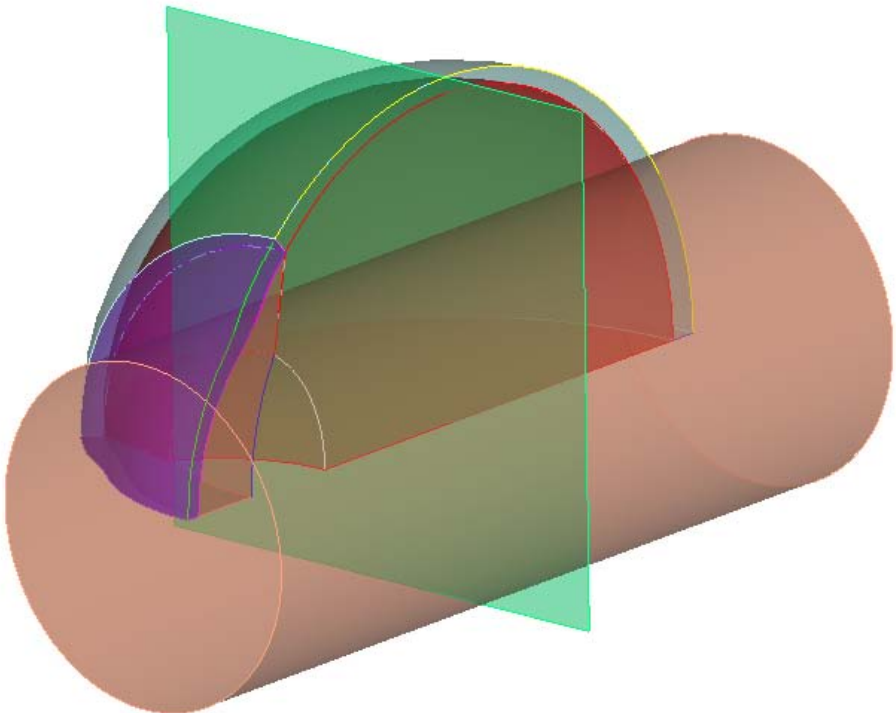

Figure 4.13: Cutting plane and cylinder shown to partition the eye quarter (transparent view)

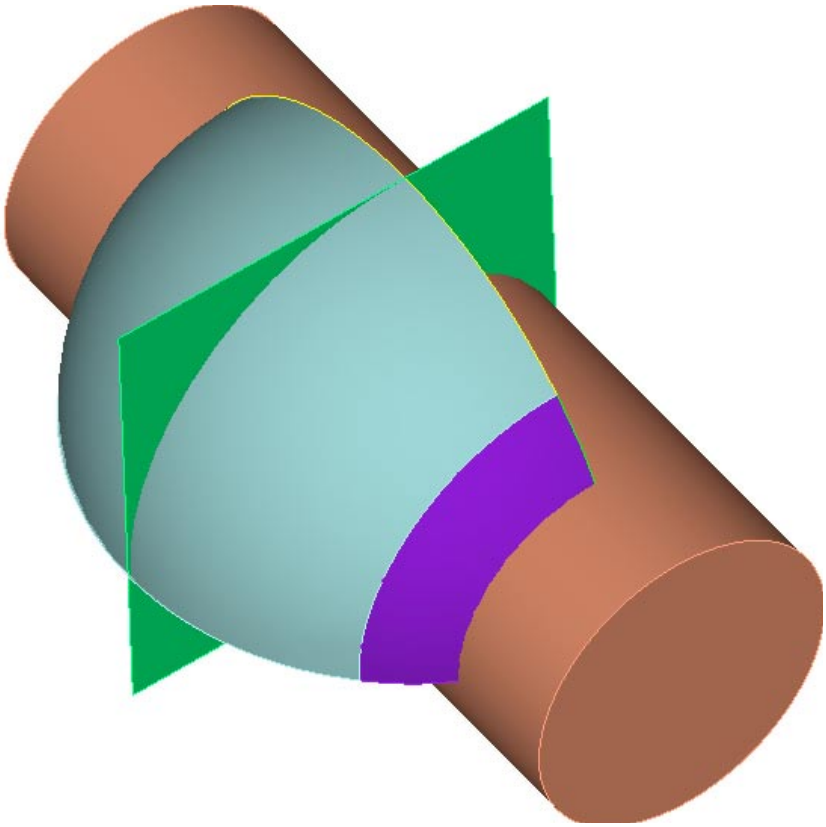

Figure 4.14: Cutting plane and cylinder shown to partition the eye quarter (solid view)

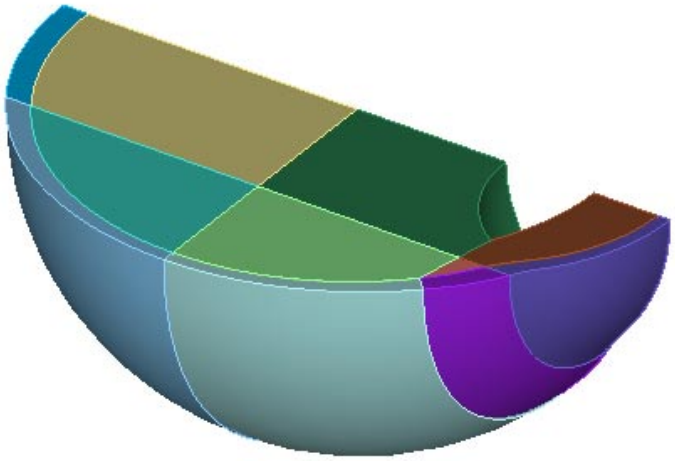

Figure 4.15: 11 volumes shown after the cutting plane and cylinder

In addition, a plane bisects the eye at the top of the equator parallel to the frontal plane (Y-Z plane). This plane is necessary as it divides the spherical eye into an octant, which will allow for easy meshing with hexahedral elements. Figure 4.15 shows the final geometry after the cylinder and plane cuts take place. There are a total of 11 volumes that will be meshed using various sweep and map commands. In Figure 4.16, the mesh quarter is shown for an adult eye with interval size 1.5 mm (scaled to an infant will make this 0.9675 mm). Figure 4.17 shows the interval size of 1.8 mm used for the adult eye (scaled to an infant will make this 1.161 mm).

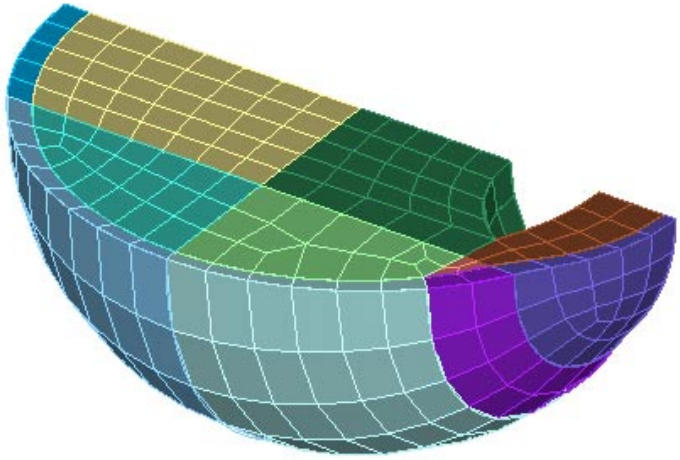

Figure 4.16: Hexahedral mesh of quarter eye with interval size 1.5 mm (adult eye)

The objective is to keep the interval size of the hexahedral and cornea-scleral shell around one millimeter for the infant eye. The mesh size with interval 1.161 mm is chosen as the aqueous mesh is very course and is not really of concern in this eye

model. The important consideration is with the retinal nodal forces and the vitreous response near the posterior pole of the eye.

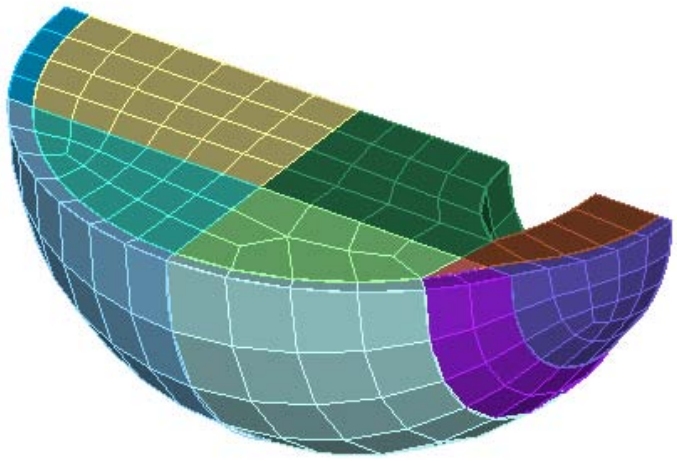

Figure 4.17: Hexahedral mesh of quarter eye with interval size 1.8 mm (adult eye)

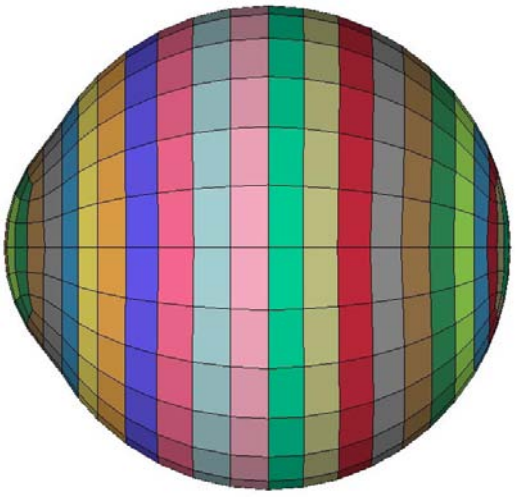

Figure 4.18: Cornea-scleral shell circumferential rings with varying thickness properties for each ring

The Cubit software also meshed the cornea-scleral shell in circumferential rings as in Stitzel et al. (2002) and Power (2001) (Figure 4.18). This allowed the grouping of properties of each ring for a total of 24 as opposed to 236 separate properties as before (Figure 4.19). The cornea and sclera shells are still created as before by replacing each solid element with a shell element at the mid-plane with the corresponding thickness information captured. Once the shell layer is created, the nodes from the vitreous and aqueous bounding surface are moved to the new location of the shell and then made coincident so that the sclera-cornea is fixed to the vitreous and aqueous.

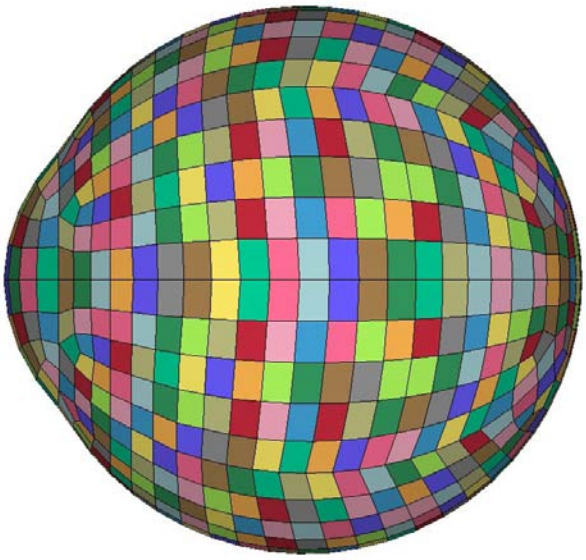

Figure 4.19: Cornea-scleral shell with each element having unique thickness property

Fatty Tissue

The fatty tissue in the ocular cavity provides cushioning and energy absorption capabilities. In addition to the tethers (optic nerve and muscles), the fatty tissue helps keep the eye positioned and acts as part of the spherical joint of the eyeball. The fatty tissue is considered as a homogeneous material; however, it is actually a "combination of an elastic phase composed of fat fibers (mainly collagen) and a fluid phase composed of fatty nodules saturated by physiological fluid" (Luboz et al., 2004, p. 204).

The only study to model the ocular cavity in a full-featured eye model is Power (2001). In this case, the fatty tissue is modeled as homogenous material composed of solid 8-node elements with a conforming space for the eye globe to fit in with a slight air gap to allow for proper contact interactions. In the Power model, the fatty tissue extends up to the equator of the eye globe (visual inspection). This fatty tissue is used for impact simulations.

In this SBS study, there is to be a rotational-translational shake, in the sagittal plane, applied to the eye, so the fatty tissue needs to extend and include the eyelid area to help confine the eye. Like the Power model, the fatty tissue is supported using the outer perimeter nodes except for the eyelid area that has the nodes unsupported. The Power model represents the complex geometry of the ocular cavity by simplifying to a pyramid shape (Figure 3.9); however, this model utilizes the geometrical information of this cavity from the Visible Human Project and the eyelid boundary from the MADYMO finite element human mesh (Figure 3.10). Therefore, the final geometry is extremely complex and includes the eye globe space with a gap for contact algorithms.

Initial attempts are made to create hexahedral meshes as Power did, but the geometry proved to be too difficult to use a manual meshing technique. Therefore, the surface mesh of the ocular cavity and eye globe is used to create a tetra-mesh (Figure 4.20).

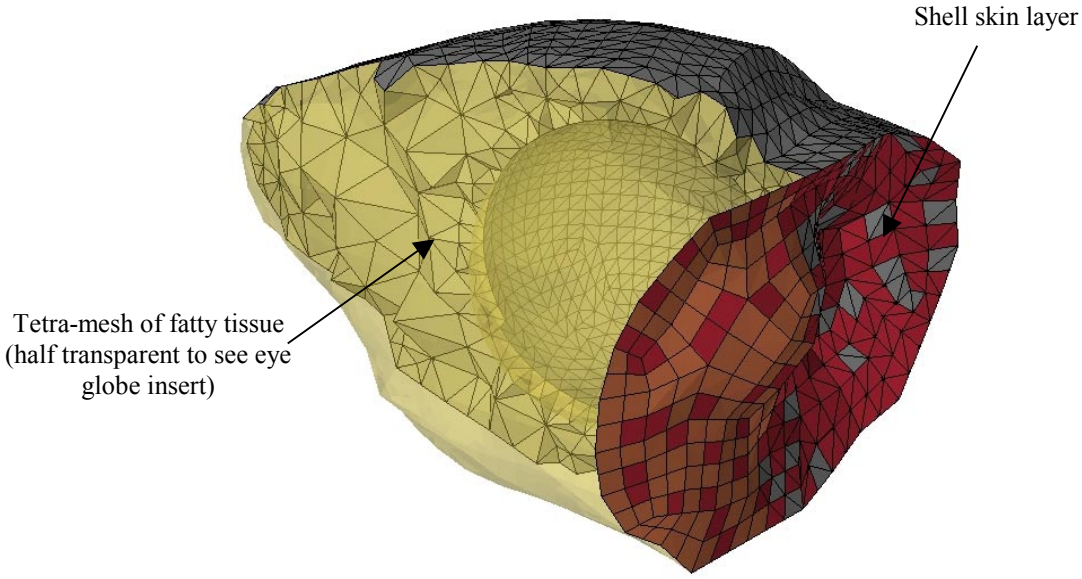

Figure 4.20: Final tetra-mesh of the fatty tissue and eye lid

In order to use the tetra-mesh function in the EasiCrash software, the surface mesh must enclose a volume. However, in this modeling case, there is the eye globe space to contend with. This issue is overcome by creating a passageway through the ocular cavity surface to the eye globe surface mesh via a manual mesh of four quad elements linking the two surfaces together (Figure 4.21 and 4.22). Once this is done, both the ocular cavity surface and eye globe surface, which is slightly larger than the actual

eye globe to allow for a contact gap, have the quad mesh split into tria elements. Finally the entire surface is selected and meshed (Figure 4.20).

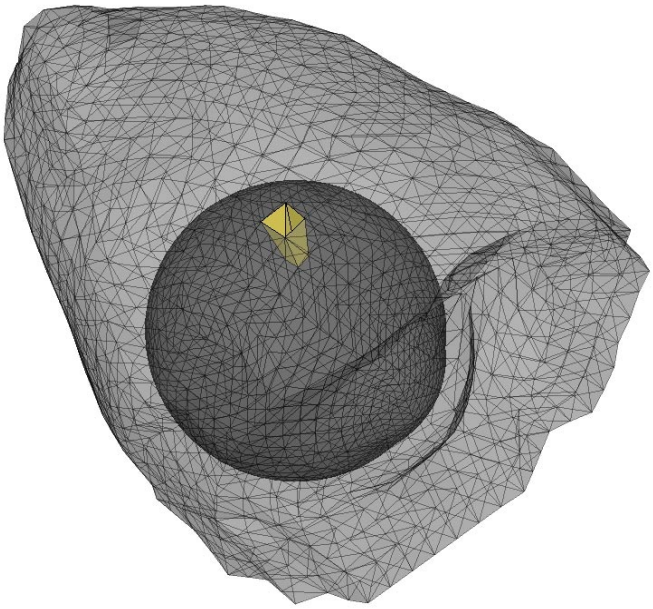

Figure 4.21: Fatty tissue surface mesh preparation for tetra-meshing (transparent view)

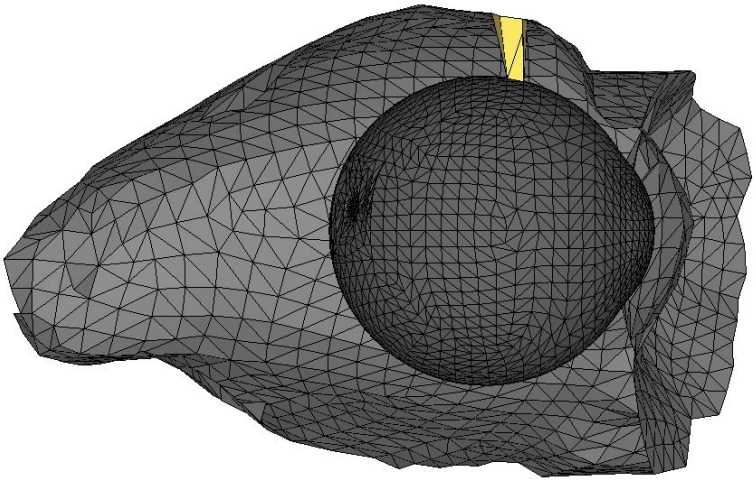

Figure 4.22: Fatty tissue surface mesh preparation for tetra-meshing (sagittal cut-away view)

Initially, the optic nerve channel was included in the fatty tissue with the eye globe space (Figure 4.23); however, the early drafts of the eye model revealed the contact interaction between the optic nerve and eye mesh became unstable near the corner where the optic nerve cavity meets the eye globe cavity. In addition, the contact of the optic nerve and the fatty tissue contributed little to the overall eye kinematics since the posterior nodes of the optic nerve are fixed. Therefore, this complexity is left out in later versions of the model. This simplification is justified, as further tests would include an analytical optic nerve (chapter 5). The analytical optic nerve model does not use a contact algorithm.

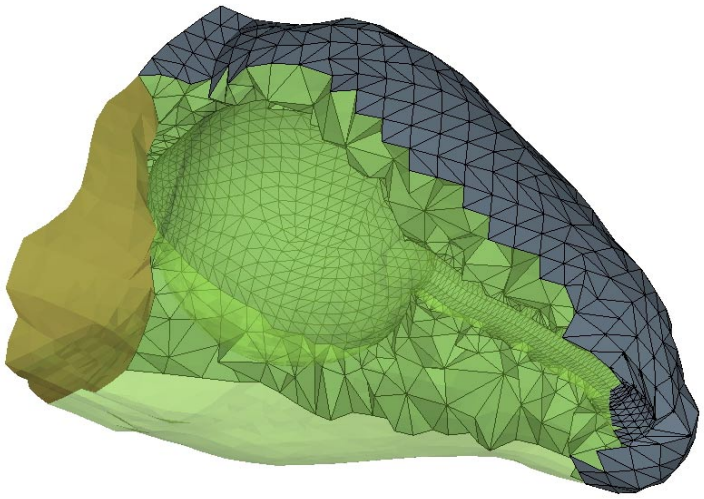

Figure 4.23: Fatty tissue tetra-mesh with optic nerve channel included (partially transparent to show cavity)

Attempts are made to create a hexahedral dominant mesh (Figures 4.9 and 4.10), but instabilities occurred in impact simulations due to the small tetrahedral

elements. Therefore, the tetra-mesh fatty tissue is used. In regards to the mesh locking that is considered in the vitreous and aqueous, the fatty tissue is to be used mostly to restrict the movement of the eye and provide some support with impact situations, so the compressive ability is more important than the shearing. Also, the fatty tissue is to be modeled with material using a Mooney-Rivlin material (Samani & Plewes, 2004; Verver, 2004) or a linear elastic material (Todd & Thacker, 1994; Luboz et al., 2004). In the Power model, the elastic material from Todd and Thacker is used. Therefore, mesh locking is not a concern in this situation. Finally, the most anterior of the fatty tissue is composed of shell elements representing the skin layer (Figure 4.20).

Conclusion

This chapter details some of the different techniques that are attempted in meshing the eye and fatty tissue. The most important considerations are given to element shape of the vitreous material, as this is the most sensitive area due to the compliancy of the material. The second consideration is the element size. Accuracy is achieved by creating an extremely small mesh; however, a balance of accuracy and time efficiency is needed as simulations involve time ranges from 250 milliseconds to 1 second. Brands (2002) investigates mesh density on cylindrical samples modeling brain tissue and shows that the angular displacements increase as the mesh is refined. Refining the mesh also increases peak values by 4% and shows a decrease in radial

displacements. Therefore, it is reasonable to assume similar trends are possible by modifying the mesh density in the eye vitreous.

The mesh density of the cornea-scleral shell of the Power (2001) eye is shell 464 triangular elements. This density would reduce to 232 quad elements if one were to compare it with other quad element densities. The Stitzel et al. (2002) eye cornea-scleral shell mesh density is 1855 elements for one-quarter eye (7420 elements if a full eye is considered). Uchio et al. (1999) used a mesh density, for the cornea-scleral shell, of 1960 elements. In this current work, two models are investigated, namely the manually meshed eye model and the Cubit developed eye model. The mesh density of the manual eye model build is 936 quad elements for the cornea-scleral shell and 504 quad elements for the Cubit developed eye model. Therefore, the mesh is rather course compared to previous work other than the Power model.

However, the time duration in the dynamic simulation is important to consider. The Stitzel et al. model with one-quarter-eye model used a maximum simulation length of 0.6 milliseconds. Uchio et al. used their eye model in an impact study and mention that the computational time is two minutes. Power considers goggle-to-eye contact with airbag deployment. The time to fully deploy the airbag is 25 milliseconds, and there is a time history plot showing the time range from 0 to 30 milliseconds. The simulation time is 28 milliseconds as noted in the MADYMO input file supplied in Appendix B of Power (2001). The current work of the SBS eye will consider a 4 Hz shake, meaning the simulation time is 1000 milliseconds and can take 48 to 180 hours to complete based on the material properties of the vitreous (detailed in later chapters).

CHAPTER V

OCULAR SHELL LAYERS

Introduction

The current eye model is composed of membrane shell layers representing the cornea-sclera shell, choroid membrane, and the retina membrane. Most of the eye models that investigate globe rupture model only the cornea-sclera layer. Therefore, mechanical properties of the choroid and retina are negligible to the mechanical strength of the eye (Graebel & van Alphen, 1977). However, this study is particularly interested in investigating retinal forces at the posterior wall of the eye, so the retina and choroid are more important to consider. This investigative study will use elastic properties for the cornea and sclera. The material is highly non-linear (Uchio et al., 1999); however, inclusion of the nonlinear stress-strain curve would require a Poisson's ratio of zero (a limitation of the MADYMO software). In addition, the choroid and retina are considered linear elastic in this eye model.

Current literature explains that the retina and choroid exhibit hyperelastic tendencies but only give mechanical properties for an elastic model (Graebel & van Alphen, 1977; Friberg & Lace, 1988; Moses, 1985; Wu, Peters, & Hammer, 1987; Stevens et al., 1992). Of particular importance are the retinal adhesive or detachment forces in this study. These forces are used to determine possible thresholds in retinal damage (hemorrhaging or detachment). Utilizing various techniques, this force has been reported to be 0.06 to 0.17 N/m for rabbit eye strips, depending on peeling rate

(deGuillebon, 1972), to 0.14 N/m for monkey eyes by inducing blebs (Kita & Marmor, 1992).

Sclera and Cornea

The cornea, a clear membrane, is located in the anterior most portion of the eye containing five layers (epithelium, Bowman's membrane, stroma, Descement's membrane, and the endothelium) (Hoeltzel et al., 1992). The thickness of the cornea varies throughout the layer (Woo et al., 1972). The cornea is avascular, viscoelastic, and resistant to deformation (Hogan, 1963). The sclera shell forms the outermost layer of the eye and is avascular and composed mostly of collagen (Hogan, 1963). The cornea and sclera provide protection for the intraocular tissues. Material testing of these structures is done using a membrane inflation or uniaxial tension strip test methodology. These materials testing studies show the cornea and sclera to exhibit non-linear behavior with rate dependency (Woo et al., 1972).

The current model uses the mechanical properties from Uchio et al. (1999) for the cornea and sclera (Figure 5.0). Uchio et al. determined the material properties of the cornea and sclera by performing uniaxial tensile tests. Power (2001) compares stress-strain curves from other sources and shows the Uchio et al. strip testing to have the steepest slope. Power (2001) uses the Uchio et al. material as this testing determined the mechanical properties up to failure; the model is used to predict globe rupture. MADYMO, the software used by Power, allows the data points for the stress

strain curve to be inserted directly in a material type hysteresis. Unfortunately, this material property has no way of entering the Poisson's ratio and is set to zero.

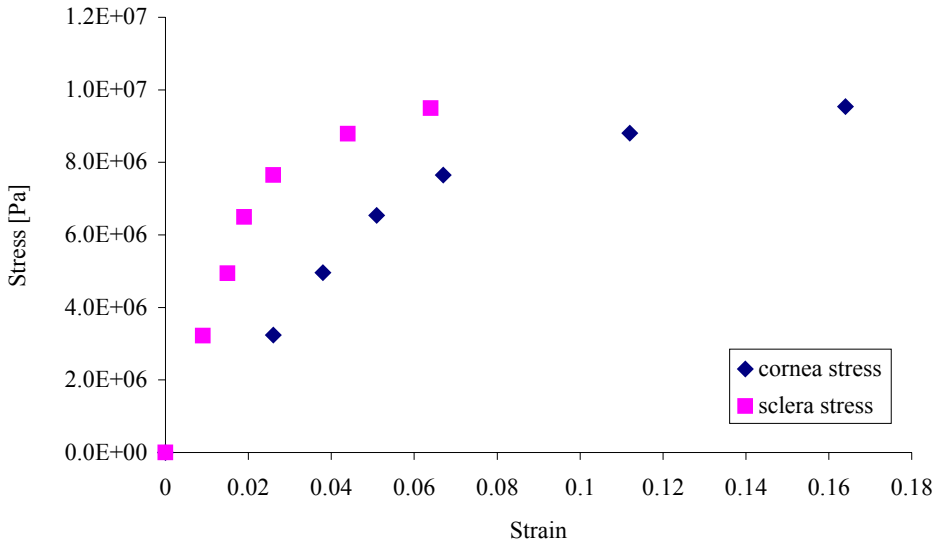

Figure 5.0: Stress-strain experiment data points for the cornea and sclera (Uchio et al., 1999).

The Uchio et al. test showed the Poisson's ratio for the cornea to be 0.42 and 0.49 for the sclera. Stitzel et al. (2002) use an orthotropic material using the Uchio et al. materials. The Poisson's ratio is assumed to be 0.5. The compressive stiffness is made to be 1/100 of the stiffness in tension for the Stitzel et al. for the cornea and sclera shell material. In the current model, the cornea and sclera shell are not to be considered in globe rupture prediction, so the elastic modulus from Figure 5.0 is determined to be 124 MPa and 358 MPa for the cornea and sclera shell respectively. The Poisson's ratio is set to be the same as the Uchio et al. test. In order to account for weakness in compression (Battaglioli & Kamm, 1984) as done by Stitzel et al., the compressive stiffness is set to 1/100 of the tension stiffness by specifying the

reduction factor equal to 0.01 in the MADYMO isolin material card. This reduction factor is used in conjunction with the tension only switch to scale down the negative principle stresses. The density is set to 1076 kg/m^3 for the cornea (Duck 1990) and 1400 kg/m^3 for the sclera (Power 2001). The shell is composed of four node membrane elements with varying thickness (Figure 4.2) information to model zero resistance from bending as past studies. The Uchio et al. material properties are chosen by Power (2001) since they take both the cornea and sclera samples to failure.

The choice is made to use the material parameters from Uchio et al. in this eye model as it has been used in previous validation studies concerning globe rupture (Power, 2001; Stitzel et al., 2002) and in other dynamic parameter studies (Kisielewicz et al., 1998; Uchio et al., 1999; Uchio et al., 2001; Uchio et al., 2003; Uchio et al., 2004). As can be seen in Figure 5.0, the curves are non-linear but do exhibit a linear region and a non-linear region, which could be considered the plastic region of the curve. However, one must use caution in making this assumption of plasticity. Uchio et al. took each sample to failure and plotted the average results of both the sclera and cornea tissue samples (Figure 5.0). Therefore, it is not clear if these samples would return to their original undeformed state or close to it. Further, hysteresis effects and strain rate are not mentioned in the Uchio et al. study (perhaps a quasi-static rate was used). Despite using this material, serious consideration is given to other studies that measure the mechanical properties of the cornea and sclera.

Curtin (1969) performed uniaxial tension tests on sclera tissue from human and porcine eyes. A maximum stress level of 7.5 grams/mm^2 is used to model equivalent intraocular pressure of 100 mm Hg upon a 1 mm thick scleral wall. These

tension tests are conducted on anterior, equatorial, and posterior eye samples. These tests are concerned with loads within the physiological limits of the eyes and do not take the tissue samples to failure. However, the hysteresis effect is noted in Figure 5.1 for the posterior sclera of a human eye. This information could be used directly in the MADYMO using a finite element material card that can model the hysteresis effects. However, the Poisson's ratio would be set to zero, and there could be extrapolation issues with the low strain limits (only four percent range in Figure 5.1).

However, there is interest in determining a constitutive material model that could be used to fit[6] this data that would be suitable for finite element analysis. Particularly, hyperelastic behavior has been used to describe the choroid (Moses, 1965) and some of the stress-strain plots for the sclera and cornea tissue exhibit similar trends (at least for certain levels of strain) (Curtin, 1969; Woo et al., 1972; Graebel & Van Alphen, 1977; Friberg & Lace, 1988; Hoeltzel et al., 1992; Buzard, 1992).

Hyperelastic behavior can be considered in MADYMO by using the Mooney-Rivlin (Rivlin & Thomas) constitutive equation for solid 8-node elements using two material parameters and specifying the Poisson's ratio. In the case where the deformations can be considered small, the Mooney-Rivlin equation can be considered in this form (5.0):

$$W = A(I_1-3) + B(I_2 -3) \qquad (5.0)$$

Where W is the strain energy, A and B are the material parameters of the first and second invariants of the strain tensor, and I_1 and I_2 are the strain invariants.

[6] The curve fits, in this chapter, are done using the Levenberg-Marquardt method.

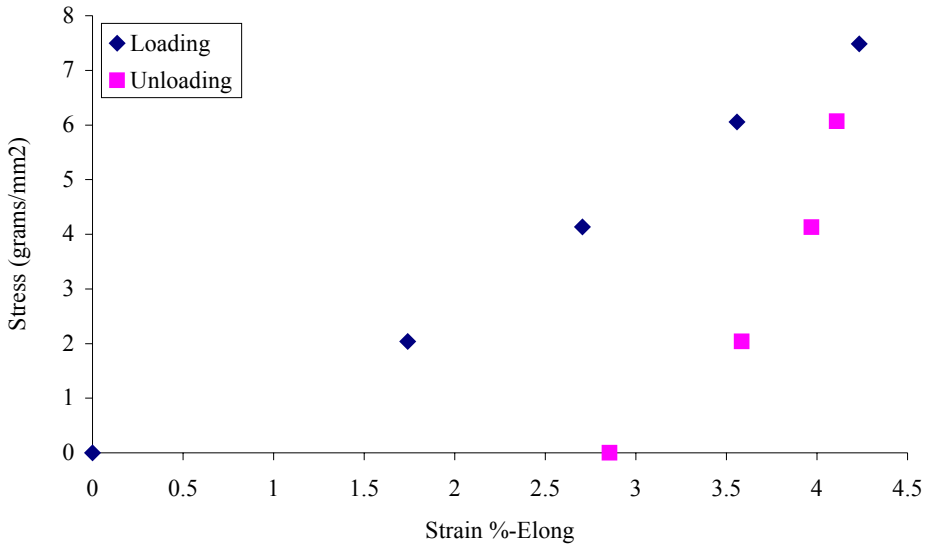

Figure 5.1: Stress-Strain curve from Curtin (1969) showing the loading and unloading of the human posterior sclera for low strain.

The strain invariants are in terms of extension ratios λ_1, λ_2, and λ_3 so that

$$I_1 = \lambda_1^2 + \lambda_2^2 + \lambda_3^2 \text{ and } I_2 = \frac{1}{\lambda_1^2} + \frac{1}{\lambda_2^2} + \frac{1}{\lambda_3^2} \qquad (5.1)$$

If the extension ratios are aligned such that they are located parallel to the principle axis, and assuming the surface of the sample is force free, then $\sigma_3 = 0$. So that the incompressibility condition implies $\lambda_1\lambda_2\lambda_3=1$ and $\lambda_2 = \lambda_1^{-1/2}$. Then the strain invariants can be considered in this form letting $\lambda_1 = \lambda$:

$$I_1 = \lambda^2 + \frac{2}{\lambda} \text{ and } I_2 = 2\lambda + \frac{1}{\lambda^2} \qquad (5.2)$$

Which gives,

$$\sigma = 2\left(\lambda - \frac{1}{\lambda^2}\right)\left(\frac{\partial W}{\partial I_1} + \frac{1}{\lambda}\frac{\partial W}{\partial I_2}\right) \qquad (5.3)$$

Where $\partial W/\partial I_1$ is the material parameter of the first invariant (called A from now on); $\partial W/\partial I_2$ is the material parameter of the second invariant (called B from now on); and, σ is the uni-axial stress in extension. Equation (5.3) is in terms of engineering strain as is typically recorded in the material property determination studies conducted on the ocular shell layers. Therefore, the relationship is as follows and is similar to that used by Williams (1980) for material parameter fits for polyurethane liner material (equation is used for tensile and compressive stress with curve through the origin):

$$\sigma_e = 2A\left(\lambda - \frac{1}{\lambda^2}\right) + 2B\left(1 - \frac{1}{\lambda^3}\right) \qquad (5.4)$$

Where σ_e is the engineering stress, and the other parameters are defined above.

Another constitutive equation that describes hyperelastic behavior for a wide range of strain hardening is the Ogden formulation (5.5) (Shergold, Fleck, & Radford, 2006).

$$\phi = \frac{2\mu}{\alpha^2}\left(\lambda_1^\alpha + \lambda_2^\alpha + \lambda_3^\alpha - 3\right) \qquad (5.5)$$

Where ϕ is the strain energy density per undeformed unit volume, (λ_1 to λ_3) are the principal stretch ratios, α is the strain-hardening exponent, and μ acts as the shear modulus under infinitesimal straining. For uniaxial compression or tension, the Ogden equation takes the following form (Shergold, Fleck, & Radford, 2006) (5.6):

$$\sigma = \frac{2\mu}{\alpha}\left[\lambda^{\alpha-1} - \lambda^{-1-\left(\frac{\alpha}{2}\right)}\right] \qquad (5.6)$$

Where σ is the engineering stress, and the other variables are defined as in (5.5). This equation is also implemented in some finite element codes (unfortunately not MADYMO at this time).

Shergold, Fleck, and Radford conduct a comparative study with the Ogden and Mooney-Rivlin constitutive equations. They show that the Mooney-Rivlin equation is inappropriate for describing strong strain-hardening characteristics. Some of the figures in their study show the Mooney-Rivlin fits are good up to the point of strain hardening while the Ogden fit is rather good in the entire region. Interestingly, some of the studies that describe the cornea and sclera to follow an exponential stress-strain behavior (Woo et al., 1972; Graebel & Van Alphen, 1977) have poor fits with the Mooney-Rivlin equation but excellent fits with the Ogden formulation due to a sharp rise in strain hardening. The Woo et al. and Graebel and Van Alphen studies will be examined.

The plot from Curtin (Figure 5.1) shows a good fit with the Mooney-Rivlin and Ogden formulation as seen in Figure 5.2. The Curtin sclera sample shows a good fit with the hyperelastic formulations for the Mooney-Rivlin and Ogden. The coefficients for the Mooney-Rivlin are 4.19×10^{6} Pa for A and -4.04×10^{6} Pa for B. The coefficients for the Ogden fit are 3.24×10^{1} for α and 3.57×10^{5} Pa for μ. The correlation constants for the Mooney-Rivlin and Ogden are 0.999 and 0.998, respectively.

Friberg and Lace (1988) conducted simple tension tests on choroid and sclera strips. Figure 5.3 illustrates the stress-strain data points for four strip orientations of the sclera. Friberg and Lace use data points to determine an average elastic modulus

for the sclera. They show that the modulus varies with location with the anterior region having an averaged modulus of 2.9 +/- 1.4x10^6 Pa and 1.8 +/- 1.1x10^6 Pa for the posterior region.

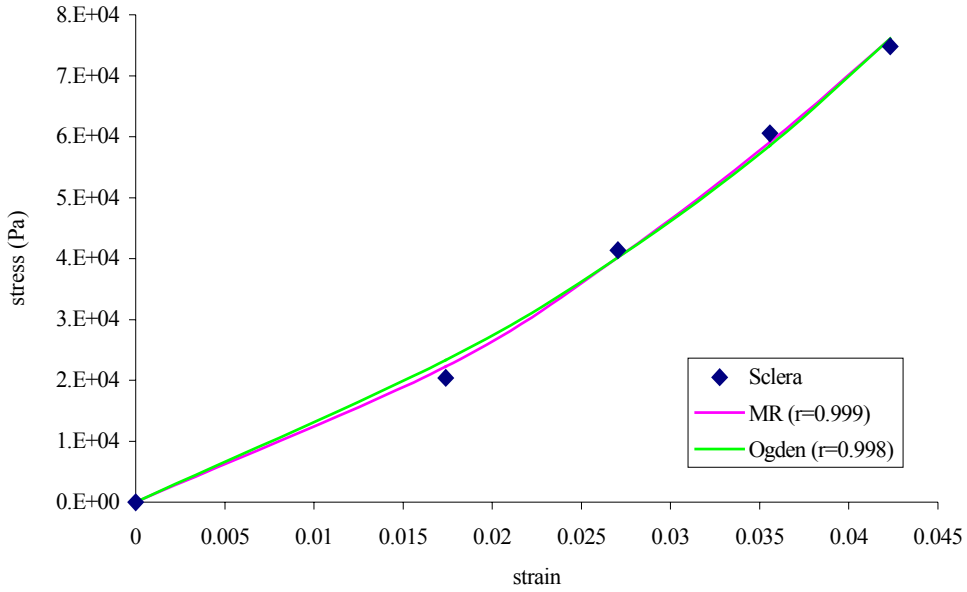

Figure 5.2: Curve fit for the Curtin human posterior sclera comparing the Mooney-Rivlin and Ogden constitutive equations for strains below 5%.

It is apparent from Figure 5.3 that the strip testing for the posterior region exhibits more compliant behavior and is in agreement with the testing done by Curtin (1969). The samples from Figure 5.3 are fit to hyperelastic material properties as well as a linear fit (as done in the Friberg and Lace study). It can be seen that the hyperelastic fits are a better match than the linear fit chosen in the study (Figures 5.4 to 5.7). All the coefficients, modulus of elasticity, and correlations are compiled in Table 5.0. The curve fitting shown in Figures 5.4-5.7 are done by zeroing out the initial stress and strain in order to let the intercept equal zero. The Young's moduli reported in Table 5.0 agree with the reported values from Friberg and Lace (1988).

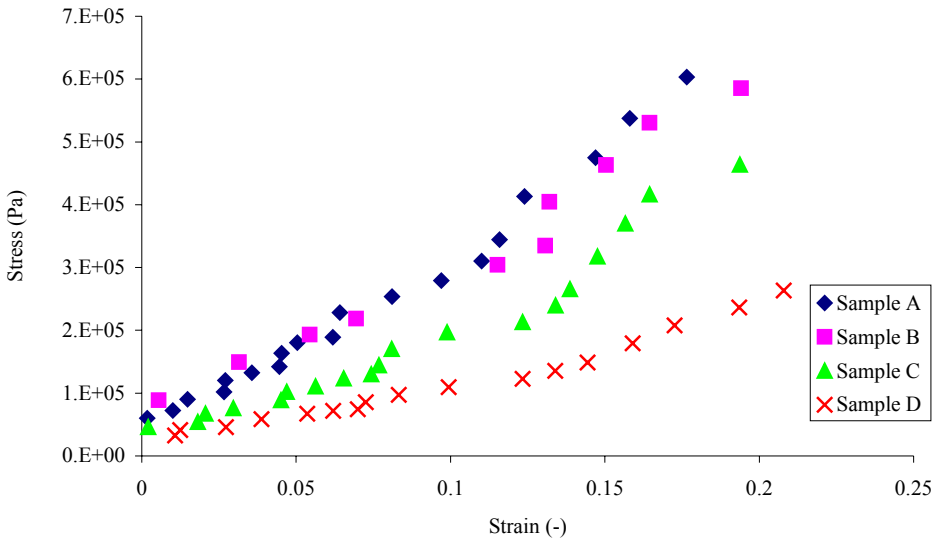

Figure 5.3: Stress-strain relationship from Friberg and Lace (1988) from strips of sclera tissue with the following orientations: Sample A: anterior circumferential, Sample B: radial inferotemporal, Sample C: radial supernasal, Sample D: posterior circumferential.

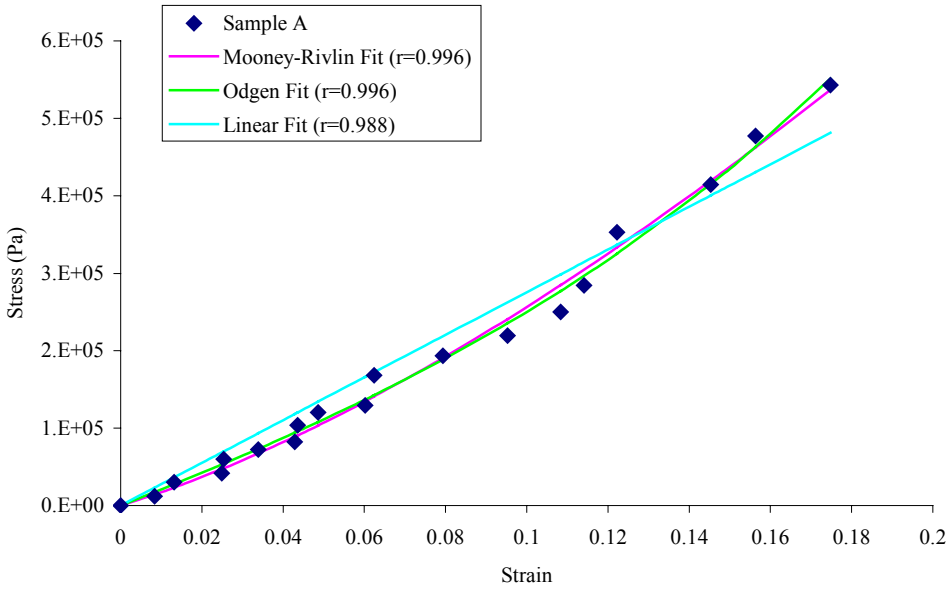

Figure 5.4: Curve fit of the sample A sclera strip from Friberg and Lace (1988).

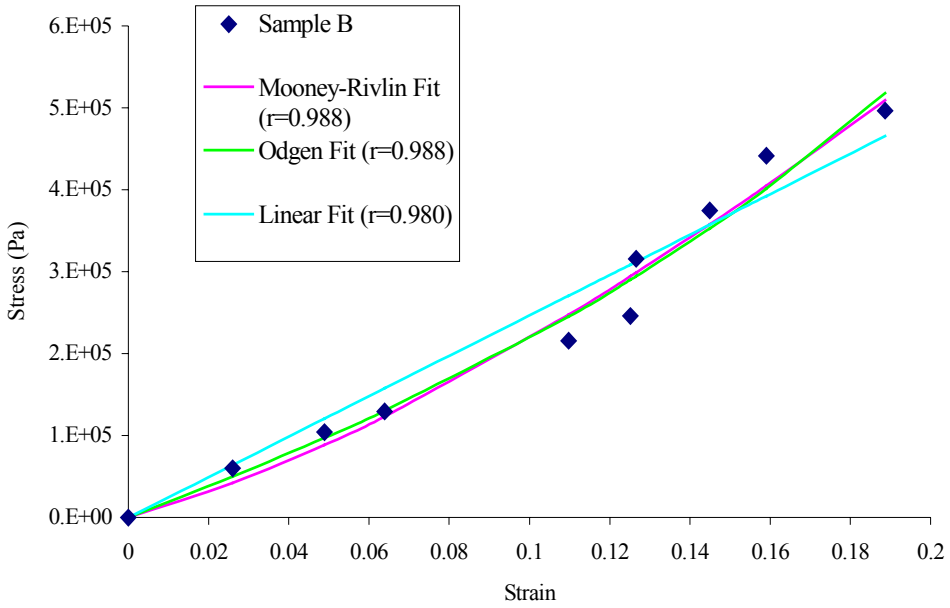

Figure 5.5: Curve fit of the sample B sclera strip from Friberg and Lace (1988).

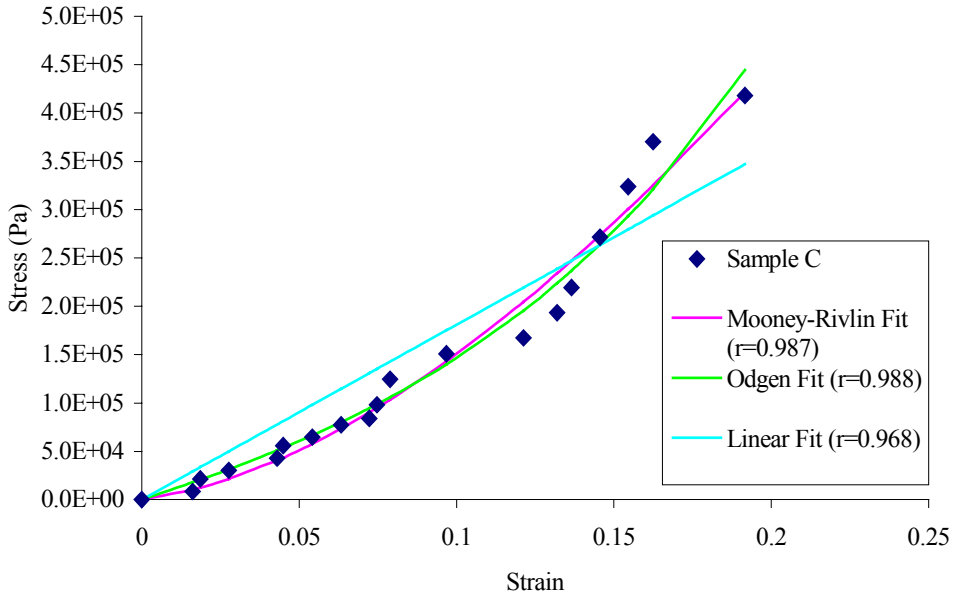

Figure 5.6: Curve fit of the sample C sclera strip from Friberg and Lace (1988).

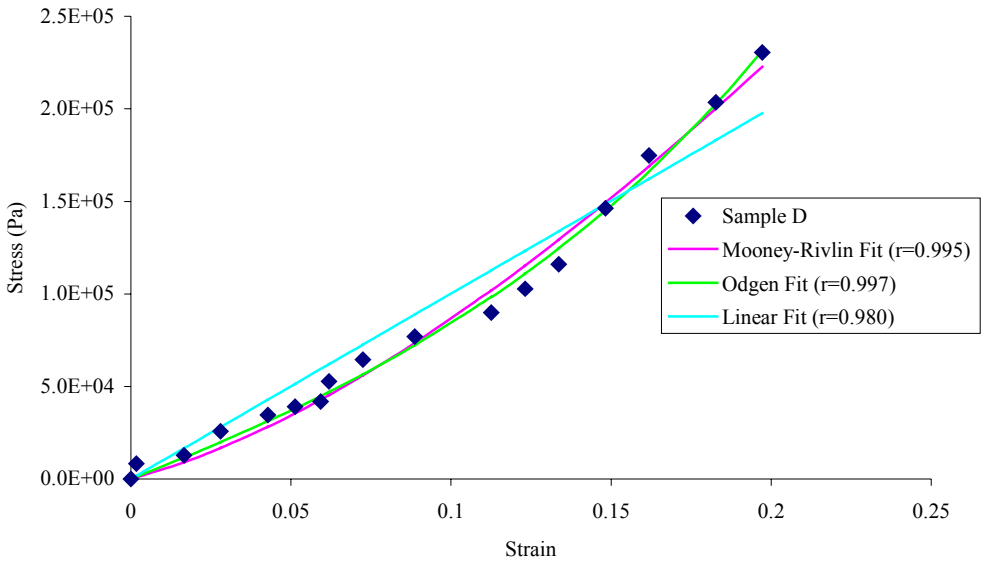

Figure 5.7: Curve fit of the sample D sclera strip from Friberg and Lace (1988).

Table 5.0: Summary of material parameters for the samples A-D for the sclera strip tensile test conducted by Friberg and Lace (1988).

Sclera Strip Sample	Mooney-Rivlin Material Parameters		Odgen Material Parameters		Young's Modulus	Correlation factor r
	A (Pa)	B (Pa)	α	μ (Pa)	E (Pa)	MR/Odgen/Linear
A	2.5E6	-2.2E6	10.4	6.9E5	2.8E6	0.996/0.996/0.988
B	2.1E6	-1.9E6	9.4	6.2E5	2.5E6	0.988/0.988/0.980
C	2.3E6	-2.2E6	13.2	3.6E5	1.8E6	0.987/0.988/0.968
D	9.6E5	-8.8E5	10.8	2.3E5	1.0E6	0.995/0.997/0.980

Buzzard (1992) shows a plot of the sclera and cornea for stress versus strain. The relationship, on visual inspection, appears to show hyperelastic properties, like Friberg and Lace. This plot is based on the work of Hoeltzel et al. (1992). In the Hoeltzel et al. study, the cornea tensile testing on samples is fit to the following constitutive equation:

$$\sigma = \alpha(\varepsilon - \varepsilon_s)^{\beta} \qquad (5.7)$$

Where α is a scale factor in units Pa, ε is the strain, ε_s is referred to as the slack strain (difference between zero strain and the smallest strain in initiate load bearing in the sample),and β is the exponent of the non-linear relationship. This slack strain factor is removed by zeroing out the stress and strain so that (5.7) simply becomes:

$$\sigma = \alpha(\varepsilon)^{\beta} \qquad (5.8)$$

Figures 5.8 and 5.9 show the data points for the cornea and sclera curve fitted with the constitutive equation (5.8) along with the Mooney-Rivlin and Odgen hyperelastic models. The power fit defined by (5.8) for the cornea is in agreement with the tabulated value for the human cycle 1-3 in Hoeltzel et al. (1992). The material parameters and the correlation factors are tabulated in Table 5.1. In this case, all three of the constitutive models fit the data very well for the given strain levels.

Table 5.1: Material Parameters determined for the cornea and sclera from the Buzard (1992) data points.

Test Sample	Scale and Power Parameters		Mooney-Rivlin Parameters		Odgen Parameters		Correlation factor r		
	α (Pa)	β	A (Pa)	B (Pa)	α	μ (Pa)	Power	MR	Odgen
Cornea	3.08E7	1.85	8.26E6	-8.22E6	35.41	4.13E5	1.000	0.999	0.999
Sclera	3.08E8	2.18	3.31E7	-3.32E7	76.65	5.96E5	0.999	0.999	0.999

Woo et al. (1972) and Graebel and van Alphen (1977) determine constitutive fits for the ocular tissues. Woo et al. use a membrane method for determining the properties of the cornea, sclera, and optic disc (optic nerve head). Graebel and van

Alphen consider the sclera and choroid using strips in uniaxial tension tests. Both studies consider the constitutive equations for the sclera to be of the following form:

$$\sigma = \alpha(e^{\beta\varepsilon}-1) \qquad (5.9)$$

Where σ is the stress, α is a scale factor in units Pa, β is the exponent factor, and ε is the strain. Woo et al. provide the values for α and β used in (5.9); then are tabulated in Table 5.2.

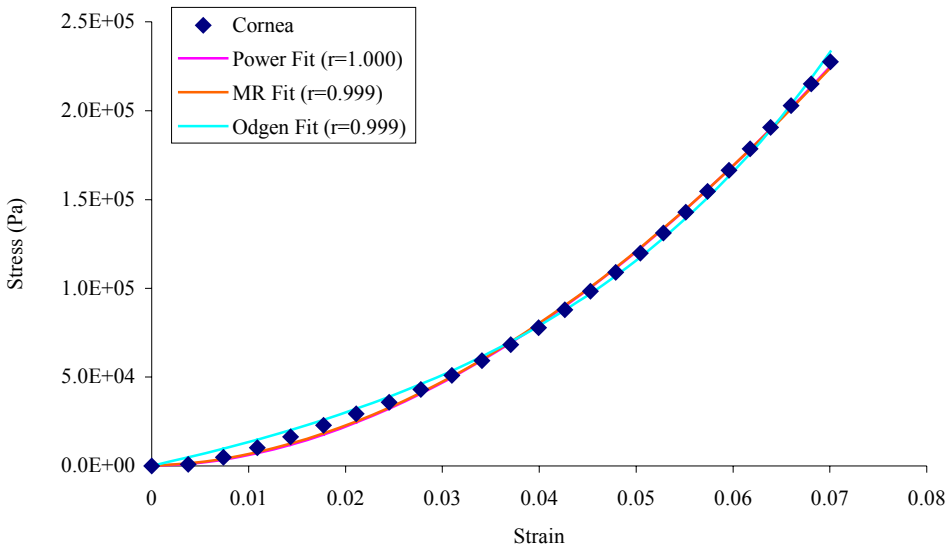

Figure 5.8: Cornea stress-strain with curve fit from Buzard (1992).

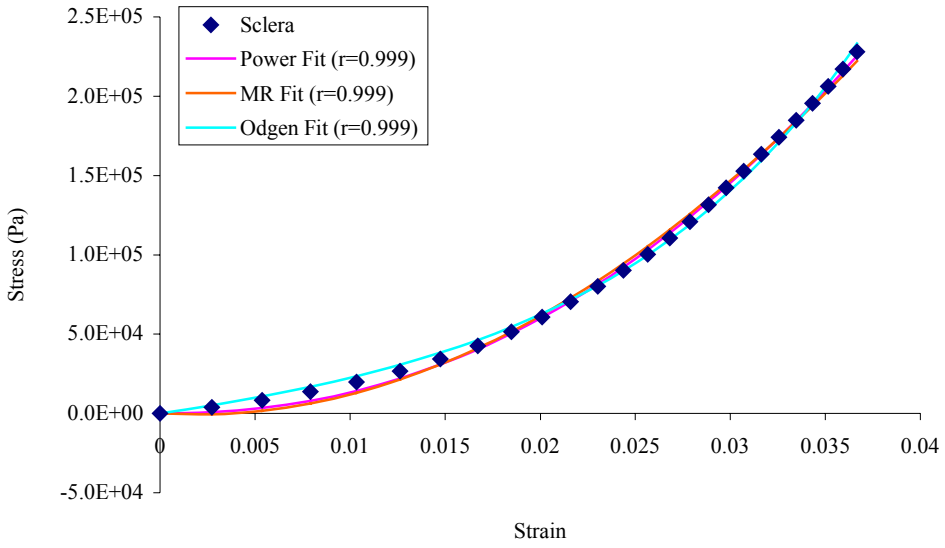

Figure 5.9: Sclera stress-strain with curve fit from Buzard (1992).

Table 5.2: Material parameters as defined in Woo et al. (1972) for the cornea, sclera, and optic disc

Material Parameters	Sclera	Cornea	Optic Disc
α (Pa)	1.8E5 Pa	5.4E4	7.7E4
β	41.8	28.0	11.5

The material constants shown in Table 5.2 are based on determining the tri-linear moduli for each of the structures. Then the slopes of the tri-linear moduli are aligned to create an effective stress versus strain curve that allows the fit of (5.9) with the determination of the material parameters to be found by a least-squares method. Using the material parameters, curves for the cornea, sclera, and optic disc (ONH) are plotted in Figure 5.10.

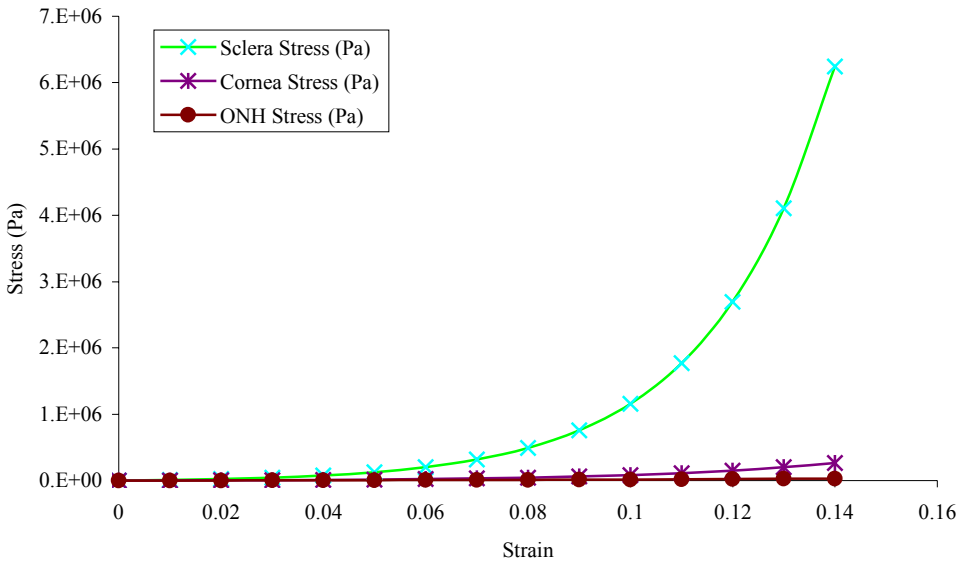

Figure 5.10: Stress versus strain plot of the Woo et al. (1972) sclera, cornea, and ONH using the provided material parameters.

As illustrated, the sclera stress exhibits a strain hardening around 10% strain. The other ocular shells also exhibit similar trends but appear linear in Figure 5.10. As shown in the work done by Shergold, Fleck, and Radford (2006), the Mooney-Rivlin fit is acceptable for low strain (below 3% for the sclera in Figure 5.11, below 8% for the cornea in Figure 5.12, and below 16% for the ONH). The Ogden fit also shows good correlation in the mentioned strain levels.

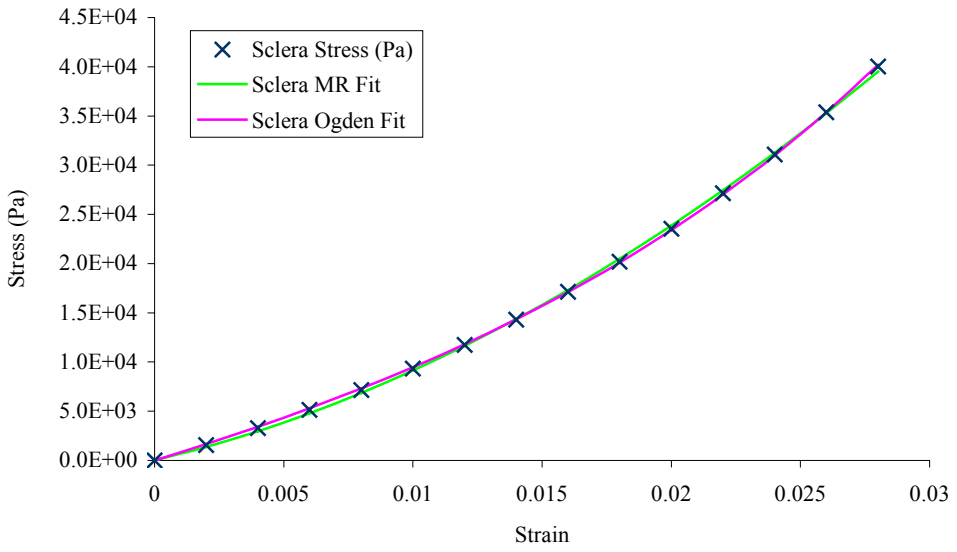

Figure 5.11: Hyperelastic fits with sclera stress versus strain defined by (5.9). Correlation is 1.000 for both fits.

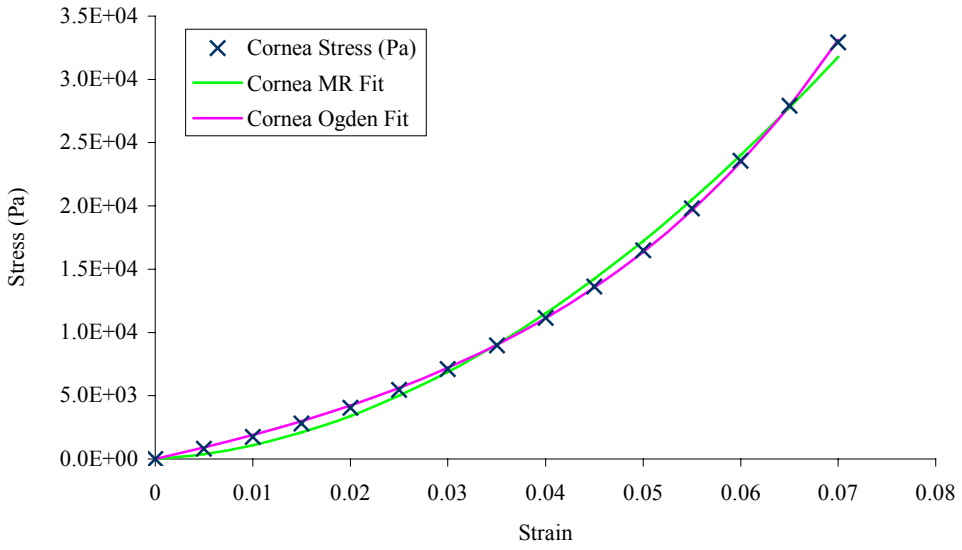

Figure 5.12: Hyperelastic fits with cornea stress versus strain defined by (5.9). Correlation is 0.999 for the Mooney-Rivlin fit and 1.000 for the Ogden fit.

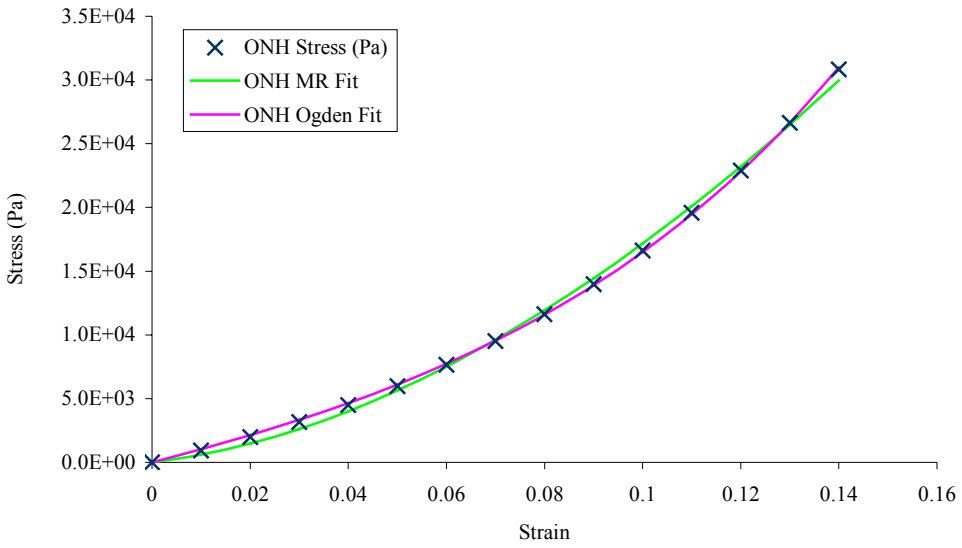

Figure 5.13: Hyperelastic fits with the ONH stress versus strain defined by (5.9). Correlation is 0.999 for the Mooney-Rivlin fit and 1.000 for the Ogden fit.

However, as seen in Figures 5.14 to 5.16, the fit for the Mooney-Rivlin constitutive equation is inferior despite having correlations above 0.900. The worst fit is associated with the ramp up of strain hardening as seen in Figure 5.14. What appears to happen is the stress is negative for strain levels below 10%; this does not make physical sense. The Ogden fit in this case is able to handle the fit nicely with a correlation equal to 1.000. Shergold, Fleck, and Radford explain the Ogden fit is good because the strain hardening exponent α is almost independent of strain rate while μ increases with strain rate (5.6). The values for the curve fits are tabulated in Table 5.3. In particular, the Mooney-Rivlin material parameters determined from Figures 5.11 to 5.13 are shown with Ogden fits from Figures 5.14 to 5.16. It would be inappropriate to tabulate the Mooney-Rivlin parameters determined from Figures 5.14 to 5.16.

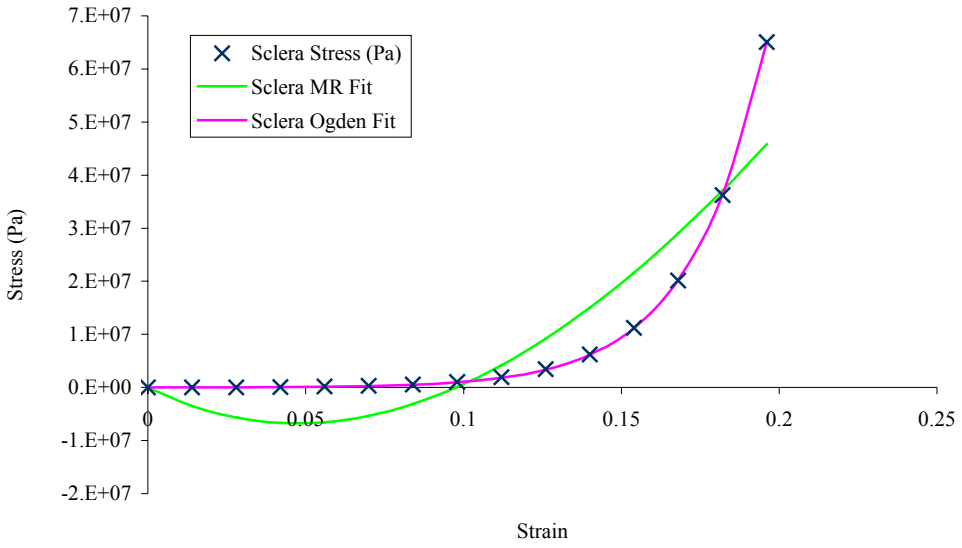

Figure 5.14: Hyperelastic curve fits with the Woo et al. (1972) sclera material with behavior from (5.9).

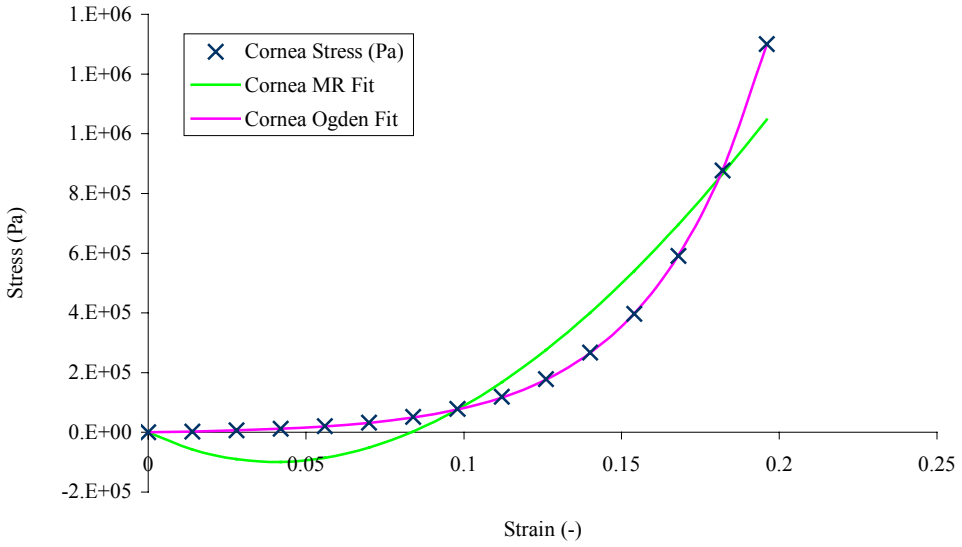

Figure 5.15: Hyperelastic curve fits with the Woo et al. (1972) cornea material with behavior from (5.9).

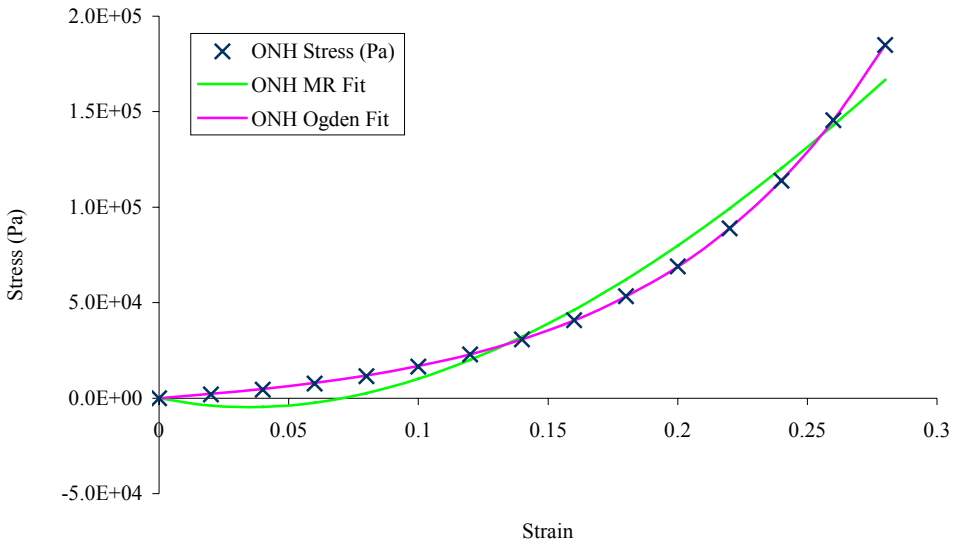

Figure 5.16: Hyperelastic curve fits with the Woo et al. (1972) ONH material with behavior from (5.9).

Table 5.3: Material parameters for the hyperelastic constitutive fit to the Woo et al. (1972) materials.

Ocular Tissue	Mooney-Rivlin Parameters		Ogden Parameters		Correlation factor r	
	A (Pa)	B (Pa)	α	μ (Pa)	MR	Odgen
Sclera	1.00E7	-1.49E7	50.22	2.44E5	0.833	1.000
Cornea	2.15E6	-3.21E6	34.03	5.98E4	0.918	1.000
ONH (Optic Disc)	4.98E5	-7.36E5	16.15	3.56E4	0.974	1.000

Graebel and Van Alphen (1977) also consider (5.9) when fitting the material behavior for the sclera samples. The parameters α and β appear to increase with age (exception to eye number 6 where α is extremely low). A total of nine eyes are used, and each sample has its own curve fit to determine the material parameters for the constitutive fit. Of particular interest is the youngest eye specimen from a four-year-old. Similar trends can be seen in Figure 5.17, where the attempted Mooney-Rivlin

fit fails to describe the trend over the strain range when the strain hardening is included. The Ogden fit, again, excels at lining up with the data points. In Figure 5.17, the baseline stress versus strain curve is provided by using $\alpha = 205.7$ and $\beta = 46.56$ from Graebel and van Alphen (1977). In this case, the Ogden parameters are 53.86 for α and 3691 Pa for μ with a correlation factor of 1.000. The Mooney-Rivlin, which should not be used, is 3.01×10^6 Pa for A and -3.22×10^6 Pa for B with a correlation of 0.929. Throughout these curve fits, one would think that the correlation factors of 0.900 and greater would indicate a superior fit; however, it is obvious that visual inspection of the fit should also be used to influence final decisions.

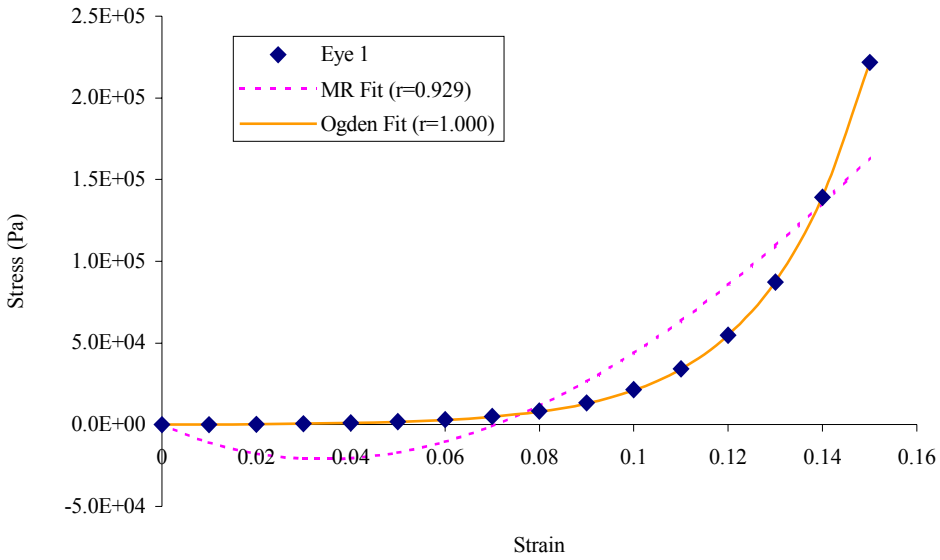

Figure 5.17: Hyperelastic curve fit to the sclera sample from Eye 1 (4-year-old) using parameters from Graebel and van Alphen (1977).

When comparing the material parameters of the sclera and cornea, it is apparent that the constitutive equations used from one study to the next vary tremendously, due to the type of testing performed (membrane inflation or strip test), age of the specimen, preparation of the specimen, species of the specimen, and the cycle loading to remove hysteresis effects. Uniformly comparing these samples by curve fitting to hyperelastic material parameters describes these tissues as having hyperelastic behavior. The exception seems to be the material testing done by Uchio et al. where they do not consider the hysteresis of the sample and just load to failure. However, the Uchio et al. material is chosen because it has been previously used in dynamic simulations studies that are able to predict globe rupture. In addition, the Mooney-Rivlin formulation in the MADYMO software can only be used for solid 8-node elements while most of the studies consider shell membrane elements that do not resist bending. This current study will therefore consider the membrane elements for the ocular shells with the Uchio et al. material parameters applied in order to focus on the parametric studies for the vitreous body.

Choroid

The choroid is a thin, highly vascular (with extensive nerve supply) membrane that supplies nutrition to the retina and anterior portion of the eye. This tissue exhibits some of the traits of erectile tissue (Hogan, 1971). The entire traits of the choroid are still unknown as all testing that has been done are postmortem and in vitro (uniaxial elongation testing). There is no question that the rich blood supply would affect the stiffness characteristic of the choroid. Friberg and Lace (1988)

suspect that in vivo testing would reveal stiffer characteristics, especially in compression. In addition, Friberg did measure the choroid thickness (0.08 mm) but assumed the in vivo thickness to be 0.42 mm on account of the full blood vessels. Testing by Moses (1965) and Graebel and van Alphen (1977) assumes a thickness of 0.02 mm and 0.16 mm, respectively. Further, Graebel and van Alphen explain that the elastic behavior of the choroid exhibited a power law behavior and tends to be less elastic with age. Moses (1965) explains that the choroid exhibits hyperelastic behavior; the choroid "appears to be an elastomer" (p. 938). An elongation versus grams plot of a meridional strip of choroid shows the repeat loading with hysteresis loops.

This information does offer flexibility as one could use the non-linear characteristics and capture the hysteresis information in the MADYMO material model type hysteresis (elastic isotropic material model with hysteresis). This is assuming the Poisson's ratio is zero which, more likely, it is 0.5 for incompressible materials.

Another option would be to fit the curve to a hyperelastic constitutive equation (disregarding the hysteresis looping) since the author suggests that the material is hyperelastic. Using (5.4) (Williams, 1980), the Mooney-Rivlin parameters (A and B), can be solved. Curve fitting, after translating the curve (Figure 5.18) to start at zero force at zero elongation, and converting to stress versus strain, the Mooney-Rivlin parameters are determined to be 4.9×10^6 Pa for A and -4.8×10^6 Pa for B.

MADYMO has a constitutive equation for hyperelastic material using the Mooney-Rivlin behavior (5.4). For comparison, a two parameter Ogden fit is also provided by (5.6), a specialized case for uniaxial compression or tension (Shergold, Fleck, & Radford, 2006). This particular constitutive equation yields –27.9 and 4.1×10^5 Pa for α and μ, respectively. A comparison is provided (Figure 5.19) that compares the measured stress versus strain for the assumed thickness of 0.02 mm of the choroid sample strip with initial length equal to 16 mm and width equal to 6 mm. Both the Mooney-Rivlin and Ogden constitutive equations fit the data quite well with correlations close to one. Moses (1965) determines the elastic modulus using (5.10), from seven eyes, for the meridional and equatorial orientations and tabulates them. The Young's modulus corresponding to the strip sample used in Figure 5.18 is given as 4.2 MPa (calculated on choroidal strips one cm wide by one cm in length).

$$E = \frac{F \cdot l}{w \cdot t \cdot \delta} \qquad (5.10)$$

Where E is the Young's modulus, F is the force, l is the length of the strip, w is the width of the strip, t is the thickness (assumed to be 0.002 cm), and δ is the elongation. The highest value recorded in the Moses work is a Young's modulus of 6.9 MPa (converting from grams/cm^2) for a meridional strip (eye number 5).

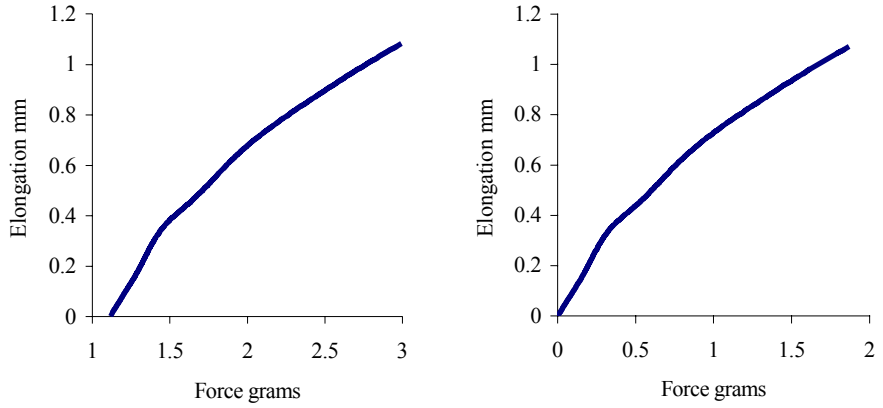

Figure 5.18: Elongation versus force of a choroid strip sample (Meridional Eye #7) from Moses (1965) with curve shifted to go through the origin for proper curve fitting (hysteresis loop removed).

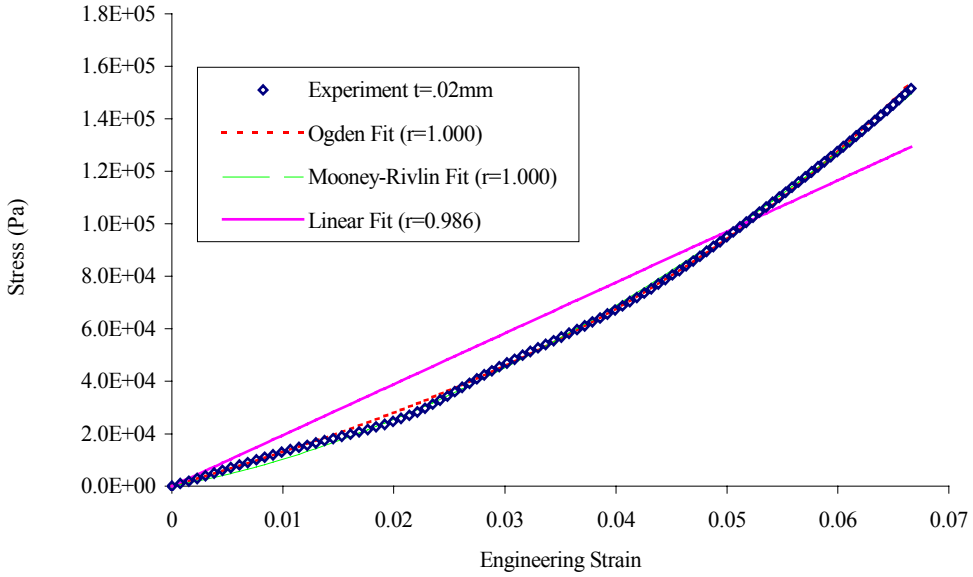

Figure 5.19: Curve fit of stress versus strain with Mooney-Rivlin and Ogden models from Moses (1965).

However, if one were to use the strip sample size information given for eye sample 7 (6 mm in width and 16 mm in length), then the modulus would change using (5.10) to 10.1×10^6 Pa for the second loading cycle and 6.5×10^6 Pa for the first

loading cycle (as used in the curve fit in Figure 5.19). In addition to the hyperelastic fits, a linear fit is also done to determine the elastic modulus for comparison and is equal to 1.9×10^6 Pa which is lower than that specified in the Moses work.

However, as Graebel and van Alphen suggest, Moses is reporting the secant modulus, so using the first and last data point in Figure 5.19 would yield an elastic modulus of 2.3×10^6 Pa, which still is inconsistent with the calculated values using (5.10). One explanation for this difference in elastic moduli is properly due to sample size. Moses reports the sample size in a plot for eye number 7 for the meridional strip as having width equal to 6 mm and length equal to 16 mm. However, in another area, the tabulated values for Young's modulus, in units gm/cm^2, use choroidal strip sizes of 1 cm in width and length. One alarming issue is the assumed thickness of the choroidal sample being 0.002 cm. Comparing this thickness to the Graebel and van Alphen uniaxial strip test study, which uses an assumed thickness of 0.16 mm, the difference is eight times smaller. This smaller thickness would also explain why the elastic modulus is two orders higher in magnitude than the modulus reported by Graebel and van Alphen. Graebel and van Alphen show that the choroid fits a power law for the stress-strain behavior as follows:

$$\sigma = \sigma_0(\varepsilon/\varepsilon_0)^a \qquad (5.11)$$

Where the σ_0 is arbitrarily chosen to be 5×10^3 Pa, ε_0 and a are determined by a least-square fit, and ε is the strain. As in the sclera study, the eye sample from the four-year-old is used in this curve fit examination and is shown in Figure 5.20. The Mooney-Rivlin formulation displays negative strain for positive stress in Figure 5.20. The Mooney-Rivlin fit is compared to (5.11) where the coefficients in the power law

are determined to be 2.30 for a and 0.2945 for ε_0 assuming a σ_0 equal to $5x10^3$ Pa. The Ogden fit is rather good with α equal to 6.40 and μ equal to $6.45x10^3$ Pa and a correlation factor equal to 0.999. The Mooney-Rivlin is shown to exhibit negative stress for positive strain at around 2% strain, which is not correct. It is concluded that relationships that are fit to constitutive models using (5.9) or (5.11) should not be converted to Mooney-Rivlin parameters unless only a small region of the stress versus strain is of interest.

Friberg and Lace (1988) consider the choroid in uniaxial testing using strips from human eyes. Specimens are cut from different locations and orientations like the scleral strip samples (Figure 5.21). The choroidal strips in this case are taken from the radial orientation (radial direction is in the posterior-anterior direction while circumferential strips are considered in the superior-inferior directions). As can be seen in Figure 5.21, sample A from the inferotemporal region is less compliant than the samples B and C. The thickness in this study is measured using a calibrated reticule and a microscope as opposed to assuming a thickness. The average thickness is then calculated to be 0.08 mm. The study linear fits the data points to determine the average elastic modulus of the anterior choroidal strips to be 2.2 +/- $1.5x10^5$ Pa, the posterior choroidal strips to be 7.5 +/- $7.0x10^5$ Pa, and the radial strips to be 8.2 +/- $4.8x10^5$ Pa. The total average elastic modulus across all locations is 6.0 +/- $2.8x10^5$ Pa with an average stress failure of the samples to be 3.3 +/- $1.3x10^5$ Pa. As can be seen in Figure 5.21, sample A from the inferotemporal region is less compliant than samples B and C. The thickness in this study is measured using a calibrated reticule and a microscope as opposed to assuming a thickness. The average thickness

is then calculated to be 0.08 mm. The study linear fits the data points to determine the average elastic modulus of the anterior choroidal strips to be 2.2 +/- 1.5x10^5 Pa, the posterior choroidal strips to be 7.5 +/- 7.0x10^5 Pa, and the radial strips to be 8.2 +/- 4.8x10^5 Pa.

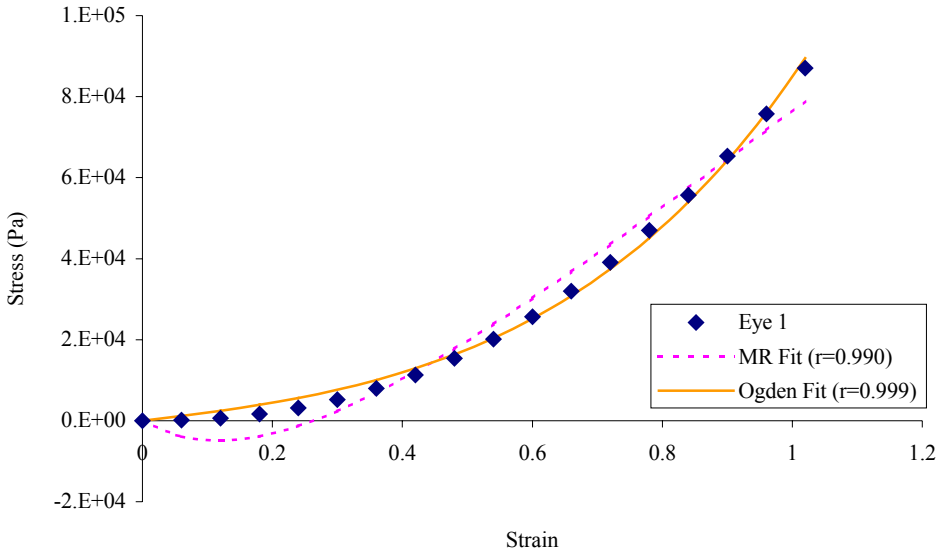

Figure 5.20: Hyperelastic curve fit with the choroid sample from a 4-year-old eye specimen from the Graebel and van Alphen (1977) study.

The total average elastic modulus across all locations is 6.0 +/- 2.8x10^5 Pa with an average stress failure of the samples to be 3.3 +/- 1.3x10^5 Pa. Curve fits for each of the samples noted in Figure 5.21 are shown in Figures 5.22 to 5.24, and the final results are tabulated in Table 5.4. These data points are shifted so that the first data point starts with zero stress at zero strain before curve fitting is attempted. As a comparison, the elastic modulus determined by the curve fit shown in Figures 5.22 to 5.24 in Table 5.4 compares well with that reported by Friberg and Lace (1988).

Taking the average gives $9.4x10^5$ Pa, which is comparable to the average determined by Friberg and Lace.

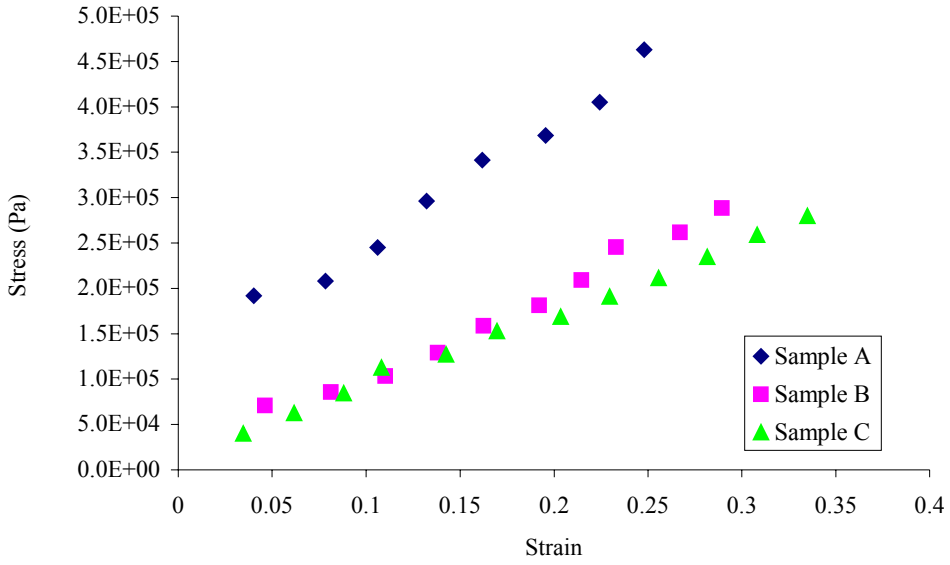

Figure 5.21: Choroidal data points from strip samples of the Friberg and Lace (1988) study. Sample A is taken from the radial inferotemporal region. Sample B is taken from the radial superonasal region. Sample C is taken from the radial superotemporal region.

Curve fits for each of the samples noted in Figure 5.21 are shown in Figures 5.22 to 5.24, and the final results are tabulated in Table 5.4. These data points are shifted so that the first data point starts with zero stress at zero strain before curve fitting is attempted. As a comparison, the elastic modulus determined by the curve fit shown in Figures 5.22 to 5.24 in Table 5.4 compares well with that reported by Friberg and Lace (1988). Taking the average gives $9.4x10^5$ Pa, which is comparable to the average determined by Friberg and Lace.

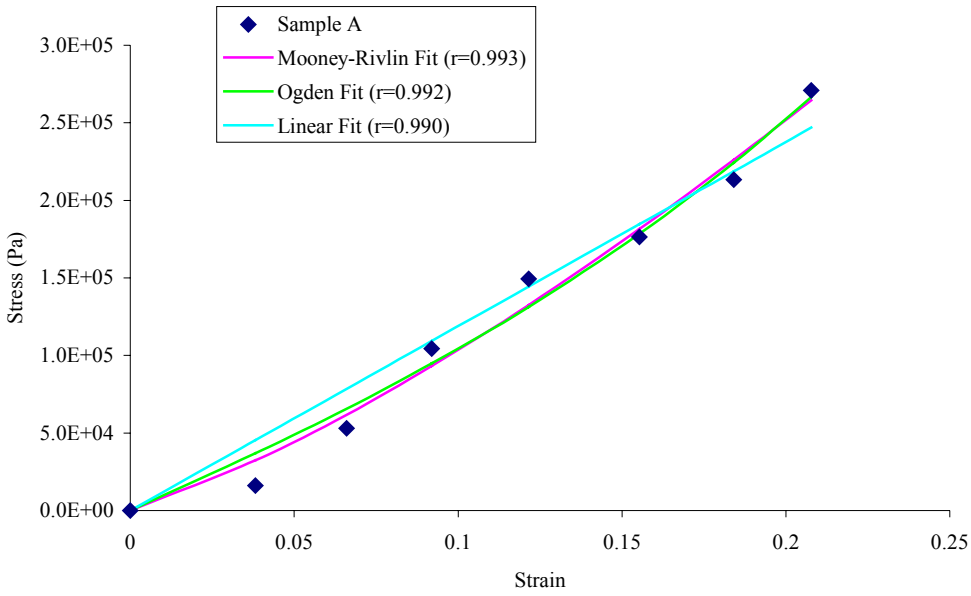

Figure 5.22: Curve fit for the choroidal strip sample A from Friberg and Lace (1988).

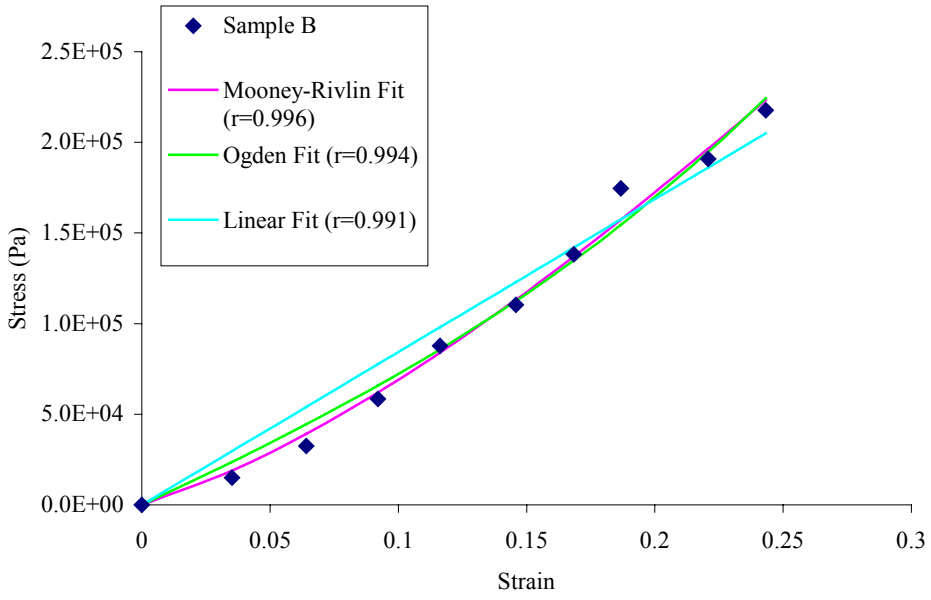

Figure 5.23: Curve fit for the choroidal strip sample B from Friberg and Lace (1988).

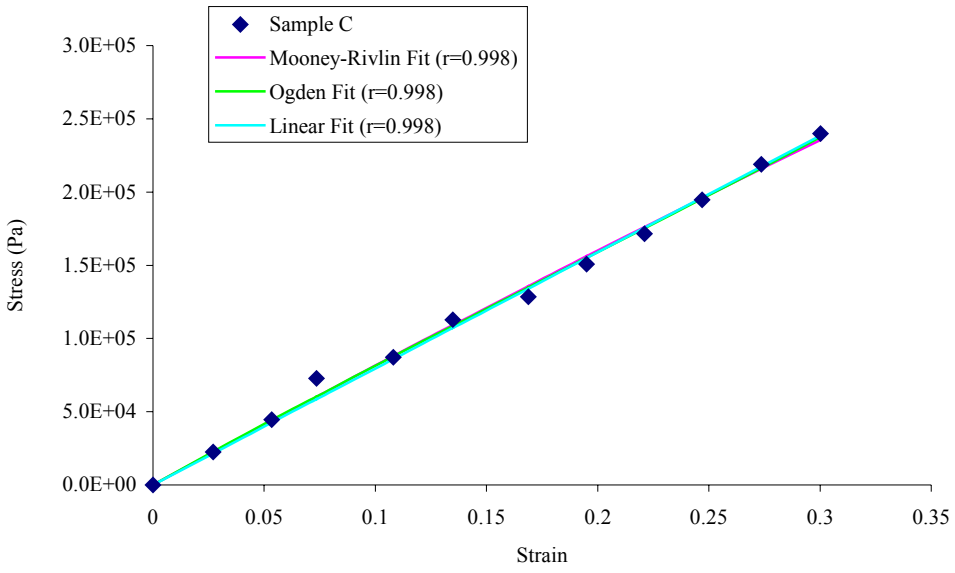

Figure 5.24: Curve fit for the choroidal strip sample C from Friberg and Lace (1988).

Table 5.4: Compilation of the material parameter fits for the linear and hyperelastic formations for the choroidal strips from Friberg and Lace (1988).

Choroidal strip samples	Linear fit	Mooney-Rivlin fit		Ogden fit		Correlation factor r		
	Elastic Modulus (Pa)	A (Pa)	B (Pa)	α	μ (Pa)	Lin	MR	Ogden
Sample A	1.19E6	9.09E5	-7.92E5	8.16	3.12E5	0.990	0.993	0.992
Sample B	8.43E5	6.57E5	-5.84E5	7.63	2.20E5	0.991	0.996	0.994
Sample C	7.95E5	2.61E5	-1.24E5	3.64	2.84E5	0.998	0.998	0.998

Friberg and Lace also estimate the choroidal thickness in living tissue to be approximately 0.43 mm. Coleman and Lizzi (1979) determine the in vivo choroidal thickness to accuracy better than 20 μm using ultrasound technique. The value reported in the posterior region of the eye is 471 μm, which is extremely close to that approximated by Friberg and Lace (percent difference of about 5% from estimating).

However, some of the other estimates or assumptions for choroidal thickness are much smaller and can affect the final modulus.

In the current eye model the choroid properties from Graebel and van Alphen are used with a thickness of 0.471 mm using shell membrane elements. Comparing the elastic modulus from Graebel and van Alphen to Moses, Graebel and van Alphen use the thickness of 0.16 mm and recalculate the Moses modulus to be 16.35×10^4 Pa (averaging all meridional and equatorial sample values), which is almost double the final average of 9.68×10^4 Pa from the Graebel and van Alphen work. However, it is not clear how Graebel and van Alphen exactly converted the Moses values as averaging all the moduli for the meridional strips for the initial loading in Moses gives 3.48×10^4 grams/cm^2. Converting this value to Pascal's gives 3.48×10^6 Pa. Then converting the thickness from 0.002 cm to 0.16 mm gives 4.35×10^5 Pa, which is off by 2 ½ times the reported conversion of 1.71×10^5 Pa. The Friberg average elastic modulus is 6.0×10^5 Pa, which is higher than the afore mentioned elastic modulus of 9.68×10^4 Pa reported by Graebel and van Alphen, but closer in magnitude to the averaged value of 4.35×10^5 Pa (using Graebel and van Alphen thickness with the Moses reported values) and the curve fit modulus from Figure 5.19.

Retina

This section is concerned with the biomechanical properties of the retina (specifically the posterior retina). The general term retinal hemorrhaging is used perhaps because most of the hemorrhaging occurs in the retinal layers. As understood

by Levin (2000), retinal hemorrhaging is a generic term that simply means bleeding in the eye. This work considers the retina as a thin membrane composed of shell membrane elements with an elastic modulus and a uniform thickness. The element layer shares a common node with the sclera, choroid, and vitreous body. This is done to keep the model simple to avoid complex contact interactions with the interfacing layers. However, there is investigation into possible adhesive strengths that will be discussed.

The retina is a very thin, delicate, and clear tissue lining the inner eye and interfacing the vitreous body and choroid layer through the pigment epithelium (Hogan, 1963). The retina varies in thickness with the thickest portion near the optic disk measuring 0.56 mm thinning to 0.18 mm to the equator, and then to 0.1 mm at the ora serrata (Hogan, 1963).

Currently, information on the mechanical properties of the retina as compared to the cornea-sclera shell and choroid is scarce. Perhaps, it is because the tissue is so compliant compared to the other ocular tissues that it is simply disregarded (Wu, Peters, & Hammer, 1987). However, there are more interesting studies concerning the adhesive strength that are considered by Kita and Marmor (1992) and Zauberman and deGuillebon (1972). An investigation into the retinal properties in simple elongation is presented (Wu, Peters, & Hammer, 1987). In this study, the retina is taken from various orientations from bovine and rabbit eyes (meridional with meridional vessel (MM), meridional without visible vessel (MN), and equatorial (EN)). The samples are tested at various strain rates ranging from 0.36 mm/s to 3.6 mm/s. Figure 5.25 shows a plot of a MM specimen with three cycles of loading.

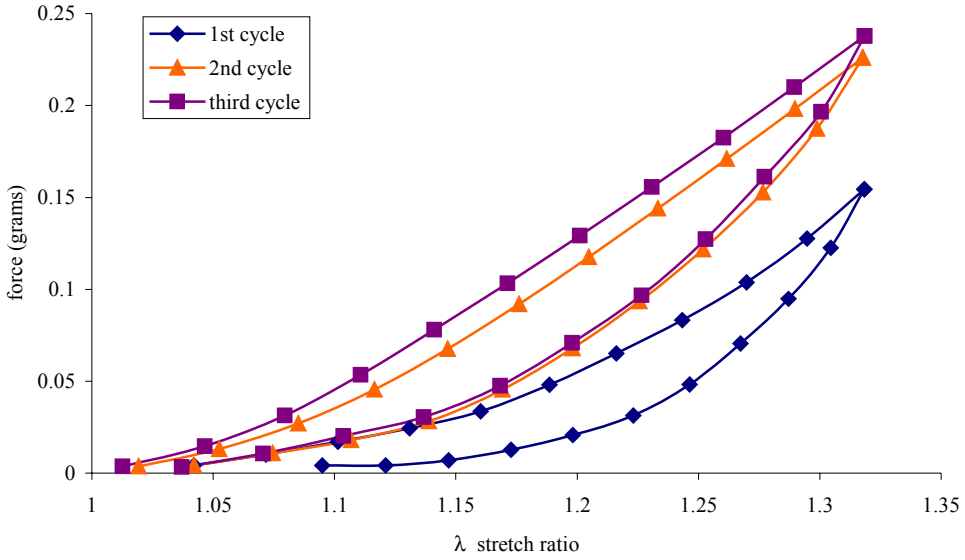

Figure 5.25: Loading of retinal strip sample from Wu et al. (1987) showing the three cycles with hysteresis. Specimen label is MM 81 with stretch rate equal to 0.87 mm/s.

The first cycle in Figure 5.25 is rather compliant as opposed to the other two cycles. Wu et al. suggest this is a result of blood loss in the sample and that it affects the mechanical properties significantly. It is probably more prudent to consider the first cycle only and disregard the other cycles; however, Wu et al. compile the results afterwards with this preconditioning applied to the samples. The behavior of the force versus stretch ratio is then fit to a constitutive equation of similar form used by Graebel and van Alphen (1977) (5.11). The exception is that force is used instead of the stress and leads to (5.12):

$$F = F_0\left(\frac{\varepsilon}{\varepsilon_0}\right)^a \qquad (5.12)$$

Where F is the force in grams; F_0 is chosen to be 0.24 grams for the MM group samples and 0.12 grams for the MN and EN group samples; ε is the strain considered

here as λ-1; ε_0 and a are the coefficients determined from curve fitting. Wu et al. uses samples with widths equal to 4.5-5.0 mm and do not consider the thickness through measuring or assuming. However, Wu et al. do compare the values with the Graebel and van Alphen work and show that the coefficients determined are within similar ranges. Further, the choroid elastic modulus is listed from Graebel and van Alphen, and then they list a tangent modulus at a magnitude lower ($0.46\text{-}0.58\text{x}10^4$ Pa) at a middle stress level equal to $1.2\text{x}10^3$ Pa. In the Graebel and van Alphen work an arbitrary stress is chosen to be $5\text{x}10^3$ Pa for the choroidal strip testing. Obviously, Wu et al. do consider the retinal thickness some how. Assuming this middle stress level of $1.2\text{x}10^3$ Pa is based on the $F_0 = 0.12$ grams would indicate an original cross-sectional area of approximately $1\text{x}10^{-6}$ m^2 or 1 mm^2. Assuming that the width mentioned in their sample size is 5 mm would indicate a thickness of 0.2 mm for the retina. This thickness would indicate that Wu et al. considered the thickness of the posterior region of the eye for the elastic modulus calculations. Therefore, an attempt is made to convert the values in Figure 5.25 into stress versus stretch ratio for the first cycle loading curve (Figure 5.26). Different constitutive equations are then fit to the data using the F_0 converted to σ_0 in (5.11) for the power fit. The values are then tabulated in Table 5.5 for comparison.

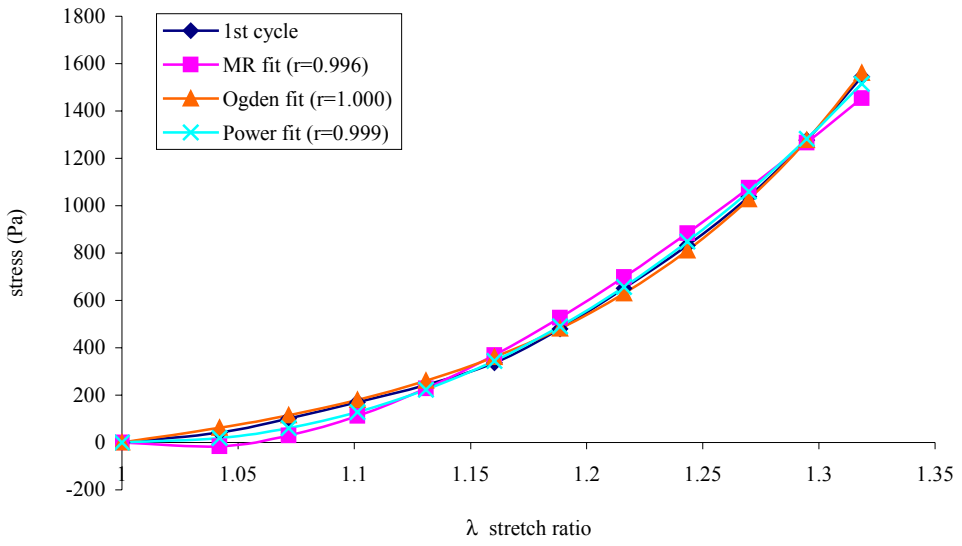

Figure 5.26: Curve fit to retina sample strip MM for the first cycle loading from Wu et al. (1987).

Table 5.5: Compilation of the constitutive equation fits for the retina sample strip MM for the first cycle loading from Wu et al. (1987).

Retinal Strip	Power fit		Mooney-Rivlin fit		Ogden fit		Correlation factor r		
	a	ε_0	A (Pa)	B (Pa)	α	μ (Pa)	Power	MR	Ogden
Sample MM 81	2.15	0.29	4.91E3	-5.19E3	11.96	454.1	0.999	0.996	1.000

The curve fit shows excellent correlation with all of the constitutive equations. However, the Mooney-Rivlin fit does dip into negative stress for positive stretch indicating a poor fit regardless of the correlation factor equaling 0.996.

The Ogden fit is good in describing the behavior, as is the power fit. The coefficients of the Power fit are within the reported range of Wu et al. (1.53-2.21 for a and 0.1810-0.5333 for ε_0). Using the coefficients from Table 5.5 for the power fit gives a

strain level of 0.28576 for a stress level of $1.2x10^3$ Pa (indicated as the middle stress level). Therefore, the calculated elastic modulus for the Wu et al. sample shown in Figure 5.25 is $0.42x10^4$ Pa and is lower than the reported range of $0.46\text{-}0.58x10^4$ Pa. The lower value is a result of not including the preconditioning factor and is presumably more representative of the true in-vivo sample. Interestingly, Wu et al. mention that the tensile strength is roughly twice the adhesive strength comparing the results with the work of deGuillebon and Zauberman (1972).

Jones, Warner, and Stevens (1992) consider the retina to be an elastic membrane sheet in their determination of the mechanical properties using a mathematical model. Bovine retina is excised and placed on a metal washer with known dimensions. A no-slip boundary condition is imposed on the retinal membrane by applying adhesive to the washer. A suture using a 10.0 nylon thread is inserted into the middle of the sample and a bead of adhesive is allowed to traverse down the thread. Once the adhesive is dried, stretching is imposed via the suture and the height of deformation and traction force are recorded. An idealized model is constructed using various equations that are numerically solved resulting in a need for an elastic constant, k, so that the equations can fit the data profile (which has not been provided as a plot as in other studies). Ultimately, a k value of 2 N/m provides an elastic modulus of $2x10^4$ Pa with a difference of 7% in predicting the force compared to the actual experimental measurements. The thickness used in these calculations is 0.1 mm for the retinal membrane and the results are in good agreement with those of Wu et al. ($2x10^4$ Pa from Jones et al. compared to $0.46\text{-}0.58x10^4$ Pa from Wu et al.), which is about four times as stiff compared to Wu et al. The retinal membrane in this

work is considered to be an elastic membrane with material properties using the Young's modulus determined by Jones et al., Poisson's ratio equal to 0.49 to model incompressibility, a density equal to 1000 kg/m^3, and a thickness of .14 mm indicated in a figure showing the variation of retinal thickness in the human eye in Wu et al. and Hogan (1963). The influence of the thickness is also from Jones et al. There seems to be an indication that the thickness of 0.14 mm is spread throughout the retina with a sharp increase of 0.21-0.23 in a small posterior location (the optic disk area) and then thinning out towards the edges (ora serrata) to a thickness of about 0.10-0.13mm.

Interestingly, the thickness of the retina is also measured by spectrally deriving the retinal thickness in order to subtract the value from the choroid plus retina to determine the choroidal thickness in the work done by Coleman and Lizzi (1979). In this study, ultrasound methods are employed to measure the in-vivo choroidal thickness. The thickness indicated in a figure is 170 μm for the retina with an asterisk to indicate that the value is indirectly derived. This value is really close to the assumed value used in the current model.

Concerning retinal detachment and adhesive strength, two methods of testing have been employed. Traction force of the retina is measured by peeling the retina from a choroid strip (Zauberman & Deguillebon, 1972; Zauberman, Deguillebon, & Holly, 1972; deGuillebon & Zauberman, 1972; Marmor, Abdul-Rahim, & Cohen, 1980) or bleb formations are induced in-vivo, and the pressure difference is used in determining the retinal adhesive force (Kita et al., 1990; Kita & Marmor, 1992). Another study induces blebs (bubbles of fluid beneath the retina and above the

choroid) in-vitro (Kain, 1984). This retinal force is really a determination of the pigment epithelium strength, which acts as an adhesive attaching the retinal processes to the choroidal layer (indicated in a diagram from Kain (1984)). In the peeling studies, deGuillebon and Zauberman show that the adhesion is influenced by the peeling rate. At low peeling rates, the retina pulls off the choroid strip rather smoothly (rates of 2 and 8.5 mm/min). At higher rates, the choroid and retina would stay attached and peel away from the sclera shell (42 mm/min). And finally, at a rate of 210 mm/min, the retina peeled away in a jerky manner with partial detachment of the choroid from the sclera. A plot of force (mg) versus peeling rate (mm/min) and a plot of elongation (%) versus peeling rate (mm/min) is provided in this study.

Considering a midlevel force of 80 mg occurring at a peeling rate of approximately 15 mm/min (read from plot) gives an elongation of approximately 24% interpolated from the second plot. Also, given that the strip width is indicated to be 6.5 mm, one can determine the force per length. In this case, the strip sample is oriented 23 degrees counterclockwise from the horizontal. The sample is then affixed to a metallic rod attached to a glass tube with a force transducer. As the sample is pulled in the apposing direction the normal and shear force can be determined and converted to SI units and is equal to 0.12 N/m for the total force and 0.1 N/m for the normal component and 0.05 N/m for the shear component. This retinal detachment study uses rabbit eyes and is comparable to the work done by Kita et al. in various studies with live rabbit in-vivo studies.

In the case of the Kita et al. experiments, bleb formations are induced in live rabbits and the pressure difference is used to determine the adhesive force per length using (5.13) the following:

$$P_S - P_V = 2T / R \qquad (5.13)$$

Where P_S is the subretinal pressure, P_V is the intravitreal pressure, T is the tension, and R is the radius of the sphere (bleb). The value for the rabbit adhesive force is reported to be 0.18 N/m (Kita et al. 1990). In another study, (Kita & Marmor, 1992) a comparison is made with living rabbit, cat, and monkey eyes. In this study, the adhesive force for the rabbit is reported to be 0.1 N/m, 0.18 N/m for cats, and 0.14 N/m for monkeys. However, it is not clear why the rabbit eyes in one study would go from 0.18 N/m down to 0.1 N/m since both studies consider Dutch rabbits. However, it is interesting to note that two different methods of measuring retinal adhesion would yield values of retina force per unit length that are approximately the same for rabbit retina. The current eye model proposes the use of this retinal adhesive force from the monkey eyes (0.14 N/m) as an indication of failure in the retinal-choroid layer.

Further, an assumption is made that failure would not occur in the retinal-vitreous layer (Levin, 2000). Levin explains that in severe shaking, it is possible to have focal or complete detachment of the retina. A forensic pathological study indicates that the incidence in retinal detachment is 63% (Green et al., 1996). Further, this high incident rate is likely due to the vitreous traction. Levin mentions that hemorrhagic detachment can occur but is rarely observed. Retinal hemorrhages with detachment are rarely observed perhaps due to the subretinal resorption times

(Negi & Marmor, 1986). As indicated above, the retinal adhesive force is within a comparable range amongst the test samples studied given the different species, testing methods, and whether or not the animal is alive. Perhaps, this would indicate the pigment epithelium is similar for human (and even infant) eyes. In this case, bleb resorption time is reported to be 187-561 minutes varying the bleb fluid (Negi & Marmor, 1986). This would provide enough time for the retina to reattach to the pigment epithelium before an infant is examined for possible SBS. Further, it is suggested that this absorption could occur and still show retinal hemorrhaging. Therefore, given the physiological properties of infant eyes, it is quite possible that retinal detachment with hemorrhaging is more common in SBS.

In order to include this detachment information in the biomechanical eye model, the MADYMO software is capable of modeling node-node welds. Therefore, the once coincident nodes of the retina are moved in the normal direction of the element to provide a small gap between the choroid and retina. Then, node-node welds are introduced binding the choroid node with the once coincident retina node. This model would still have the retina sharing the nodes with the outer surface of the vitreous body solid however. In this study, the focus is on the posterior region of the eye; therefore, only the nodes in the posterior pole are considered for the node-node weld (Figure 5.27).

Contact interactions would then be included between the retina and choroid so as to prevent the retina from seeping out of the sclera shell during applied motions. The preferred way to model this adhesive force would be to model the retina-choroid interface as a de-lamination process ((Kostopoulos et al., 2002). In this case, the

nodes of the choroid and retina would remain coincident until a force is reached that would separate them. This would make more physical sense. Another area that welds in the eye model mentioned is with sutures after LASIK surgery (Uchio et al., 2004). Interestingly, a force breach of 0.16 N (comparable to the retinal adhesion force) is used for the propylene suture strength. In Uchio et al.'s work, it is not clear if the mentioned spot-weld is the same type of node-node weld used in the MADYMO software, where one cannot have zero distance between the welded nodes.

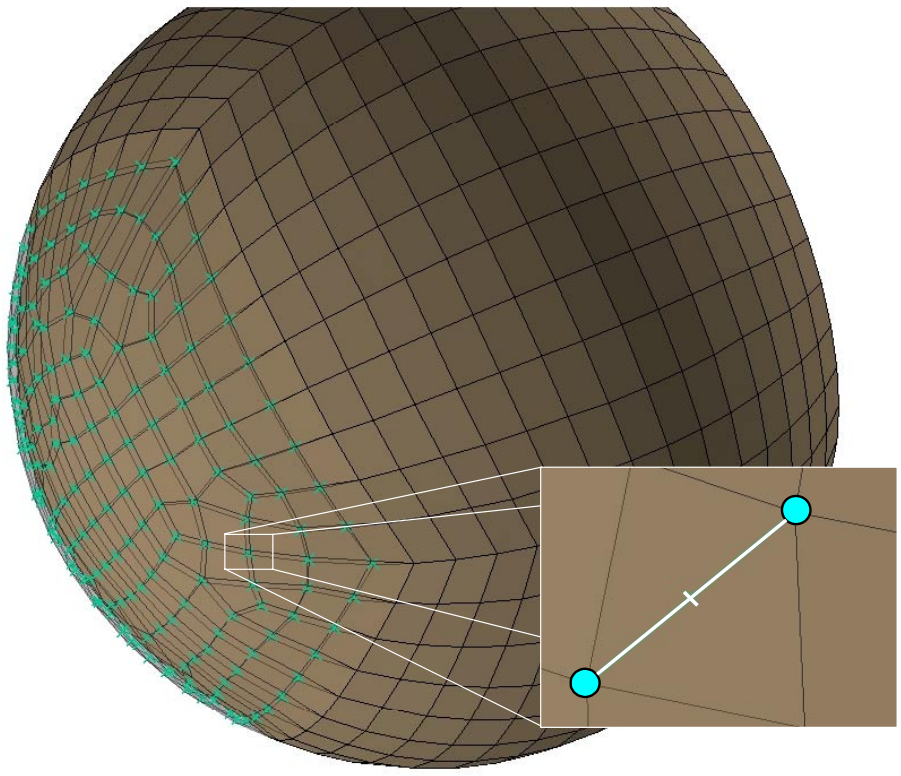

Figure 5.27: Detail of node-node weld implemented in the biomechanical model between the choroid layer (wire-frame) and the retinal layer (shaded-wire-frame).

The spot-weld as modeled in MADYMO (5.14) uses the normal and shear force component in the following form:

$$\left|\frac{F_n}{F_{n_{\max}}}\right|^{a_n} + \left|\frac{F_s}{F_{s_{\max}}}\right|^{a_s} < 1 \qquad (5.14)$$

Where Fn is the force parallel to the line connecting the two nodes; Fs is the perpendicular force to the line connecting the two nodes; Fn_{max} and Fs_{max} are the maximum allowable normal and shear force components; a_n and a_s are the exponents that determine the shape of the rupture. Therefore, if one were to consider purely normal force, these exponents would each equal infinity. If only the shear component were considered, then the exponents would each equal one. Lastly, if a combination of shear and normal force were used (mentioned in an example in MADYMO syntax in the reference manual section), then each of the exponents would equal two. In Figure 5.27, when motion is imposed on the entire eye, nodes between the weld act as spherical joints and have no resistance (at least visually). Using exponents each equal to two yields a similar response as if they are infinity. It is assumed that the shear effects would have a minimal effect and so only the normal force is considered by specifying the Fn_{max} equal to 0.14 N and $a_n = a_s$ = infinity. An arbitrary value is set for Fs_{max} in case of syntax errors. The response of adding nodal welds will be discussed in a later chapter.

Conclusion

A comprehensive investigation into the ocular tissue layers has been conducted. Immediately apparent is the breadth of biomechanical models and mechanical property determinations of the cornea and sclera. In this section, researchers have either done strip testing or membrane inflation with finite element methods used to help determine the material properties. The material properties of the ocular shells, from previous research, have not explicitly been fit to a hyperelastic material form. This chapter provides these material property fits from previous literature on the ocular shell layers. It appears the trend is either to report the values in a plot or fit a constitutive equation using power laws or exponential forms (5.7) (5.8) (5.9). Unfortunately, the MADYMO code utilized in this dissertation does not support these forms.

Extensive work has been done on the cornea-sclera shell with regard to globe rupture prediction and other impact studies using the work from Uchio et al. The work done on the choroid is not as comprehensive as the cornea and sclera. Perhaps, the lack of study is due to the trend of study, which is concerned with impact trauma to the cornea-scleral shell.

The choroid is also considered in hyperelastic fits as Moses (1965) mentions hyperelastic properties are exhibited by the choroid. Current research presented in this chapter has measured the choroid in uniaxial elongation using excised strips. The choroid is highly vascular and preconditioning the sample would increase the rigidity (as in the case with the retinal preconditioning, Figure 5.25) (Wu, Peters, & Hammer, 1987).

The retina membrane mechanical properties are mostly concerned with adhesive force with the pigment epithelium. However, two groups (Wu, Peters, & Hammer, 1987; Jones, Warner, & Stevens, 1992) do consider the actual mechanical properties of the membrane itself either by strip testing or elongating vertically from an affixed position on a metal washer.

This chapter looks into the mechanical properties of the cornea, sclera, choroid, and retina. Further, research has been presented that discusses the retinal adhesive strength and a possible modeling technique using the node-node weld method to model retinal detachment.

CHAPTER VI

EXTRA-OCULAR RESTRAINTS

Introduction

This chapter will consider the eye tethers, which are composed of the muscle-tendon attachments and the optic nerve. The fatty tissue contains a spherical void (Figure 4.20) containing the eye globe and helps restrict the motion of the eye so that it behaves mostly as a spherical joint. The optic nerve modeling is approached by two methods of research. The first method of modeling the optic nerve is as a full finite element cylinder attached to the posterior eye using literature from optic nerve head (ONH) studies. These studies are mostly concerned with glaucoma (Bellezza, Hart, & Burgoyne, 2000; Sigal, Flanagan, & Tertinegg, 2004) and the biomechanics of the ONH and the lamina cribrosa. However, there is a compilation of mechanical properties from Sigal et al. that are considered in the SBS eye model. All of these ONH studies that contain finite element analysis are considered for static analysis.

In this study, the optic nerve is going to be utilized as a tether, as suggested by Levin (2000), in order to investigate the dynamic reaction at the posterior eye region. Collins et al. (1969) have measured the damping and stiffness parameters of the eye during surgery. These parameters are utilized as the plant parameter in muscle model studies conducted by many authors. These parameters are for an adult eye and are modified in such a way as to achieve the same response when shifting the location of the nerve and also when scaling the properties down to an infant eye.

The material parameters for the finite element optic nerve are assumed to be the same for an infant and adult, so only the geometry is scaled. Initially, investigation into the use of full finite element muscles is considered as these have the ability to capture the detailed geometry from the Visible Human Project transverse slice scans. However, material properties for these finite muscles are rather sparse for usage in the MADYMO code.

In addition, modeling the muscle mechanics by inducing neural excitation to the muscles in order to produce saccades is desirous. Therefore, the complexity of the Hill-type muscle is considered with major influence from Winters and Stark (1985 and 1988) concerning the parameters of the muscles and tendons. Most of these studies consider the eye parameters in terms of rotation; however, for usage in the SBS model, these parameters are converted to lengths using the globe radius arm (Robinson, 1981). Considerable analysis using step inputs and comparing the position, velocity, and acceleration response of the eye (plant) is done to calibrate the modeling parameters using Winters (1985). Modifying these parameters is done for an infant eye and calibrated to achieve the same response as the adult.

Utilizing these analytical muscles allows flexibility in examining the dynamic response of the eye while saving computational time. A comparison of the dynamic response of the different optic nerves suggested (finite element and analytical) and the muscles is presented in this chapter.

Fatty Tissue

The fatty tissue is modeled using tetrahedral meshing with the most anterior surface containing a layer of membrane elements modeling the skin. The skin layer mechanical properties are used from Verver (2004), which specifies an elastic modulus equal to 0.15 MPa, a density equal to 1000 kg/m^3, and a Poisson's ratio of 0.46. In addition, a damping coefficient equal to 0.05 is specified as biological structures exhibit some material damping (MADYMO 6.2). This elastic modulus is ten times that used by Chabanas, Luboz, and Payan (2003) (15 kPa). In addition, Chabanas et al. used a Poisson's ratio equal to 0.49 for incompressibility. The thickness of the skin layer is set to 1 mm and is within the range of 0.5 to 4 mm for the facial dermis layer (Chabanas, Luboz, & Payan, 2003). A total of four materials have been examined for use in the eye model (Table 6.0).

In conjunction with the contact interactions, the fatty tissue holds the eye globe in place and helps absorb energy. The eye globe placement is such that there is a gap as shown in Figure 6.0. This gap ensures that the nodes of the eye globe surface do not initially penetrate the elements of the fatty tissue. Three primary cases are considered in this research regarding the eye model, the impact case, pure shaking case, and saccade movements. These cases will be discussed in later chapters. However, depending on the case, different mechanical properties and contact interactions are used. This typically depends on the amount of energy absorption that is required from the fatty tissue. For example, the saccade movements do not require energy absorption; rather they are required to keep the eye in place allowing mostly rotational motion without translation. The saccade simulations use the Todd and

Thacker (1994) material properties as used in the Power (2001) model. This material is extremely stiff compared to the other fatty tissue mechanical properties (Figure 6.1); however, in this particular case, the saccade positional output is calibrated to an analytical model from Winters (1985), which considers the eye simply as a revolute joint for horizontal eye motion.

Therefore, in conjunction with the Todd and Thacker fatty tissue, the contact algorithm is such that a penetration gap is introduced with size equal to 0.4 mm. This results in a net physical gap of around 0.4 mm in the sagittal plane. However, this gap also happens to be the minimum gap without nodes of the eye globe penetrating the gap layer. Any larger specifications of this contact gap resulted in some of the nodes penetrating the gap layer, albeit the gap is of the order $1x10^{-7}$ meters.

Since the biological materials in this study are so compliant, effort is made to prevent initial penetrations of the nodes, as the contact algorithm in the MADYMO code will introduce velocity to the node in order to position the node at the surface of the element or specified gap. The contact interactions use a penalty method for the contacting node-element relationship. The maximum force parameter for these contacts is defaulted to 1.00 as recommended in the MADYMO reference manual. However, with the more compliant materials this parameter has been set as low as 0.1-0.001 when instabilities occurred in previous test runs. The contact between the fatty tissue and the eye globe is considered frictionless.

The impact simulations use the materials provided by Verver (2004), which are half the values, reported in the MADYMO version 6.2 Human models manual. The Samani and Plewes (2004) materials are considered for the impact simulations;

however, instability occurs when using this material as some of the elements in the fatty tissue tetra-mesh undergo severe element deformation as this material is extremely compliant. Compounding this instability is the assumption that the fatty tissue is supported by the orbital socket as in previous studies (Power, 2001; Luboz et al., 2004).

Table 6.0: Comparison of material properties considered for the fatty tissue.

Source	Material Model	E (Pa)	A (Pa)	B (Pa)	Poisson's Ratio	Density [7] (kg/m^3)
Todd & Thacker	Elastic	$4.7x10^4$	-	-	0.49	999.0
Luboz et al.	Elastic	$2.0x10^4$	-	-	0.1	999.0
Verver	Hyperelastic	-	$1.65x10^3$	$3.35x10^3$	0.49	928.0
Samani & Plewes	Hyperelastic	-	310	300	0.49	928.0

The material parameters of Samani and Plewes (2004) as well as Verver (2004) are used in the SBS model for comparison. The purpose of using the more compliant materials in the impact and SBS runs is to provide energy absorption of the fatty tissue. The contact interactions used in the impact and SBS simulations (discussed in chapter 8) use the same method as the saccade simulations. A comparison is made between the difference of having a contact gap function specified and not having one in Figures 6.2 and 6.3. These figures show the simulation of impact simulation at times 0, 5, and 10 milliseconds into the impact. The initial

[7] The density is from Power (2001) for the elastic material models and Duck (1990) for the hyperelastic material models.

distance between the fatty tissue and the most posterior node (shown in Figure 6.0) is 0.97 mm. The minimum distance, based on this initial 0.97 mm gap, for the simulation where a 0.4 mm contact gap is specified, is 0.383 mm. Therefore, for the contact gap simulation, the penetration into this gap is about 0.017 mm. The minimum distance for the simulation where no contact gap is specified is –0.136 mm. This means that the sclera shell penetrates into the fatty tissue by 0.136 mm. The time history, (Figures 6.4 and 6.5) comparing the no contact gap to the contact gap simulation, shows that the position of the most posterior node is greater for the no gap simulation as a result of momentum build up. The first spike in the positional data (Figure 6.4) shows a maximum displacement of the most posterior node of the eye globe to be approximately –2.0 mm for the no contact gap simulation versus –1.25 mm for the contact gap simulation. As expected, the acceleration plot also shows higher values. Most noticeable is the acceleration of the no contact gap simulation at the time 8-10 msec range. During this time, the no contact gap simulation spikes to values close to the initial loading. In the physiological case, it is more likely that there is not an air gap between the fatty tissue and the eye globe; therefore, it is suggested that specifying a contact gap is more conservative (and perhaps more realistic).

The Luboz et al. (2004) is not used in this model, as the material is comparable (Figure 6.1) to the Verver (2004) material but with a Poisson's ratio of 0.1. The rationale behind using 0.1 is that the orbital tissue is considered poro-elastic.

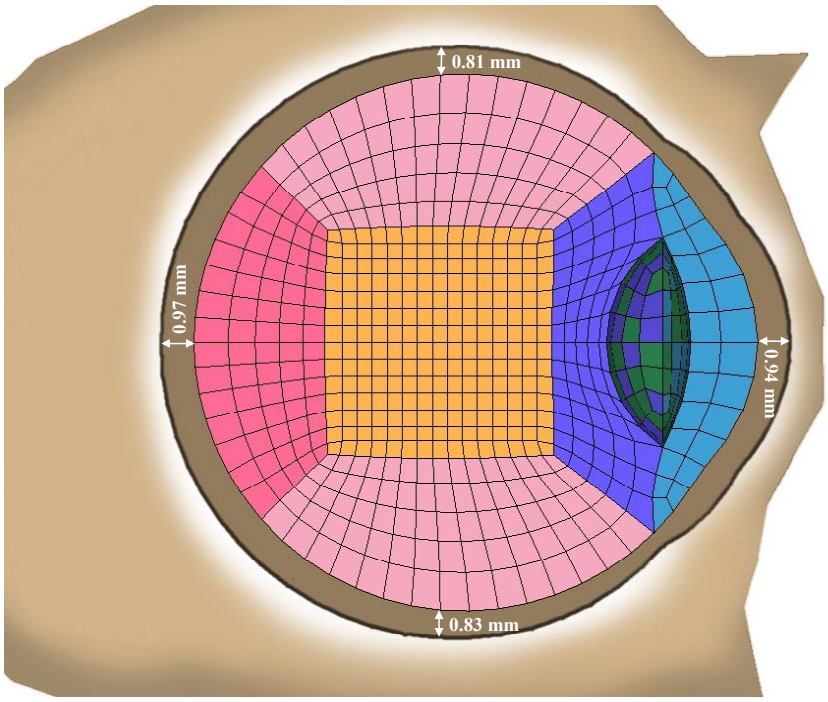

Figure 6.0: Sagittal view of eye model showing the gap dimensions from the cornea-scleral shell to the fatty tissue void.

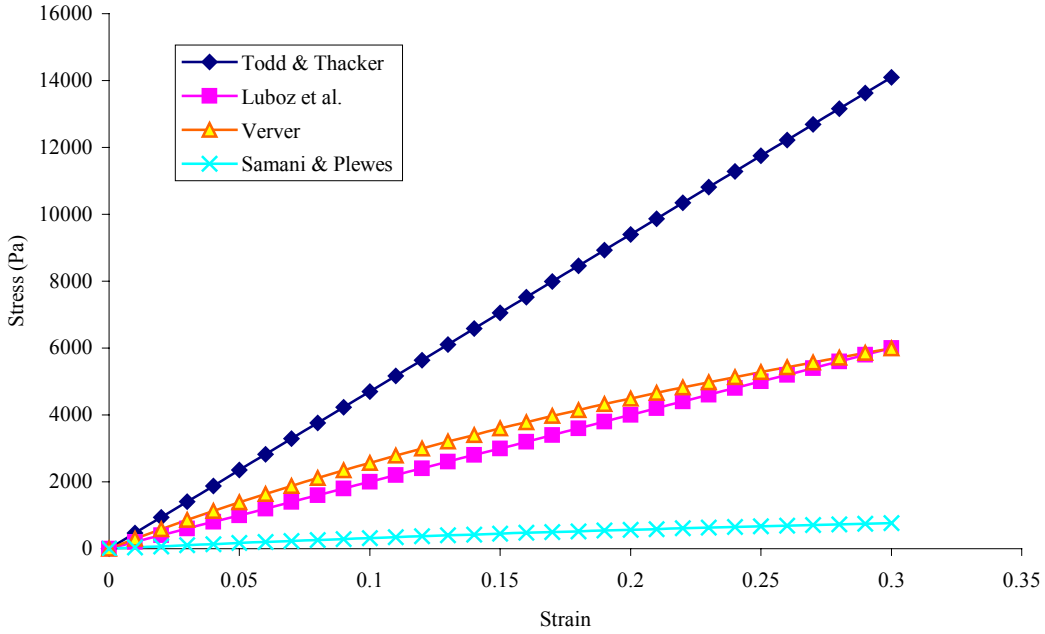

Figure 6.1: Comparison of fatty mechanical properties of different research groups. The constants for the elastic and hyperelastic constitutive equations are in Table 6.0.

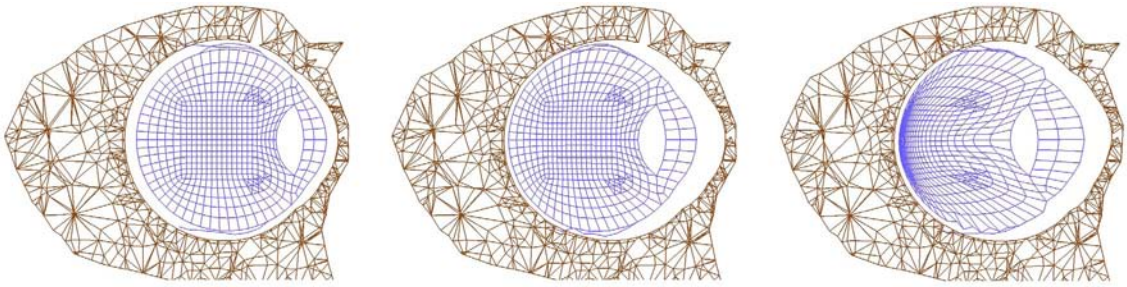

Figure 6.2: Impact simulation showing sagittal slice of the eye globe and fatty tissue. From left to right, the animation captures are taken at 0, 5, and 10 milliseconds. Apparent in all three views is the small contact gap.

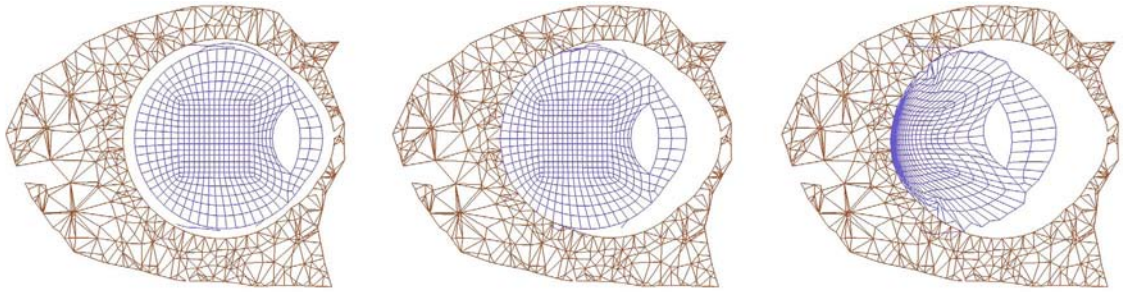

Figure 6.3: Impact simulation showing sagittal slice of the eye globe and fatty tissue. From left to right, the animation captures are taken at 0, 5, and 10 milliseconds. This simulation does not use the contact gap algorithm causing more momentum build-up (compare with Figure 6.2), which results in greater eye globe compression.

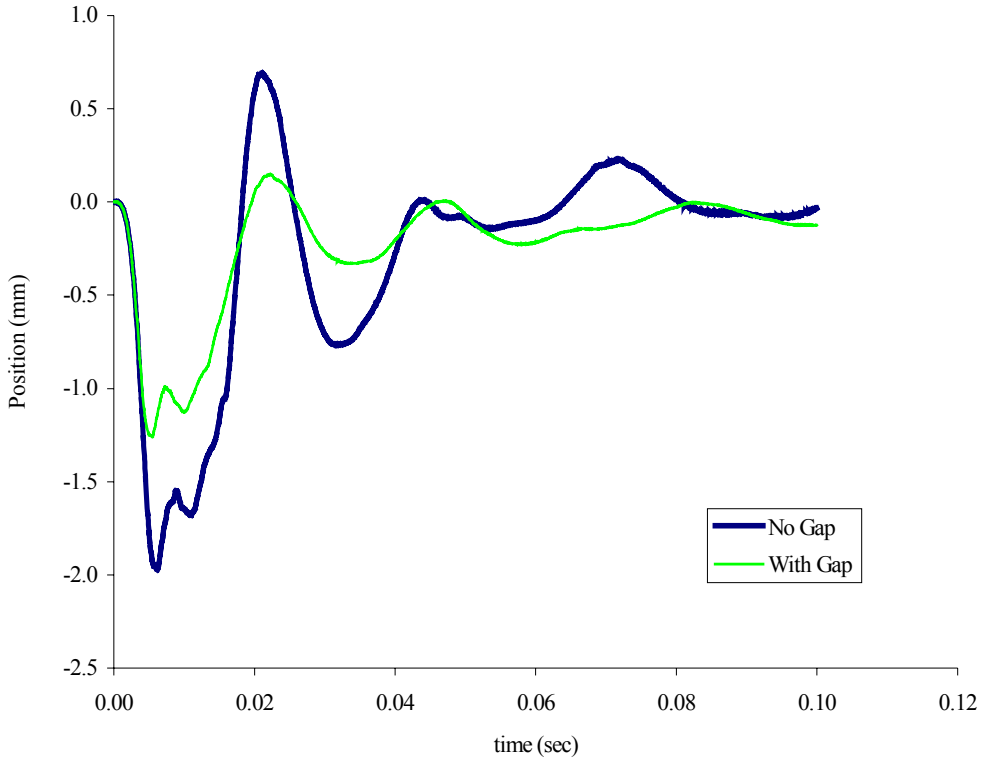

Figure 6.4: Relative displacement of the most posterior node comparison from the no contact gap and with contact gap simulations.

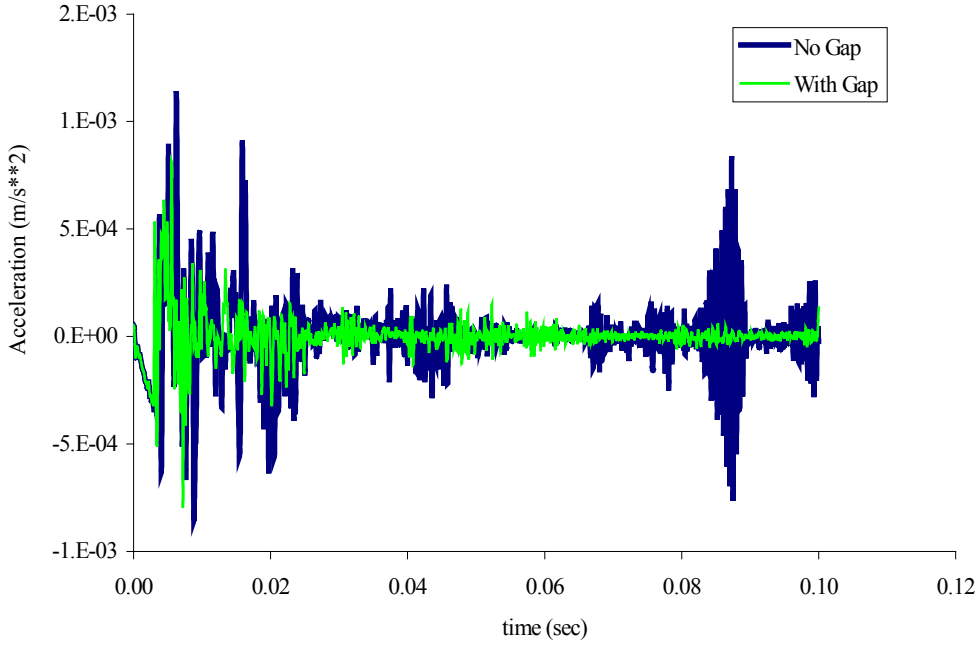

Figure 6.5: Acceleration of the most posterior node comparison from the no contact gap and with contact gap simulations.

Optic Nerve

The optic nerve in this study is considered to be a tether and is of interest in SBS (Levin, 2000). Levin suggests that the nerve is firmly attached to the eyeball with some slack. Injury can be localized at these tether locations (including muscles) as a result of motion to the eye. The optic nerve in this study is fixed at the apex (entry point in the posterior ocular cavity) for both the analytical and finite element nerves.

Considering the analytical model, the mathematical models in previous works consider the horizontal motion of the eye (Collins, Scott, & O'Meara, 1969; Lehman & Stark, 1979; Lehman & Stark, 1979; Robinson, 1981;Winters & Stark, 1985; Winters & Stark, 1988). These analytical models consider the eye as the "plant" which acts as a revolute joint in horizontal motion. The stiffness is estimated to be 0.5 grams/degree (2.5 grams/mm using radius arm of 12 mm) for the passive orbital tissues Collins et al. (1969). This stiffness is estimated during corrective surgery of 12 strabismus adult patients. Robinson (1981) considers the passive orbital tissues by the following (6.0):

$$P = 0.48\ E + 1.56x10^{-4}E^3 \qquad (6.0)$$

Where P is the force and E is the displacement. Out to 20 degrees rotation, the cubic term can be neglected resulting in a stiffness coefficient equal to 0.48 grams/degree, which is comparable to Collins et al. The following is considered (6.1) for modeling the movement of the eye system (Lehman & Stark, 1983):

$$I\ddot{\theta} + B\dot{\theta} + K\theta = N \qquad (6.1)$$

Where I, B, and K are the plant parameters equal to $2.7x10^{7}$ Nms^2, $9.3x10^{-5}$ Nms, and $1x10^{-2}$ Nm. The inertia of the eye is determined assuming a density of 1 $gram/cm^3$ and a radius equal to 1.1 cm. In order to construct a rigid body eye model that will be used to calibrate the positional response to that of Winters (1985), the values for I, B, and K are taken from Winters and Stark (1985) and are equal to $3x10^{-7}$ $kg\text{-}m^2$, $1x10^{-4}$ Nms, and $1x10^{-3}$ Nm.

A model is constructed containing a body with a mass of $5.6x10^{-3}$ kg and inertial properties for $I_{xx} = I_{yy} = I_{zz} = 3x10^{-7}$ $kg\text{-}m^2$. The joint of this body is a revolute joint with the damping and stiffness equal to $1x10^{-4}$ Nms and $1x10^{-3}$ Nm, respectively. An initial rotation of 30 degrees is applied and the simulation duration is one second. The rotational time history is then used as a calibration in order to shift the location of the nerve from a revolute joint to a location lateral (translational nerve) to the eye globe (Figure 6.6).

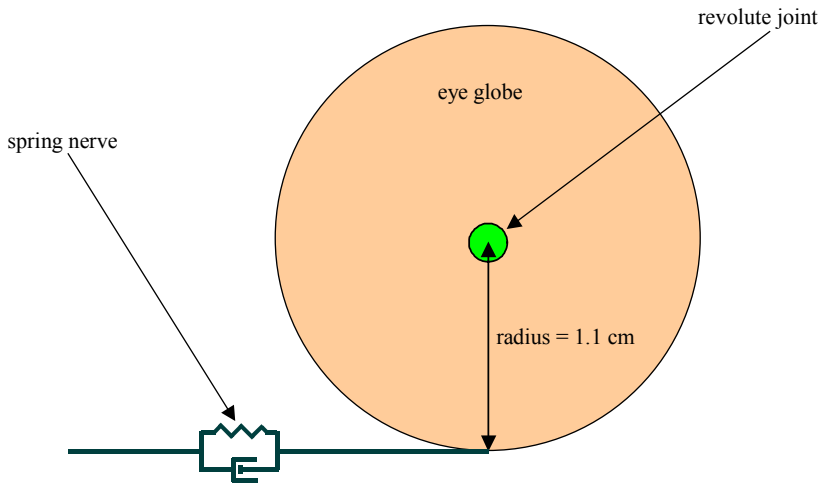

Figure 6.6: Diagram of analytical eye model with passive plant properties. The spring nerve is a conversion of rotational constants to linear constants.

The revolute joint from the initial model has the stiffness removed. The nerve parameters are then scaled to an infant so that the response is the same (Figure 6.7). The infant plant mass is 1.5×10^{-6} kg and the inertia is 3×10^{-8} kg-m^2 with rotational damping and stiffness (1×10^{-4} Nm for the stiffness and 1×10^{-5} Nms for damping) converted to translational values, via the rotational arm with length 7.1 mm, equal to 1.98 N/m for the stiffness and 0.198 Ns/m for the damping. The positional response is the same for the adult rotational stiffness model (as used in Winters (1985)), the adult translational spring, and the infant translational spring.

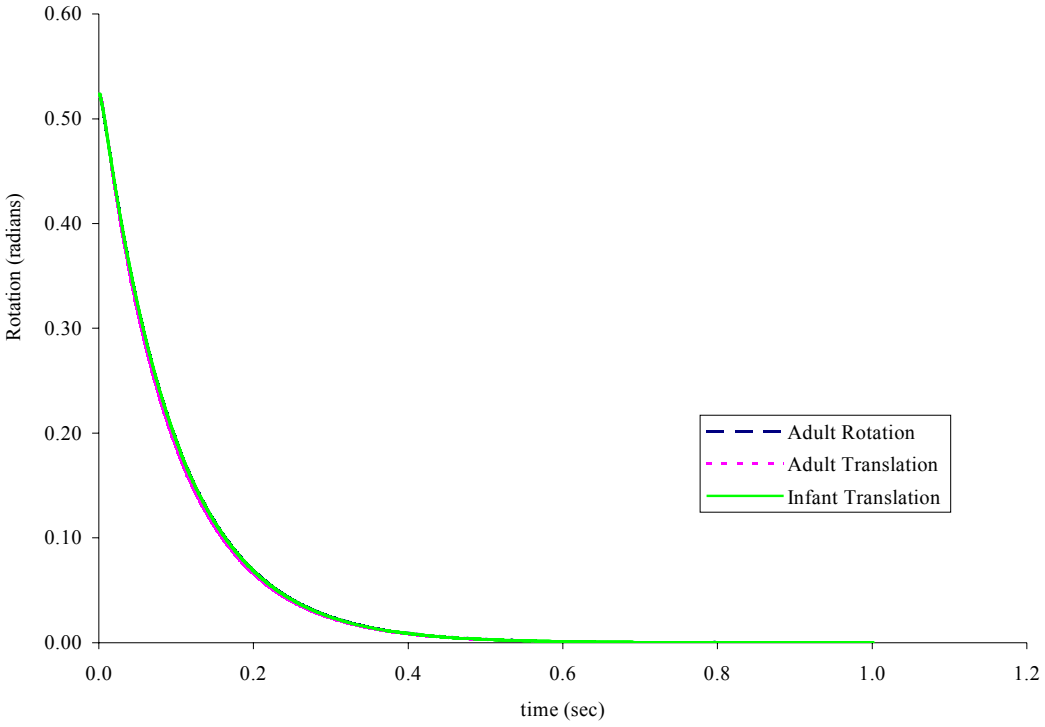

Figure 6.7: Rotational response comparison of the analytical plant models.

In order to match the response of an infant to an adult (Figure 6.7), the frequency is matched so that the stiffness constant for the infant optic nerve can be determined ($\omega_{nAdult} = \omega_{nInfant}$). Similary, the damping ratio is set equal ($\zeta_{Adult} = \zeta_{Infant}$) so that the damping coefficient for the infant optic nerve can be determined. Therefore, $K = \omega_n^2 I$ and $c_{eq} = 2\zeta(IK)^{1/2}$ with ω_n equal to 57.7 rad/sec and ζ equal to 2.89 (over-damped case). This is consistent with the findings of Lehman and Stark (1983) with the eye movement system being highly damped. This damping is not captured in the finite element model of the optic nerve that will be discussed further. The developed nerve-spring response is correct for a one-degree motion such as an eye fixed with a revolute joint. However, the simulation to be considered involves general motion, so the response of the spring has to show resistance to more than translational motion (as shown in Figure 6.6). Therefore, before incorporating a nerve-spring into the main simulation model, a simplified model of the infant eye is created with diameter 15 mm (Figure 6.8).

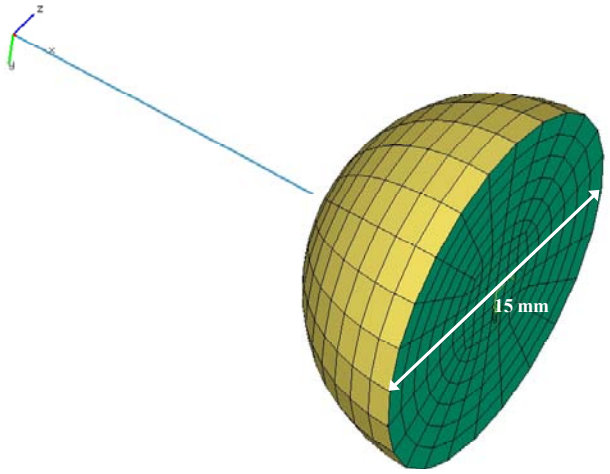

Figure 6.8: Developed eye model for testing the spring-nerve response with anterior section removed at the meridian to show vitreous mesh detail.

The eye model geometry is a sphere and is composed of solid brick elements (vitreous body only) meshed using the CUBIT software by considering an octant of the geometry. The outer ocular shell layer, of this simple eye model, is made into scleral material with uniform thickness (0.6 mm). The spring-nerve is constructed using a beam element in order to consider tension, bending and torsional loading. The material properties and element number are detailed in Table 6.1.

Table 6.1: The material properties and number of elements used in spring-nerve development testing. All material parameters and density are in SI units.

Ocular Component	Element Type	Number of Elements	Element Property	Material Type	Material Parameters[8]	Density[9]
Vitreous Body	8-node solid	2688	SOLID8 reduced integration	ISOLIN	E=43/ν=0.49/ Damp=200.0	999.0
Sclera Shell	4-node shell	552	MEM4 reduced integration	ISOLIN Tension only	E=3.58x10^8/ν=0.49/ reduction factor = 0.01	1400
Spring-Nerve	2-node Beam	1	BEAM2_ DISCRETE	KELVIN3D_ NL	Loading and damping functions Figure 6.9	-

The sclera shell uses the Uchio et al. (1999) material properties, discussed in chapter 5 (Figure 5.0), for the linear region of the curve. The spring-nerve beam element has its orientation specified (Figure 6.8) such that the local x-axis points from the apex node to just posterior the scleral shell. The y and z-axis point into the inferior and medial directions, respectively. The orientations are needed when specifying the

[8] The vitreous material is derived from the works of Weber and Landwehr (1982) and will be discussed in chapter 7.
[9] Density information is from Power (2001).

loading and damping functions for the bending, tension, and torsional loading of the spring (Figure 6.9).

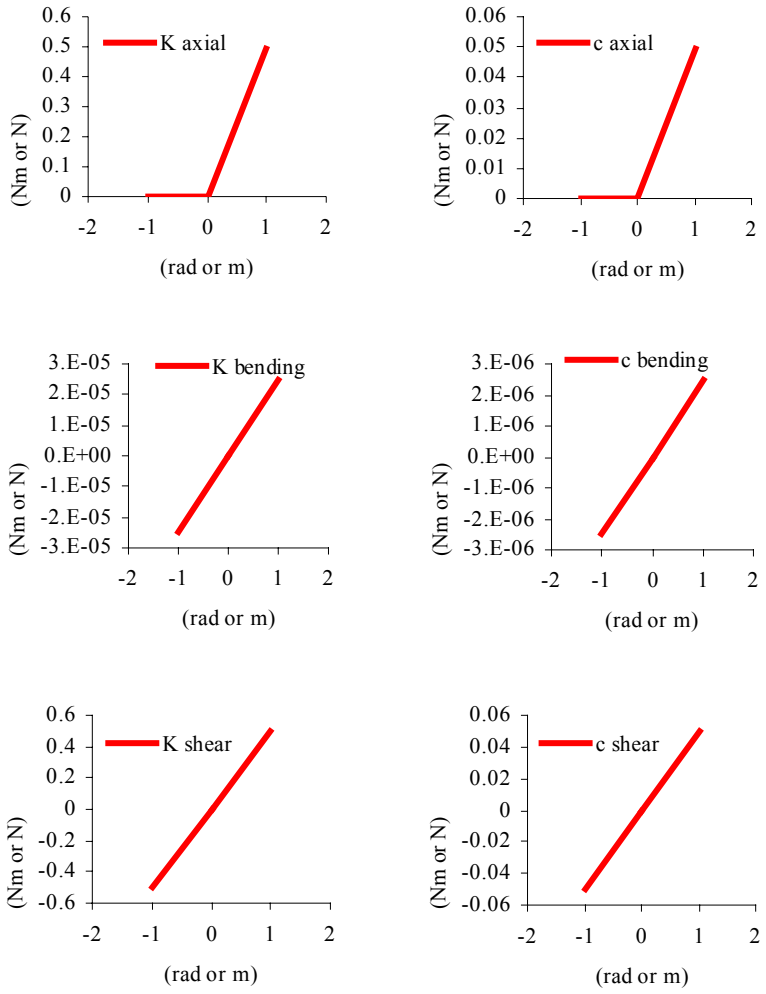

Figure 6.9: Spring-Nerve stiffness characteristic functions for axial, bending, and torsional resistance. The axial loading is such that only tension is enabled (hence, the need for KELVIN3D_NL property method).

The spring-nerve is attached to the eyeball by using a simple constraint where the nodal degrees of freedom for a group of nodes are set equal (Figure 6.10).

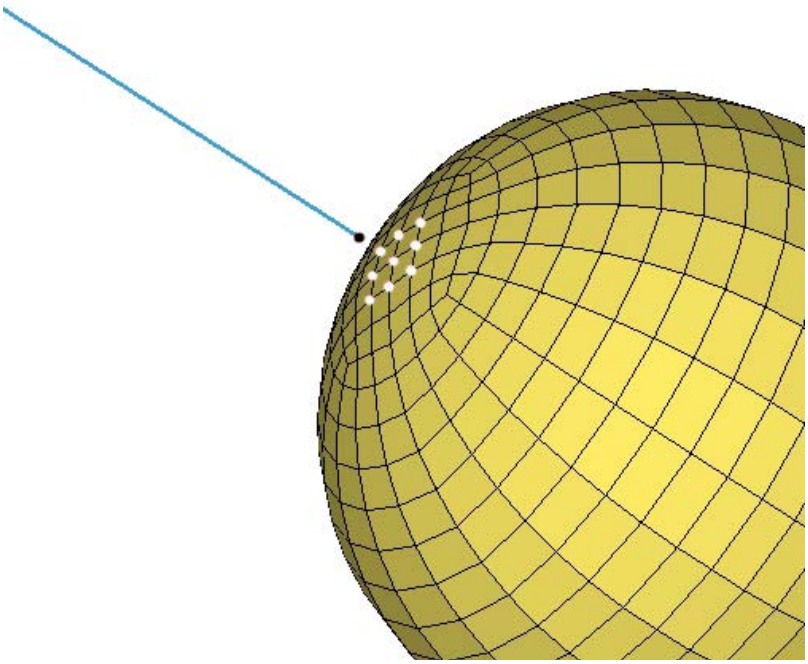

Figure 6.10: Selected nodes for simple constraint relationship. The black node belongs to the nerve group, and the white nodes (forming the ONH) belong to the optic nerve head group.

Initially, the node of the optic nerve (black node in Figure 6.10) was made to be the same node as the most posterior node on the eye globe (middle white node in Figure 6.10); however, the node attachment acted as a spherical joint with no resistance. Therefore, it was necessary to add the simple constraint. The eye model in Figure 6.8 is positioned so that the axial direction of the spring-nerve is pointing downward in the negative z-axis direction. To view the response due to gravity, the field is applied at a 45° angle with respect to the z-axis so that the eye model behaves as a pendulum (Figure 6.11) and then let go.

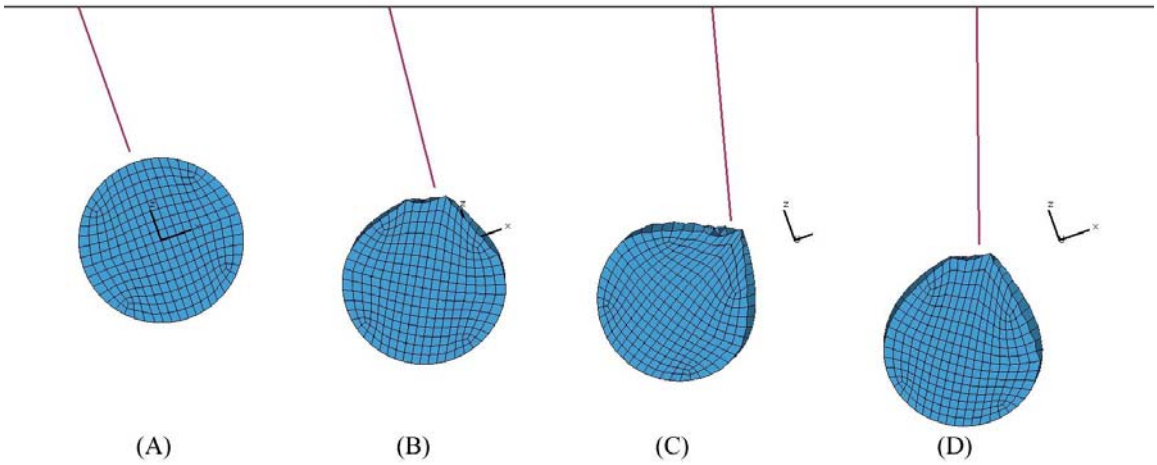

Figure 6.11: Animation sequence of the simplified eye globe and spring nerve (A is at time 0 milliseconds, B is at 50 milliseconds, C is at 100 milliseconds, and D is at 200 milliseconds).

The simulation (Figure 6.11) is actually taken to 0.75 seconds, but not much changes after 200 milliseconds as a result of the heavy damping from the spring-nerve ($\zeta = 2.89$). There is some pinching effect that is apparent in Figure 6.11c because of the definition of the ONH. This pinching effect is also observed in the actual SBS runs that will be discussed in chapter 8. The simulation is analogous to a balloon membrane filled with gel-fluid and attached to a semi-rigid tube. For extreme impact simulations, large deformations can cause the ocular shell to pinch off a section of the vitreous (Stitzel et al. 2002). The studies considered in this work do not take the eye to extreme impacts, so the pinching effect of the rear optic nerve is not as extreme, but it still provides an area of relatively higher stress as postulated by Levin (2000).

The properties developed and tested in this test eye model are then incorporated into the actual eye model by using the original geometry of the finite

element nerve. Five spring-nerve beam elements are created and attached to the posterior region (Figure 6.12) of the eye using material parameters from Figure 6.9 (dividing by 5 for the equivalent stiffness).

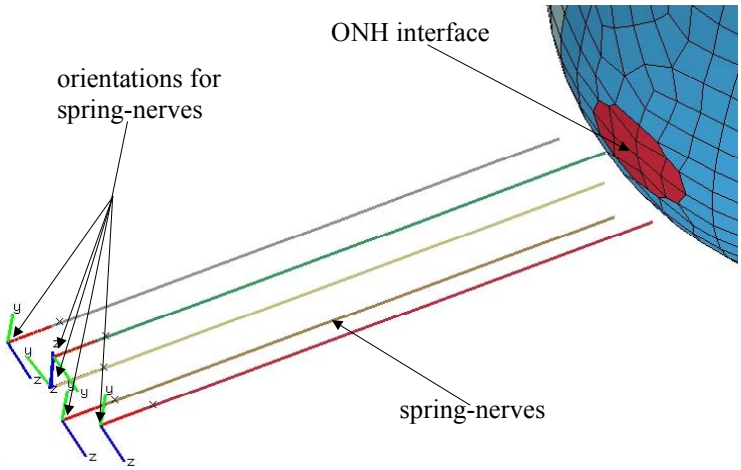

Figure 6.12: Layout of the spring-nerve and ONH interface for the SBS eye model.

There are five individual simple constraint groups for each of the spring-nerves in Figure 6.12 so that the ONH interface does not completely behave as a rigid disc (Figure 6.13). The ONH interface is composed of the same material properties as the sclera shell with thickness equal to 0.6 mm and uses membrane elements, which account for in-plane stress and strain. However, the simple constraint groups make each section of the ONH behave as rigid shells that help to induce the pinching as mentioned in Figure 6.11c.

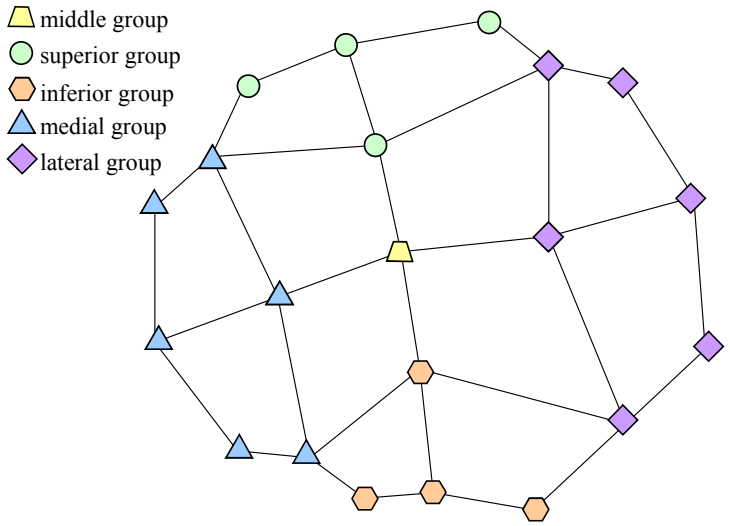

Figure 6.13: The ONH detailing the simple constraint groups for the corresponding spring-nerve. There are five groups in total.

The ONH dimensions are approximately 3 mm (lateral-medial) and 2.5 mm (superior-inferior) and are within reported ranges for infants (Newman et al., 2002). The actual shapes of the ONH and optic nerve are approximate so that the vitreous mesh remains at an optimum shape. This is a valid modeling method as the optic nerve is only considered to be a tether. The length of the nerve is approximately 14.7 mm.

The finite element nerve is actually created by extruding the ONH along the length of the nerve. The original apex attachment point is derived from the same location as the Visible Human dataset while the ONH location is defined based on Hogan (1963) (Figure 3.7). The material parameters are from Sigal et al. (2004) for their model 3 run. In this case, the pre-laminar neural tissue, lamina cribrosa, scleral-cornea, post-laminar neural tissue, and pia mater are considered. Values are tabulated and an average value for the elastic modulus is specified. As in Sigal et al.'s study

the optic nerve is made up of solid neural tissue and a membrane layer representing the pia mater. The pia mater in Sigal et al. is given the same modulus as the sclera shell. The finite element properties and element type are detailed in Table 6.2.

Table 6.2: The material properties and number of elements used in the finite element optic nerve model based on the Sigal et al. (2004) literature. All material parameters and density are in SI units.

Ocular Component	Element Type	Number of Elements	Element Property	Material Type	Material Parameters	Thickness	Density
ONH	4-node shell	12	MEM4 reduced integration	ISOLIN	$E=3x10^5$/ $\nu = 0.49$	$6x10^{-4}$	1000
Neural Tissue	8-node solid	168	SOLID8 reduced integration	ISOLIN	$E=3x10^4$/ $\nu = 0.49$/ damp =0.2	-	1000
Pia Mater	4-node shell	224	MEM4 reduced integration	ISOLIN	$E=3x10^6$/ $\nu = 0.49$/ damp=0.2/ reduction factor=0.01	$5.35x10^{-4}$	1000

The density information is not reported in Sigal et al. and is set to 1000 kg/m^3 (the same as water). The assigned density is within published values for the spinal chord nerve, which is 1038 kg/m^3 (Duck, 1990). The pia mater thickness in Sigal et al. is set to 0.06 mm thickness; however, for the SBS eye model this thickness has been increased to .535 mm, which is more representative of the sclera thickness in the posterior region. The reason for modifying the thickness is that the material of the optic nerve sheath is the outermost layer while the pia mater is between the arachnoid and dura (Hayreh, 1984). The dura in this case has similar properties as the sclera shell and is also considered so in the Sigal et al. work where the elastic modulus for

both materials is set to 3 MPa. Poisson's ratio is set to 0.49 in the Sigal et al. work to model incompressibility and 20% material damping is applied to account for the fact that biological structures exhibit some form of damping (MADYMO 2006).

The finite element model (Figure 6.14) of the optic nerve and ONH is by no means physiologic in this SBS model as the current model is mostly concerned with the vitreous material. Levin (2000) does explain that the optic nerve has been reported to hemorrhage in SBS abuse studies. In the current work, the focus is on the posterior vitreo-retinal forces with the extra-ocular tethers acting on the eye globe. Future studies will investigate further the optic nerve sheath and the fluid layer that is between the dura and pia mater. This fluid layer actually is greater just posterior the ONH entry point and the nerve, due to the fluid build up, have been reported to be bulbous (Hayreh, 1984).

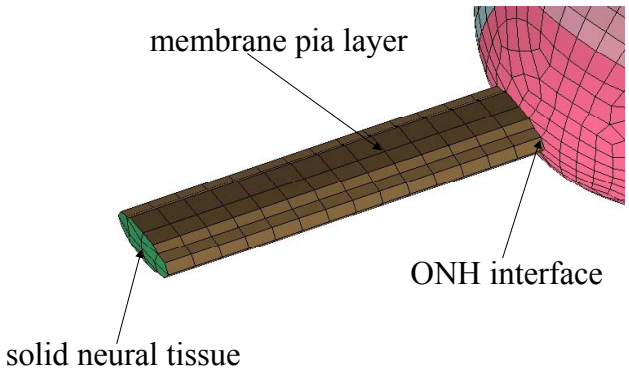

Figure 6.14: Layout of the finite element optic nerve and ONH interface for the SBS eye model. The material properties are from Sigal et al. (2004).

Extra-Ocular Muscles

There are six extrinsic muscles (Figure 6.15a and b) of the eyeball that provide the fastest and most precise movement in the human body (Tortora & Grabowski, 2001). A saccade (fast movement of the eye like reading this text) movement of the eye can reach peak velocities up to 1000 deg/sec (Lehman & Stark, 1979).

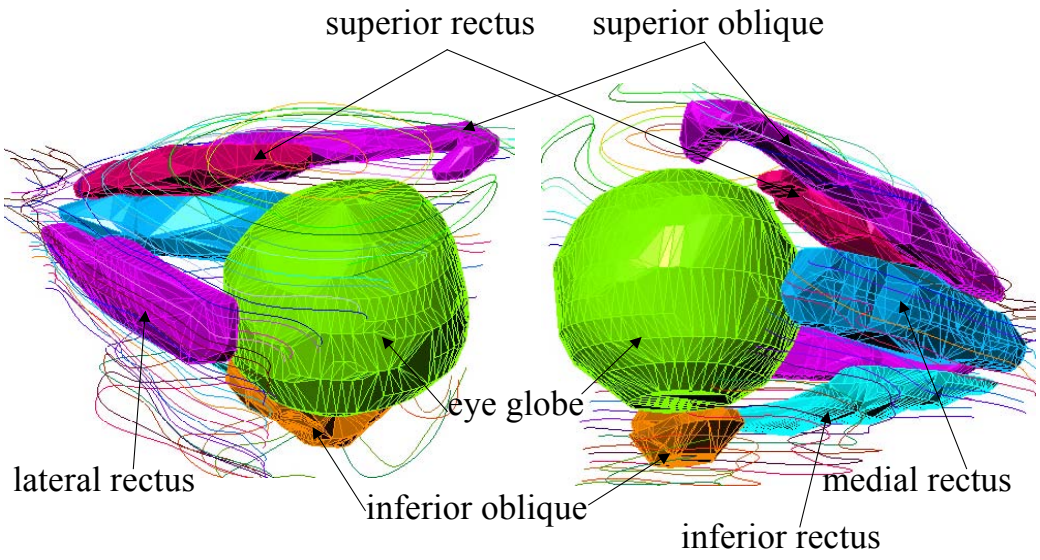

Figure 6.15: Layout of extra-ocular muscles of the eye. Geometry build-up is created from the Visible Human Project transverse slices.

The muscles (Figure 6.15) of the eye provide three planes of motion: horizontal rotation, vertical rotation, and torsional rotation. However, the torsional rotation is dependent on the horizontal and vertical rotations by phenomena known as Listing's

law (Lockwood-Cooke, Martin, & Schovanec, 1999). In the saccade studies presented, only horizontal motion is to be considered by neural excitation to the lateral and medial recti muscles while the other muscles will remain in a minimally active state "Hatze passive state" (Hatze, 1977; MADYMO, 2004). During the impact and shaking simulations, this passive state is considered for all the six muscles. The muscles to be in a passive state during a shaking episode as mentioned in Levin (2000) and act as mere tether attachments to the eyeball. The muscles depicted in Figure 6.15 are used to approximate the attachment points near the apex of the socket, the trochlea attachment, and the attachment to the eyeball.

Details of the actual eyeball-to-tendon attachment in the Visible Human Project transverse slice data are difficult to discern. Therefore, using anatomical diagrams (Figure 3.7) (Hogan, Alvarado, & Weddell, 1971), the attachment points of the muscles are refined at the eyeball by extending a tendon from the muscle end to the nodes of the sclera shell. The tendon width (scaling of adult widths) is approximated from Hogan et al. and is mentioned in Table 6.3. The actual width varies, as the attachment points of the nodes are approximate to the actual locations of the tendon attachments. The length of the muscles is first determined by fitting a three-dimensional curve through the muscle body starting from the posterior of the muscle to the anterior. The distance from the anterior muscle end to the eye attachment is considered to be the tendon length. The thickness of the muscles is determined from (6.2):

$$t = \frac{m}{lw\rho} \qquad (6.2)$$

Where t is the thickness, m is the mass, l is the length of the muscle, w is the width of the muscle, and ρ is the density. The density is 1041 kg/m^3 (Duck, 1990) for muscle tissue and the mass is 0.1 grams for an ocular muscle (Winters & Stark, 1988).

Actually the mass is different for each of the muscles (Rath, 2005); however, for the purpose of calibrating to the position output from Winters (1985), the mass is made the same for all recti and oblique muscles in the eyes in this study. The mass for the infant eye, utilizing the scaling factor of 64.5%, is approximately $3x10^{-5}$ kg (0.03 grams). Rath (2005) tabulated the muscle lengths and physiological cross-sectional areas for the work of Tian and Volkmann. Using this information and scaling to the infant, the average mass for the Tian specimen measurements is $1.79x10^{-4}$ kg and $1.42x10^{-4}$ kg for the Volkmann. The mass used from the Winters and Stark study is a magnitude less than the Rath; however, the mass contribution is relatively insignificant as will be presented later with the eye movement calibration study. The thickness is irrelevant for the muscles (will be using analytical muscles) but is assumed to be the same for the muscle and tendon attachments. The tendons will be made of membrane finite elements so that the attachment points into the eye globe provide a distributed force due to muscle pull. The final dimensional information for the muscles and tendons is provided in Table 6.3.

The purpose of the thickness information of the tendons is so that the force versus elongation function of the tendon can be converted to stress versus strain. Rather than using a spring element, like the optic nerve, the tendon utilizes three-node membrane elements attached to the eye globe so that the muscle-pull force can be distributed. In addition, a contact algorithm between the eye globe and tendons is

specified so that the tendon wraps around the eye as it rotates (as opposed to penetrating through the eye).

Table 6.3: Dimensional information for the muscle and tendons in the infant eye simulation model.

Muscle Name	Muscle Length (mm)	Tendon Length (mm)	Tendon Width at globe attachment (mm)	Tendon Thickness (mm)
Oblique Superior	29.87	8.10	6.98	0.2
Oblique Inferior	9.42	3.87	6.78	0.3
Rectus Superior	17.13	8.06	6.15	0.2
Rectus Inferior	19.10	7.41	6.15	0.2
Rectus Medial	17.91	8.04	5.76	0.2
Rectus Lateral	18.84	8.20	6.18	0.2

As with the fatty tissue to eye shell contacts, the tendon to eye globe contact uses a penalty algorithm (6.3) (MADYMO, 2004)

$$F_c = (K/V_0)A^2\psi[\min(\lambda, MAX\_FORCE\_PAR * t_e)] \qquad (6.3)$$

Where MAX_FORCE_PAR, a tuning parameter, is equal to 0.1 (the fatty to eye shell uses the recommended value equal to 1.0); F_c is the contact force; K is the bulk modulus of the contact segments penetrated; V_0 is the initial volume of the contact segment; A is the area of the contact segment; ψ is the penalty factor (the default value is 0.1 and is recommended not to change this value); λ is the penetration of the contact node; t_e is the penetrated element thickness that is multiplied by the MAX_FORCE_PAR. The parameter value is reduced to stabilize the contacts and prevent undue nodal velocities of the tendon as they penetrate the sclera shell. The contact, as a result, is more compliant, which is acceptable in this study and provides

realistic globe motion. The contact interaction is such that the nodes of the tendon shell elements contact the elements of the sclera shell. In this case, no contact gap is specified. The contact gap is not really needed in this case and saves computation time.

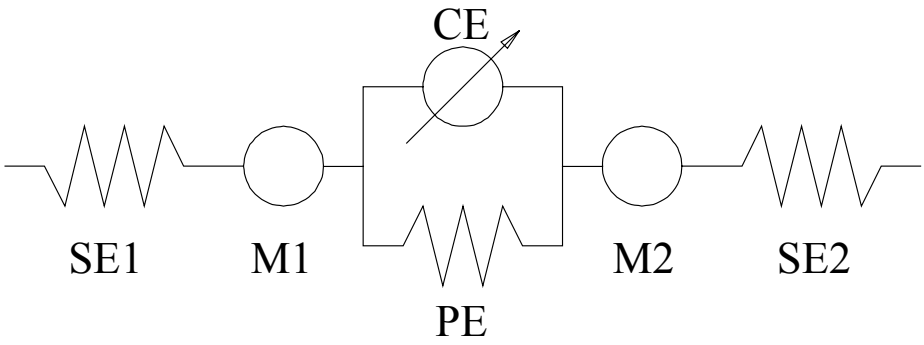

Figure 6.16: A Hill-type muscle schematic as implemented in MADYMO (2004).

The muscles used in this study are the Hill-type (Hill, 1950) formulation (Figure 6.16). The series elastic element (SE) represents the tendons; the mass (M1 and M2) represent the muscle mass; the parallel elastic element (PE) represents the passive strength of the muscle; the contractile element (CE) represents the dynamic properties of the muscle (Figure 6.16). In addition, complex controls can be implemented into the muscle models, but in this study, the muscles are either considered passive or neural excitation is imposed as a function of time. Figure 6.16 represents just one schematic that can be used to model the muscles. Depending on the muscle, the mass or one (both) of the series elements can be eliminated. The current study considers Figure 6.17 for the muscles used in the final SBS eye.

The calibration studies that used the Winters (1985) step excitation showed the similar response as Figure 6.16 and 6.17. In addition, simply attaching the muscle with no SE or mass calibrated well to the Winters work as will be discussed.

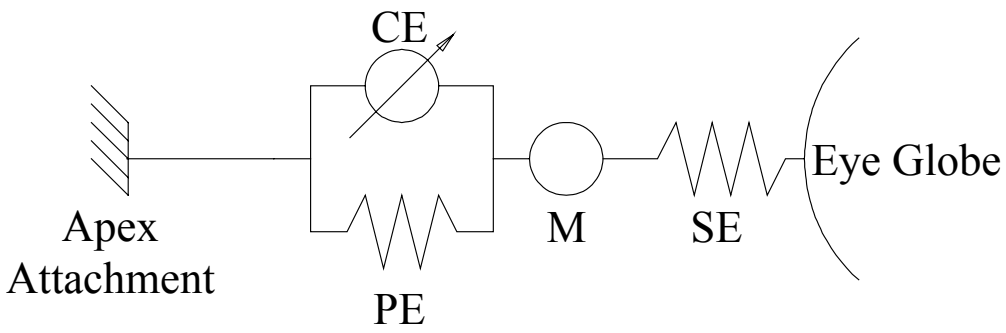

Figure 6.17: Muscle model used in the SBS eye model. The CE is not used (Hatze passive) in the SBS and impact studies.

The muscle model used in Figure 6.17 is influenced by the calibration studies, but the finite element models involved are also considered. The deviation of Figure 6.17 is for the oblique muscles. The oblique inferior is attached to the base of the ocular socket and the oblique superior loops through the trochlea point (modeled as a tying with zero friction and is analogous to a mathematical eyelet). The Hill-type muscle used in MADYMO cannot directly attach to a node, providing a simple model. The attachment of the Hill-type muscle has to be located on a rigid body or to the inertia space (ground). However, taking advantage of this fact, the finite element series element is attached to the sclera nodes, and then the posterior end of the tendon

is supported on the mass body with a free joint. The parent body of the masses is the attachment body, which is the root body of the entire skull complex located at the occipital condyle (allowing one to simply fix the entire model on a standard dummy). The Hill-type muscle (CE and PE) are then attached to the mass body and then to the attachment body at a location determined by the Visible Human geometry. This hybrid analytical-finite element muscle is robust, generalized (offering one to introduce controls or time function neural excitation), optimized for computation time, and most important, validated with previous literature for horizontal motion (Figure 6.18).

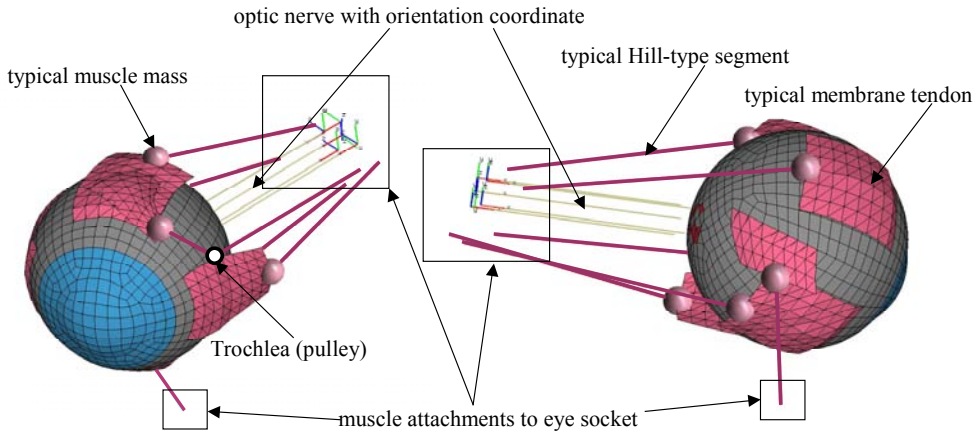

Figure 6.18: Muscle and tendon details of the SBS eye model.

The geometrical considerations of the muscle-tendons have been presented. Now the material parameters for the Hill-type muscles are investigated (PE, CE, and SE). The total muscle force is (6.4):

$$F_{muscle} = F_{CE} + F_{PE} \qquad (6.4)$$

Where F_{muscle} is the sum of the passive and active part of the muscle. The maximum force generated from a muscle is determined from (Winters & Stark, 1988) (6.5):

$$F_{max} = 0.5A_{pcs}\ [\text{MPa}] = 0.5\left(\frac{m}{2\rho t}\right)\sin(2\alpha)\ [\text{MPa}] \qquad (6.5)$$

Where m is the muscle mass, t is the muscle thickness, ρ is the density, A_{pcs} is the physiological cross sectional area, α is the pennation angle, the value 0.5 MPa is the peak muscle stress.

Therefore, the passive force (6.4) from (Winters & Stark, 1988) is (6.6):

$$F_{PE} = \left(\frac{F_{max}}{e^{PE_{sh}} - 1}\right)\left(e^{\left(\frac{PE_{sh}}{PE_{xm}}\right)(l_r - 1)} - 1\right) \qquad (6.6)$$

Where PE_{xm} is the relative elongation $(l-l_{ref})/l_{ref}$ and PE_{sh} is the shape of the force-length curve. Also noteworthy, F_{PE} is F_{max} when $l_r = PE_{xm} + 1$. The passive force of the muscle is only considered when the muscle is stretched beyond the reference length (Table 6.3); therefore, for $l_r < 1$, the F_{PE} contribution is zero.

The active muscle behavior is given by (MADYMO, 2004):

$$F_{CE} = A\ F_{max} f_H(v_r) f_L(l_r) \qquad (6.7)$$

Where A is the activation and varies between 0 (rest state) and 1 (maximum activation); $f_H(v_r)$ defines the normalized active force-velocity relationship (Hill curve); $f_L(l_r)$ is the normalized active force-length relationship. The force-velocity relationship considered takes the following form (MADYMO, 2004):

$$f_H(v_r) = \begin{cases} 0 & v_r \le -1 \\ \dfrac{1+v_r}{1-v_r/CE_{sh}} & -1 < v_r \le 0 \\ \dfrac{1+v_r\, CE_{ml}/CE_{shl}}{1+v_r/CE_{shl}} & v_r > 0 \end{cases} \qquad (6.8)$$

Where $v_r = v / V_{max}$ (V_{max} is the maximum shortening velocity and is a function of muscle fiber composition (Winters & Stark, 1985)), CE_{sh} is the shape parameter of the force-velocity during normal shortening, CE_{shl} is the shape parameter of the force-velocity during lengthening, CE_{ml} is the ultimate tension during lengthening. The work done by Winters and Stark (1985) uses a similar formulation as (6.8) for torque-velocity noting that the V_{max} and shape parameters are scaled to obtain the inverted Hill-curve (where the values are typical 1/3 of the shorting muscle values) (Winters and Stark 1988). Therefore, only the Hill shape parameter CE_{sh}, the V_{max}, and the F_{max} are needed to obtain the force-velocity relationship. The CE_{sh} and V_{max} are a function of muscle fiber composition. CE_{ml} is typically $1.3*F_{max}$ and CE_{shl} is typically 0.5 (Winters & Stark, 1985).

The next force contribution to the F_{CE}, the normalized active force-length relationship is represented by (MADYMO, 2004):

$$F_L(l_r) = e^{-\left(\frac{l_r - 1}{S_k}\right)^2} \qquad (6.9)$$

Where the parameter S_k determines the width of the active force-length curve. However, the curve represents a gaussian-type shape and is also known for the torque-angle relationship to be (Winters, 1985):

$$M(\theta) = e^{-\left(\frac{\theta - MX_{oo}}{MX_{sh}}\right)^2} + MX_{sl}\left(\theta - MX_{oo}\right) \qquad (6.10)$$

Where M(θ) is the normalized torque, θ is the joint angle, MX_{oo} is the angle at the maximum moment, MX_{sh} is the gaussian-type shape parameter, MX_{sl} is the linear slope coefficient. These values are tabulated in Winters and Stark (1985); however, direct curve fitting using 6.10 is performed, and then the torque-angle relationship is converted to force-length via the radius of the eye globe. Finally, the S_k value from 6.9 is determined from the curve fit.

The series elastic element can also be determined from (6.6) by replacing the PE_{xm} and PE_{sh} with SE_{xm} and SE_{sh}, which have similar meanings as the PE parameters (xm is the rotation or length at M_{max} or F_{max} and sh is the shape) (Winters & Stark, 1988). However, for the tendons, a function of force versus strain (l_r-1) will be specified for the characteristic materials. The force will further be divided by the A_{pcs} term for the membrane elements representing the tendons.

The values for the muscle and tendon parameters are presented in the Winters work in terms of torque and rotations; however, for inclusion into the SBS model, these values are converted to force and length parameters. The force-length relationship f_L of the ocular muscle is determined by curve fitting the Winters (1985) ER curve for eye rotation and solving for the shape parameters from (6.10) (Figure 6.19). The values are first normalized before determining the parameters (MX_{oo} = -0.515, MX_{sh} = 1.38, MX_{sl} = 0.048 determined from curve fitting). The values are comparable to the tabulated values in Winters & Stark (1985). Figure 6.19 is provided for completeness; however, the original values are converted to relative length (l_r) and the relative force (f_L) and then (6.9) is used to determine the parameter

S_k = 0.35 (MADYMO has a default value of 0.54). The passive element parameters are also determined from curve fitting a torque-rotation plot from Winters (1985) and compared to Winters and Stark (1985). Finally, the values are converted to force-length values using the radius of the eye globe (radius = 1.1 cm (Winters & Stark, 1988)). The passive element parameters are in Table 6.4. The values from the curve fit and those directly read from the Winters and Stark (1985) table are comparable.

Table 6.4: Passive element parameters determined from curve fitting and directly from Winters tabulation.

	PE_{sh}	PE_{xm}	F or M max
From Winters Table	4	60 deg	0.01 Nm
From Curve Fit	3.32	58.57 deg	0.01 Nm
Winters Table Converted	3.32	0.258	1 N

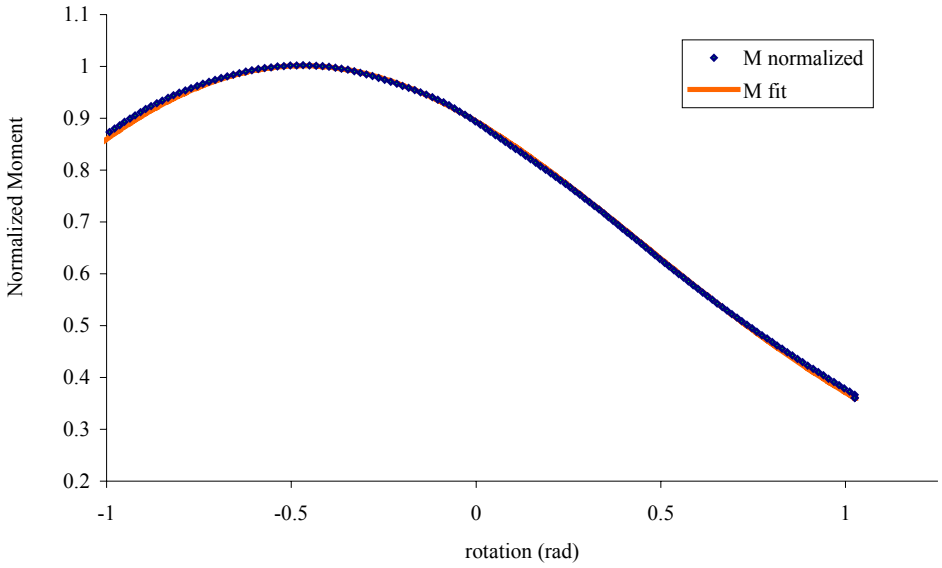

Figure 6.19: Curve fit of moment-rotation relationship of the eye rotation from Winters (1985).

Finally, Figure 6.20 shows the relationship for both the passive and active element relative force versus relative length based on the determined parameters. The values for the force-velocity relationship are curve fitted from Winters (1985) by taking the torque-angular velocity relationship and converting to force-velocity by using the radius of the eye globe giving a V_{max} = 0.495 m/s and a F_{max} = 1 N. The shape parameters are then determined from (6.8) by curve fitting (CE_{sh} = 0.437, CE_{shl} = 0.0797, and CE_{ml} = 1.38). The data points from Winters (1985) and (6.8) are compared in Figure 6.21. Interestingly, CE_{ml} is about 1.3 * F_{max}; however, CE_{shl} is not close to 0.5 (Winters & Stark, 1985).

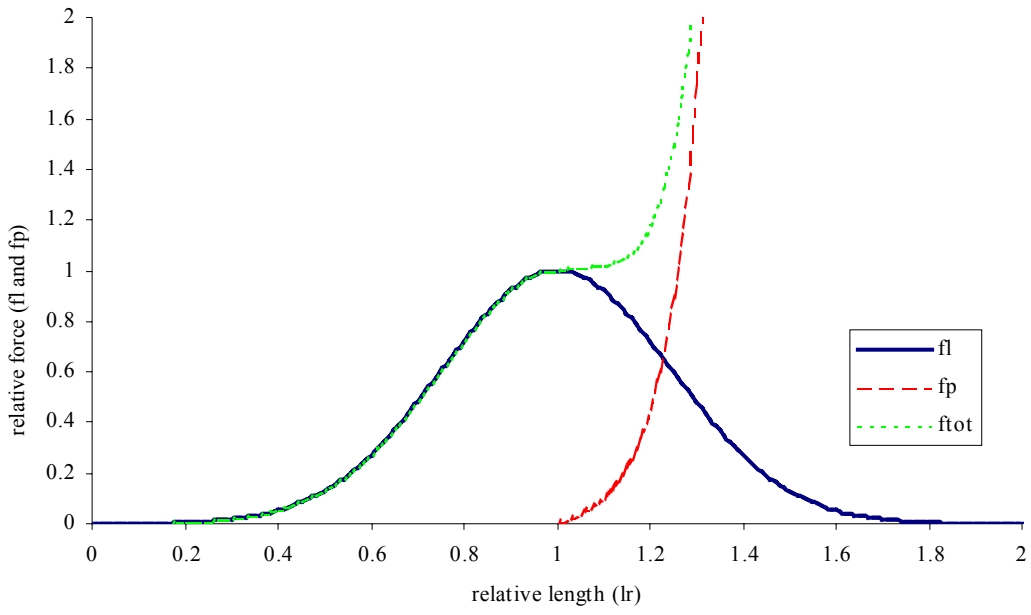

Figure 6.20: Relative force versus relative length for both the passive and active muscles with the total contribution shown as the addition of both curves.

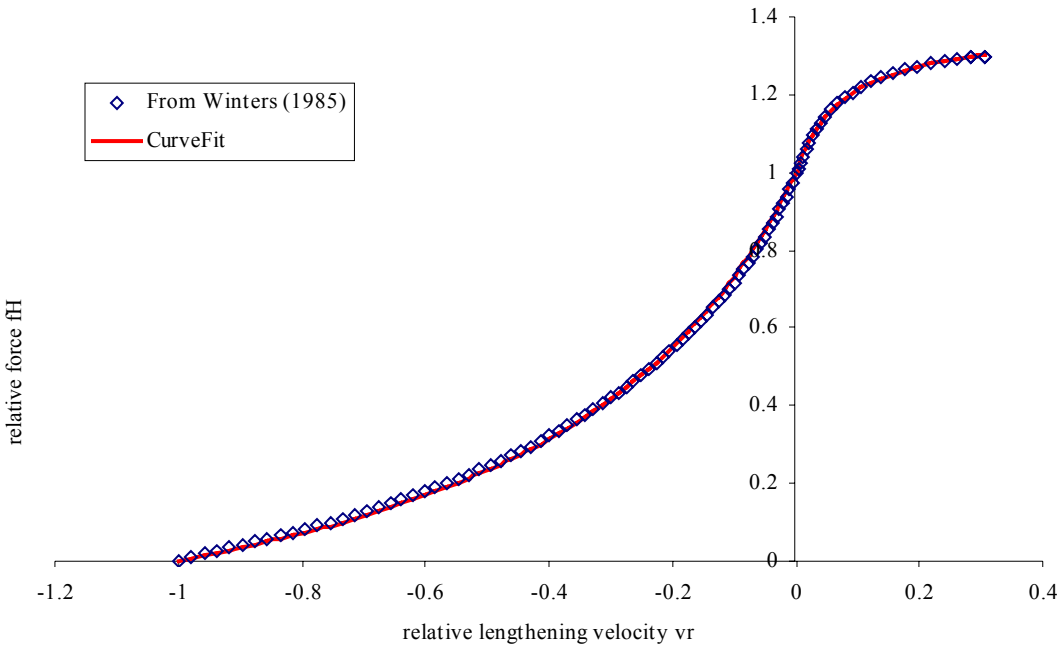

Figure 6.21: Force-velocity curve $f_H(v_r)$ comparing the curve fit values to the data points (Winters, 1985).

Curve fitting using (6.6) and the data from Winters (1985), the series elastic constants are determined and compared to tabulated values from Winters and Stark (1985) (Table 6.5). For inclusion into the model, the torque-rotation is converted to force-elongation by considering the eye globe radius when converting the moment to force and also the muscle reference length (5 cm from Winters and Stark (1988)). Specifically, the rotation given in degrees is converted to strain by (6.11):

$$\varepsilon = \frac{\frac{\theta \pi r}{180} + l_{muscle}}{l_{muscle}} - 1 \qquad (6.11)$$

Where ε is the strain (also considered $l_r - 1$), θ is the rotation in degrees, r is the radius of the eye globe, l_{muscle} is the reference length of the muscle equal to 5 cm (Winters & Stark, 1988).

The force-strain constants are also in Table 6.5.

Table 6.5: Series elastic constants from curve fitting using (6.6) to Winters (1985).

	SE_{sh}	SE_{xm}	F_{max} or M_{max}
From Winters Table	1.6	20 deg	0.01 N-m
Curve fit to Winters data	1.56	20 deg	0.01 N-m
Winters converted data	1.64	0.091 m/m	1 N

The curve fit values are in good agreement with the tabulated values from Winters and Stark (1988). The final force versus strain is shown in Figure 6.22, where the data from Winters (1985) is converted from rotation versus torque. In addition, the curve fit using (6.6) is also shown reflecting the constants used in Table 6.5. Interestingly, when F_{max} is equal to 1 N, the strain is equal to SE_{xm} using (6.6). The tendons in the SBS eye model utilize the force-strain curve plot from Figure 6.22. In order to do this, the material type HYSISO from MADYMO is selected which allows one to model the stress-strain of materials with various types of hysteresis characteristics.

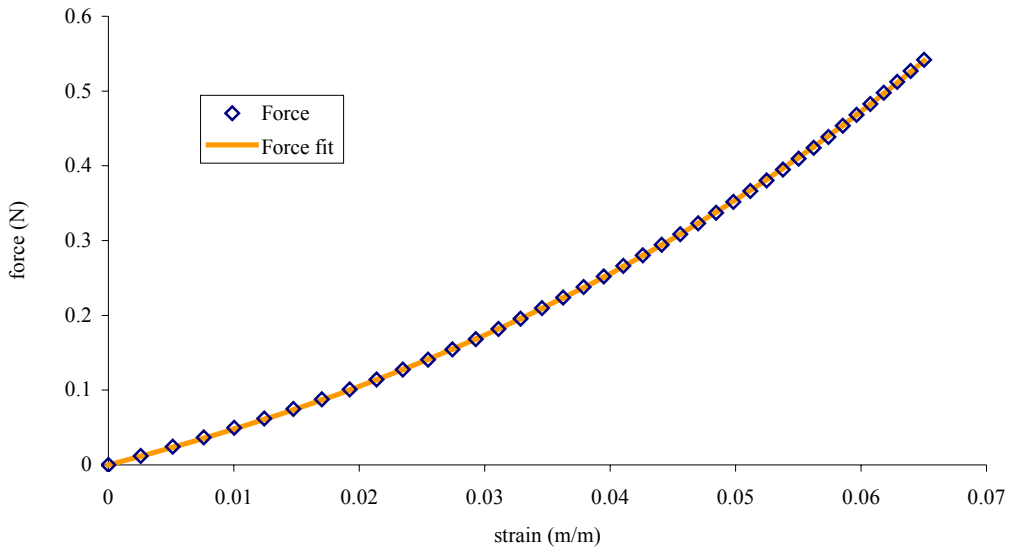

Figure 6.22: Tendon force versus strain curve fit from Winters (1985) compared to (6.6).

However, the original four-node shell membrane elements needed to be converted to three-node membrane elements in order to use the material type. The material also considers tension only and the density of the material is 1165 kg/m^3 (average value for ox tendon from Duck (1990). The tendons are split into three groups when modifying the function derived from Figure 6.22. That is, the recti muscles use a multiplier of 8.33×10^5, the superior oblique uses a multiplier of 1.11×10^6, and the inferior oblique uses a multiplier of 5.56×10^6. These multipliers are the inverse of the A_{pcs} used to convert the force to stress. The tendons in this model are stiffer than the muscle tissue and are only engaged when the muscle is stretched beyond the physiological limits. Winters also considered this issue by only exciting the muscles for horizontal motion of the eye within physiological limits.

The final consideration in the active force (6.7) is the muscle activation. The activation dynamics of muscles is described to be an "ideal neuro-controller input signal" (Winters, 1985) that is separated into two parts: neural excitation and active state dynamics. The latter is the electro-chemico-mechanical contraction coupling dynamics that is considered the measured EMG[10] signal (Winters, 1985). The neural excitation is described by (Van Der Horst, 2002):

$$\frac{dE}{dt} = \frac{u - E}{T_e} \quad 0 \le E \le 1 \qquad (6.12)$$

Where E is the normalized neural excitation, t is the time, T_e is the excitation time constant, and u is the normalized neural input ($0 \le u \le 1$). The active state dynamics are represented by (Van Der Horst, 2002):

$$\frac{dA}{dt} = \frac{E - A}{T_a} \quad 0 \le A \le 1 \text{ and } T_a = \begin{cases} T_{ac} & E > A \\ T_{da} & E \le A \end{cases} \qquad (6.13)$$

Where A is the normalized active state, T_{ac} is the activation time constant, and T_{da} is the deactivation time constant. Finally, t_{act} is the delay time that is incorporated into the u(t) function. The time constants are determined by the mass and the fraction of slow fibers in the muscle (Winters & Stark, 1988). For the eye, the time constants and model delay are (Table 6.6). The delay time, t_{act}, is extremely small for the eye as opposed to the neck muscles (t_{act} = 74 ms) (Van Der Horst, 2002).

[10] EMG stands for electromyography and is the study of muscle electrical signals.

Table 6.6: Activation time constants for the eye motion (Winters, 1985).

	Activation T_{ac} (ms)	Deactivation T_{da} (ms)	Activation Delay t_{act} (ms)	Neural Excitation T_e (ms)
Eye motion	5	30	2	30

The muscle activation is important to consider, as the muscle never stays in a full activation state for long without fatigue setting in. In order to include the activation state into the model, the signal function is used in the control system model in the SBS eye model. This is a straightforward way to model the eye dynamics without the need for complex PID controllers and is also used by Winters (1985). Essentially, a unit step function, u(t), with the activation delay included, is inputted into the system. Then, using the times constants (Table 6.6), the neural (6.12) and activation (6.13) response is determined.[11] Therefore, given a unit step input, with a t_{act} = 2 ms, with width of 50 ms produces the neural and activation curves represented in Figure 6.23.

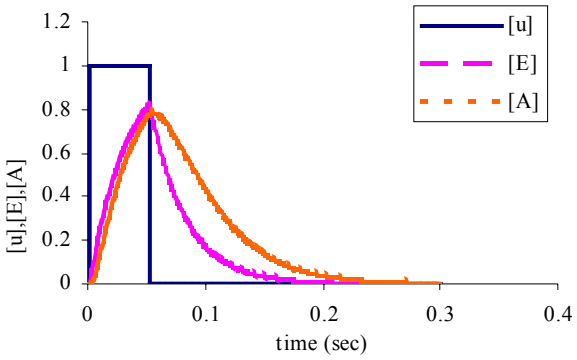

Figure 6.23: Time signals with input u(t); E is the neural excitation; A is the activation state.

[11] Using a fourth-order Runge Kutta method for solving (6.12) and (6.13) given u(t) and $T_a(t)$ (RK, 2005).

Muscle Calibration Dynamic Study

Using the parameters determined for the Hill-type muscle model, an analytical model is created and modified to compare the response to work done by Winters (1985). The first model, for an adult horizontal eye motion, considered is like the analytical model described in the optic nerve section, where a rigid body with radius 1.1 cm is modeled with a revolute joint. The stiffness information of the "plant" is the same as in the optic nerve section ($I = 3x10^{-7}$ Nms^2/rad, $K = 1x10^{-3}$ Nm/rad, $c = 1x10^{-4}$ Nms/rad). The lateral and medial muscle is modeled by attaching the segment to the eye body at the specified radius with a length of 5 cm. The posterior segment is attached to a body with a mass of 0.1 grams.

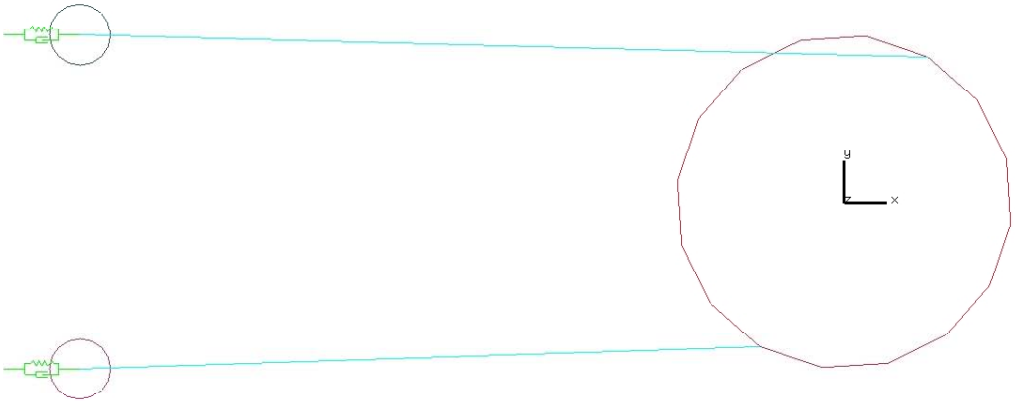

Figure 6.24: Analytical adult eye model for use in neural signals. Calibrated with Winters (1985).

This mass is attached to a separate system with a free joint, allowing all degrees of motion. This mass is then attached to a kelvin element representing the tendon body. The tendon uses the stiffness information from Figure 6.22 and is attached to the

background. The model is then given an initial rotational displacement of –30 degrees to correspond to the initial rotation specified by Winters (1985) when considering idealized neural signals (Figure 6.24).

The medial muscle will act as the agonist and the lateral the antagonist. The simulation time is 1000 ms and starts by placing the eye at an initial steady-state position near the extreme of the mid-operating range of movement. The antagonist muscle at this point is at a larger contraction than the agonist with co-contraction level 3% neural activity. The antagonist muscle neuro-input is specified with a 100% neural activity for 500 ms duration.

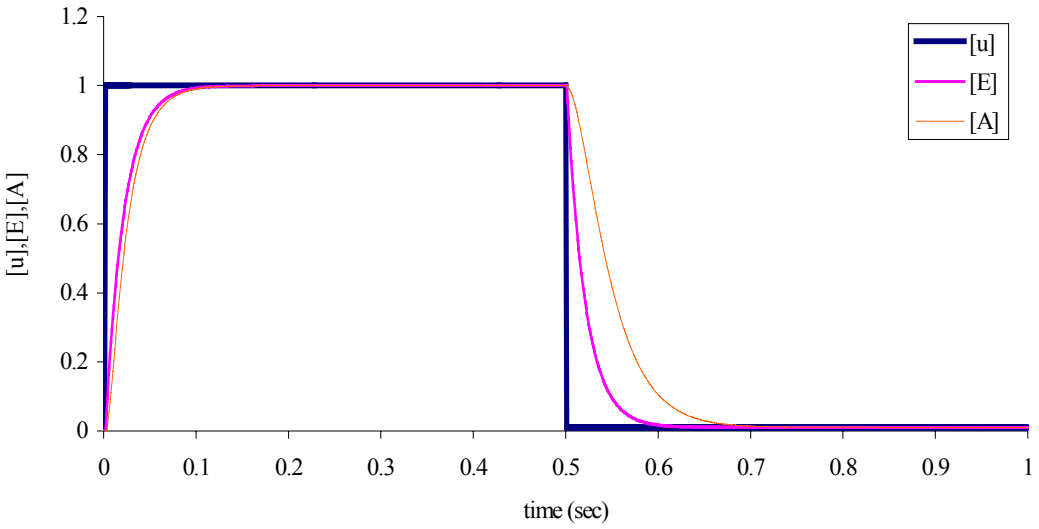

Figure 6.25: Time signals of the neuro-input u(t), neural excitation E and activation state A.

After the 500 ms, both step functions for the agonist and antagonist go to a minimal value of 1% neural activity (Winters, 1985). In the Winters study, the

agonist muscle has varying levels of neural activity showing the sensitivity. Using all the time constants from Table 6.6, the signal function for the neural and active state is determined by inducing the neuro-input, u(t) (Figure 6.25). In Figure 6.25, the neuro-input does include the t_{act} = 2 ms duration. The antagonist muscle uses Figure 6.26 as the signal input.

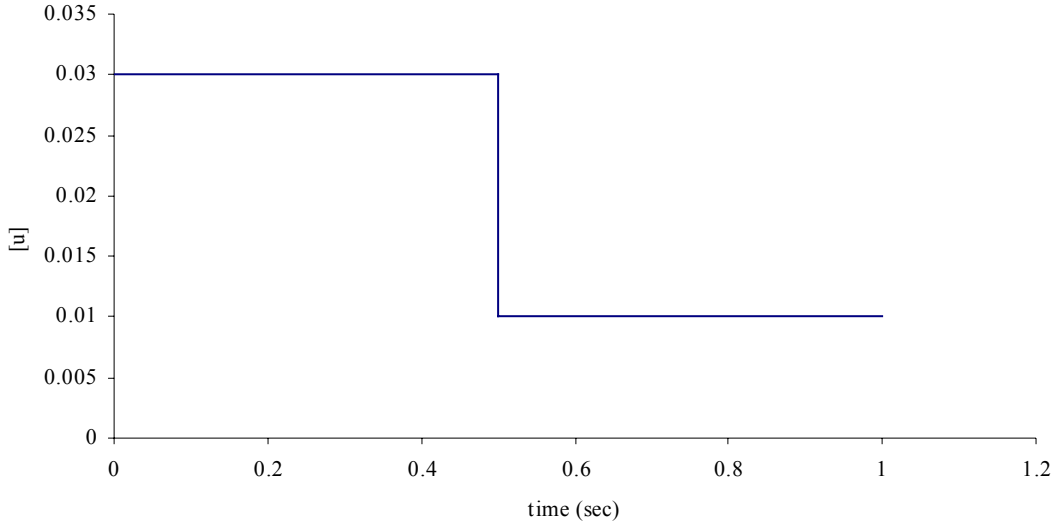

Figure 6.26: neuro-input signal for the antagonist muscle.

The antagonist muscle uses u(t) directly as the input and predicts the position very well to the Winters (1985) output Figure 6.27. This model is labeled "calibrated" in Figure 6.27. The muscle modeling in this analytical eye model considers the muscle mass posterior attaching to a tendon.

In the MADYMO applications manual (MADYMO, 2004) there is an example of a neck model with a muscle model similar to Figure 6.16 with the difference being a mass body centered with two muscles attached in series and with a muscle-tendon attached to both ends. The logic with this three-mass system is to prevent artificial rotations from the muscle system. Therefore, the analytical model has been expanded to include this situation (Figure 6.28). The muscle mass is divided into three parts and attached at the extreme ends of the total muscle segments. The middle attachment point has the center mass where both muscle segments meet. The tendon characteristic is divided into two parts with one tendon attaching to the eye globe and the other to the background.

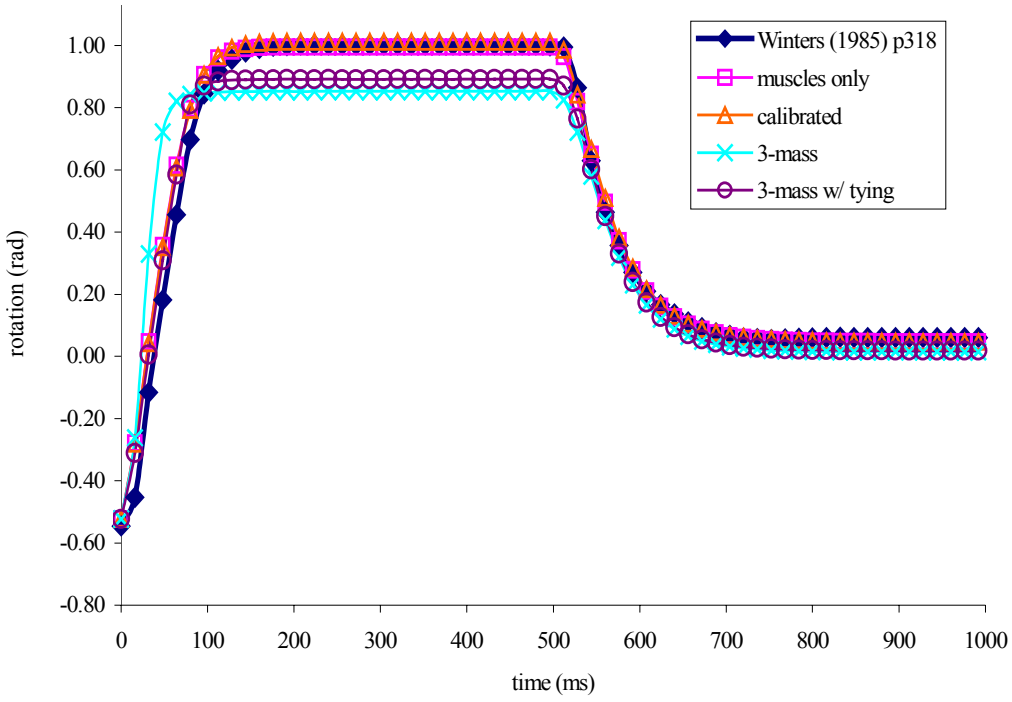

Figure 6.27: Comparison of the rotational output from the muscle systems. The muscle only and calibrated models predict the Winters (1985) model for horizontal eye motion well.

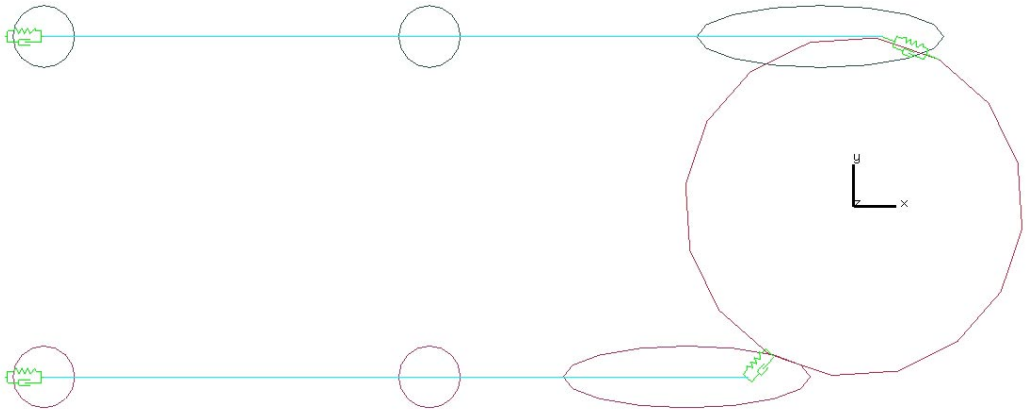

Figure 6.28: Analytical adult eye model for use in neural signals. Modifications include two muscles in series with three masses divided along the total length of the series muscle. Tendons are attached at the eye globe and the posterior end of the series muscle.

The analytical muscle described in Figure 6.28 does not compare well with the same activation levels as the calibrated model. This model is labeled 3-mass in Figure 6.27. The muscles are added in series, which would affect the shortening force of the muscle; therefore, the 3-mass model is further modified to only have one muscle total with the middle mass acting as a tying. This tying is similar to that used in the superior oblique muscle where the trochlea point is modeled as a slip ring rigidly attached to the attachment body. In this case, the middle muscle body is attached to a free joint but still acts as a slip ring of the single continuous muscle segment. The response (labeled 3-mass w/ tying) of the rotation in Figure 6.27 is only marginally better than the 3-mass system with two muscles in series.

The last model to consider is the case with only the muscle segment attached to the eye globe and to the background. This system (Figure 6.29) does not include the mass or the tendons and predicts the rotation versus time as well as the calibrated

model (label is muscle only in Figure 6.27). The correlation factor, comparing the muscles only with the calibrated model, is 0.995 for the muscles only and 0.996 for the calibrated. The difference in the predictability of the muscle only model is an indication that the effects of the mass and tendon are insignificant for this neural input.

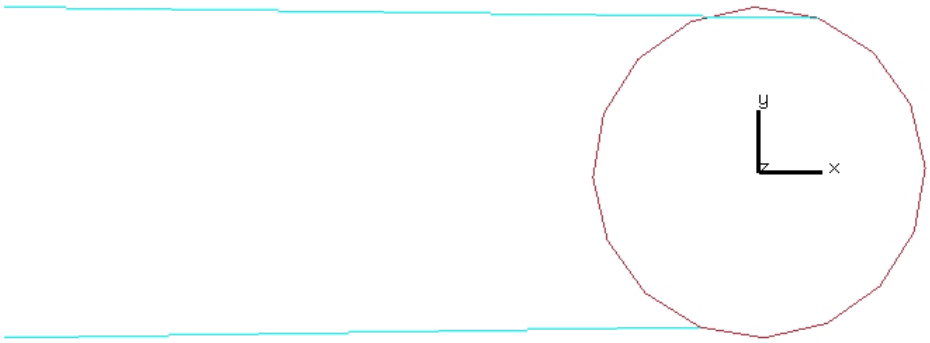

Figure 6.29: Analytical adult eye model for use in neural signals. Only the analytical muscle is considered with the eye globe.

While using the simple model represented in Figure 6.29 is ideal, the attachment points of the muscles can only be on rigid bodies and not finite element nodes. In addition, the attachment point of the muscle to a single node would create more of an artificial stress point versus a tendon attached to a line of nodes. Further, the analytical muscle has no means of contacting the eye globe while the tendon can wrap the eye during the limits of rotation or translation of the eye providing a more realistic motion and interaction with the eye. Figure 6.30 shows that the derived

muscle parameters for the Hill-type muscle match the response of the Winters (1985) model.

Another examination is considered where a saccade is induced considering an operating range of 40 degrees. The eye model is initially positioned at –20 degrees with a neural excitement applied to the agonist muscle and a minimal activation of 1.1% is applied to the antagonist muscle for the 200 ms duration. The motion change takes place from –20 to 20 degrees in about 60 to 70 ms and maintains the final rotation of 20 degrees for the rest of the simulation (Figure 6.30).

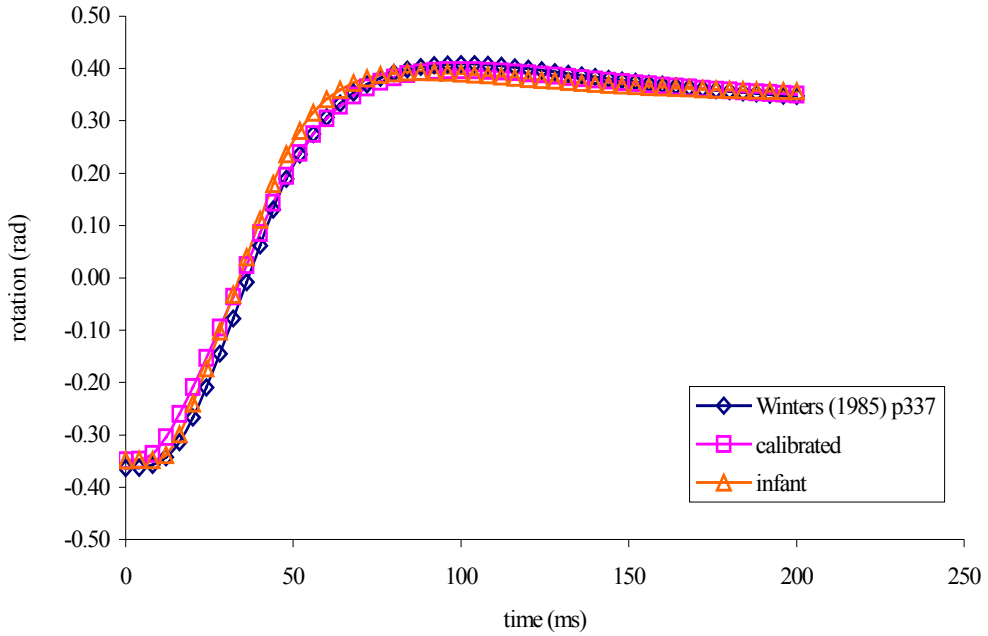

Figure 6.30: Eye model behavior due to a 40 ms u(t) pulse. Comparison to Winters (1985), the calibrated eye, and the scaled down infant eye model.

The calibrated eye model is excited with the same neuro-input that is applied to the Winters model (Figure 6.31) in order to achieve the matching response. The infant model scales the geometry, inertia, mass, and optic nerve response. However, only the reference length in the Hill-type muscle is modified keeping the shape parameters the same as an adult. The tendon also uses the same stiffness properties as the adult. The overall force of the muscle (6.4) needs to adjust by modifying the activation of (6.7). In order to approximate the response, the neuro-input is adjusted (Figure 6.32) by lowering u(t) over the 40 ms range from 100% activation to 35% activation. Modifying the step response in this way shows a correlation factor of 0.997 for the infant eye while the adult eye is 0.999 (Figure 6.30).

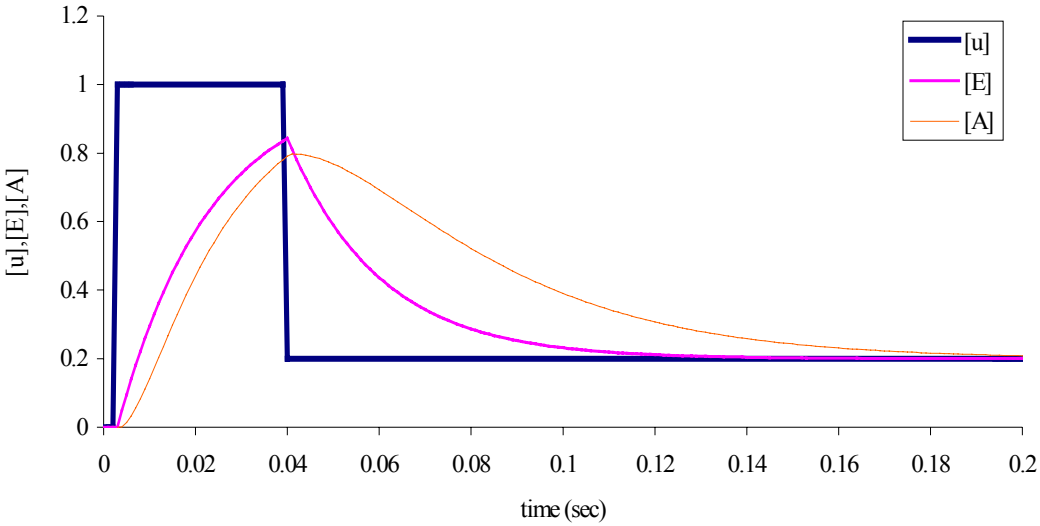

Figure 6.31: Adult eye time signals of the neuro-input u(t), neural excitation E and activation state A for the 40 degree saccade movement.

In addition to lowering the activation level of the u(t) for the infant eye, further modifications are done by delaying the start of the neuro-input by 8 ms (t_{act} = 8 ms). And finally, after the 40 ms pulse width is complete the agonist muscle neuro-input equals 15% as opposed to 20% for the adult eye. The antagonist muscle is set at 7% neural activity for the duration of the simulation. The purpose of including the saccade calibration is to use the neural excitation in the SBS eye when considering the response of various vitreous materials. Therefore, a comparison is made between the finite element infant eye (SBS model) and the analytical rotation response as a result of the neuro-input from Figure 6.32.

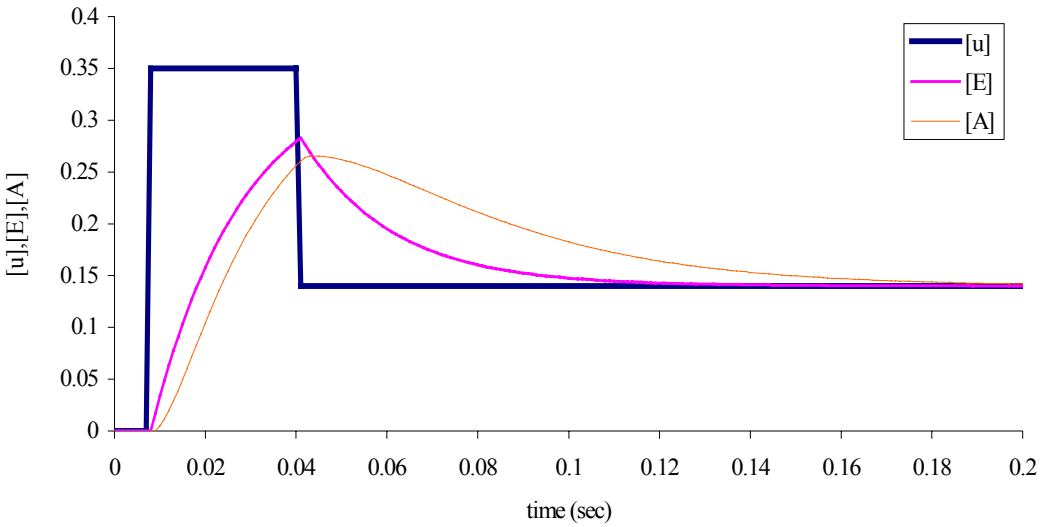

Figure 6.32: Infant eye time signals of the neuro-input u(t), neural excitation E and activation state A for the 40 degree saccade movement.

A saccade is induced using the neuro-input from Figure 6.32 to the finite element eye for both the analytical nerve (Figure 6.12) and the finite element nerve using the material properties from Sigal et al. (Figure 6.14). The rotational response in Figure 6.30 starts at –20 degrees; however, the finite element models will only start at normal rest position (0 degrees) looking forward. The induced saccade will have only a maximum rotation of approximately 20 degrees. A comparison of the infant eye models using the finite element method is detailed in Figure 6.33. The only difference in the models is the type of optic nerve model used. The angle from the finite element model is approximated by:

$$\theta = a\cos\left(\frac{2l^2 - d^2}{2l^2}\right) \qquad (6.14)$$

Where θ is the angle of the eye rotation measured at the equator of the eye ball (Figure 6.34), d is the distance of the medial node in the equator plane relative to the position at the start of the simulation, and l is the distance from the medial node to the center of the eye. This angle is approximate since the eye is also allowed to translate in the fatty tissue and the motion is not completely in the horizontal plane. However, the point of this comparison is to visualize the overall kinematics of the finite element eye when a saccade is induced.

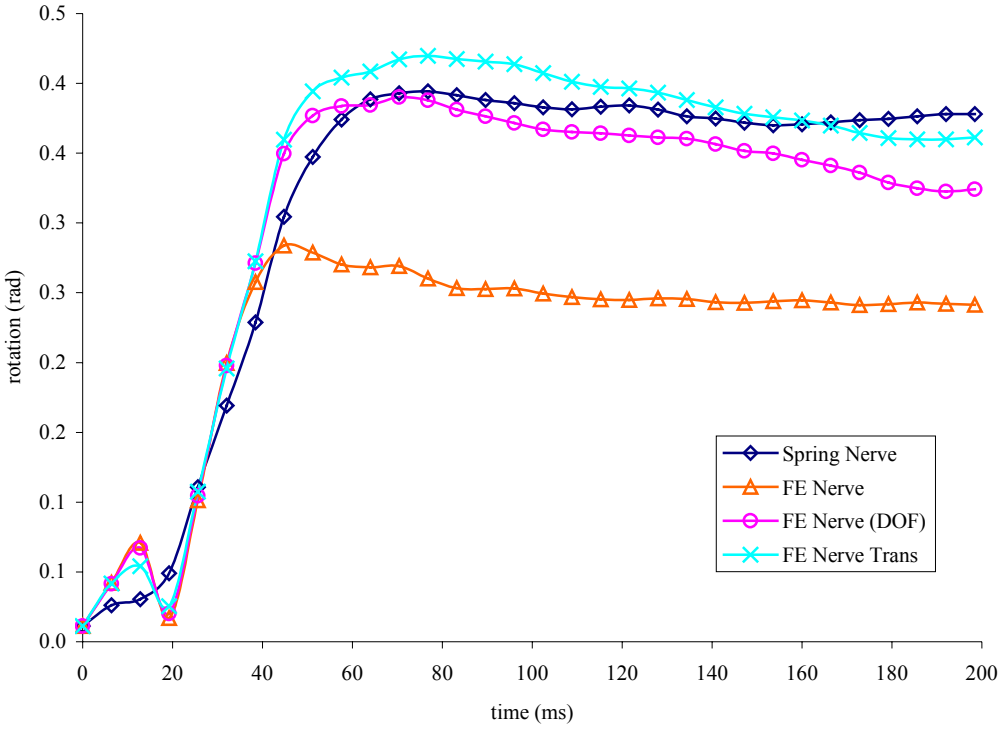

Figure 6.33: Comparison of the finite element eye models with a 20° saccade.

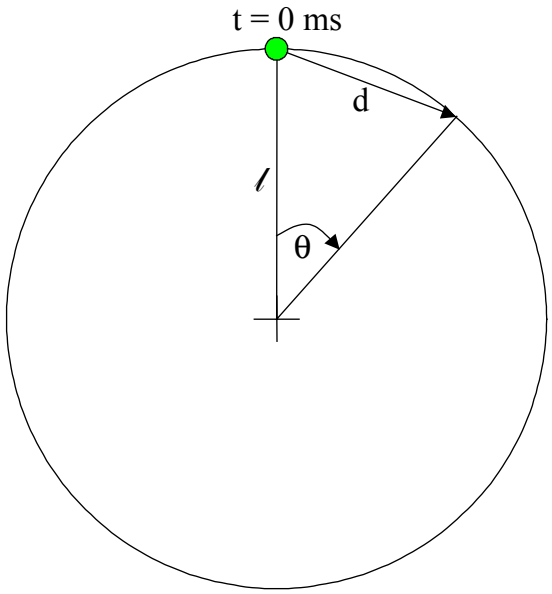

Figure 6.34: Angle determination of the eye globe with a saccade movement using (6.14).

The eye globe cannot achieve the maximum angle of 20° when the FE Nerve is completely supported and plateaus around 11.5 degrees. Modifying the support, the FE Nerve (DOF) model allows translation in the global X direction and rotation about the global Y and Z-axes. The reasoning behind this method is to introduce slack (Levin, 2000) into the nerve and have comparable response to the analytical nerve model. Modifying the supports helps to achieve this goal but is not totally correct, as the optic nerve is not aligned along the X; rather it is 30 degrees from the axis. Further complicating matters, the nodes have to be supported in all degrees when supported on a body. The FE Nerve (DOF) is supported to the background; however, this support method is not applicable in the general simulations with the harmonic shaking and impacts. Therefore, the next model in Figure 6.33 (labeled FE Nerve Trans) considers a body attached to the apex of the ocular cavity proximal to the optic nerve supports. This body utilizes a translational joint that is oriented along the axis of the finite element optic nerve. The supports of the optic nerve are then fixed to this body to allow slack in the nerve and achieve a like response as the analytical spring nerve model. The results are comparable for the spring nerve and FE nerve Trans model.

Conclusion

This chapter has covered the aspects of the fatty tissue interfacing the eye globe and the ocular tethers. Important consideration is given to the contact interactions between the fatty tissue and the eye globe. Also important to mention,

the contact interactions in the entire eye model are reduced to a minimum to avoid introducing undue complexity and instability into the model. The optic nerve is influenced by major studies in eye motion controls and from glaucoma investigations. Details are explained regarding the modifications of the optic nerve properties for inclusion into the infant SBS eye model. The Hill-type muscle model is used in the SBS eye model and explanation of the parameters and constitutive equations is given. The response of the eye with the Hill-type muscles is compared to Winters (1985) and correlates well. Finally, the saccade neuro-input is considered and calibrated to the Winters (1985) response by reducing the activation level for the infant eye so that a similar saccade motion is achieved. This response is then imposed on finite element model with the analytical optic nerve and the finite optic nerve. Modifications to the support of the finite element optic nerve are included so that a similar response is achieved compared to the Winters (1985) study and the analytical optic nerve. This saccade motion is of interest when comparison is performed in the next chapter between different material properties for the vitreous body.

CHAPTER VII

A PARAMETER STUDY OF THE VITREOUS HUMOR DURING SACCADIC MOVEMENTS IN AN INFANT EYE

Abstract

A parametric investigative study is conducted where various vitreous materials are considered in a finite element eye model. The ocular shell, muscle tethers, optic nerve, and encasing fatty tissue are considered in this model. The model utilizes a LaGrangian mesh when considering five vitreous material candidates. In addition, the constitutive material models are also varied to understand the response. A comparison of the shear strain located at the equatorial wall is compared between the candidate vitreous materials, as eye radius is proportional to the maximum shear (David et al., 1998). A 20-degree saccadic horizontal motion is induced to the eye using Hill-type muscles (Winters, 1985). A comparison between different optic nerve models is also considered along with the mesh density of the finite element model.

The vitreous materials respond drastically from each other. Some of the vitreous materials are not appropriate to use in a LaGrangian mesh due to high shear strains as a result of compliant shear moduli. The purpose of this study is to determine which vitreous materials would be suitable for use in impact and pure harmonic shaking simulations.

Introduction

A finite element model of an infant eye that includes the extra-ocular muscles, optic nerve and fatty tissue-eyelid enclosure is presented. The geometry of an adult eye is scaled to infant dimensions using the eye globe diameter (Hogan, Alvarado, & Weddell, 1971) to give a scale factor of 0.645 (infant eye diameter / adult eye diameter = 16 mm / 24.8 mm). The optic nerve diameter, as a result of scaling, is compared to values measured using ultrasound measurements from children age 10 days to 13 years old (Newman et al., 2002) and are comparable to the infant dimensions.

Two models for the optic nerve (analytical spring-type and finite element model) will be investigated. Considering the analytical model, the mathematical models done in previous works consider the horizontal motion of the eye (Collins, Scott, & O'Meara, 1969; Lehman & Stark, 1979; Lehman & Stark, 1979; Robinson, 1981;Winters & Stark, 1985; Winters & Stark, 1988). These analytical models consider the eye as the "plant" which acts as a revolute joint in horizontal motion. The properties are scaled from the adult to infant ($\omega_{nAdult} = \omega_{nInfant}$ and $\zeta_{Adult} = \zeta_{Infant}$) matching the same dynamic response (over-damped spring model).

The finite element model of the optic nerve models the optic nerve head, pia mater, and the nerve tissue (Sigal, Flanagan, & Tertinegg, 2004). In the finite element optic nerve model, the material properties are assumed to be the same for an infant. Both optic nerve models are supported in the apex of the ocular socket, which is built up from the Visible Human transverse dataset.

The muscle tethers considered in the model are a Hill-type (Hill, 1950; MADYMO, 2004) with a lumped muscle mass attached to membrane element tendons that are affixed to the eye globe sharing common nodes. The analytical muscle parameters are derived from the work of Winters (1985). The tendons are also adapted from Winters (1985) with modifications so that membrane elements can be utilized. The parameters of the muscles and tendons are not scaled to an infant; however, the muscle force for the active response is scaled in order to get comparable responses to neural excitation. Currently, there is no data on infant extra-ocular muscles or the fiber composition, which is what the muscle parameters are based on (Winters & Stark, 1988).

The fatty tissue that encases the eye globe is modeled using similar properties as Power (2001), which uses the properties from Todd and Thacker (1994) for determination of an elastic modulus for buttocks tissue. This modulus is stiffer than other soft tissue studies (Luboz et al., 2004; Samani & Plewes, 2004; Verver, 2004); however, this study is going to consider the horizontal saccade motion (Winters, 1985) so that the fatty tissue and eye globe behave as a revolute joint. There is still going to be rotations about the other two axes, but the values are minimal. The interface between the eye globe and fatty tissue is considered by using a contact gap with a penalty method algorithm (MADYMO, 2004). Contact interactions with soft biological tissues are kept to a minimum to simplify the model and reduce instability.

The ocular shell tissues are composed of the cornea-sclera shell, choroid layer, and retina layer. All the ocular shells are considered to be membranes (Graebel & Van Alphen, 1977; Uchio et al., 1999; Wu, Peters, & Hammer, 1987). The anterior

portion of the eye containing the aqueous, lens, and cilliary body are modeled as well. The lens and cilliary body properties are adapted from Power (2001) and the aqueous is considered to be composed of the same material as the vitreous (Stitzel et al.). The aqueous is actually more fluid than the vitreous body (Hogan, Alvarado, & Weddell, 1971); however, the current study is concerned with the vitreous body shear strain at the equatorial posterior pole, and the aqueous is assumed not to influence the strain during the saccadic motion.

Several vitreous materials will be included into the eye model for investigation. However, the mechanical properties determined need to be converted into suitable parameters for use in the MADYMO software. An investigation into the shear strain is then conducted comparing the vitreous materials from different studies using different constitutive models in order to investigate the response.

One material investigation will utilize an elastic modulus (Landwehr, 1982). Four other vitreous materials (Bettelheim & Wang, 1976;Tokita, Fujiya, & Hikichi, 1984; Power, 2001; Nickerson et al., 2005) will be considered viscoelastic using three constitutive models in the MADYMO software (linear viscoelastic (CPL) with deviatoric and hydrostatic coupling, linear viscoelastic (REF) with deviatoric and hydrostatic stresses decoupled, and non-linear viscoelastic (SOL) considering shear softening). The material model variants have the same naming convention as used in the Brands (2002). The vitreous material in this study will be considered homogenous given the current material determinations. The vitreous is of course not homogenous and it various throughout (Lee, Litt, & Buchsbaum, 1992).

The shear strain is then compared amongst all the vitreous materials, constitutive equation, and models. David et al. (1998) developed an analytical viscoelastic model using properties from Lee et al. (1992) in order to study the shear stress during a saccadic eye movement. The shear stress is proportional to radius of the globe implying that measurements should be taken at the equator of the globe. In addition, animation sequences of the transverse section at the equator are compared for each computation (23 simulations total).

Vitreous Body

The vitreous body, occupying four fifths of the volume of the eye globe, provides structural support for the outer ocular tissues and helps maintain intraocular pressure (Hogan, Alvarado, & Weddell, 1971). The vitreous is a clear gel-like structure composed of mostly hyaluronan with a network of collagen fibers ((Dalton et al., 1995; Sebag, 1998). Dalton et al. describe the network of collagen fibers to act as a rigid truss network while the hyaluronan provides shock-absorbing properties to the system. Nickerson et al. (2005) describe the collagen type II fibers as a network spanning the full diameter eye in a random pattern with hyaluronan molecules described as coils in between the voids of the fiber network. The tensile strength of the type II fibers has been quantified to be around 200 milligrams to 2 grams of force with elongations, before breaking, equal to 51 to 152 percent (Numata, Constable, & Whitney, 1975). The composition of fibers appears to be at greater concentrations around the ora serrata (Hogan, Alvarado, & Weddell, 1971) and is affixed to the lens

when dissection is attempted on an adult eye (Wolter, 1961). In addition, the vitreous is seen to be hanging from the posterior lens as it is lifted upwards with forceps. Quantifying the concentration of collagen fibers, in the anterior section, shows the elastic modulus to be twice that in the central and posterior regions of the eye for adults (Lee, Litt, & Buchsbaum, 1992). In addition to the structural properties, the vitreous also serves the purpose of providing nutrients to the lens and retina (Hogan, Alvarado, & Weddell, 1971) and also affects vision by scattering light (Zimmerman, 1980).

Considering the infant eye, the vitreous is more gel-like and has a higher viscosity. Further, the retina is well attached to the vitreous from the posterior pole all the way to the ora serrata (Levin, 2000). Sebag (1998) shows the vitreous of a 9-month-old child attached to the lens with a band of gray tissue posterior the ora serrata. This band of tissue is retina that could not be separated from the vitreous. Further, the vitreous gel is resting on a surgical towel exposed to air with no weeping of fluid indicated. Fluid loss is mentioned in Nickerson et al. when conducting material testing on porcine and bovine vitreous. This fluid loss tends to lower the shear modulus of the material. The vitreous posterior the lens is more firmly attached in infants and becomes less so with increasing age (Hogan, Alvarado, & Weddell, 1971). Zimmerman (1980) mentions that the young eyes often scatter less light but does not reveal age trends in viscoelasticity of the vitreous. This lack of scatter is due to the more viscous nature of the infant vitreous, which after age four shows evidence of a more liquid vitreous. By the time the human eye approaches adult size at age 14-

18, the vitreous is 20% liquid. Finally, by age 80-90, the vitreous is more than half liquid (Sebag, 1998).

Previous Models

Modeling of the vitreous in finite element models has been considered in past eye models (Uchio et al., 1999; Power et al., 2002; Stitzel et al., 2002). The vitreous body in Uchio et al. is considered using solid elements and material model specifying hydrostatic pressure of 20 mm Hg only. This material is not producible in the MADYMO software considered here; however, it is proposed that a bulk modulus is specified for this material. This is perplexing as the bulk modulus should be of the order 10^9 and not 10^3 if this is the case, and the author does not elaborate on the constitutive model for the vitreous. The aqueous is also considered using solid elements but no mention of the material properties is given.

The model considered in Power et al. also models the vitreous and aqueous as solid elements. The vitreous material is assumed to be linear elastic and is assigned a value of 42 kPa, which is a reduction of 47 kPa for human buttocks testing (Todd & Thacker, 1994).

Considering the appropriateness of this assigned modulus, a comparison is made between brain material and vitreous material studies to understand the magnitude. Most of the material studies for the brain and vitreous utilize oscillatory shear experiments for determining the viscoelastic properties (Shuck, Haynes, & Fogle, 1970; Bettelheim & Wang, 1976; Tokita, Fujiya, & Hikichi, 1984; Dalton et al., 1995; Zhou, Khalil, & King, 1996; Chirila et al., 1998; Brands, 2002; Lippert,

Rang, & Grimm, 2004; Nickerson et al., 2005). Converting the Power et al. vitreous model to a shear modulus yields 14 kPa. Morrison (1995) tabulates some of the brain material parameters used in previous finite element brain models with an average short term shear modulus of 170 kPa and 64 kPa for the long term shear modulus.

However, Morrison is persuaded to use the values from Zhou et al., which are converted from Shuck et al. oscillatory shear experiment. Therefore, the value of the short and long-term moduli is 41 and 7.6 kPa, respectively. As seen, the Power et al. shear modulus is within the lower bounds of the brain material testing. Recent work developed by Brands (2002) uses a viscoelastic model for the brain properties considering a multi-mode Maxwell model (MADYMO, 2004) as opposed to the comparison from Morrison, which considers only one mode.

A crude curve fit of the multi-mode model into one-mode shows the short and long-term modulus of the Brands porcine brain test to be 3.2 and 0.67 kPa, respectively. This is considerably smaller than what is reported in the Morrison table and would put the Power et al. vitreous out of bounds of the brain material in this case.

Vitreous material determination for the highest reporting viscoelastic shear modulus properties is provided from the work of Nickerson et al. by using a cleated rheometry tool. The initial G' for the bovine vitreous is 30 ± 12 Pa, and the final steady state value is 6.5 ± 2.0 Pa. However, the sample preparations are such that the anterior and posterior sections of the vitreous are cut away leaving the central cylindrical disc with fluid loss over a period of time. The author mentions that the initial modulus of 30 Pa is perhaps closer to the moduli of the in vivo modulus.

Therefore, the Power et al. vitreous value of 14 kPa is about 470 times the value of the Nickerson modulus. The Power et al. vitreous stiffness is approximately between measured values for adult vitreous and brain material studies. The Power et al. vitreous is influenced by the lumped soft tissue modulus from Todd and Thacker (1994), which is considerably higher than any other material determination study for soft tissue (Verver, 2004). There are plenty of observations that support a higher shear modulus for the infant eye; however, the Power et al. is probably an overestimate based on the presented material property determination studies.

The Stitzel et al. eye model considers quarter geometry of the eye, which is used for impact studies, where the eye undergoes extreme deformation. The Lagrangian elements would undergo extreme shape changes (perhaps causing negative volume elements). To overcome this problem, an equation of state (EOS) is defined for the pressure of the system using a coupling LaGrange-Euler mesh. The total stress is a combination of the hydrostatic $\left(\frac{1}{3}tr(\sigma)\right)$ and deviatoric (σ_d). The state equation chosen is the Gruneisen (Hallquist, 2004) EOS (considers the hydrostatic component) where the density, speed of sound through the material, and other coefficients are inserted. In this case the speed of sound and the density of the aqueous and vitreous are set to the same values using 1006 kg/m^3 for the average density (Duck, 1990) and 1503 m/s for the speed of sound (all other constants are set to values for water). This EOS is appropriate for very high strain rates. The bulk term is represented by $K = \rho C^2$ (where ρ is the density of the material and C is the speed of sound through the material). However, the viscous term is not introduced in this model. For low strain rates, as considered in the current model, simple

hydrostatic behavior can be modeled by using the linear polynomial model by setting all constants to zero except C_1 giving (Hallquist, 2004):

$$p = K\left(\frac{1}{V} - 1\right) \qquad (7.0)$$

Where p is the pressure, K is the bulk modulus ($K = \rho C^2$), and V is the relative volume. The same model can be used for the Gruneisen equation by setting all constants except K to zero. The bulk modulus is extremely high for the vitreous (order is 10^9), which is typical for incompressible fluids (1/K gives the compressibility). Unfortunately, there is no method in the MADYMO software that can use the EOS for fluids. In fact, this method in LS-DYNA seems to be insufficient for modeling the viscoelastic effects of the vitreous. However, for simulations that require high impacts, where the volumetric compression is a leading factor, this is a fairly robust method.

Modeling a solid bulk material in the MADYMO is quite possible using the linear viscoelastic model (LINVIS) by setting the shear modulus extremely low. In this case, the deviatoric and hydrostatic components are added together. Using this method certainly aids in resisting volumetric changes, but it also exhibits extremely stiff vitreous material that is resistant to shear as will be discussed in this work.

Vitreous Materials

Currently, there is no study that examines the mechanical behavior of infant vitreous. Further, limited studies have considered modeling the vitreous using the material parameters from these vitreous studies. Bovine vitreous samples are

prepared and tested in a torsion pendulum in order to measure the complex shear modulus from frequency ranges from 0.1 to 0.003 Hz and at temperatures from 3.6 to 41.2°C. The complex shear modulus (G' and G") is then plotted along with the loss tangent using superposition on a log-log plot (Tokita, 1984). The storage modulus (G') has the following fit:

$$G' = 6.78 f^{0.096} \qquad (7.1)$$

Where f is the frequency in Hz and the units of G' are in dyn/cm^2. Bettelheim and Wang (1976) determine the complex modulus of bovine vitreous using an oscillatory compression chuck located at three directions of the eye. The study does not provide a plot but does show the complex modulus (E' and E'') for 3.5, 11, 35, and 110 Hz. The study also mentions that the chuck would affect the behavior of the vitreous outside the cross-sectional area and introduces a referenced empirical method to account for this. However, the benefit of this testing method would keep the vitreous in place with minimal disturbance to the collagen fiber network. In the case of Tokita, the vitreous needs to be removed and sliced before it is inserted into the testing apparatus. Further, it is not clear if there is slip at the boundary walls and if there is degradation to the testing sample. The values are converted to complex shear by dividing by 3 ($\nu = 0.5$ for incompressibility).

The Bettelheim and Wang study compares the three directions of compression (medial-to-lateral, oblique direction approximately 40° to the medial-lateral direction, and along the Cloquet's canal). The results between the three directions are approximately the same (comparing the E' values). Lee, Litt, and Buchbaum (1992) perform creep tests on the vitreous by inserting a small sphere into the medium and

applying magnetic force. The testing compares the properties of the anterior, central, and posterior of human eyes. The study in 1994 includes bovine and porcine vitreous. The study fits the compliance versus time plots into a six-parameter Maxwell model in series with a Kelvin model. Unlike the Bettelheim and Wang study, differences in the elastic modulus are shown to be consistent with reports of higher concentrations of collagen fibers in the anterior section. However, the magnitudes of the modulus are comparable to Bettelheim and Wang. Landwehr (1982) also uses a steel sphere inserted into the vitreous but performs oscillations as opposed to creep testing. Interestingly, Landwehr considers the vitreous body as rubber-elastic as opposed to the viscoelastic studies conducted by other authors. Because of the collagen fiber network, the author maintains that the vitreous cannot really be considered viscoelastic and fits the data to a Voigt-Kelvin model under harmonic excitation. Using the mass of the inserted steel sphere the damping and stiffness coefficients can be solved. Work after Landwehr make mention of the study; however, no further consideration is given to study the effects or expand on the author's work.

Nickerson et al. (2005) perform oscillatory strain tests on vitreous samples from bovine and porcine eyes. Attempts are made to duplicate the procedure as in Tokita; however, wall slip was noted, so a cleated tool was developed that pierces the lubricated vitreous in order to measure the mechanical properties without wall slip. The study also measures the mass of each sample immediately and to a maximum of 150 minutes after dissection. Weeping of fluid from the samples is noted. Sample preparation involved excising the vitreous from the eye and slicing the central region

out to form a disk. This would have the effect of disrupting the collagen fiber network near the wall of the slice. Nickerson et al. report the initial and final complex moduli for both bovine and porcine with the bovine having higher values, which is consistent with previous measurements (Lee, Litt, & Buchsbaum, 1994). A plot (log G' versus time) is provided comparing the Nickerson et al. bovine and porcine storage modulus (G') with previous studies. The initial values of the storage modulus for bovine are in excess of 30 times any other study previously viscoelastic mechanical property determination study. An important observation is that the initial modulus is probably closer to the actual value in vivo. However, the plot shows the value of G' at the start to be approximately 17 Pa and decreasing to 5.5 Pa at time 90 minutes. The author does mention that this is a plot of typical time-dependent behavior, so this will be used in order to determine the time constants in the constitutive material model fits. Nickerson et al. say that the final steady state moduli represent a minimum value that is five times that of the in vivo moduli. Therefore, the steady state will be scaled (by five times) in order to achieve the proposed in vivo steady state value.

Although based on a guess, the Power (2001) vitreous will be considered in this study as well. Since the Nickerson et al. measured values are higher than any other viscoelastic study, the time constants will be considered the same for the Power (2001). It turns out that scaling the Nickerson et al. to the point where the short term modulus is the same as Power (2001) value involves a scaling factor of 1869 times. This is extremely stiff comparatively but should allow one to see the effects of the constitutive models considered in this study.

Methods

Before inclusion into the finite element eye model, the vitreous mechanical properties are converted to values that can be used in the MADYMO software. Vitreous properties are gathered from five separate studies for investigation. In particular, three of the studies are dynamic viscoelastic determination studies of the vitreous (Tokita, Fujiya, & Hikichi, 1984; Bettelheim and Wang, 1976; Nickerson et al., 2005). The fourth study is from Power (2001) using a conversion from linear elastic material. The last study by Weber and Landwehr (1982) considers the vitreous "rubber-elastic" and fits the behavior to a Voigt-Kelvin model and determines the spring and damping coefficients. These data are used to determine an equivalent elastic material model for finite element analysis. The material model naming convention will be as follows (Table 7.0):

Table 7.0: Material model labeling.

Material Label	Mechanical Behavior	Author(s)
Weber	Linear elastic with damping	Weber & Landwehr, 1982
Nick5	Viscoelastic material 5x in magnitude	Nickerson et al., 2005
Bet	Viscoelastic material	Bettelheim and Wang, 1976
Tok	Viscoelastic material	Tokita, Fujiya, & Hikichi, 1984
Power	Viscoelastic material conversion	Power, 2001

Vitreous Material Properties

The Weber values for human damping and stiffness are given as 7.35×10^{-4} Ns/m and 6×10^{-2} N/m, respectively for a steel ball inserted into the vitreous with radius 0.5 mm and density = 7850 kg/m^3 (Weber et al., 1982). A mathematical

model is created using the spring and damping attached to the mass representing the steel ball (mass is set to 1.0×10^{-4} kg). The natural frequency (ω_n) and the damping ratio (ζ) are $\sqrt{\frac{k}{m}} = 24.5$ rad/s and $c/\left(2\sqrt{mk}\right) = 0.15$, respectively. The displacement of the model is set to 2 mm at time zero and let go. The response of the position time history, $\delta = \ln\left(\frac{X_1}{X_2}\right)$, is used to match an equivalent solid beam element with a linear elastic modulus and damping for $\nu = 0.5$. The modulus and damping are then solved until the damping ratio and natural frequency are the same for the analytical and finite element model yielding the following: E = 43 Pa, damping = 200 Ns/m for $\nu = 0.5$.

The rest of the materials considered are viscoelastic and are modeled as a multi-mode Maxwell model (Figure 7.0), with the exception of the Power vitreous, which is scaled from the Nick5 fit. The storage modulus (G') versus frequency is used to curve fit to the following (Brands, 2002):

$$G' = G_\infty + \sum_{i=1}^{n} G_i \frac{\tau_i^2 \omega^2}{1 + \tau_i^2 \omega^2} \qquad (7.2)$$

Where *i* indicates the different modes (up to n = 4 modes total), τ is the relaxation time constant determined from curve fitting,[12] ω is the frequency, G_i is the short-term modulus for each mode, G_∞ is the long-term modulus.

[12] The curve fits, in this chapter, are done using the Levenberg-Marquardt method.

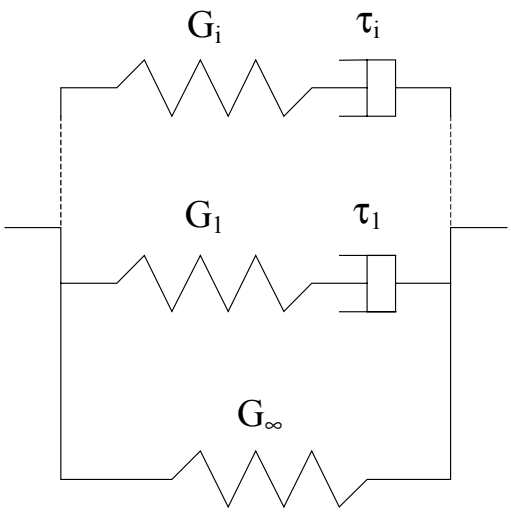

Figure 7.0: Viscoelastic schematic of the Maxell multi-mode material model used in MADYMO (2004).

The bulk modulus, $K = c_p^2\rho$ (speed of sound squared times the density of the material), is used in all the constitutive viscoelastic equations for the hydrostatic component. The speed of sound is determined to be 1506±3 m/s for the vitreous material (Thijssen, Mol, & Timmer, 1985) and the density is averaged between the aqueous and vitreous, as in Stitzel et al., and is 1006 kg/m^3 (Duck, 1990). In this case, as with Stitzel et al., the speed of sound (c_p) is considered the average between the vitreous and aqueous and is assigned the value 1503 m/s, which is the lower bound for the vitreous from Thijssen, Mol, and Timmer (1985).

Nickerson et al. averages the initial G' and G" of the bovine vitreous to be 30 ±12 Pa and 16 ± 7 Pa, respectively. The steady state values of G' and G" are reported to be 6.5 ± 2 Pa and 2.0 ± 0.6 Pa, respectively. Nickerson et al. plot a comparison of previous G' values with their own material study for the bovine and porcine vitreous. The bovine vitreous will be considered as it has higher reported moduli values. The data points from this plot are used to curve fit to a two-mode Maxell model (Figure

7.0) with R = 0.992. The data points are scaled by five so that the long-term modulus (G_∞) is approximately equal to the reported average of 30 Pa for G' in order to consider the in vivo steady-state values (Nickerson et al., 2005). The one and two modes are shown in Figure 7.1. The fit of the two-mode vitreous sufficiently fits the data points. All values are tabulated in Table 7.1.

Bettelheim and Wang (1976) determine the complex moduli (E' and E'') of bovine samples and tabulate the samples for four discrete frequency values (3.5, 11, 35, and 110 Hz). The values for the storage modulus (E') are converted to shear using $\nu = 0.5$ and plotted. A two-mode fit describes the four data points with R = 1.000 (Figure 7.2). The correlation factor does not indicate a true representation of the material; unfortunately, only the values at the four frequencies are given. Values are tabulated in Table 7.1.

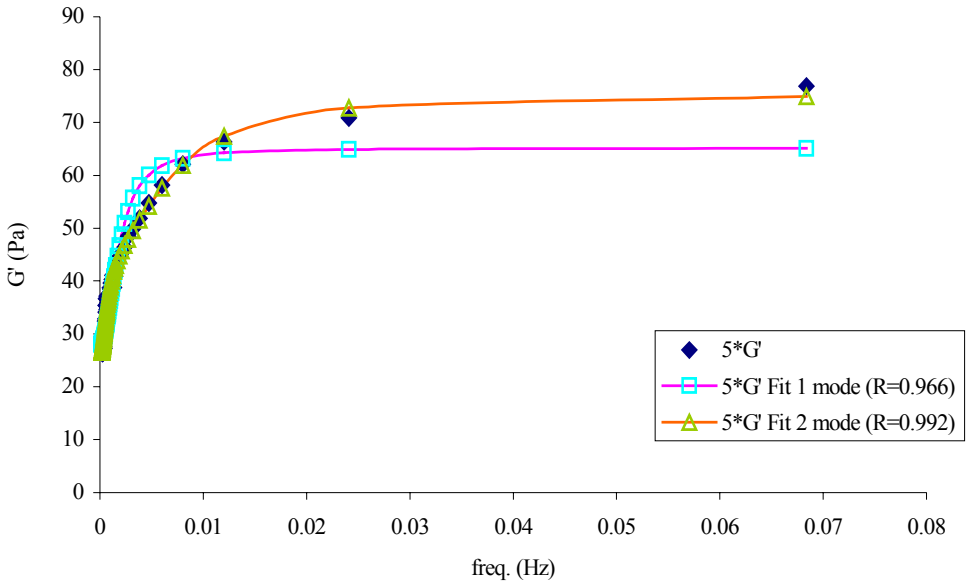

Figure 7.1: Nick5 material curve fit using a multi-mode Maxwell model.

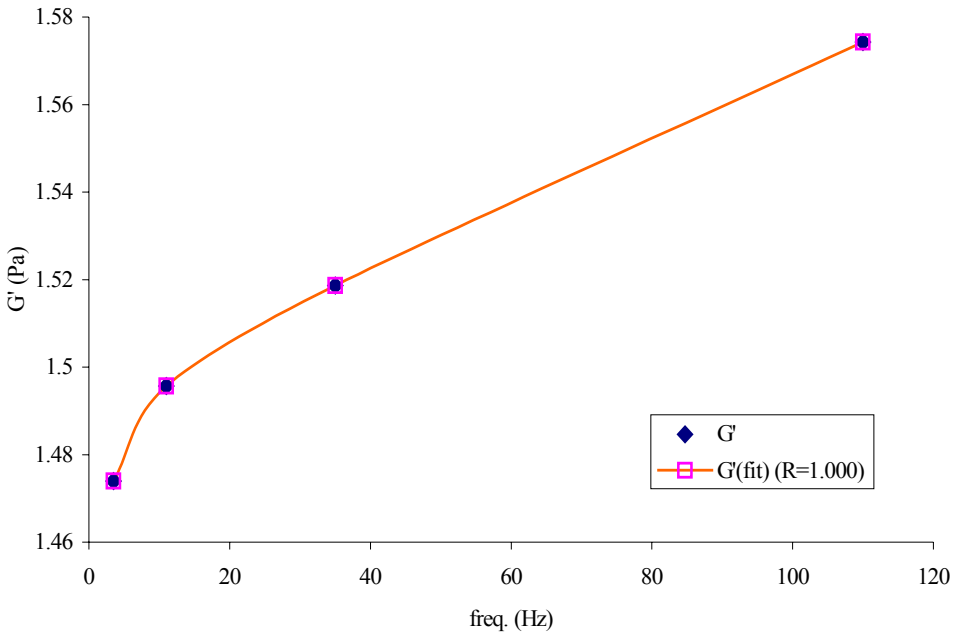

Figure 7.2: Bet material curve fit using a multi-mode Maxwell model.

The Tok material is based on curve fitting a log-log plot of the storage modulus versus frequency into (7.1) for a composite master relaxation plot for the bovine vitreous (Tokita, Fujiya, & Hikichi, 1984). The values for G' are then fit using the multi-mode Maxwell model up to four modes until the fit is good (R=0.999) (Figure 7.3). The values for the Tok material are the lowest of all the viscoelastic materials considered in this study. The material parameters are tabulated in Table 7.1.

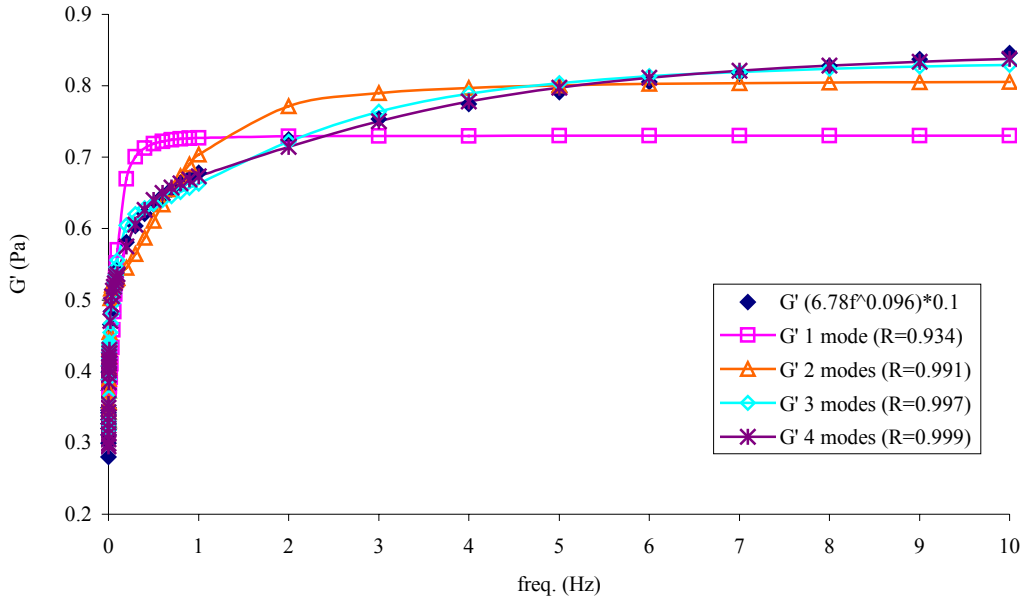

Figure 7.3: Tok material curve fit using a multi-mode Maxwell model.

The final vitreous material, Power, is based on the Power (2001) vitreous material converted to a shear modulus. The Power material is scaled from the Nick5 material by letting G_1 equal 14 kPa, which gives a scale factor equal to 1869. This material is considerably higher and is probably not representative of human infant vitreous; however, the inclusion of this material is important to illustrate the limitation of some of the constitutive material models that will be used. The material properties are tabulated in Table 7.1.

Table 7.1: Vitreous material properties for the multi-mode Maxwell model.

Material	Mode	Shear modulus G_i, i = ∞,1,2,3,4 [Pa]	Time constants τ_i, i = ∞,1,2,3,4 [sec]	Bulk modulus K [GPa]	R Fit
Nick5	1	27.65, 37.45	∞, 537.08	2.27	0.966
Nick5	2	25.48, 20.37, 29.34	∞, 1271.48, 138.79	2.27	0.992
Bet	2	1.46, 0.057, 0.139	∞, 0.025, 0.0012	2.27	1.000
Tok	1	0.375, 0.355	∞, 11.04	2.27	0.934
Tok	2	0.330,0.280, 0.197	∞, 1.31, 131.38	2.27	0.991
Tok	3	0.317, 0.210, 0.183, 0.129	∞, 0.44, 12.12, 372.11	2.27	0.997
Tok	4	0.293, 0.190, 0.147, 0.121, 0.106	∞, 0.30, 3.87, 59.34, 1162.46	2.27	0.999
Power	1	10335.34, 14000	∞, 537.08	2.27	-

Vitreous Constitutive Models

Aside from the linear elastic model used by the Weber material, three constitutive equations are considered for the viscoelastic material. The CPL material uses the MADYMO LINVIS material property, where the hydrostatic and deviatoric stress is coupled. The REF material is the MADYMO VISCO_NL material model, originally developed by Brands (2002), which decouples the hydrostatic from the deviatoric stress with the non-linear shear parameter (FNLS) set to zero. Both the CPL and REF materials are linear viscoelastic. The final consideration is the SOL material, which is the same as the REF material but with the added effects of the FNLS number. The SOL material allows for shear softening when the number is less than zero and hardening when the value is greater than zero (MADYMO, 2004). Further, use of this material model allows a correction parameter (f_3) for when FNLS < 0 that applies a small amount of stiffening to the material that has negligible effects on small strains but applies a stiffness to larger strains. This correction is good for

stabilizing the simulation but can also provide unrealistic results at high strains. Unfortunately, there are currently no experimental results available for the vitreous that can be used for the FNLS factor.

Brands (2002) uses stress relaxation experiments to investigate the non-linear strain behavior and is able to separate the strain and time dependent parts by observing that changes to the applied strain revealed parallel relaxation curves. The time dependent part is considered the damping function and is used to determine the FNLS factor. The closest study to the stress relaxation experiments is the work performed by Lee, Litt, and Buchsbaum (1992), where creep tests are conducted given a constant magnetic force. Using the methodology of Oza, Vanderby, and Lakes (2003), the creep test can be converted to shear relaxation curves. Unfortunately, the stress level (σ_0) for the creep test needs to be known for the interrelation and Lee (1992) only gives the following ratio:

$$J(t) = \frac{\varepsilon(t)}{\sigma_0} = \frac{6\pi R_{run} L(t)}{F_{mrun}} \qquad (7.3)$$

Where J(t) is the compliance, ε(t) is the strain, R_{run} is the radius of the inserted sphere, $F_{m\,run}$ is the magnetic force, L(t) is the displacement of the fluid. Further, only one force is given in Lee (1992) for the creep test, while Brands uses varying strain levels. However, for simplicity, the effects of the non-linear FNLS factor are investigated for the Nick5 material by varying the factor at levels 0.01, 0.1, 1.0, 5.0, and 10.0 (the sign is negative to indicate shear softening) and the f_3 parameter is defaulted to 0.2 (third order Mooney-Rivlin parameter).

Geometry

The model considers the eye globe with inner structures, the muscle tethers, tendons, optic nerve, fatty tissue, eyelid, and the encompassing orbital socket. Most information for the geometry is available for the adult eye. In order to consider the infant eye, the geometry of the adult eye is scaled down to 64.5% using the eye diameter from Hogan, Alvarado, and Weddell (1971) and the optic nerve sheath diameter from (Newman et al., 2002). The ocular shell dimensions are based on Woo et al. (1972) (Figure 7.4) and the lens and ciliary placement on Power (2001) (Figure 7.5).

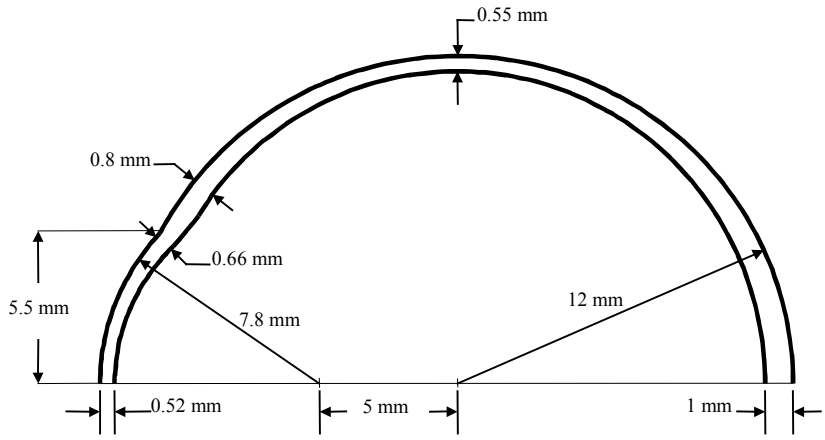

Figure 7.4: Geometry of the idealized cornea-sclero shell from Woo et al. (1972) for an adult eye.

The placement of the idealized geometry of the eye is positioned inside a built up model of the ocular cavity, muscles, optic nerve, and eyeball from the Visible Human Project transverse slice scans. The ocular cavity cone geometry is built from the Visible Human scans as is the apex muscle and optic nerve attachments, the oblique inferior, and superior attachments. The final position of the optic nerve and tendon

attachments to the eyeball are based on Hogan, Alvarado, and Weddell (1971) and differ from the Visible Human Model slightly. However, the attachment locations to the eyeball from Hogan et al. are an average of several eyes and are more appropriate to use. The fatty tissue/eye lid is considered to fill the entire ocular cavity. A void is inserted into the fatty tissue where the location of the eyeball is to be so that the eyeball is totally encased in the fatty tissue.

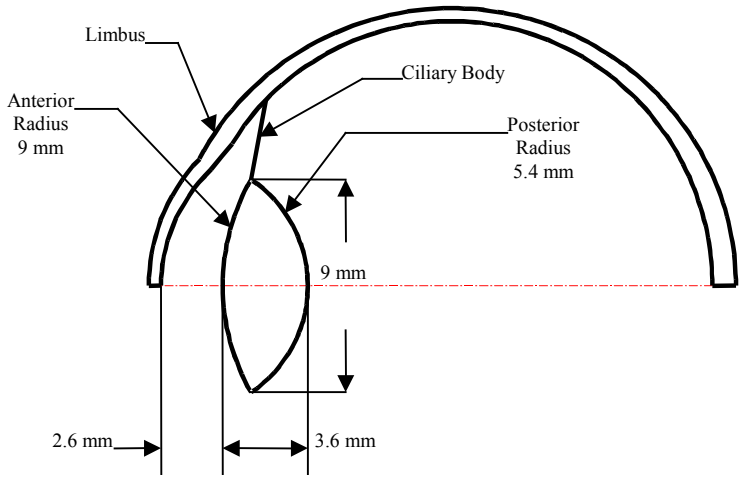

Figure 7.5: Location and dimensions of the lens and ciliary placement for an adult eye (Power, 2001).

Mesh/Model Creation

The eye model is meshed from the vitreous body outward to the ocular shell structures. The vitreous and aqueous are modeled using hexahedral elements with reduced integration to prevent mesh locking (Samani et al., 2001; Brands, 2002; Gopalakrishnan, 2002; Manzini and Putti, 2007). Two meshing methods are considered in this work: manual meshing and cubit meshing. The manual meshing

method depends on dividing the vitreous into a central cube with six sides (anterior interface to lens and ciliary, posterior side, inferior side, superior side, medial side, and lateral side). The cubit meshing utilizes the CUBIT software by dividing the volume into manageable volumes for meshing and provides a more uniform mesh. For both meshing techniques quarter symmetry is used for the build up before mirroring to build the full finite element eye model. The initial cube is meshed first and then sweeping techniques are used to extrude the solid mesh to the outer spherical surface of the eye.

The anterior section of the eye with the lens depression proved challenging but is meshed in the same extrusion manner. The mesh density of the ocular shell is around 1 mm^2 for each of the elements. In order to achieve this density, the vitreous cube had to have a much finer mesh density as the extrusion process takes elements from a smaller surface and extrudes them to a larger. The Cubit software uses the same overall ocular mesh density but is able to achieve a more uniform mesh density for the vitreous as well reducing the total element amount. The lens and ciliary body are modeled as shell elements and the aqueous is modeled using hexahedral elements. The aqueous mesh only involved extruding the posterior lens interface surface to the anterior eye globe surface (cornea region).

The sclera-corneal shell is first modeled as solid elements to capture the non-uniform thickness as shown in Figure 7.6. Each solid of the sclera-corneal layer is then converted to a shell element with the thickness information stored for each element. Power (2001) and Uchio et al. (1999) perform similar techniques by partitioning the ocular shell into bands of thickness.

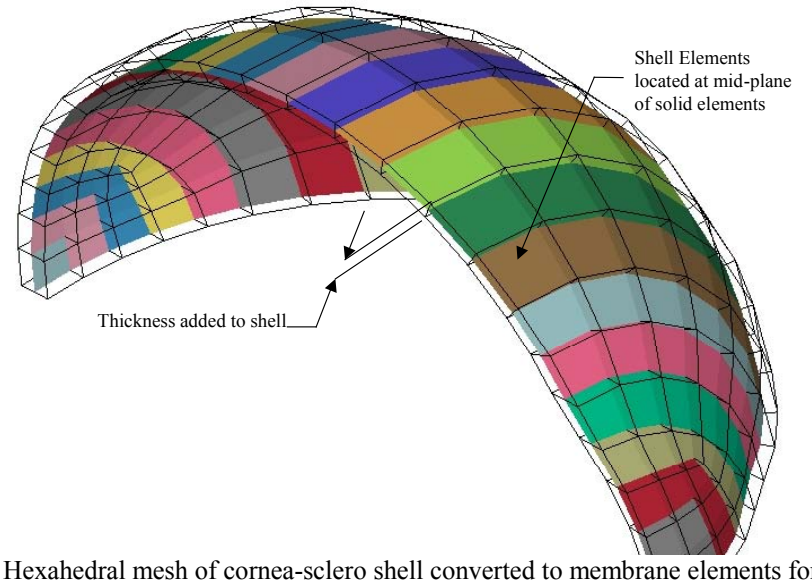

Figure 7.6: Hexahedral mesh of cornea-sclero shell converted to membrane elements for infant eye.

The shell meshing method presented here and done by Power and Uchio et al. is lacking in that there is a stepping from one element to another with the different thickness information. Stitzel et al. is able to overcome this by specifying the thickness at the nodes; this is not possible in the MADYMO software (only element thickness can be specified). Two intermediate layers are considered in the eye model to represent the choroid and retina membranes in the posterior region of the eye up to the ora serrata. All ocular shell layers are modeled using membrane elements with in plane stresses only.

The fatty tissue is meshed using the boundary of the ocular socket and larger eye globe geometry. The larger eye globe surface ensures that nodes and elements of the eye globe do not intersect or penetrate the fatty tissue elements. A contact gap will be specified between the eye globe and fatty tissue. The geometry of the fatty tissue is difficult to mesh using hexahedral elements as partitioning the volume into

sweepable sections presents a problem with the eye globe void. Meshing the volume using tetrahedral elements is simpler but not without complication. The meshing process is a two-step process. Typically, auto-meshing tetrahedral elements involves the selection of a closed volume; however, the eye globe void in the middle prevents this. Simply creating a connection between the eye globe surface mesh and the outer ocular cavity surface mesh allowed for the entire volume to be meshed- minus the connection boundary (the connection boundary is analogous to sprue in an injection molding process). Second, the connection boundary is meshed and common nodes are equivalenced to provide one monolithic volume mesh with the eye globe void (Figure 7.7). Finally, the skin layer on the anterior most section is modeled using membrane elements.

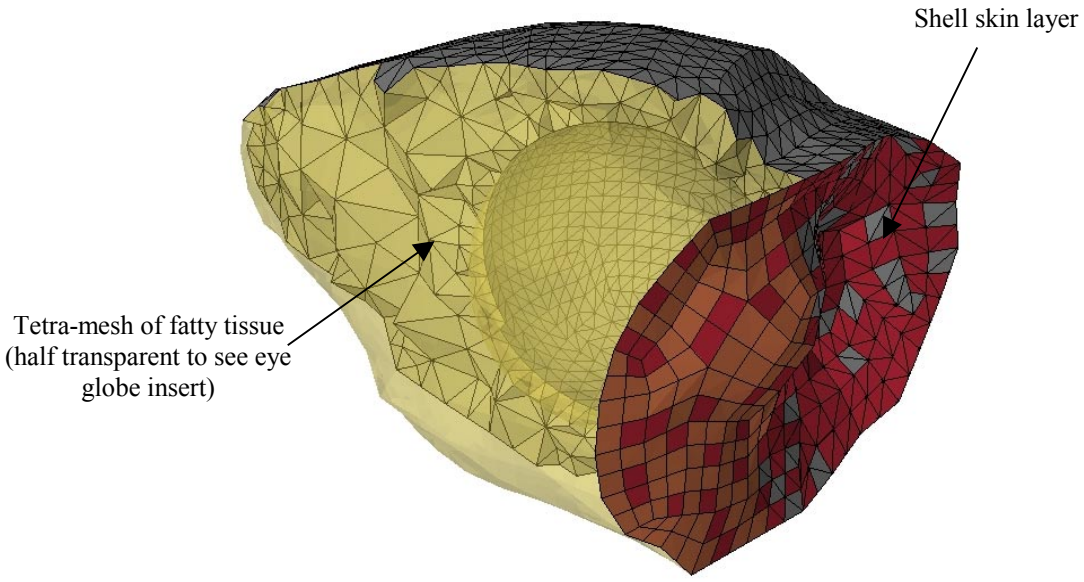

Figure 7.7: Fatty tissue tetra-mesh with membrane skin layer.

Two optic nerve models are considered in this study. The first uses analytical values (Collins, Scott, & O'Meara, 1969; Lehman & Stark, 1979; Robinson, 1981; Winters & Stark, 1985; Winters & Stark, 1988) in four beam elements attached in parallel to the posterior region of the eye globe at locations determined from Hogan, Alvarado, and Weddell (1971). The only geometrical requirements for the beam elements are the local coordinate system orientations (Figure 7.8) (cross sectional area is not used as these are simply analytical torsional, rotation, and translational spring elements).

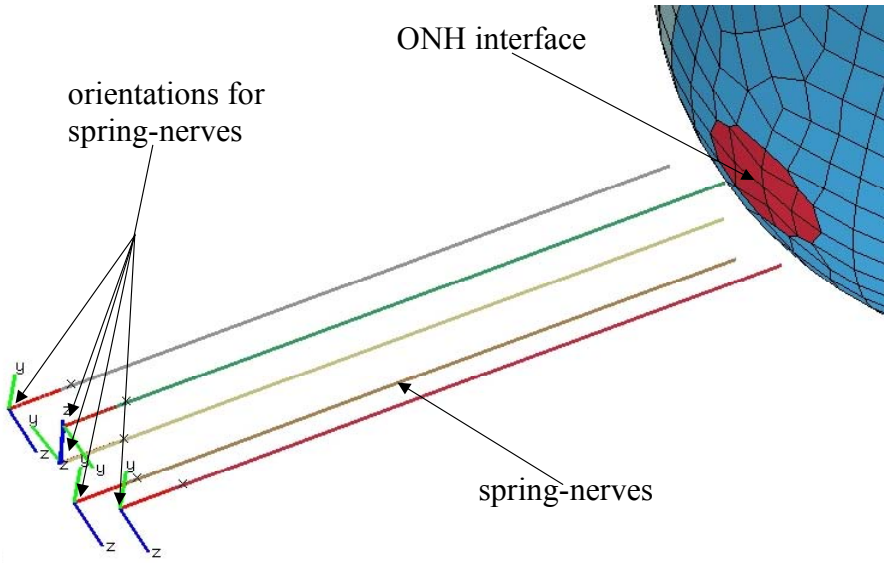

Figure 7.8: Layout of the spring-nerve and optic nerve head (ONH) interface for the infant eye model.

The posterior nerve attachments at the apex of the socket are fixed in all degrees while the anterior nerve utilizes a simple constraint equation to tie the optic nerve head to the nerve bundle.

The second optic nerve (Figure 7.9) is modeled by extruding the optic nerve head from the posterior back to the apex location. The nerve is broken into three sections to account for the optic nerve head (ONH), neural tissue, and pia mater as considered by Sigal et al. (2004). The ONH interface uses membrane elements with in plane stresses only. The pia layer also uses the membrane elements while the neural tissue is composed of solid elements. The support for the finite element optic nerve is attached to a rigid body in all degrees of freedom. The body has a translational joint along the axis of the optic nerve to allow for nerve slack and to give a similar response to the overall rotational position as the analytical optic nerve.

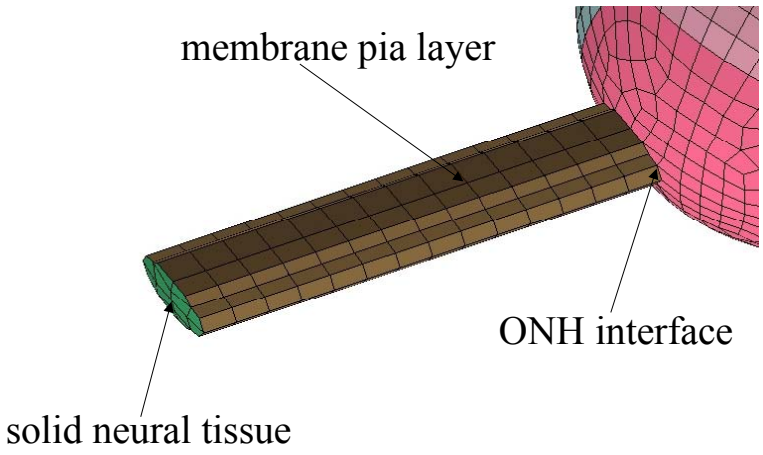

Figure 7.9: Layout of the finite element optic nerve and ONH interface for the infant eye model.

The muscles originally are based on the Visible Human transverse slices by fitting 2-D surfaces along the length of the muscle body. However, insufficient properties for the muscle exist to consider them as finite element structures. At most, only the passive behavior could be modeled. Therefore, a hybrid approach is considered by using a Hill-type muscle (Figure 7.10) that is fixed at one end and attached to a free body at the other (lumped mass). This mass body allows the tying of the finite element tendon (SE element) to the muscle and attached to the eye globe. The MADYMO software limits the Hill-type muscle attachments to rigid bodies only; therefore, node attachments are not possible.

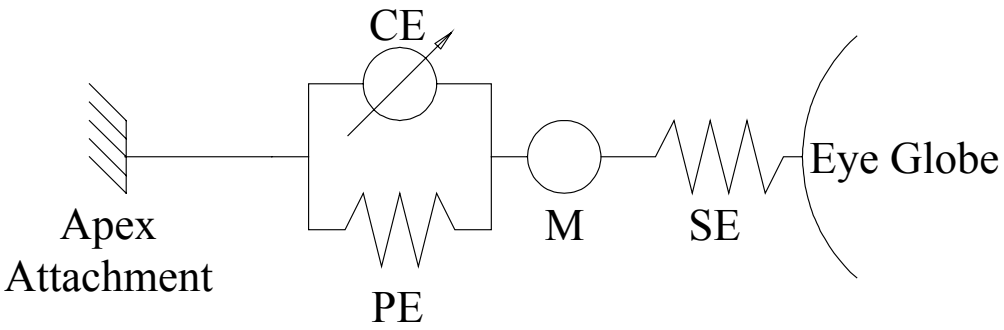

Figure 7.10: Hybrid analytical muscle-tendon model used in the infant eye saccade study.

Differences in Figure 7.10 are the oblique muscles. The inferior oblique muscle is attached at the base of the ocular socket and not the apex. The superior oblique is attached to the apex but also loops through the trochlea. The trochlea is modeled as a tying point or simple mathematical eyelet.

The tendon is modeled as three-node membrane elements with contact interactions with the scleral shell so that the tendon can wrap the eye as it undergoes a horizontal saccadic movement. The tendon elements are modeled as surfaces so that the attachment points to the sclera shell distribute the stresses versus a one-point connection with artificial force spikes. Consideration for the infant eye involves scaling the analytical properties of the rigid body muscle mass and the muscle tying location points and are presented in Table 7.2. The details of the muscle and tendon placement are represented in Figure 7.11.

Table 7.2: Dimensional information for the muscle and tendons in the infant eye simulation model.

Muscle Name	Muscle Length (mm)	Tendon Length (mm)	Tendon Width at globe attachment (mm)	Tendon Thickness (mm)
Oblique Superior	29.87	8.10	6.98	0.2
Oblique Inferior	9.42	3.87	6.78	0.3
Rectus Superior	17.13	8.06	6.15	0.2
Rectus Inferior	19.10	7.41	6.15	0.2
Rectus Medial	17.91	8.04	5.76	0.2
Rectus Lateral	18.84	8.20	6.18	0.2

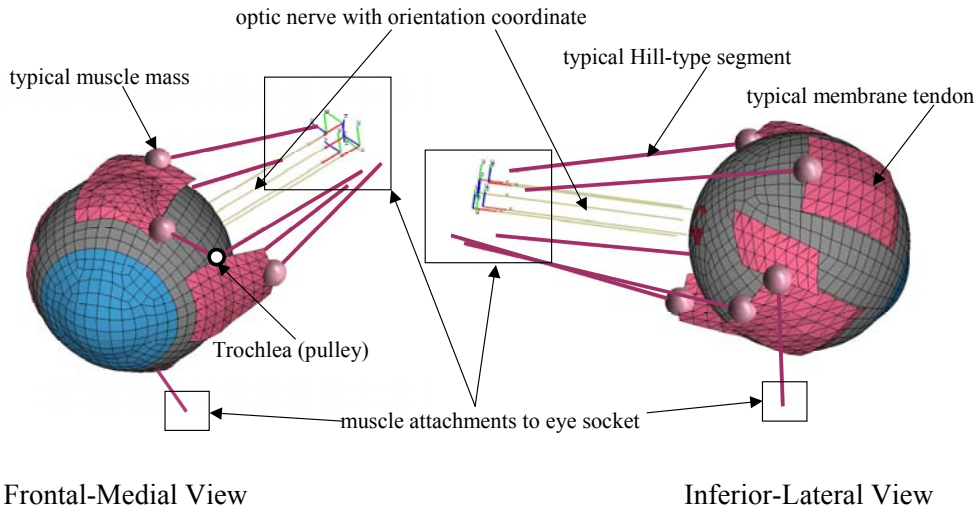

Figure 7.11: Muscle and tendon details for the infant eye model.

Contact Interactions

Contact interactions introduce complexity and computational time to the model efforts. However, some contacts are unavoidable and are needed to represent realistic behavior. Two major contacts are considered in the presented eye model, fatty tissue to scleral-cornea shell and the tendons to the sclera shell. The fatty tissue contact uses a contact gap (Figure 7.12) to minimize the overall geometrical gap. The algorithm uses a penalty method (MADYMO, 2004):

$$F_c = \left(\frac{K}{V_0}\right) A^2 \psi \left[\min\left(\lambda, MAX\_FORCE\_PAR \cdot t_e\right)\right] \qquad 7.4$$

Where MAX_FORCE_PAR, a tuning parameter, is equal to 1.0; F_c is the contact force; K is the bulk modulus of the contact segments penetrated; V_0 is the initial volume of the contact segment; A is the area of the contact segment; ψ is the penalty

factor (default value is 0.1 and is recommended not to change this value); λ is the penetration of the contact node; t_e is the penetrated element thickness that is multiplied by the MAX_FORCE_PAR. The penalty factor (ψ) for the tendons is reduced to 0.1 when contacting the sclera shell to reduce the contact force. This was necessary to reduce localized artificial nodal motions that resulted from the penetrating nodes of the tendons into the eye globe. A contact gap for the tendon-scleral shell is not used. The most important contact, the fatty tissue with the scleral-corneal shell, creates a spherical joint with the eye globe and provides motion that is comparable to the Winters (1985) horizontal motion studies. The tendon to sclera contact is of secondary importance and provides realistic behavior of the muscle without muscle penetration into the eye globe. The analytical muscle segments or beam-tendons are unable to contact the eye globe making the membrane tendons necessary.

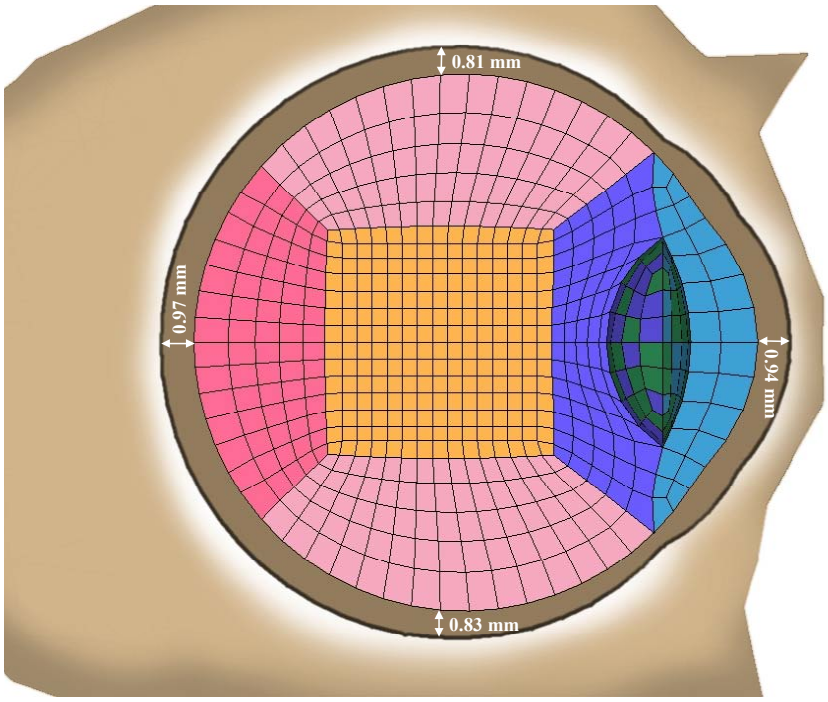

Figure 7.12: Sagittal view of eye model showing the geometrical gap dimensions between the fatty tissue and eye globe.

Material Properties

Unlike previous finite element eye models (Uchio et al., 1999; Power et al., 2002; Stitzel et al., 2002), large deformations are not considered in this study. Therefore, some of the non-linear materials of the ocular shells can be considered in the linear region. The cornea and sclera material are based on the work of Uchio et al. (1999) where the ocular shell can be considered a membrane (Woo et al., 1972). Power (2001) used the MADYMO software and modeled the cornea and sclera using a hysteresis material type definition allowing one to insert the non-linear stress-strain curves directly. However, in this case $\nu = 0.0$, and only three node membrane elements can be used. The Stitzel et al. model also uses the material properties of Uchio et al. using LS-DYNA and an orthotropic formulation. The current model

considers the cornea and sclera shells to be material linear elastic using the modulus from Uchio et al. up to the point before increases in strain result from decreases in stress. The modulus, as reported by Stitzel et al., is 124 MPa and 358 MPa for the cornea and sclera, respectively. To account for the compressive stiffness, a reduction factor is set for the tension only elastic material to $1/100^{th}$ of the stiffness in tension (Stitzel et al.) and to circumvent possible stability issues which could result from pure tension-only material (especially if contact interactions are used) (MADYMO, 2004). The mass density of the cornea and sclera is set to 1076 kg/m^3 (Duck, 1990) and 1243 kg/m^3 (Uchio et al., 1999), respectively. Stitzel et al. assumes incompressibility by setting $\nu = 0.49$ for both materials, while this study uses the values for the cornea and sclera directly from Uchio et al. (0.42 and 0.49 for cornea and sclera).

The choroid (Graebel & Van Alphen, 1977) and retina (Jones, Warner, & Stevens, 1992) are also considered to be membrane structures as well with linear-elastic, tension-only material characteristics. As reported, the elastic modulus for the retina and choroid are 20 kPa and 96.8 kPa, respectively. The density is set to 1000 kg/m^3 and $\nu = 0.49$ for incompressibility. The retina is a very thin, delicate, and clear tissue lining the inner eye and interfacing the vitreous body and choroid layer through the pigment epithelium (Hogan, 1963). The retina varies in thickness with the thickest portion near the optic disk measuring 0.56 mm thinning to 0.18 mm to the equator, and then to 0.1 mm at the ora serrata (Hogan, 1963). However, the retinal thickness is set to 0.14 mm for the current investigation (Wu, Peters, & Hammer, 1987). The choroid is a thin, highly vascular (with extensive nerve supply) membrane supplying nutrition to the retina and anterior portion of the eye. This

tissue exhibits some of the traits of erectile tissue (Hogan, 1971). The entire traits of the choroid are still unknown as all testing that has been done are postmortem and in vitro (uniaxial elongation testing). There is no question that the rich blood supply would affect the stiffness characteristic of the choroid. Friberg and Lace (1988) suspect that in vivo testing would reveal stiffer characteristics, especially in compression. In addition, Friberg did measure the choroid thickness (0.08 mm) but assumed the in vivo thickness to be 0.42 mm on account of the full blood vessels. Testing by Moses (1965) and Graebel and van Alphen (1977) assumed a thickness of 0.02 mm and 0.16 mm, respectively. In this study the thickness of Graebel and van Alphen is used (thickness is 0.16 mm).

The lens is made rigid as in the previous eye models (Uchio et al. 1999; Power, 2001) and has little influence during the saccadic motion where the posterior region is of interest. The ciliary body attaches the lens to the ocular shell and the modulus is set to 350 kPa (Fisher, 1986). The density and ν are from Power et al. and are 1600 kg/m^3 and 0.40, respectively. The anterior section of the eye is not modeled in detail as the focus of the study is with shear strain at the posterior scleral wall. The vitreous material considerations have been presented; however, the aqueous is also considered. In this case, the aqueous for all simulation is set to the same material as the *Weber* vitreous material, which has the added benefit of quicker computational times. The viscoelastic materials with the bulk (K) modulus around 10^9 Pa in magnitude increase the computational efforts tremendously.

The fatty tissue is modeled using an elastic modulus from (Todd & Thacker, 1994) and the same density and ν as Power et al., where E = 47 kPa, density is 999

kg/m^3 and ν is 0.49. The stiffness characteristic of the Todd and Thacker tissue is extremely stiff compared to other studies (Figure 7.13); however, to model the horizontal saccade, as in Winters (1985), limits on the fatty tissue deformation are desired. In this way, the combination of the eye globe and fatty tissue create a spherical joint without considering the fatty tissue so rigid that contact interactions could be problematic.

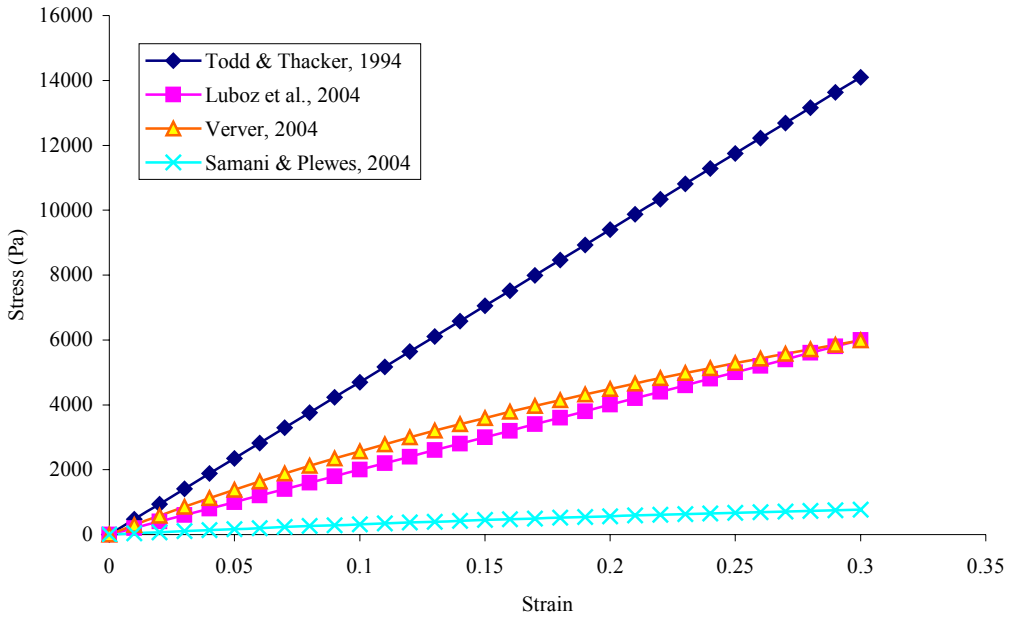

Figure 7.13: Comparison of fatty mechanical properties of different research groups illustrating the extreme stiffness characteristic of the Todd & Thacker soft tissue properties.

The material parameters for the finite element optic nerve (Sigal nerve) are based on the work of Sigal et al. (2004), which compiles mechanical properties from previous works and averages the values for the elastic moduli for all the structures

considered. The density information is not reported in Sigal et al. and is set to 1000 kg/m^3 and is within published values for spinal chord nerve tissue (1038 kg/m^3) (Duck, 1990). The pia mater thickness in Sigal et al. is set to 0.06 mm; however, for the infant eye model the thickness is increased to 0.535 mm so that the most outer sheath of the optic nerve is included (Hayreh, 1984) and is within values reported for the posterior sclera shell and is more representative of the dura layer. The ONH thickness is set to 0.6 mm. Poisson's ratio (ν) is assigned a value of 0.49 to model incompressibility and 20% material damping is assigned as biological structure exhibit some form of damping (MADYMO, 2006). Further, as will be described in the analytical optic nerve model, the optic nerve does have considerable damping (over-damped actually) (Lehman & Stark, 1983). The neural tissue modulus is assigned 0.03 MPa (Sigal et al., 2004) and the pia mater/dura layer is assigned a modulus of 3 MPa (Sigal et al., 2004). The ONH is given a modulus of 0.3 MPa (Sigal et al., 2004).

The considerations of the analytical optic nerve properties consider mathematical models in previous works for horizontal eye motion (Collins, Scott, & O'Meara, 1969; Lehman & Stark, 1979; Lehman & Stark, 1979; Robinson, 1981; Winters & Stark, 1985; Winters & Stark, 1988). These analytical models consider the eye as the "plant" which acts as a revolute joint in horizontal motion. The eye system "plant" parameters can be modeled as the following (Lehman & Stark, 1983):

$$I\ddot{\theta} + c\dot{\theta} + K\theta = N \qquad (7.5)$$

Where I, c, and, K are the plant parameters $3x10^{-7}$ $kg\text{-}m^2$, $1x10^{-4}$ Nms, and $1x10^{-3}$ Nm (Winters & Stark, 1985), respectively. Scaling these parameters to an infant is trivial

and involves matching the natural frequency and damping ratios to the adult system such that I, c, and, K are equal to $3x10^{-8}$ kg-m2, $1x10^{-5}$ Nms, and, $1x10^{-4}$ Nm, respectively. Conversion to translational values is desired and achieved by using the infant eye radius with length 7.1 mm. These values are then used in non-linear 3-dimensional Kelvin element material (spring-damper type material), which are composed of the axial, bending, and shear values (Figure 7.14). The non-linear Kelvin material is necessary as can be seen in the first two plots of the axial stiffness where compressive values are set to zero (specifying linear in MADYMO only allows insertion of a single stiffness number).

The Hill-type muscle consists of a passive (PE), contractile (CE), and series (SE) component (Figure 7.10). In addition, the mass can be modeled as a lumped parameter. The total muscle force is the summation of the contractile and passive force contributions:

$$F_{muscle} = F_{CE} + F_{PE} \qquad (7.6)$$

The passive force is considered when the muscle is stretched beyond the reference length and the active muscle behavior is given by (MADYMO, 2004):

$$F_{CE} = AF_{max}f_H(v_r)f_L(l_r) \qquad (7.7)$$

Where A is the activation and varies between 0 (rest state) and 1 (maximum activation); $f_H(v_r)$ defines the normalized active force-velocity relationship (Hill curve); $f_L(l_r)$ is the normalized active force-length relationship. The necessary parameters that define the behavior of the muscles are presented in Table 7.3. Also presented is the series element (SE), which is then converted into values suitable for the membrane tendon with material type hysteresis so that the stress-strain curve can

be directly inserted. The density of the tendons is set to 1165 kg/m^3, which is the average value for ox tendon (Duck, 1990). The parameters are a function of muscle fiber composition (Winters & Stark, 1985) and are assumed to be the same for infant muscles.

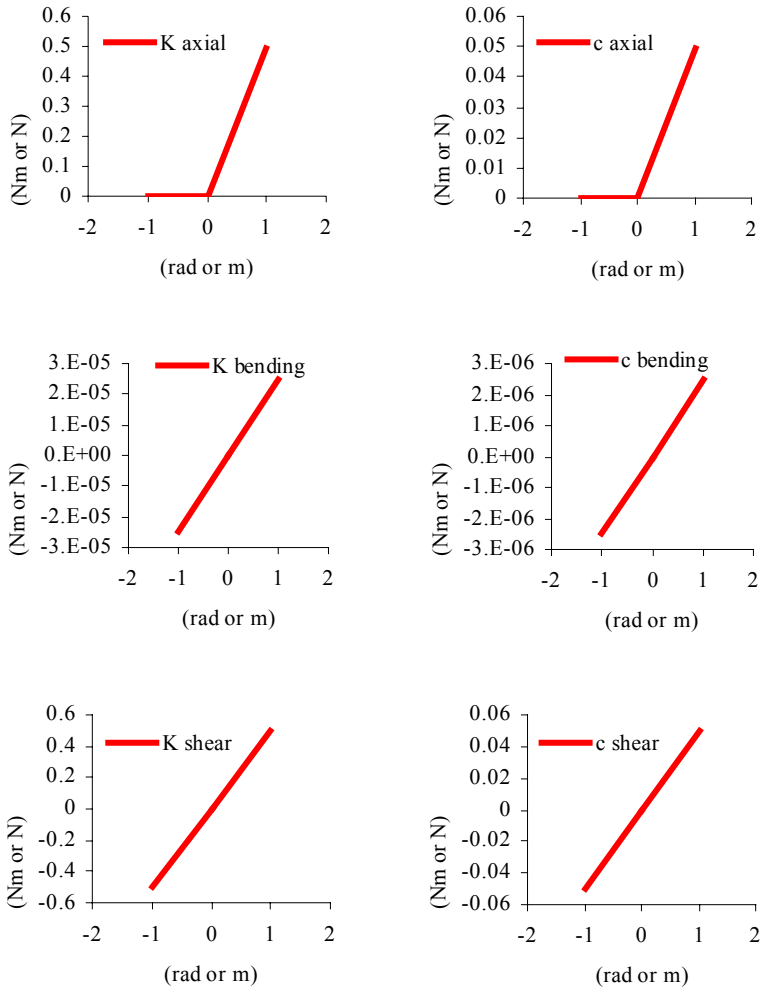

Figure 7.14: Spring-Nerve stiffness characteristic functions for axial, bending and torsional resistance for the infant optic nerve.

Table 7.3: Hill-type parameters for the CE, PE, and SE elements. Parameters are based on the work of Winters & Stark (1985 & 1988) and Winters (1985).

Hill-type parameter	Element type	Symbol	Value
Maximum muscle force	CE	F_{max}	0.909
Maximum shortening velocity	CE	V_{max}	0.495
Shape force-velocity shortening	CE	CE_{sh}	0.437
Shape force-velocity lengthening	CE	CE_{shl}	0.0797
Ultimate tension during lengthening	CE	CE_{ml}	1.381
Width of active force-length curve	CE	S_k	0.35
Relative elongation	PE	PE_{xm}	0.258
Shape force-length curve	PE	PE_{sh}	3.321
Shape force-length	SE	SE_{sh}	1.64
Relative elongation	SE	SE_{xm}	0.091

The activation dynamics are considered by solving two differential equations for neural excitation and general activation. The neural excitation is described by (Van Der Horst, 2002):

$$\frac{dE}{dt} = \frac{u - E}{T_e} \quad 0 \le E \le 1 \qquad (7.8)$$

Where E is the normalized neural excitation, t is the time, T_e is the excitation time constant, and u is the normalized neural input ($0 \le u \le 1$). The active state dynamics are represented by (Van Der Horst, 2002):

$$\frac{dA}{dt} = \frac{E - A}{T_a} \quad 0 \le A \le 1 \text{ and } T_a = \begin{cases} T_{ac} & E > A \\ T_{da} & E \le A \end{cases} \qquad (7.9)$$

Where A is the normalized active state, T_{ac} is the activation time constant, T_{da} is the deactivation time constant. Finally, t_{act} is the delay time that is incorporated into the u(t) function. The time constants are determined by the mass and the fraction of slow fibers in the muscle (Winters & Stark, 1988). For the eye, the time constants and model delay are presented in Table 7.4. The delay time, t_{act}, is extremely small for the eye as opposed to the neck muscles (t_{act} = 74 ms) (Van Der Horst, 2002).

Table 7.4: Activation time constants for the eye motion (Winters, 1985).

	Activation T_{ac} (ms)	Deactivation T_{da} (ms)	Activation Delay t_{act} (ms)	Neural Excitation T_e (ms)
Eye motion	5	30	2	30

The muscle activation is important to consider, as the muscle never stays in a full activation state for long without fatigue setting in. In order to include the activation state into the model, the signal function is used in the control system model in the SBS eye model. This is a straightforward way to model the eye dynamics without the need for complex PID controllers and is also used by Winters (1985). Essentially, a unit step function, u(t), with the activation delay included, is input into the system. Then, using the times constants (Table 7.4), the neural (7.8) and activation (7.9) response is determined.[13] In order to model the eye rotation similar to Winters (1985) saccadic motion for the adult eye, the neuro-input, u(t) is scaled until the response of the infant eye matches the adult eye dynamics. The final activation is then inserted into the infant model (Figure 7.15) so that the agonist response is assigned for the rectus medial muscle and the antagonist response is assigned for the rectus lateral muscle. The activation value for all other muscles is set to 0.005 to represent the minimal active rest-state (Hatze, 1977).

The rotational response is compared between the finite element optic nerve (Sigal nerve) and the analytical spring-nerve model (Figure 7.16). The saccade, for the eye, starts at rest position, zero degrees, and then rotates to the left by 20 degrees within 45 ms and held constant for the rest of the simulation time up to 200 ms.

[13] Using a fourth-order Runge Kutta method for solving (7.8) and (7.9) given u(t) and $T_a(t)$ (RK, 2005).

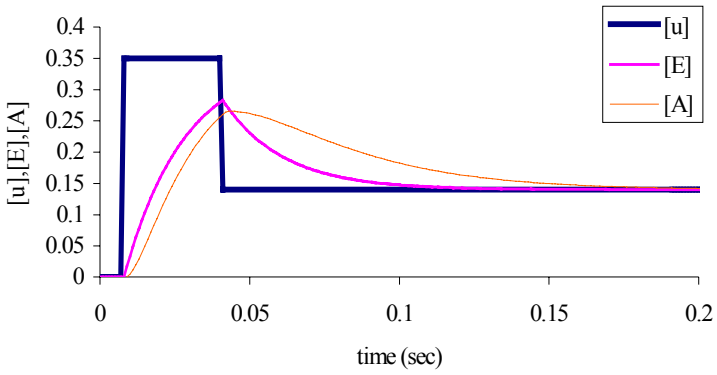

Figure 7.15: Infant eye time signals of the neuro-input u(t), neural excitation E and activation state A for the 20 degree saccade movement.

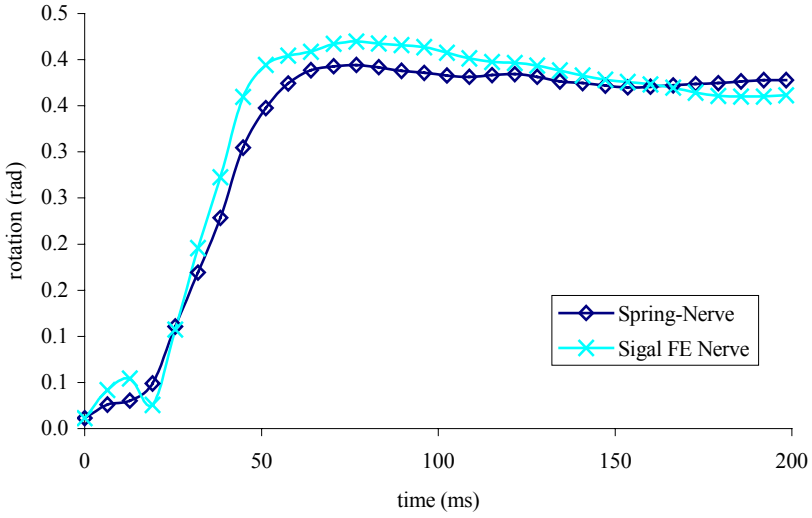

Figure 7.16: Comparison of the finite element eye models with an induced 20° saccade.

Simulation Matrix

Very little work has been done to include vitreous materials that are not based on the bulk modulus alone in dynamic eye simulations. An exception to this is the study by David et al. (1998) where the fluid motion of the vitreous humor is modeled

during a saccade. The optic nerve has been considered from different studies (Sigal et al., 2004; Winters, 1985) to investigate the effects on shear strain. Also, the meshing density is investigated (Brands, 2002). Also considered are the various constitutive models (REF, CPL, and SOL) for the viscoelastic materials, as well as the elastic vitreous material.

Two primary eye models are considered (Cubit meshing and manual meshing). The Cubit and the manual meshed eye are detailed in Table 7.5. The optic nerve material properties and element information is tabulated in Table 7.6 for both the analytical and Sigal nerve. The same nerves are used for both the Cubit meshed eye and the manual meshed eye and have the same element density. Both these meshes are utilized in comparing the vitreous materials for the REF constitutive equation for all the vitreous materials, except the Weber material, which uses an elastic modulus with damping coefficient. This REF material will decouple the deviatoric stress from the hydrostatic and provide the most extreme shear strains. The Cubit mesh is used to study the shear strains of the CPL constitutive equations. The CPL material couples the deviatoric stress with the hydrostatic, and will illustrate the effects of very low shear moduli with a very high bulk modulus. To study the effects on non-linearity, the SOF material will be used, which is based on REF but with the FNLS (non-linear factor) incremented.

Table 7.5: Material properties and element number for the Cubit and manual meshed eye model.

Ocular Component	Element Type	Element No# Cubit Mesh	Element No# Manual Mesh	Element Property	Material Type	Material Parameters	Thickness (mm)	Density (kg/m^3)
Cornea	4-node shell	84	60	MEM4 reduced integration	ISOLIN Tension only	E= 124 MPa / ν = 0.42 / Reduction factor = 0.01	Figure 7.4 (varies)	1076
Sclera	4-node shell	420	872	MEM4 reduced integration	ISOLIN Tension only	E = 358 MPa / ν = 0.49 / reduction factor = 0.01	Figure 7.4 (varies)	1243
Vitreous	8-node hexahedral	1620	7300	SOLID8 reduced integration	ISOLIN / REF / CPL / SOF	Weber or Table 7.1	-	1006
Aqueous	8-node hexahedral	108	304	SOLID8 reduced integration	ISOLIN	Weber mat'l: E = 43 Pa / ν = 0.49 / damping = 200	-	1006
Ciliary Body	4-node shell	48	112	MEM4 reduced integration	ISOLIN Tension only	E = 0.35 MPa / ν = 0.40	0.2	1600
Lens	4-node shell	120	120	SHELL4	RIGID	-	-	-
Retina	4-node shell	372	772	MEM4 reduced integration	ISOLIN	E = 20 kPa / ν = 0.49	0.14	1000
Choroid	4-node shell	372	772	MEM4 reduced integration	ISOLIN	E = 96.8 kPa / ν = 0.49	0.16	1000
Tendons	3-node shell	36-48	48-96	MEM3 Reduced integration	HYSIS O Tension only	Table 7.3 SE element properties Reduction factor = 0.1	0.2	1041
Fatty Tissue	4-node tetrahedral	16552	16552	SOLID4	ISOLIN	E = 47 kPa / ν = 0.49	-	999
Skin	4-node shell	272	272	MEM4	ISOLIN	E = 0.15 MPa / ν = 0.46 / damping = 0.05	1	1000

Unfortunately, the non-linearity has not been investigated for the vitreous and is only considered for the Nick5 material. The non-linearity is defined as not imposing a constitutive equation on the behavior (Brands, 2002). This factor is determined from stress relaxation tests. Finally, the Weber and Nick5 vitreous materials are used to compare the effects of both the Sigal nerve and analytical nerve with the Cubit and manual meshed eye. The Weber material uses the elastic modulus and the Nick5 material uses the REF material for this comparison. All simulations

(Table 7.7) are run using the saccadic motion (Figure 7.16) and the equatorial shear strain at the posterior pole of the eye is examined.

Table 7.6: Material properties and element number for the Sigal and analytical spring optic nerves.

Ocular Component	Element Type	Element no# for Sigal nerve	Element no# for spring nerve	Element Property	Material Type	Material Parameters	Thickness	Density
ONH	4-node shell	12	12	MEM4 reduced integration	ISOLIN	$E=3x10^5$/ $\nu = 0.49$	$6x10^{-4}$	1000
Neural Tissue	8-node solid	168	0	SOLID8 reduced integration	ISOLIN	$E=3x10^4$/ $\nu = 0.49$/ damp =0.2	-	1000
Pia Mater	4-node shell	224	0	MEM4 reduced integration	ISOLIN	$E=3x10^6$/ $\nu = 0.49$/ damp=0.2/ reduction factor=0.01	$5.35x10^{-4}$	1000
Spring Nerve	2-node beam	0	4	BEAM2 DISCRETE	KELVIN 3D_NL	Figure 7.14	-	-

Table 7.7: Simulation matrix of all the vitreous materials. C = cubit mesh, M = manual mesh, SP = spring nerve, and S = Sigal nerve

Vitreous Material	Constitutive Model	Model Type			
		C & SP	M & SP	C & S	M & S
Weber	Elastic	X	X	X	X
Nick5	REF	X	X	X	X
Nick5	CPL		X		
Nick5	SOL (FNLS=0.01)		X		
Nick5	SOL (FNLS=0.1)		X		
Nick5	SOL (FNLS=1.0)		X		
Nick5	SOL (FNLS=5.0)		X		
Nick5	SOL (FNLS=10.0)		X		
Bet	REF	X	X		
Bet	CPL		X		
Tok	REF	X	X		
Tok	CPL		X		
Power	REF	X	X		
Power	CPL		X		

Results

A comparison is made between the various runs from the simulation matrix (Table 7.7). Specifically, the shear strain is calculated, assuming planar strain, by taking the outermost vitreous element at the posterior pole and in the equatorial plane of symmetry of the eye (Figure 7.17). A similar method is employed by Brands (2002) for testing the wall shear in silicon filled cups during loading. The shear strain is then:

$$\gamma(t) = \tan\left[a\cos\left(\frac{R^2 + W^2 - M^2}{2RW} \right) \right] \qquad (7.10)$$

Where $\gamma(t)$ is the shear strain, R is the eye radius, M is the distance from the eye center to the node point, W is the distance from the node point to a node located at the posterior wall pole.

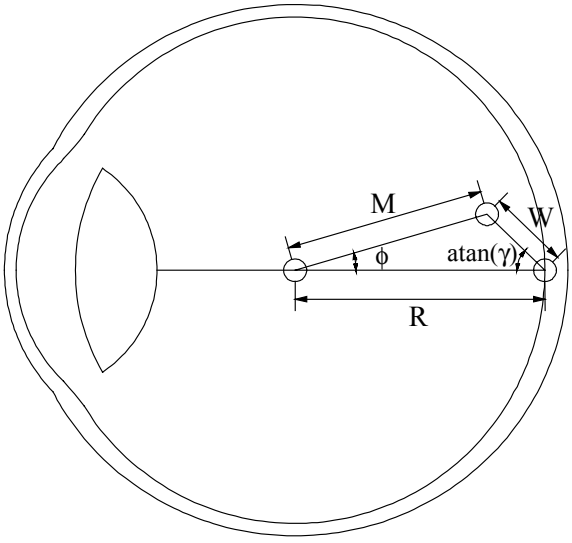

Figure 7.17: Graphical description of strain determination of the vitreous.

If one considers simple shear then the maximum principal strain is (Brands, 2002):

$$\lambda(t) = \left[1 + \frac{\gamma(t)^2}{2} + \gamma(t)\sqrt{1 + \frac{\gamma(t)^2}{4}} \right]^{\frac{1}{2}} - 1 \qquad (7.11)$$

Equation 7.11 is considered for comparison in strain time history of the vitreous material. In addition to strain time history plot comparisons, each simulation is represented by an animation sequence (Figures A.1 to A.23) of at most six views showing a transverse slice at the equator of the eye globe exposing the vitreous mesh details. The typical time increment of 20, 40, 60, 80, 120, and 180 ms is shown for all runs except for the vitreous material using the Bet vitreous material with the REF constitutive model (Figure A.8) and the Tok vitreous material with the REF constitutive model (Figure A.9). Both of these simulation models, utilizing the manual mesh (Table 7.5), become unstable due to high shearing strains that cause the elements along the wall to have negative volume errors.

Comparing the five vitreous models of the manual meshed eye with the REF constitutive equations for the viscoelastic materials (Figure 7.18) show the Tok and Bet simulations terminating at 50 ms due to instability. The shear strains approach 80% for these compliant materials. The Nick5 material reaches a strain level of 30% around the 50 ms mark, while the Weber and power vitreous models are well below 3% strain (Figure 7.19). Brands (2002) investigated the effects of mesh density and showed an increase of angular displacements with increased mesh refinement. The manual meshed vitreous is 4 ½ times the number of elements than the Cubit meshed

vitreous due to the methods of meshing as explained. As a result the Cubit mesh shows lower strain values than the manual meshed vitreous (Figure 7.20).

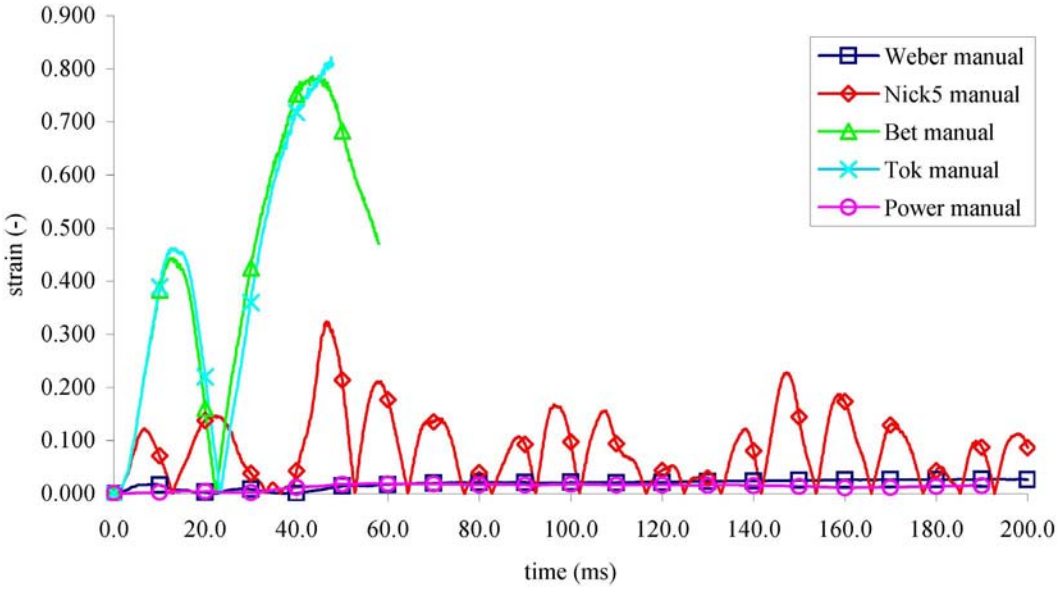

Figure 7.18: Shear strain comparison of eye models with the manual meshed eye. Material models are REF for the viscoelastic materials and elastic for the Weber model.

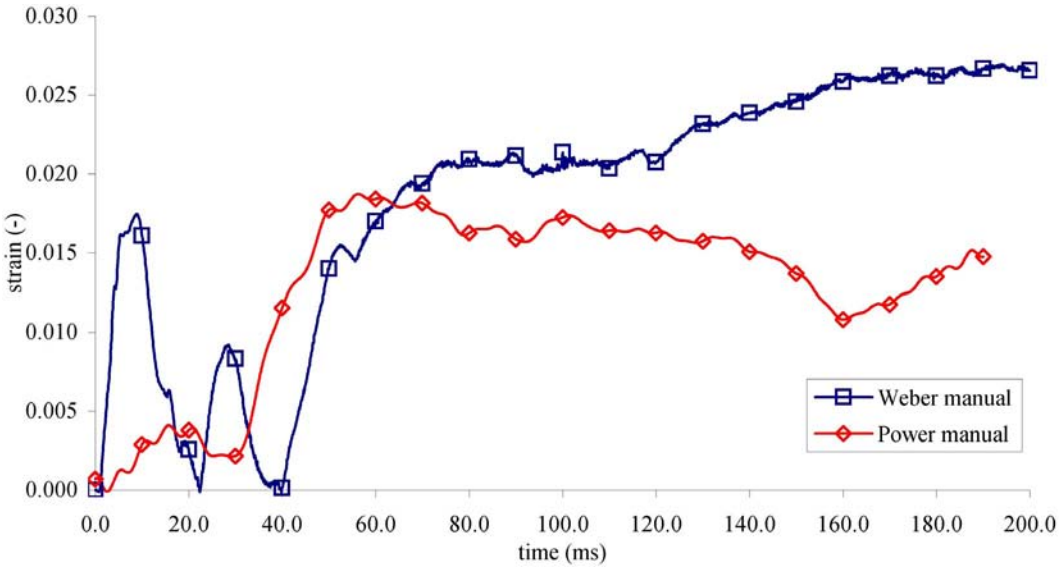

Figure 7.19: Shear strain comparison of eye models with manual meshed eye showing the Weber (elastic) and the Power (REF).

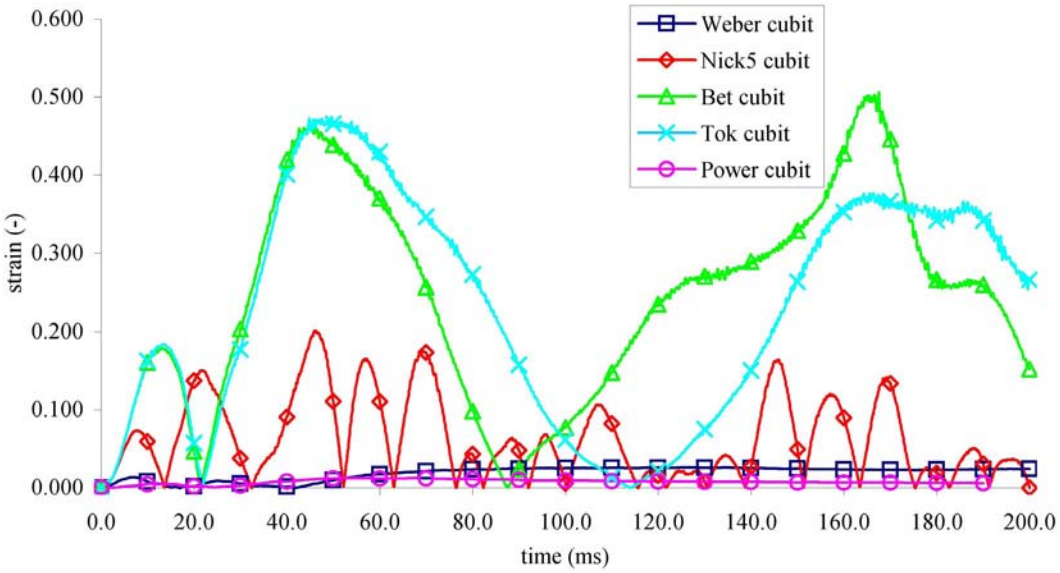

Figure 7.20: Shear strain comparison of eye models with the Cubit meshed eye. Material models are REF for the viscoelastic materials and elastic for the Weber model.

Isolating the vitreous materials to one per plot while highlighting the difference between the two meshing methods, Figures 7.21 to 7.25 show the time histories of the shear strain. Notable are the Tok and Bet material models where the manual meshed models become unstable around 50 ms, the Cubit mesh (courser mesh) has the effect of stiffening the elements and results in lower shear strain allowing the simulation to complete. However, Figures A.3 and A.4 highlight element distortions at 180 ms for the Tok material model. This is perhaps an area where the reduced integration causes some of the hourglass modes despite specifying an hourglass parameter of 0.5, which is at the highest range specified in the reference manual in the MADYMO 6.2 software. This hourglass parameter of 0.5 is used for all simulations, and the software default is 0.1. Using the material type VISCO_NL for the REF and SOL requires reduced integration with the hourglass parameter. The LINVIS material that is used for the CPL material can use the full integration method for the elements but results in mesh locking and is not used.

The shear strain in Figure 7.21 for the Weber vitreous shows minimal difference between the Cubit and manual mesh. Interestingly, the Cubit mesh has a higher strain between times 50-150 milliseconds. The rest of the vitreous models show a pronounced increase in shear strain for a more refined mesh. The Nick5 vitreous (Figure 7.22) at around 50 ms has a shear strain of about 20% for the Cubit mesh versus 32.5% for the manual; an increase of 12.5%. Brands (2002) notes an increase of 10.8% for refinements of the cup simulation meshes. The Bet material (Figure 7.23) has a reduction to 45% shear strain for the Cubit mesh versus the 80% for the manual mesh for an increase of 35%. The trend in the Tok manual mesh

(Figure 7.24) appears to want to increase past 80% shear strain, but the simulation becomes unstable at this point. Reducing the mesh density, the Cubit mesh as a shear strain around 45%, similar to the Bet material. The Power material also shows an increase in strain with an increase in mesh density (Figure 7.25). The shear strain at 50 ms decreases to about 1.25% for the Cubit mesh. The Power vitreous is so stiff that filtering using a low pass filter was necessary, which is compounded with little damping in this material model.

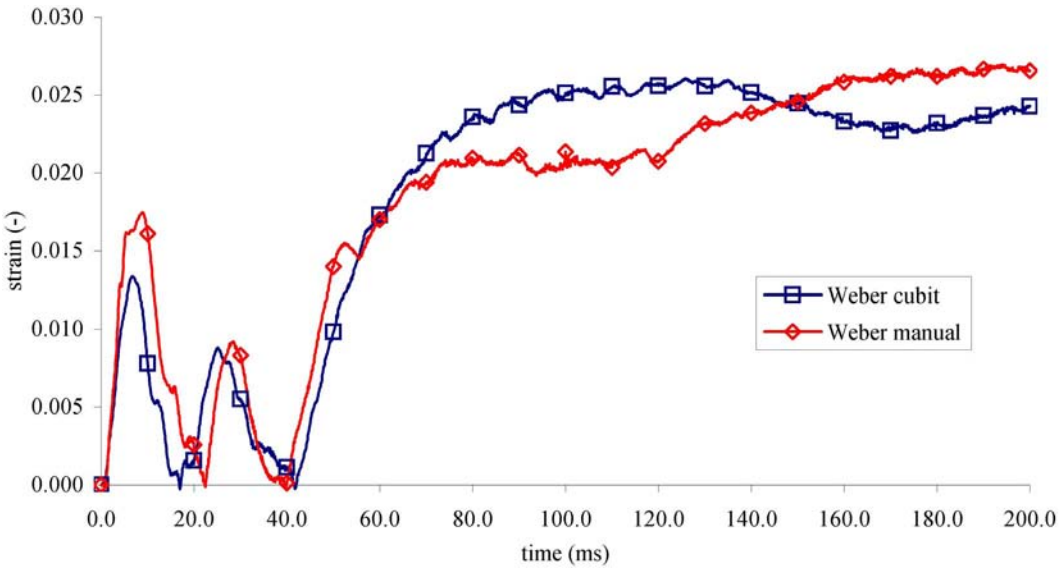

Figure 7.21: Comparison of the Cubit and manual eye meshed models for the Weber vitreous.

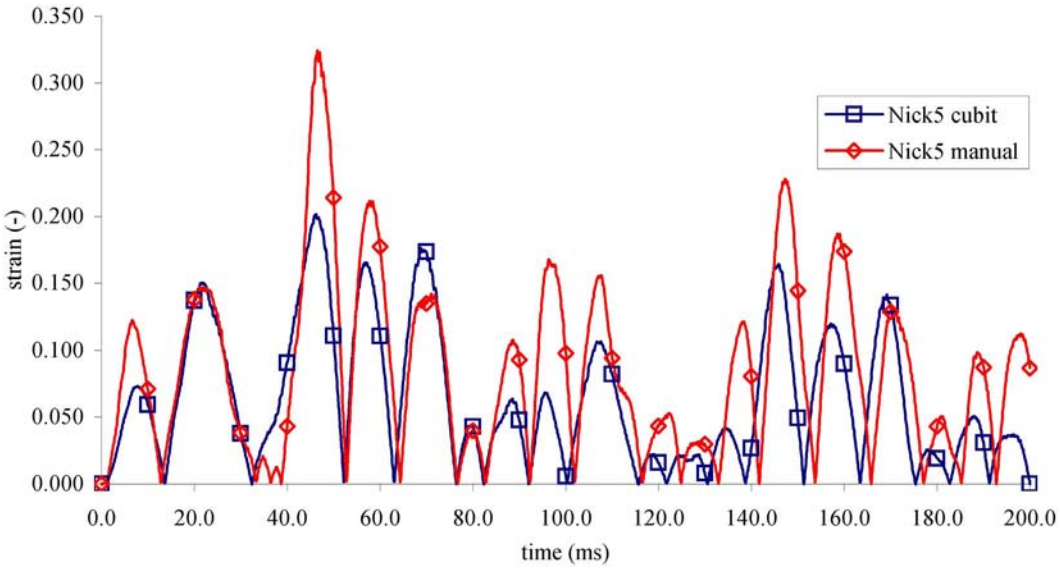

Figure 7.22: Comparison of the Cubit and manual eye meshed models for the Nick5 vitreous.

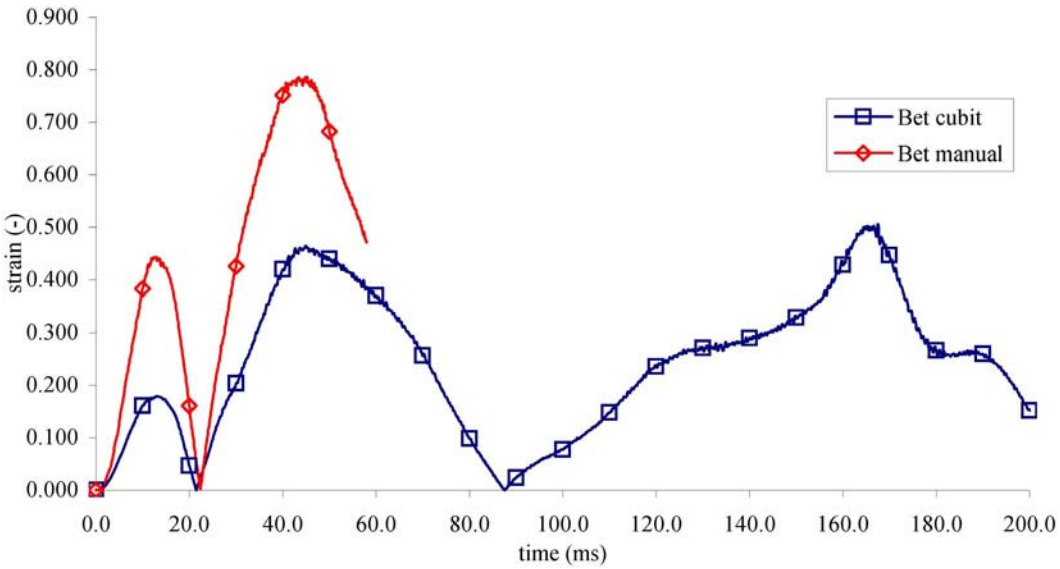

Figure 7.23: Comparison of the Cubit and manual eye meshed models for the Bet vitreous.

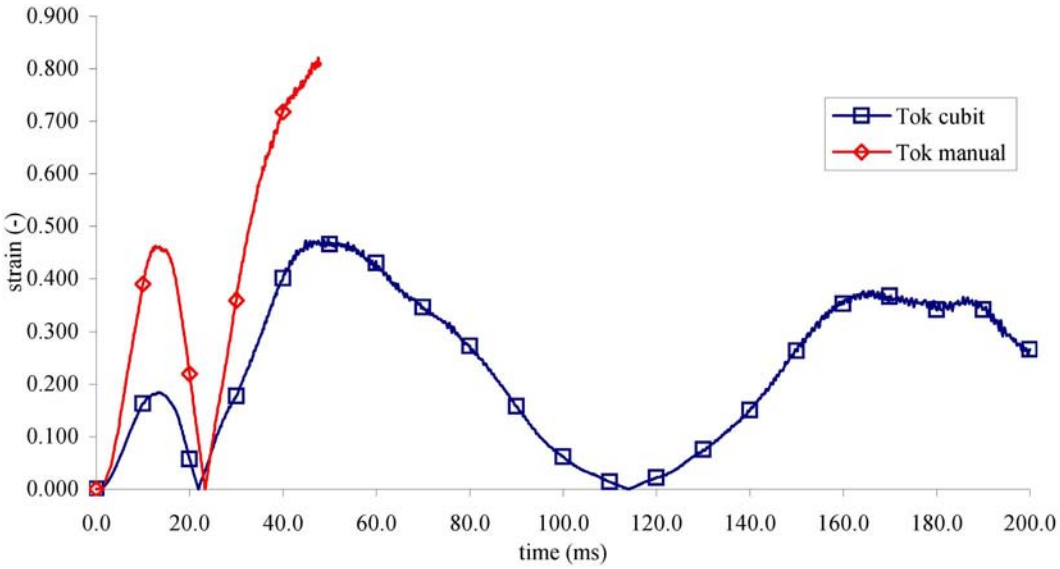

Figure 7.24: Comparison of the Cubit and manual eye meshed models for the Tok vitreous.

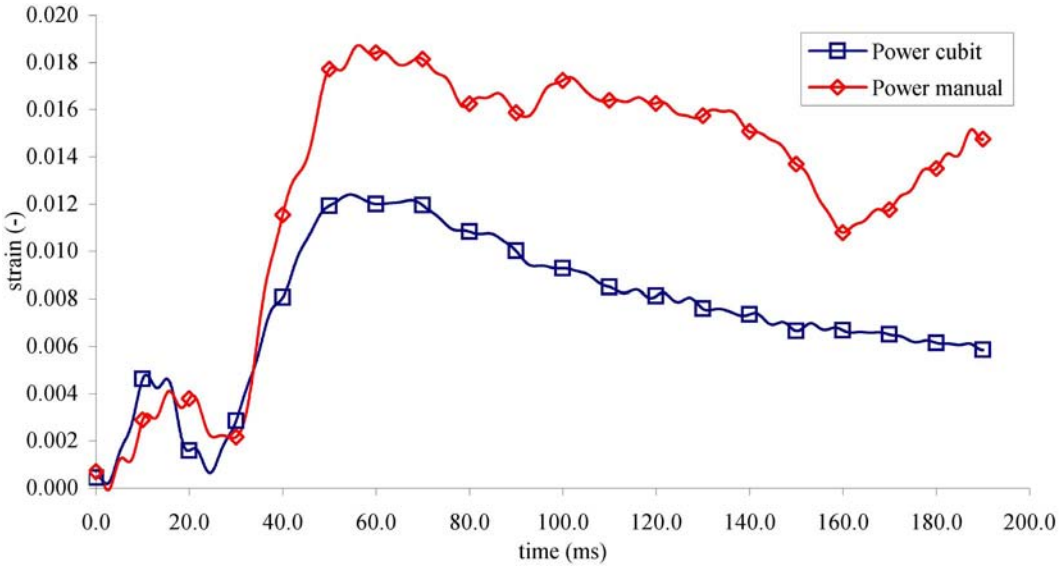

Figure 7.25: Comparison of the Cubit and manual eye meshed models for the Power vitreous.

The CPL constitutive model is compared to the viscoelastic vitreous materials (Figure 7.26) for the manual meshed eye model. Apparent is the minimal difference

between the Nick5, Bet, and Tok vitreous materials. In this case, the bulk modulus is the same while the shear modulus is relatively low. The Power vitreous material, using the CPL model, is an exception as the shear modulus is considerably high compared to the bulk modulus and shows very little difference with the REF (Figure 7.27).

The SOL constitutive model is investigated using the Nick5 vitreous material by modifying the FNLS (Figure 7.28). Comparing it to the REF material, very little difference is noted in the FNLS = 0.01 and 0.1. As the FNLS increases to 1, the shear strain at about 50 ms decreases a bit but shows peaks that are higher and delayed from the REF material throughout the simulation. The decrease is most extreme at FNLS = 10.

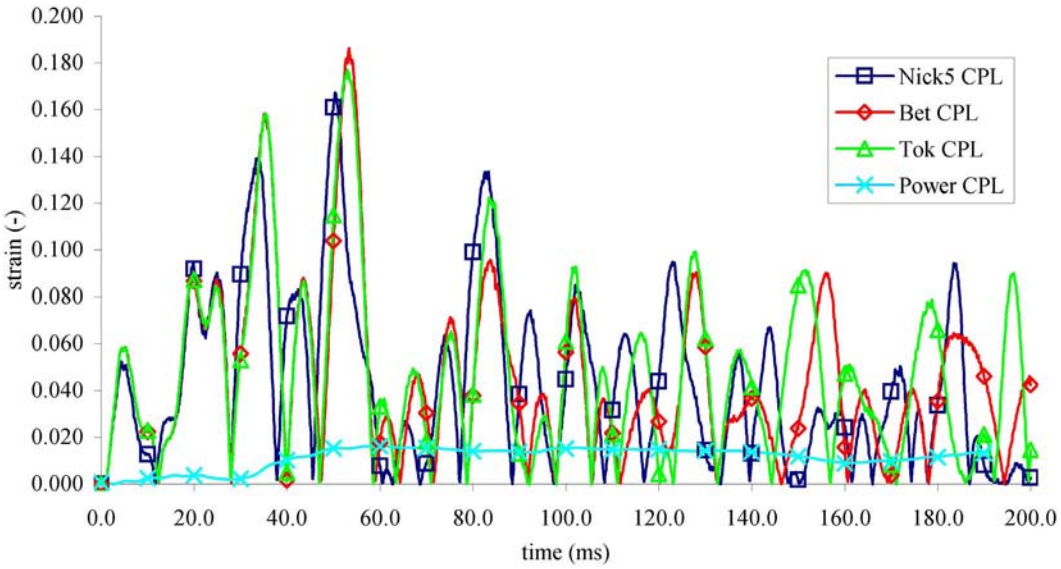

Figure 7.26: Comparison of the CPL constitutive models for the viscoelastic vitreous materials using the manual meshed eye model.

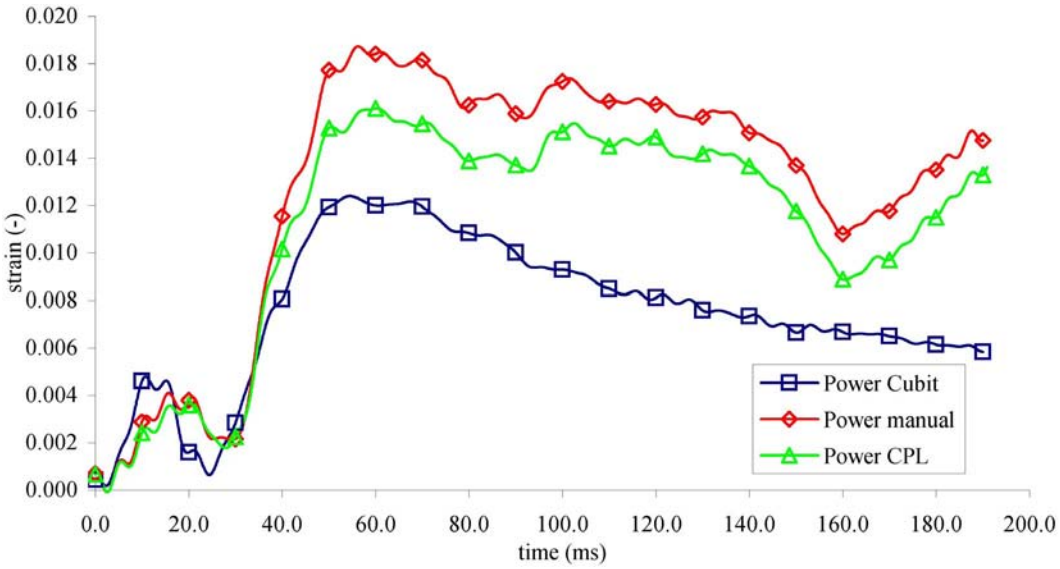

Figure 7.27: Comparison of the Power vitreous shows the differences between the REF Cubit, REF manual, and CPL manual models.

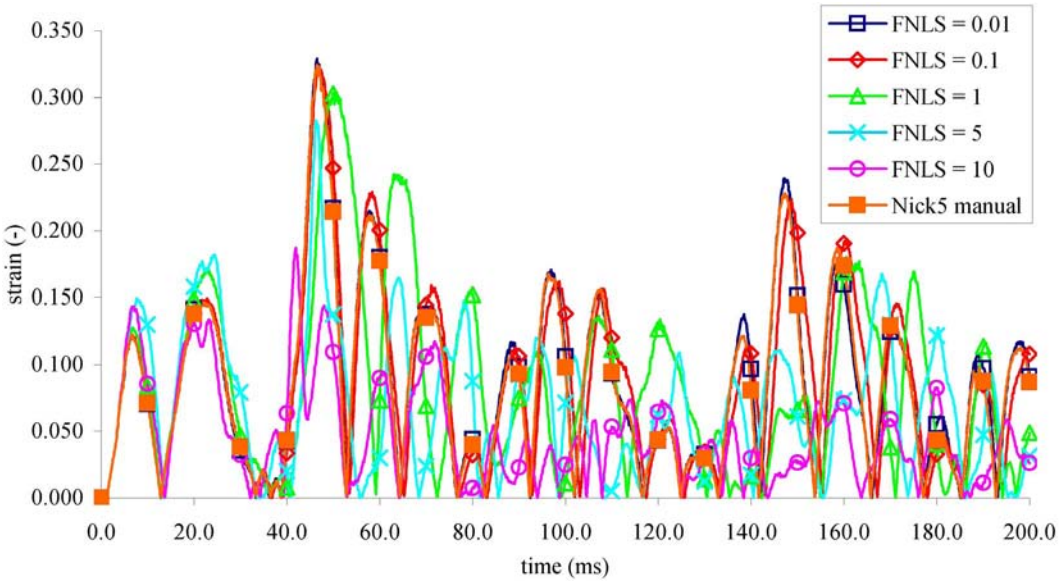

Figure 7.28: Comparison of the SOL constitutive model for the Nick5 vitreous material with the manual meshed eye model.

Inclusion of the Sigal optic nerve is compared to the Weber and Nick5 vitreous material using the REF model for the Nick5 (Figure 7.29). A comparison between the Cubit and manual mesh is shown and the shear strain for the Nick5 around 50 ms is 40% for the manual mesh and 30% for the Cubit mesh. The Weber vitreous material shows little difference between the meshed models using the Sigal nerve. However, comparing the analytical nerve to the Sigal nerve shows an increase in shear strain for both the Weber vitreous model (Figure 7.30) and the Nick5 (Figure 7.31). An increase from 2.5% to 4% in shear strain is due to the Sigal nerve in the Weber vitreous material. In Figure 7.31, the Nick5 vitreous material uses the manual meshed eye model for comparison showing the difference between the analytical optic nerve for the REF and CPL material models with the Nick5 vitreous using the REF model with the Sigal nerve. Addition of the Sigal nerve increases the shear strain by 10% from the Nick5 REF model.

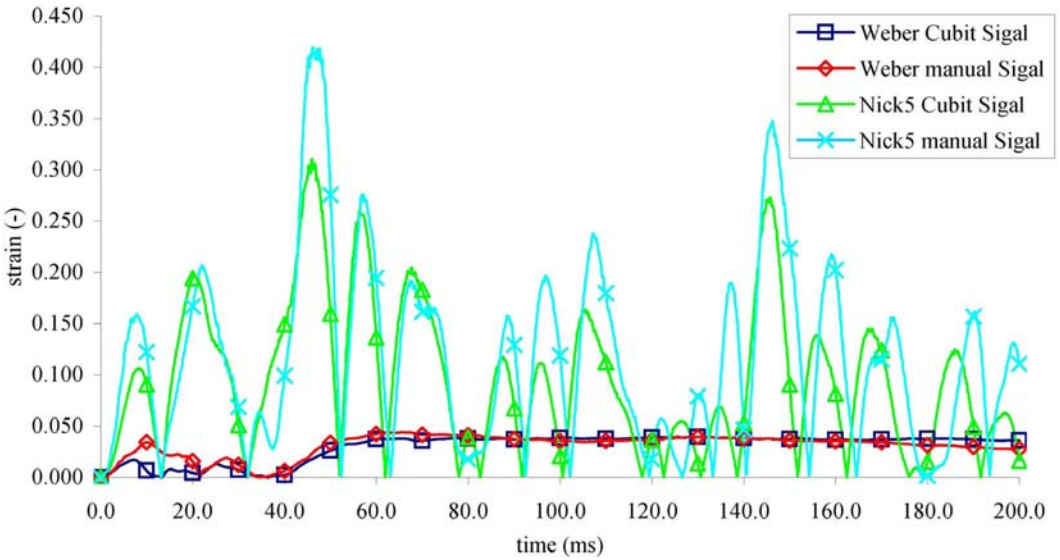

Figure 7.29: Comparison of the Weber and Nick5 vitreous models using the Sigal optic nerve model.

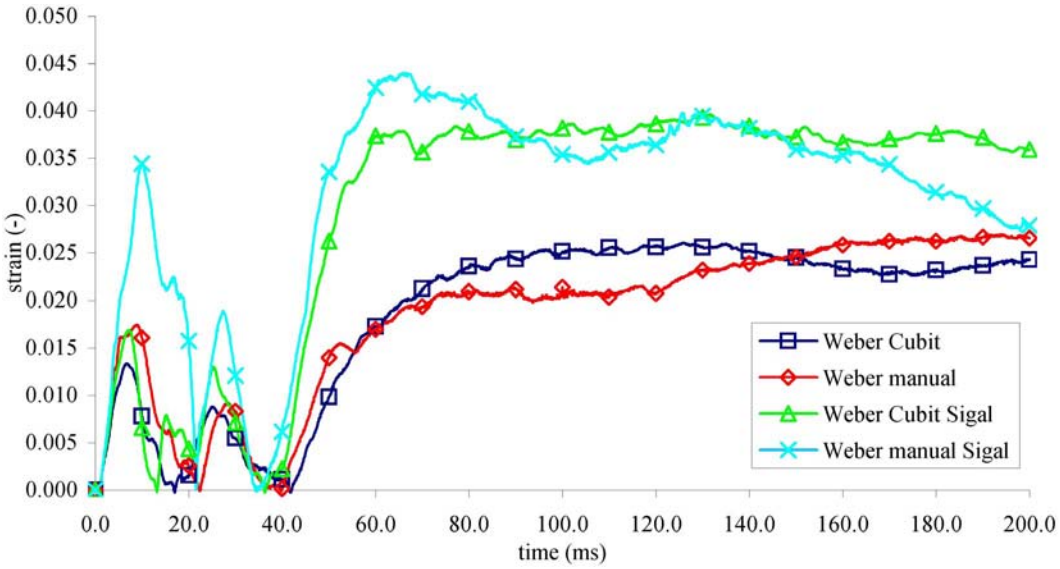

Figure 7.30: Comparison of the Weber vitreous material with the Cubit and manual meshed eye and the analytical and Sigal optic nerve models.

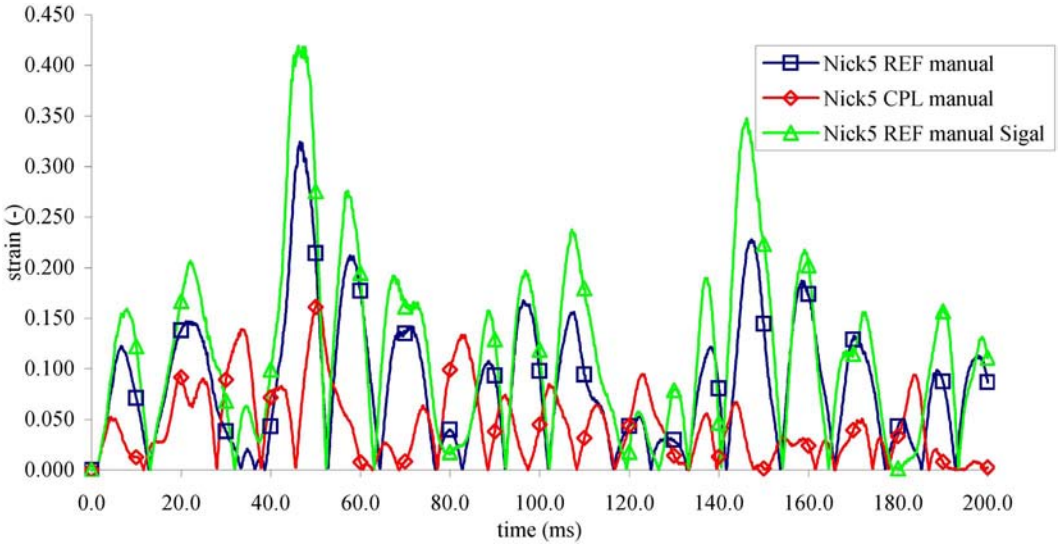

Figure 7.31: Comparison of the Nick5 vitreous material using the manual meshed eye model with the REF and CPL constitutive models and the analytical and Sigal optic nerve models.

Discussion

In the current work, vitreous materials are compared with varying constitutive models. The REF material decouples the deviatoric and hydrostatic behavior and results in a greater shear strain (Figure 7.18). The angular displacement is extreme for the low shear modulus materials (Figures A.3, A.4, A.8, A.9). When the CPL model is used, very little difference is noted between the viscoelastic models for the Nick5, Bet, and Tok vitreous materials. In this case, the bulk modulus is coupled with the shear strain. Assuming simple shear, then (Brands, 2002):

$$\tau = G\left(\gamma + \frac{2}{3}\gamma^3\right) + \frac{1}{2}K\gamma^3 \qquad (7.12)$$

Where τ is the shear stress, G is the shear modulus, γ is the shear strain, K is the bulk modulus. In the case of Bet vitreous, G = 1.46 Pa and K = 2.27 GPa for small shear strains (γ = 1%), the hydrostatic behavior is an astounding 78000 times greater. This difference is more extreme for the Tok vitreous, which is the most compliant of all the materials.

The Nick5 vitreous material is several times that of the Bet and Tok materials and still the hydrostatic behavior is 3800 times greater. The effects of the coupling are minimal for the Power vitreous material where the hydrostatic is only 8 times greater (Figure 7.27). The CPL material disregards the low shear modulus properties for the vitreous and behaves as in previous studies for simple hydrostatic material (Uchio et al, 1999; Stitzel et al. 2002). The SOL material (Figure 7.28) is also investigated for the Nick5 material by varying the non-linear factor (FNLS) to account for shear softening (Brands, 2002; MADYMO, 2004).

The Weber vitreous is comparable to the Power (Figure 7.19) in that the shearing is minimal. The small strains of around 2.5% are a result of using an elastic modulus based on the assumption that the vitreous is "rubber-elastic" (Weber & Landwehr, 1982). This material also showed little sensitivity to mesh density (Figure 7.30) as opposed to the viscoelastic models.

The Tok material (Figure A.9) exhibits high angular displacements of the vitreous material next to the sclera wall while the middle remains unchanged causing instability. Decreasing the mesh density (Figure A.4) allows the simulation to complete with ill-shaped elements in the center of the vitreous material.

The Bet vitreous behaves in a similar manner where the manual meshed model (Figure A.8) undergoes shearing near the sclera wall while the center remains still. However, the decreased mesh density (Cubit mesh) simulation (Figure A.3) response does not produce ill-shaped elements as the Tok material.

The effects of the optic nerve are also considered for the Weber (Figure 7.30) and Nick5 (Figure 7.31) vitreous materials. The Sigal optic nerve model has the effect of increasing the shear strain. This is visually apparent in the Nick5 vitreous model comparing the simulation sequence at time 80 ms (Figures A.7 and A.23). The angular displacement is more cyclonic with the Sigal optic nerve than the analytical model.

Conclusion

A model is presented that considers a complete model of the infant eye with muscle activation. A 20-degree saccade (Winters, 1985) is applied for horizontal motion and the response of the vitreous is examined. A total of five vitreous materials are examined based on previous literature. In addition, shear strain increases with further refinements to the mesh density for the viscoelastic materials (Brands, 2002). The elastic vitreous model (Weber vitreous) does not have an appreciable increase with mesh density however.

The optic nerve is considered from different studies. The analytical model is based on actual measurements (Collins, Scott, & O'Meara, 1969) and is used in horizontal eye motion studies (Lehman & Stark, 1979; Lehman & Stark, 1979; Robinson, 1981; Winters & Stark, 1985; Winters & Stark, 1988). The second optic nerve (Sigal nerve) is considered in studies concerned with the ONH (Sigal, Flanagan, & Tertinegg, 2004) and builds the model on previous material parameters. The inclusion of this nerve model exhibits higher shear strain in the various vitreous materials.

In addition to the mesh density, optic nerve, and vitreous materials, the effects of constitutive models are examined. Brands (2002) examines the difference between the REF, CPL, and SOL and notes the effects. Similar trends are realized in the vitreous materials where the decoupling of the deviatoric and hydrostatic stresses (REF material) show higher shear strains and the CPL material results in a larger contribution of the hydrostatic stresses since the bulk modulus is considerably higher than the more compliant shear modulus. Unfortunately, little work has been done on

the vitreous to determine the non-linear effects so that the SOL material can be used. Current studies fit the response of the vitreous to viscoelastic equations or other formulations. Brands (2002) determines the shear softening parameter by not imposing a constitutive fit and includes this into the viscoelastic material. This nonlinear effect is determined by shear relaxation experiments and none have been done for the vitreous body.

Previous finite element eye models that consider the vitreous for impact simulations either assume the parameters (Power, 2001) or specify a bulk modulus (Uchio et al., 1999; Stitzel et al., 2002). When examining the shear strain, however, specifying the bulk may not be enough to model the vitreous behavior.

Weber and Landwehr (1982) is the only group not to consider the vitreous as viscoelastic and determine the stiffness and damping of the vitreous material. The work of Weber and Landwehr is sited in Nickerson et al. (2005) where previous vitreous studies (Bettelheim & Wang, 1976; Zimmerman, 1980; Tokita, Fujiya, & Hikichi, 1984; Lee, Litt, & Buchsbaum, 1992) are considered "unsatisfactory."

A major limitation of this study is the physiological differences of the infant vitreous. Currently, there exists no study that determines the material parameters of the infant eye. The next limitation is the use of solid elements with extremely compliant vitreous materials. Instability is an issue with element shape during the saccadic motion and no doubt will cause problems for more violent simulations that would consider impacts or shaking. Improvements to the simulation would perhaps include a coupling of the Euler-Lagrange mesh that would include the viscosity of the

vitreous body and would eliminate the possibility of large deformations to the elements as in Stitzel et al. (2002).

Currently, the likely vitreous candidates to use in aggressive impact simulations with a Lagrangian mesh would be the Weber and Nick5 vitreous materials. The Tok and Bet are too compliant to be considered. The Power vitreous is unrealistically high but is considered in this study to show the effects of a high shear modulus with a coupled bulk modulus.

CHAPTER VIII

AN INVESTIGATIVE STUDY USING AN INFANT EYE MODEL FOR DETERMINATION OF RETINAL HEMORRHAGING IN SHAKEN BABY SYNDROME DYNAMICS

Abstract

Shaken Baby Syndrome (SBS) is a form of abuse in which an infant, typically six months or less (Duhaime et al., 1998), is held and shaken. Direct impact does not have (Levin, 2000) to take place; however, conflicting studies would disagree (Duhaime et al., 1987). In the investigation using biomechanical models, a brain model has been developed modeling the brain tissue, bridging veins, and the cerebrospinal fluid (CSF) layer (Morison, 2002). This brain model undergoing simple harmonic shaking, agrees with the premise that pure shaking would cause bridging vein failure.

Expanding this model, a full-featured eye model complete with surrounding boundary tissues is presented. The same harmonic motion used in Morison is considered here as well as an impact study (Duhaime et al., 1996). Retinal hemorrhaging is investigated by comparing the retinal forces at the posterior wall proximal the macular region. Quantifying retinal adhesive failure (Kita et al., 1989 & 1990) gives a possible threshold into retinal injury and is also considered in possible detachment (Green et al., 1996) in abuse studies. The current investigative study does support possible retinal damage due to pure shaking only with forces that breach the

thresholds adapted from Kita et al. –these forces are more sustained than for the impact study. However insightful these models are, caution is still suggested in considering this parametric study as an absolute determination as more work needs to be done to help validate some of the select materials that are adapted for the infant eye model.

Introduction

Clinical observations and diagnosis of SBS started when Caffey (1972, 1974) coined the phrase *Whiplash Shaken Infant Syndrome*. In the following years this diagnosis would simply be called Shaken Baby Syndrome. The actual mechanism of injury is debatable, but the injuries associated with SBS are subdural hematomas (SDH) (Duhaime et al., 1996), diffuse axonal injury (DAI) (Margulies & Thibault, 1992; Jafari et al., 1997; Bain & Meaney, 2000; Prange & Margulies, 2001), and retinal hemorrhaging (Lambert, Johnson, & Hoyt, 1986; Gilliland, Luckenbach, & Chenier, 1994; Betz et al., 1996; Gilliland, Luckenbach, & Chenier, 1994; Kapoor et al., 1997). There appears to be evidence that bilateral SDH and retinal hemorrhaging would indicate abuse while unilateral injuries would be associated with accidental impacts or falls (Duhaime et al., 1996). This would also lead to the belief that to get bilateral SDH and retinal hemorrhaging the infant would have been shaken vigorously about the sagittal plane (Gilliland & Folberg, 1996; Levin, 2000). Further, Levin defines SBS as a form of child abuse "in which the perpetrator violently shakes

an infant resulting in brain, skeletal and/ or retinal haemorrages (p. 151)." However, the force required to cause injury is not agreed upon and is a source of controversy.

Levin asserts, "retinal hemorrhage is perhaps no more specific as fracture and one surely would not suggest that all fractures are the same in terms of pathogenesis or aetiology" (p. 157). Further retinal hemorrhages can be described by the location and severity. Kapoor, Shiffman, Tang, Kiang, and Woodward (1997) describe the mapping of the hemorrhages in the different layers of the retina (e.g. preretinal, intraretinal, subretinal). Lancon, Haines, and Parent (1998) and Betz et al. describe the distribution of hemorrhages. Lambert, Johnson, and Hoyt (1986) examined optic nerve sheath hemorrhages. Optic nerve sheath hemorrhaging is perhaps attributed to the slack in the nerve sheath combined with the passive response of the ocular muscle attachments (Levin). Green et al. concludes that hemorrhages were most likely to occur in the posterior pole in a study including 16 children who died from SBS. Gilliland, Lieberman, Milroy, and Parsons (1996) claim that these peripheral retinal hemorrhages are from acceleration-deceleration injury with a few cases involving direct head trauma. Levin concludes, "The findings of massive hemorrhages throughout the retinal surface at all layers reflects a shaking aetiology [(i.e., the study of cause)] unless proven otherwise" (p. 161).

A parametric model of an infant eye is presented that is able to quantify retinal forces due to a documented shaking frequency (Morison, 2002). This eye model is built using a variety of material properties that have been reported for the eye tissues, optic nerve, extra-ocular muscles, and fatty tissue. The geometry of the infant eye is scaled from the adult eye model and is based on idealized eye geometry (Woo et al.,

1972) and the dataset from the Visible Human Project. MADYMO (2004) software, which is able to combine finite element analysis with rigid-body computation, is used to model the simulation. The infant eye model is mostly finite element based containing the ocular membrane shells that represent the cornea-sclera shell, the choroid, and the retina. Inside the eye globe, the vitreous body and aqueous humor are divided into two chambers by a simplified lens-ciliary body structure. Posterior to the eye the optic nerve is considered using an analytical approach from mathematical models done in previous work for horizontal eye motion (Lehman & Stark, 1979; Lehman & Stark, 1979; Robinson, 1981; Winters & Stark, 1985; Winters & Stark, 1988). Specifically, most of the "plant" properties are determined by measuring the damping and stiffness during surgery (Collins, Scott, & O'Meara, 1969).

In addition to this analytical model, a simple finite element model is also considered where the soft tissue material properties are determined from Sigal, Flanagan, & Tertinegg (2004). The focus of the finite element optic nerve (Sigal nerve) is the optic nerve head (ONH), but the material properties are averaged from previous research in this study.

The muscle tethers are modeled as Hill-type (Hill, 1950; MADYMO, 2004) segments attached to finite element tendons with lumped-mass muscle bellies. These analytical muscle properties are primarily derived from the Winters (1985) work. Although sophisticated controls and/or functions can be used to model muscle activation, the current study only considers the muscles as passive tethers, and support for this is found in the work of Levin (2000) where orbital shaking is described by the muscle tethers and slack in the optic nerve.

The fatty tissue and anterior tissue including the eyelid skin are modeled encasing the eye globe. Interfacing the eye globe and fatty tissue boundary is a small contact gap with contact logic specified so that forces can be transmitted between the soft tissue bodies.

The geometry of the infant is scaled from an adult using the infant dimensions of the eye globe diameter (Hogan, Alvarado, & Weddell, 1971) to give a scale factor of 0.645. In agreement with this factor is the optic nerve diameter measurements using ultrasound from children with age range 10 days to 13 years old (Newman et al., 2002). The analytical optic nerve is scaled based on this information comparing the dynamic response of the adult (setting the natural frequency and damping ratio equal). The properties for the muscles are assumed the same as adult muscles since no information for infant eye muscles exists. In addition, all mechanical properties that are measured from adult or other species is not scaled and assumed the same.

Retinal detachment has been reported in SBS (Green et al., 1996) and is noted in Levin be fairly uncommon perhaps based on the resorption tines of the sub-retina (Negi & Marmor, 1986). Modeling the detachment is possible using the MADYMO software and relies on physically separating the retina from the choroid by moving the nodes a very small distance normal and away. Then a node weld is used with strength properties (Zauberman & DeGillebon, 1972; Zauberman, DeGuillebon, & Holly, 1972; DeGuillebon & Zauberman, 1972; Marmor, Abdul-Rahim, & Cohen, 1980, Kita et al., 1990; Kita & Marmor, 1992) applied that allows the weld to break when the defined strength is breached. Ideally, a de-lamination (Kostopoulos et al, 2002) process would define the behavior better allowing the nodes of the retinal-

choroid boundary to be coincident. However, the node-weld syntax must have a distance between the nodes greater than zero. A study using the node-weld technique for eye sutures has been implemented (Uchio et al., 2004) however. Once the weld is broken, the once constrained nodes are free to move requiring additional contact algorithms of the intra-ocular tissues or the inside structures would be free to move outside the eye globe.

A well-defined shaking motion is applied to the eye model such that the equivalent motion would be the same as the perpetrator grabbing the torso of the infant. The frequency of the shake, 4 Hz, is documented in Duhaime et al. (1987) and is perhaps the most vigorous frequency possible considering the head starts at –60 degrees representing the chin resting on the torso (Morison, 2002). The total amplitude is ±60 degrees and represents the maximum range of motion possible.

For comparison, a well-documented impact (Duhaime et al., 1996) is considered where a father is swinging an 8-month old infant in a seated position. The father is hunched over and is cradling the infant underneath the infant's legs close to the knees. The swing motion is to-and-fro and the infant accidentally strikes his occiput on the floor. The pulse information is gathered by simulating this effect using the MADYMO (2004) CRABI (Child Restraint AirBag Interaction) 12 month ATD (anthropometric test dummy). A simulation matrix is performed, and the retinal forces are investigated.

Methods

The eye model is influenced by previous impact studies (Uchio et al., 1999; Power et al., 2002; Stitzel et al., 2002) where the cornea and sclera are concerned. Further influence is introduced in the ciliary and lens structures from Power (2001) that separates the aqueous humor from the vitreous body. In addition, the Power model did include the fatty tissue up to the eye globe meridian with passive muscles modeled as membrane elements. The proposed model considers the fatty tissue as an entire enclosure with the eyelid skin. Parameterization is performed for the fatty tissue enclosure by consideration of two compliant, hyperelastic (Rivlin & Thomas) materials.

In addition, current literature on muscles is more complete for the analytical Hill-type (Winters & Stark, 1985 and 1988; Winters, 1985; Lehman & Stark, 1979 & 1983) than for finite element based muscles (Duck, 1990; Power, 2001; Zobitz, Luo, & Au, 2001; Hirokawa & Tsuruno, 2000; Sarma et al., 2003). Most of the finite element muscle materials only consider passive behavior. Johansson, Meier, and Blickhan (2000) investigate muscle modeling using finite element analysis with the inclusion of the Hill-type muscle formulation in the constitutive equation. The proposed model will consider a hybrid muscle-tendon, where the muscle is an analytical muscle with the contractile element and passive element. The tendon is a finite element membrane representing the series elastic element.

The optic nerve is modeled as an analytical spring-damper (Kelvin element) (Winters and Stark, 1985) and also as a finite element structure modeling the neural tissue and pia mater (Sigal et al., 2004).

Simulations are performed for an impact with duration of 100 ms and a four-cycle shake (frequency is 4 Hz and amplitude is ±60 degrees) lasting one second.

Geometry

The model considers the eye globe with inner structures, the muscle tethers, tendons, optic nerve, fatty tissue, eyelid, and the encompassing orbital socket. Most information for the geometry is available for the adult eye. In order to consider the infant eye, the geometry of the adult eye is scaled down to 64.5% using the eye diameter from Hogan, Alvarado, and Weddell (1971) and the optic nerve sheath diameter from (Newman et al., 2002). The ocular shell dimensions are based on Woo et al. (1972) (Figure 8.0) and the lens and ciliary placement on Power (2001) (Figure 8.1).

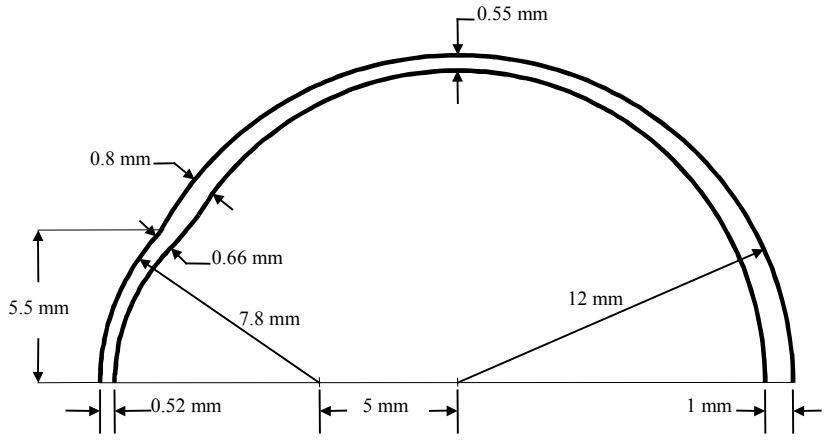

Figure 8.0: Geometry of the idealized cornea-sclero shell from Woo et al. (1972) for an adult eye.

The placement of the idealized geometry of the eye is positioned inside a built up model of the ocular cavity, muscles, optic nerve, and eyeball from the Visible Human Project transverse slice scans (Figure 8.2). The ocular cavity cone geometry is built from the Visible Human scans as is the apex muscle and optic nerve attachments, the oblique inferior, and superior attachments. The final position of the optic nerve and tendon attachments to the eyeball are based on Hogan, Alvarado, and Weddell (1971) and differ from the Visible Human Model slightly. However, the attachment locations to the eyeball from Hogan et al. are an average of several eyes and are more appropriate to use. The fatty tissue/eye lid is considered to fill the entire ocular cavity. A void is inserted into the fatty tissue where the location of the eyeball is to be so that the eyeball is totally encased in the fatty tissue.

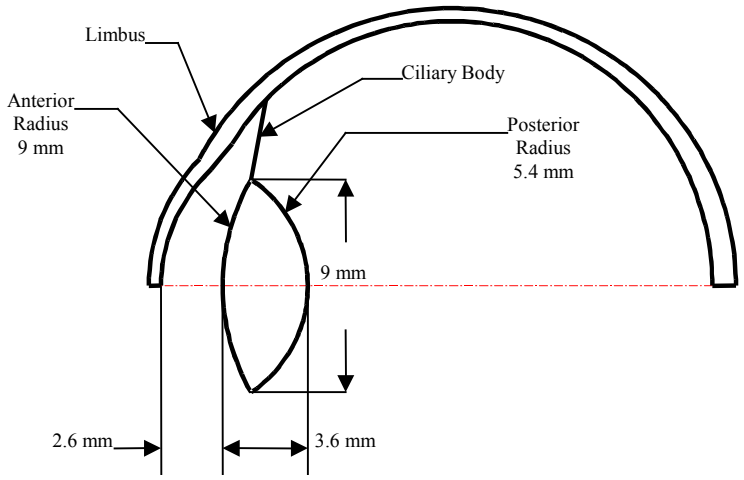

Figure 8.1: Location and dimensions of the lens and ciliary placement for an adult eye (Power, 2001).

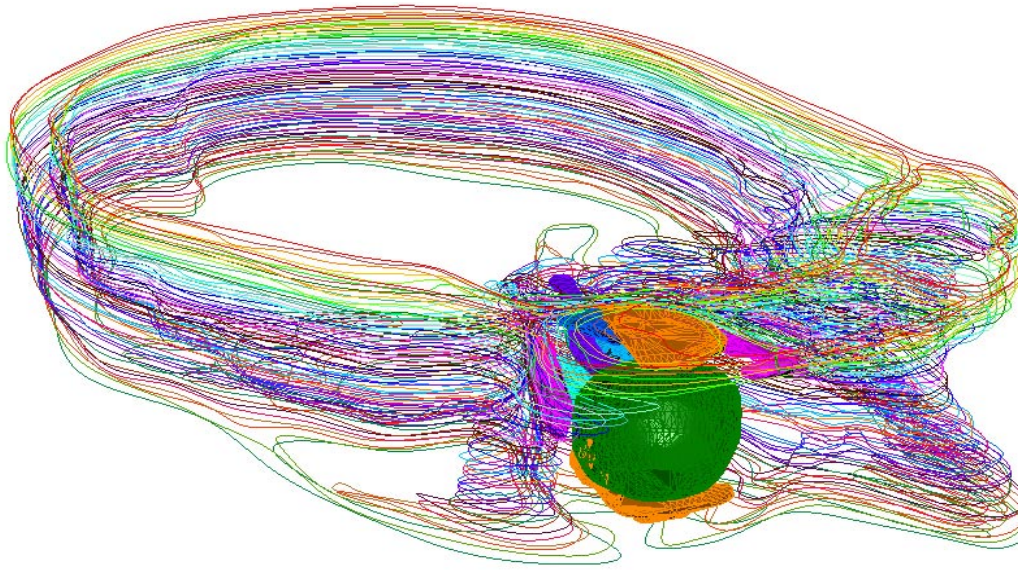

Figure 8.2: Complete build up of spline curves offset 1 mm based on Visible Human Slices

Model Creation

The eye model uses the idealized geometry of the ocular shells (Figure 8.0) with the lens and ciliary dimensions (Figure 8.1) for meshing of a quarter eye with final meshing mirrored about the sagittal and transverse planes of the eye. The model is built from the inside out starting with the vitreous and aqueous. The vitreous and aqueous are modeled using hexahedral elements with reduced integration to prevent mesh locking (Samani et al., 2001; Brands, 2002; Gopalakrishnan, 2002; Manzini and Putti, 2007). This mesh-locking phenomenon is most apparent with viscoelastic materials.

The vitreous quarter is divided into five parts with a central cube and a generalized volume using the surface of the top, side, front, and back of the cube to the outer cornea-sclera shell (Figure 8.3).

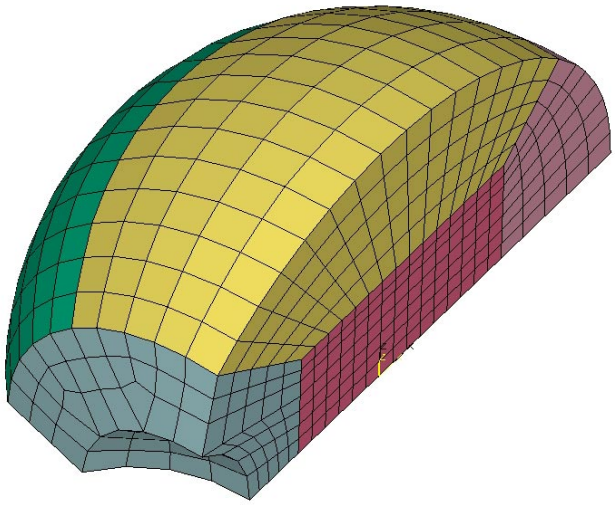

Figure 8.3: Partitioning of the vitreous for hexahedral meshing (one quarter shown).

Sweeping of shell elements is performed to fill the volume by selecting the two surfaces in an extrusion process. During the extrusion, the element count is set to five elements thick for each of the volumes interfacing the cubed volume (Figure 8.3). The overall outer ocular shell mesh density is around one millimeter square for each element. The vitreous mesh is modified until this density is achieved. The anterior surface of the vitreous quarter mesh is then used to extrude the aqueous to the cornea-scleral shell on the anterior of the eye.

Once the solid vitreous and aqueous are created, the cornea-scleral shell is modeled as solid elements to capture the non-uniform thickness. Unfortunately, the meshing method used for vitreous and aqueous makes uniform meridian bands of thickness anterior to posterior of the eye shell impossible without restricting the outer eye shell mesh and possibly creating ill-shaped hexahedral elements. Uniform thickness bands are specified in the previous eye models (Uchio et al., 1999; Power et al., 2002; Stitzel et al., 2002) simplifying the thickness specifications. Instead, a

macro is developed to create a shell at the mid-plane of each of the solid elements representing the sclera and cornea capturing the thickness information at the same time (Figure 8.4). Utilization of this macro for the quarter eye geometry creates 16 separate parts for the cornea each with unique thickness and 240 parts for the scleral shell with unique thickness specifications.

The other ocular tissues in the model are meshed based on the outer surface of the vitreous and aqueous. The retina and choroid are duplicated from the surface elements posterior to the aqueous-vitreous boundary. The ciliary body and lens are duplicated from the anterior face of the vitreous and the posterior face of the aqueous. All tissues inside the eye share the same common nodes. The vitreous-retina-choroid-sclera share the same nodes and influence of this type of condition is supported where the infant vitreous is reported to be more difficult to remove. The vitreous-ciliary body-lens-aqueous nodes are shared and represent the same physiologic conditions for infants and adult eyes where the collagen fibers are greater around the ora serrata (Hogan, Alvarado, and Weddell, 1971; Wolter, 1961; Lee, Litt, & Buchsbaum, 1992).

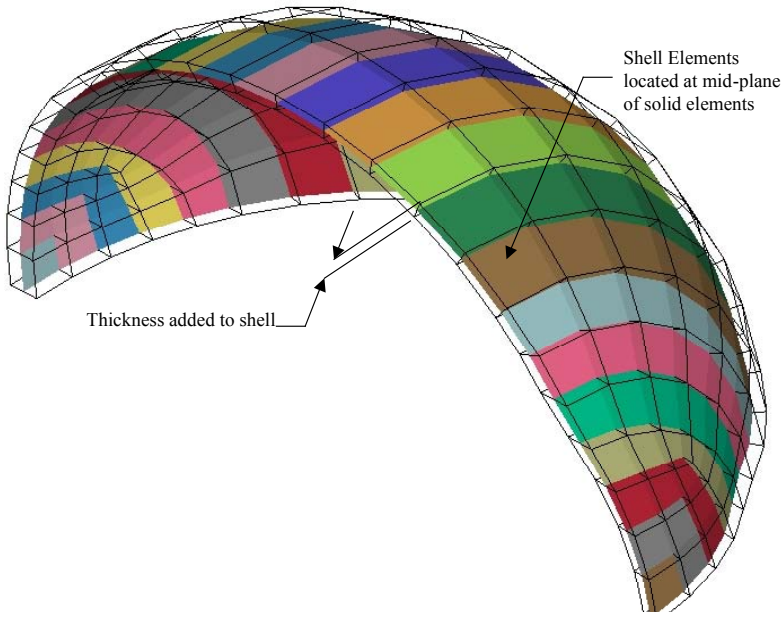

Figure 8.4: Conversion of solid cornea and sclera elements to shell elements

The optic nerve head (ONH) near the posterior pole of the scleral shell is approximated based on Hogan, Alvarado, and Weddell (1971) location. The elements in this region are modified slightly (Figure 8.5 A) to approximate the diameter of the optic nerve in a roughly circular shape while being mindful of element shape. To model the finite element optic nerve, this ONH is extruded posterior towards the apex location determined from the "Visible Human" data slices. The finite element optic nerve is then filled with a solid hexahedral mesh with an outer membrane quadrilateral mesh sharing the same nodes (Figure 8.5 B). The analytical optic nerve is modeled using five beam elements with locations influenced by the extruded finite element nerve model in the general locations (central, superior, inferior, lateral, medial) (Figure 8.5 A). To tie the analytical nerve bundle to the ONH five individual simple constraint groups are created so that each beam-nerve is attached to a region in

the ONH (Figure 8.5 C). Initially, the analytical beam elements were directly attached to the sclera nodes; however, the node attachment acted as a spherical joint with no bending resistance.

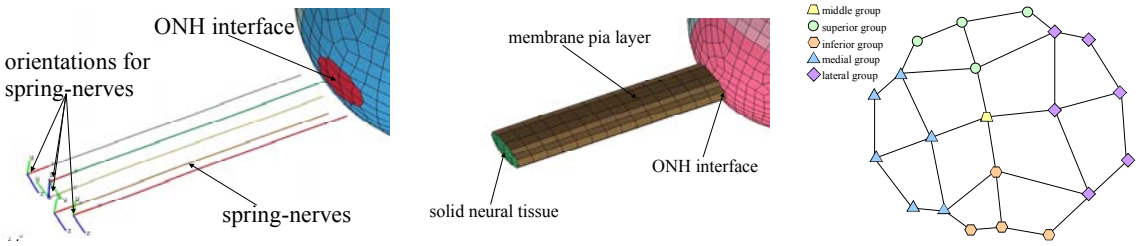

(A) (B) (C)

Figure 8.5: **A:** ONH interface detailing the analytical spring nerves. **B:** Extrusion of the ONH is performed to build finite element nerve model. **C:** Simple constraint group layout for tying the analytical optic nerve to the posterior sclera.

The fatty tissue in the ocular cavity provides cushioning and energy absorption capabilities. Further, along with the ocular tethers, the fatty tissue helps keep the eye positioned to form part of a spherical joint with the eye globe. The mesh of the fatty tissue is composed of tetrahedral elements with membrane elements modeling the skin layer on the anterior most surface. Meshing the fatty tissue involved using the ocular cavity (Figure 8.2) and the surface of a larger eye globe. This larger globe introduces a physical gap between the two structures. The final two surfaces are then meshed using three node elements and the volume between filled with solid tetrahedral elements. What results is a solid object with a spherical void (Figure 8.6) that houses the eye globe.

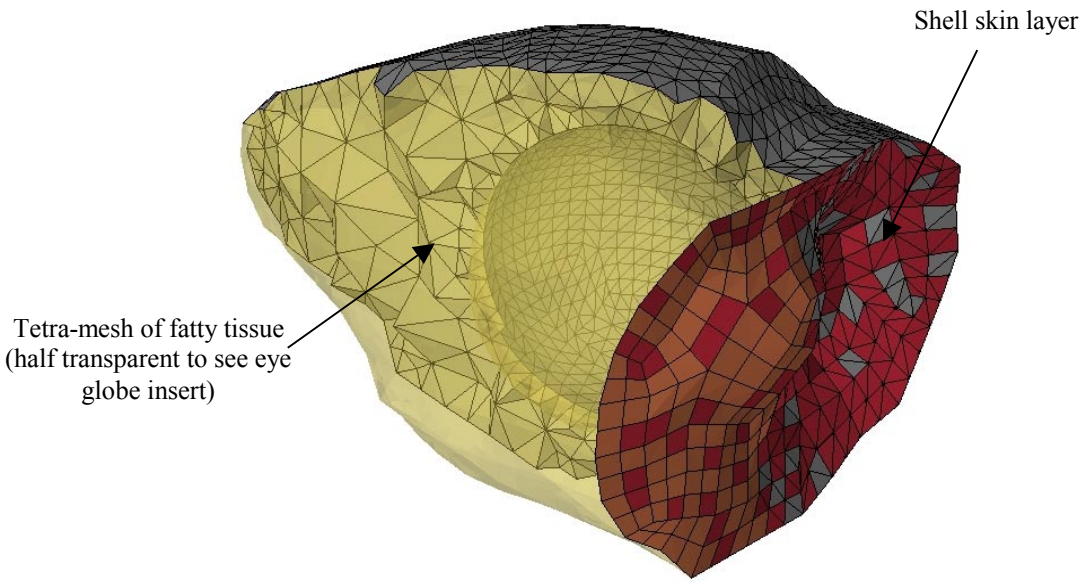

Figure 8.6: Fatty tissue tetra-mesh with membrane skin layer.

The extra-ocular muscles are originally based on the Visible Human information by approximating a 2-D surface along the muscle length. The attachment to the eye globe shell is accomplished using the information from histological studies (Hogan, Alvarado, & Weddell, 1971). The surfaces for the muscles are then modified so that only the tendon portion attached to the eye remains while analytical muscle segments defined only by points replace the original surface location (Figure 8.7). Tendons are then meshed using 3-node membrane elements sharing common nodes with the sclera shell and supported on lumped mass bodies, which interface the analytical muscle segments.

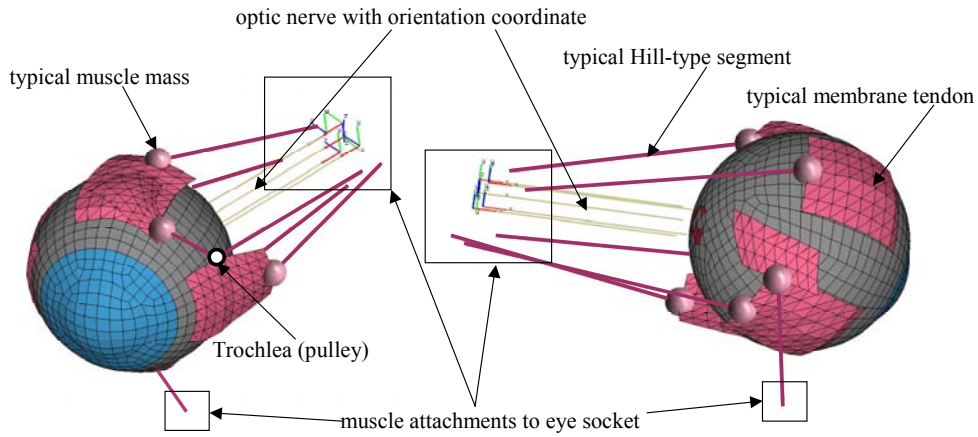

Figure 8.7: Muscle and tendon details for the infant eye model.

The complete eye model is shown (Figure 8.8) with a quarter cut from the eye globe exposing the interior sections. The fatty tissue is also sectioned by removing one quarter and made transparent so that the finite element optic nerve is visually exposed.

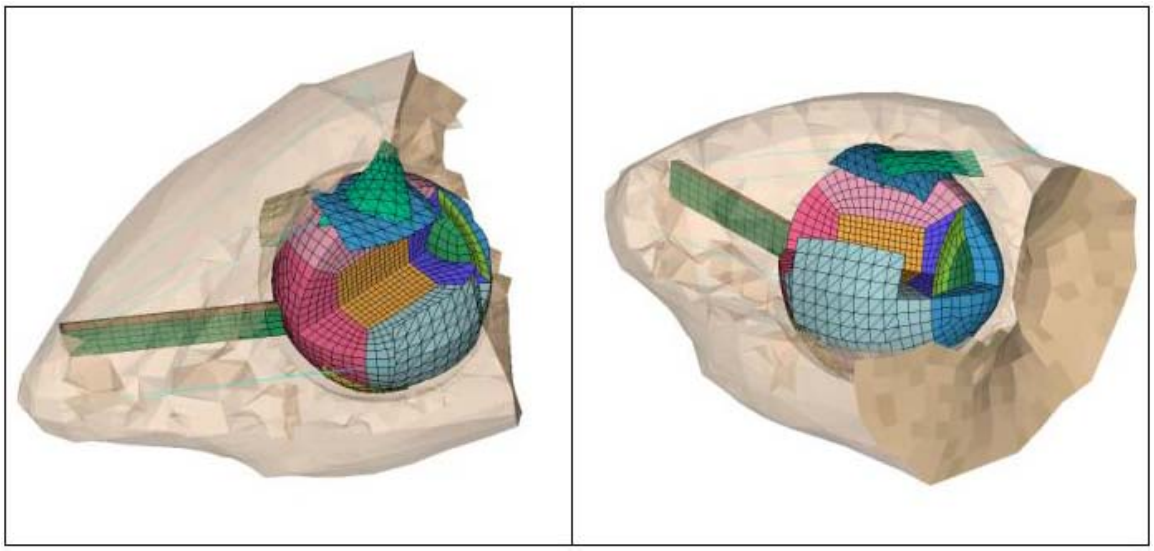

Figure 8.8: Entire eye model showing the posterior-lateral and anterior-lateral views.

Material Definitions

The eye model contains a number of material properties from previous literature. Most of the finite element models of the past, involved in dynamic simulations, develop the eye to model impact cases (Uchio et al., 1999; Power et al., 2002; Stitzel et al., 2002). In these models the cornea and sclera are considered to be membrane material consistent with Hoeltzel et al. (1992). In addition, the vitreous body and aqueous are modeled using a hydrostatic formulation in Uchio et al. and Stitzel et al., while Power et al. propose an elastic value based on an estimation from fatty tissue (Todd & Thacker, 1994). None of these studies considers the retina, choroid, or optic nerve attachment. This is perhaps appropriate as the case studies only consider impact to the cornea and proximal to the cornea. Only the Power et al. study considers modeling the eye with fatty tissue and muscle tethers, while Uchio et

al. fix the eye directly to the skull and Stitzel et al. model the eye in vitro utilizes the same fatty tissue as Power et al.

The current model considers all previous ocular structures including the retina, choroid, and optic nerve. In addition, the fatty tissue is modeled encasing the eye globe with detailed muscle models tethering the eye.

The cornea and sclera material are based on Uchio et al. test strips taken to failure. There is a linear region of these materials up to the point before increasing strain results in decreasing stress. The moduli, as reported by Stitzel et al., for the linear region are 124 MPa and 358 MPa for the cornea and sclera, respectively. To account for the compressive stiffness, a reduction factor is introduced in this tension only material so that the compression factor is $1/100^{th}$ of the tension (Stitzel et al.). Specifying the reduction factor also aids in reducing instability that may occur with the tension-only material with contact interactions (MADYMO, 2004). The mass density of the cornea and sclera is set to 1076 kg/m^3 (Duck, 1990) and 1243 kg/m^3 (Uchio et al.), respectively. The Poisson's ratio, ν, is measured for cornea and sclera (Uchio et al.) and is 0.42 and 0.49, respectively.

The choroid is a thin, highly vascular membrane supplying nutrition to the retina and anterior eye. This tissue exhibits traits similar to erectile tissue (Hogan, Alvarado, & Weddell, 1971). Current studies only consider the elastic modulus for the choroid (Graebel & Van Alphen, 1977) and are used in this eye model (Table 8.0). The thickness of the choroid in this eye model is a uniform 0.16 mm as presented in Graebel and Van Alphen. However, the postmortem testing produces a thinner representative thickness and is closer to 0.42 mm in vivo (Friberg and Lace,

1988). This estimate of 0.42 mm is very reasonable compared to ultrasound techniques showing the choroid to be 0.471 mm in vivo (Coleman & Lizzi, 1979).

The retina is a very thin, delicate, and clear tissue lining the inner eye and interfacing the vitreous body and choroid layer through the pigment epithelium. The retina varies in thickness with the thickest portion near the optic disk measuring 0.56 mm thinning to 0.18 mm at the equator, and then to 0.1 mm at the ora serrata (Hogan, Alvarado, & Weddell, 1971). The mechanical properties of the retina (Table 8.0) are from Jones, Warner, and Stevens (1992). Although the retina varies in thickness throughout the eye, a value of 0.14 mm (Wu, Peters, & Hammer, 1987) is used for the entire membrane structure. This thickness is reasonably close to ultrasonic measurements (0.17 mm) (Coleman & Lizzi, 1979).

The lens is considered rigid in this study as in previous dynamic models (Uchio et al., 1999; Power, 2001). The assumption is reasonable as the current model is concerned with the posterior retinal forces with no external impacts to the anterior eye. For impacts to the cornea and anterior eye shell, this assumption needs evaluating. Stitzel et al. do model the lens using an elastic modulus rather than modeling the structure as rigid so that deformation of the lens is accounted for during severe impacts.

The ciliary body is modeled (Table 8.0) the same as Power et al. where the tensile strength is assigned a value of 11 MPa. The rational behind this assignment is that collagen in rat tail tendons varies between 50 and 100 MPa and the ciliary body does have a large amount of collagen but not as much as rat tails. The same material

is utilized in the Stitzel et al. model that is also validated with experimental impacts on cadaver eyes.

Previous eye models consider the vitreous body (Uchio et al., 1999; Power et al., 2002; Stitzel et al., 2002) for eye impact studies. Uchio et al. and Stitzel et al. utilized a hydrostatic formulation. Specifically, Uchio et al. modeled the vitreous using solid elements and assigning the material a hydrostatic pressure of 20 mm Hg. The Stitzel et al. model utilized the bulk modulus of the vitreous, $K = \rho C^2$ (where ρ is the density of the material and C is the speed of sound through the material), in pressure state equation model, Gruneisen equation. Interestingly, in the Stitzel et al. model, the vitreous body is modeled using a Eulerian grid interfacing the Lagrangian element boundary. This mesh coupling approach allows the eye to undergo extreme impacts with local ocular shell pinching without simulation instability. Power et al. utilizes a linear elastic model deriving the material properties from the fatty tissue study (Todd & Thacker, 1994) and making the material 42 kPa for a total reduction of approximately 11%. However, this fatty tissue is considerably stiff compared to other studies (Luboz et al., 2004; Verver, 2004; Samani & Plewes, 2004).

The current vitreous used in this investigative study utilizes an elastic model (Table 8.0) where the vitreous is considered “rubber-elastic” (Weber & Landwehr, 1982). Because of the collagen fiber network, Weber and Landwehr claim that the vitreous cannot really be considered viscoelastic and fits the response of a steel sphere harmonically excited to a Voigt-Kelvin model. Using the mass of the steel sphere, the damping and stiffness coefficients are solved. The damping and stiffness

values for the human vitreous are 7.35×10^{-4} Ns/m and 6×10^{-2} N/m, respectively (Weber and Landwher).

In order to use this information in a constitutive model for solid hexahedral meshes, a mathematical beam model is created supplying the damping and stiffness values from Weber and Landwher directly. A mass is attached to the end of the model (mass = 1.0×10^{-4} kg) and an initial displacement of 2 mm at time zero is given. The natural frequency (ω_n) and the damping ratio (ζ) are $\sqrt{\frac{k}{m}} = 24.5$ rad/s and $\frac{c}{2\sqrt{mk}} = 0.15$, respectively. A second model with a finite element hexahedral beam is created with similar boundary conditions with initial guesses for the modulus (E) and the damping value (c). The response of the position time history, $\delta = \ln\left(\frac{x_1}{x_2}\right)$, is used to match an equivalent solid beam element (E and c) for a Poisson's ratio (ν) equal to 0.5. After a few iterations, the natural frequency and damping ratio are approximately the same as the analytical model yielding the tabulated values (Table 8.0) for the finite element model.

The aqueous humor is modeled similar to the vitreous as it is assumed the liquid nature of the aqueous has little effect on the posterior vitreous during a shake or impact fall at the back of the head.

Other vitreous materials assume a viscoelastic fit (Bettelheim & Wang, 1976; Tokita, Fujiya, & Hikichi, 1984; Lee, Litt, & Buchbaum, 1992; Nickerson et al., 2005); however, these compliant materials are unreliable under extreme rotational motions or impacts using Lagrangian meshes.

The presented eye model study utilizes two models for the fatty tissue. Both models use a hyperelastic Mooney-Rivlin material (Williams, 1980):

$$\sigma_e = 2A\left(\lambda - \frac{1}{\lambda^2}\right) + 2B\left(1 - \frac{1}{\lambda^3}\right) \qquad (8.0)$$

Where σ_e is the engineering stress, A and B are the material parameters of the first and second invariants of the strain tensor, λ is the extension ratios $(1+\varepsilon)$.

Samani and Plewes (2004) determine the hyperelastic parameters (A and B) of breast tissue samples (ex vivo) gathered from breast reduction surgery. Using the experimental force-displacement data, finite element models representing the experiment are created with the hyperelastic parameters. The parameters are modified until they converge to the experimental force-deflection curve- an optimization technique using a least-squares fit.

Verver (2004) creates a model of the buttocks for comfort studies. In this case, the material parameters are assigned based on ranges of reported values. Both the material parameters are tabulated in 8.0, and a comparison of the materials is provided in Figure 8.9.

Power et al. used the properties from Todd and Thacker, which compared to the other materials, is extremely stiff.

The material from Luboz et al. (2004) uses a linear elastic formulation with modulus set to 20 kPa influenced by previous published values. The Poisson's ratio is set to 0.1 to account for the poro-elastic properties of the fatty tissue.

All other studies use a Poisson's ratio of 0.5 for incompressibility. The overall stiffness is similar to Verver (Figure 8.9) and is not considered in this eye model study. The most compliant of these materials is the work of Samani and Plewes, which almost appears as a straight horizontal line close to zero when compared to the other material models (Figure 8.9). The density of the fatty tissue

for both the Verver study and Samani and Plewes study is set to 928 kg/m^3 (Duck, 1990). The membrane skin is modeled based on the human model study from the MADYMO software (2004) and is linear elastic.

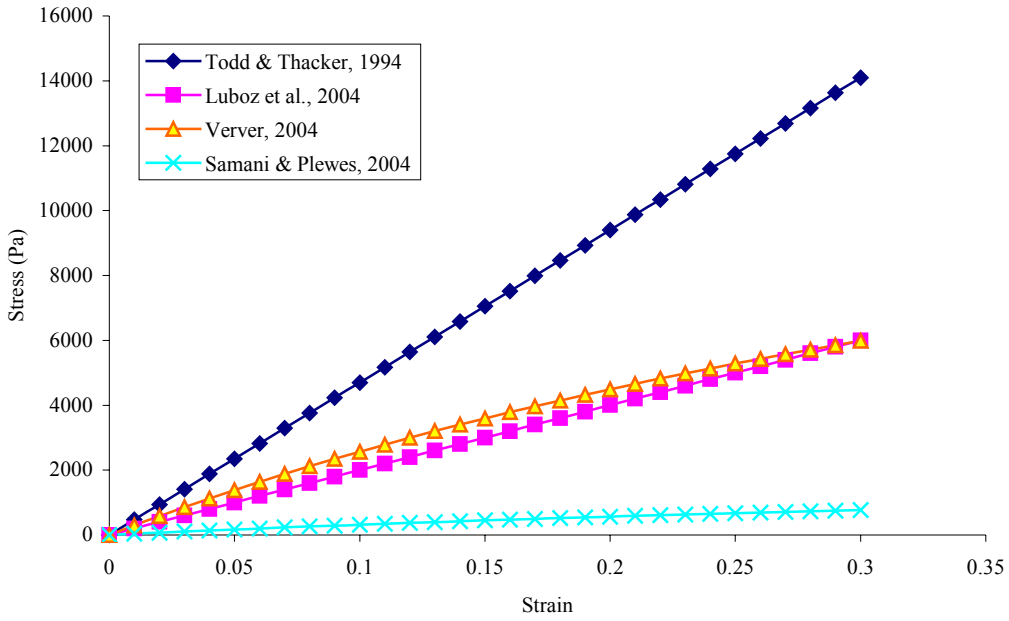

Figure 8.9: Comparison of fatty mechanical properties of different research groups illustrating the extreme stiffness characteristic of the Todd & Thacker soft tissue properties.

The muscle-tendons are modeled using a combination of Hill-type muscles (Figure 8.10) and finite element membrane tendons. The muscle is modeled using attachment points (apex location for the recti muscles) with a contractile element (CE) in parallel with a passive element (PE) attached to a point mass. This mass couples the Hill muscle with the series elastic (SE) element represented by the finite

element tendon. This tendon is then attached to the eye globe sharing common nodes with the sclera shell. The total muscle force is the summation of the contractile and passive force contributions:

$$F_{muscle} = F_{CE} + F_{PE} \qquad (8.1)$$

The passive force is considered when the muscle is stretched beyond the reference length and the active muscle behavior is given by (MADYMO, 2004):

$$F_{CE} = AF_{max} f_H(v_r) f_L(l_r) \qquad (8.2)$$

Where A is the activation and varies between 0 (rest state) and 1 (maximum activation), $f_H(v_r)$ defines the normalized active force-velocity relationship (Hill curve), $f_L(l_r)$ is the normalized active force-length relationship. The necessary parameters are provided in Table 8.1, which also accounts for the SE element that is converted to a material type hysteresis so that the stress-strain curve can be directly inserted. The density of the tendon is set to 1165 kg/m^3, which is the average value for ox tendon (Duck, 1990). The parameters are a function of muscle fiber composition (Winters & Stark, 1985) and are assumed to be the same for infant extra-ocular muscles in the parameter study. The activation dynamics can be modeled by solving two differential equations simultaneously for the neural excitation and general activation. However, this study will consider the muscles to be passive by specifying the activation (A in 8.2) at a low value of 0.005 to represent the minimal active rest-state (Hatze, 1977).

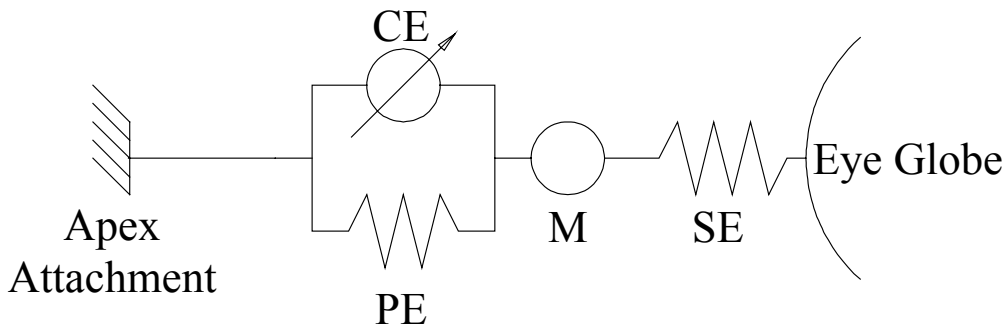

Figure 8.10: Hybrid analytical muscle-tendon model used in the infant eye SBS and impact simulations.

Table 8.0: Material properties and element number for the eye model.

Ocular Component	Element Type	Element No#	Element Property	Material Type	Material Parameters	Thickness (mm)	Density (kg/m^3)
Cornea	4-node shell	60	MEM4 reduced integration	ISOLIN Tension only	E= 124 MPa / ν = 0.42 / Reduction factor = 0.01	Figure 8.0 (varies)	1076
Sclera	4-node shell	872	MEM4 reduced integration	ISOLIN Tension only	E = 358 MPa / ν = 0.49 / reduction factor = 0.01	Figure 8.0 (varies)	1243
Vitreous	8-node hexahedral	7300	SOLID8 reduced integration	ISOLIN	E= 43 Pa/ ν= 0.49/ damping = 200	-	1006
Aqueous	8-node hexahedral	304	SOLID8 reduced integration	ISOLIN	E = 43 Pa / ν = 0.49 / damping = 200	-	1006
Ciliary Body	4-node shell	112	MEM4 reduced integration	ISOLIN Tension only	E = 0.35 MPa / ν = 0.40	0.2	1600
Lens	4-node shell	120	SHELL4	RIGID	-	-	-
Retina	4-node shell	772	MEM4 reduced integration	ISOLIN	E = 20 kPa / ν = 0.49	0.14	1000
Choroid	4-node shell	772	MEM4 reduced integration	ISOLIN	E = 96.8 kPa / ν = 0.49	0.16	1000
Tendons	3-node shell	48-96	MEM3 Reduced integration	HYSISO Tension only	Table 8.1 SE element properties Reduction factor = 0.1	0.2	1041
Fatty Tissue	4-node tetrahedral	16552	SOLID4	MOON RIV	Verver study: A = 1.65 kPa / B = 3.35 kPa / ν = 0.49 Samani & Plewes study: A = 310 Pa / B = 300 Pa / ν = 0.49	-	928.0
Skin	4-node shell	272	MEM4	ISOLIN	E = 0.15 MPa / ν = 0.46 / damping = 0.05	1	1000

Table 8.1: Hill-type parameters for the CE, PE, and SE elements. Parameters are based on the work of Winters & Stark (1985 & 1988) and Winters (1985).

Hill-type parameter	Element type	Symbol	Value
Maximum muscle force	CE	F_{max}	0.909
Maximum shortening velocity	CE	V_{max}	0.495
Shape force-velocity shortening	CE	CE_{sh}	0.437
Shape force-velocity lengthening	CE	CE_{shl}	0.0797
Ultimate tension during lengthening	CE	CE_{ml}	1.381
Width of active force-length curve	CE	S_k	0.35
Relative elongation	PE	PE_{xm}	0.258
Shape force-length curve	PE	PE_{sh}	3.321
Shape force-length	SE	SE_{sh}	1.64
Relative elongation	SE	SE_{xm}	0.091

Two optic nerve models are presented in this parametric model. The first (Figure 8.5.A) model utilizes previous mathematical models for horizontal eye motion (Lehman & Stark, 1979; Robinson, 1981; Lehman & Stark, 1983; Winters & Stark, 1985; Winters & Stark, 1988). These analytical models consider the eye to be the "plant" which acts as a revolute joint in the horizontal motion models. Originally, the stiffness and damping were measured by Collins, Scott, and O'Meara (1969) during eye surgery and can be modeled as the following (Lehman & Stark, 1983):

$$I\ddot{\theta} + c\dot{\theta} + K\theta = N \qquad (8.3)$$

Where I, c, and K are the plant parameters $3x10^{-7}$ kg-m^2, $1x10^{-4}$ Nms, and $1x10^{-3}$ Nm (Winters & Stark, 1985), respectively. Scaling these parameters to an infant yields the following for I, c, and K: $3x10^{-8}$ kg-m^2, $1x10^{-5}$ Nms, and $1x10^{-4}$ Nm, respectively. Conversion to translation values from rotational is achieved by using the infant eye radius (7.1 mm). These values are then introduced into a non-linear 3-D Kelvin element material that is composed of axial, bending, and shear characteristics (Figure 8.11).

The second (Figure 8.5.B) model is based on the work of Sigal, Flanagan, and Tertinegg (2004), where the biomechanics of the ONH and lamina cribrosa are of interest. The material parameters for the finite element nerve (Sigal nerve) are averaged values from previous literature and all considered linear elastic for a static finite element analysis (Table 8.2). The density is not reported in Sigal et al. and is set to 1000 kg/m^3. This density is within published values for spinal cord nerve tissue (1038 kg/m^3) (Duck, 1990). The pia mater thickness in Sigal et al. is set to 0.06 mm; however, for the infant eye model the thickness is increased to 0.535 mm so that pia represents the outermost optic nerve sheath. Sigal et al. do not model the dura layer (Hayreh, 1984) and only consider the pia as the outermost layer. The ONH thickness is set to 0.6 mm as well. The Poisson's ratio (ν) is assigned a value of 0.49 for incompressibility and 20% material damping is assigned (MADYMO, 2006). In comparison to the analytical model, the optic nerve is an over-damped system (Lehman & Stark, 1983).

Table 8.2: Material properties and element number for the Sigal and analytical spring optic nerves.

Ocular Component	Element Type	Element no# for Sigal nerve	Element no# for spring nerve	Element Property	Material Type	Material Parameters	Thickness	Density
ONH	4-node shell	12	12	MEM4 reduced integration	ISOLIN	E=3x10^5/ ν = 0.49	6x10^{-4}	1000
Neural Tissue	8-node solid	168	0	SOLID8 reduced integration	ISOLIN	E=3x10^4/ ν = 0.49/ damp =0.2	-	1000
Pia Mater	4-node shell	224	0	MEM4 reduced integration	ISOLIN	E=3x10^6/ ν = 0.49/ damp=0.2/ reduction factor=0.01	5.35x10^{-4}	1000
Spring Nerve	2-node beam	0	4	BEAM2 DISCRETE	KELVIN 3D_NL	Figure 8.11	-	-

The presented optic nerve models are simplified to model the tethering effects to the eye globe. Actually, the optic nerve contains a cerebral fluid layer between the dura and pia mater that is greater just posterior the ONH entry point. This fluid build up causes the nerve sheath to be bulbous at the ONH entry point (Hayreh, 1984). There are also concerns with hemorrhages in the optic nerve (Levin, 2000); however, this model limits the study to the investigation of retinal forces.

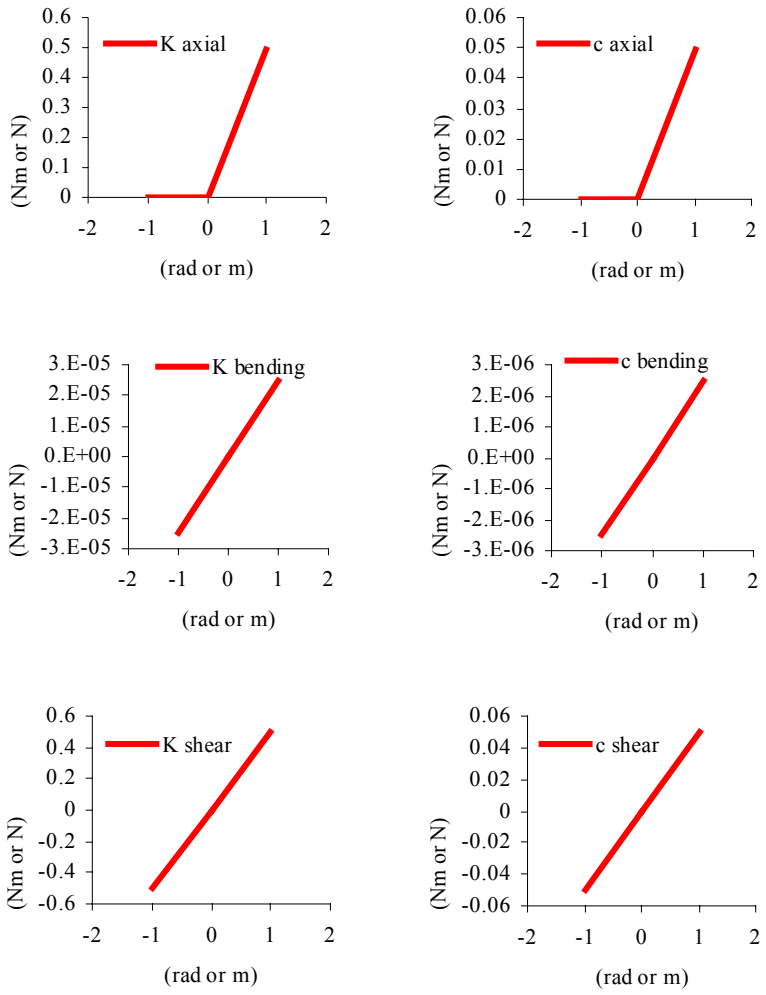

Figure 8.11: Spring-Nerve stiffness characteristic functions for axial, bending and torsional resistance for the infant optic nerve.

Retinal Detachment

On the possibility of posterior retinal detachment, Levin (2000) suggests that failure in the retinal-vitreous layer would not occur as the retina and vitreous are tenaciously attached. Levin explains that it is possible to have focal or complete detachment of the retina in severe shaking. A forensic pathological study indicates that the incidence of retinal detachment is 63% (Green et al., 1996). Levin does indicate that observations in hemorrhagic detachment are rare. This rarity is possibly due to the resorption times of the retinal to the pigment epithelium (Negi & Marmor, 1986) and the lapse in time in diagnosing SBS.

The current model investigates retinal detachment between the choroid and retina in the posterior eye by using a node-node weld technique (Figure 8.12). The retina and choroid nodes that are once common in the posterior eye are separated and the retinal node is then nudged in the normal direction away from the choroid layer a distance half the thickness of both the choroid and retina. A node-node weld algorithm is then specified using the following (MADYMO, 2004):

$$\left|\frac{F_n}{F_{n_{\max}}}\right|^{a_n} + \left|\frac{F_s}{F_{s_{\max}}}\right|^{a_s} < 1 \qquad (8.4)$$

Where F_n is normal force (the line connecting the two nodes), F_s is the shear force (perpendicular to the line connecting the two nodes), F_{nmax} and F_{smax} are the maximum allowable normal and shear force components, a_n and a_s are the exponents that determine the shape of the rupture. Therefore, if one were to consider purely normal force, the exponents would equal infinity. If only shear is considered, the

exponents would each equal one. Finally, if a combination of normal and shear force is required, the exponents would each equal two.

The current maximum force for retinal adhesion is adapted from monkey eyes (0.14 N/m) (Kita & Marmor, 1992) with no distinction of normal or shears. The bleb formation in the Kita and Marmor study would indicate that this force is normal. Further investigation in the eye simulation showed the weld attachment between the two nodes to behave as a rod attached to spherical joints. This would imply that the highest component of failure would be in the normal direction with this node-node weld. Therefore the maximum normal force (F_{nmax}) is set equal to 0.14 N and the exponents are given extremely high values, while an arbitrary value is set for maximum shear force (F_{smax}).

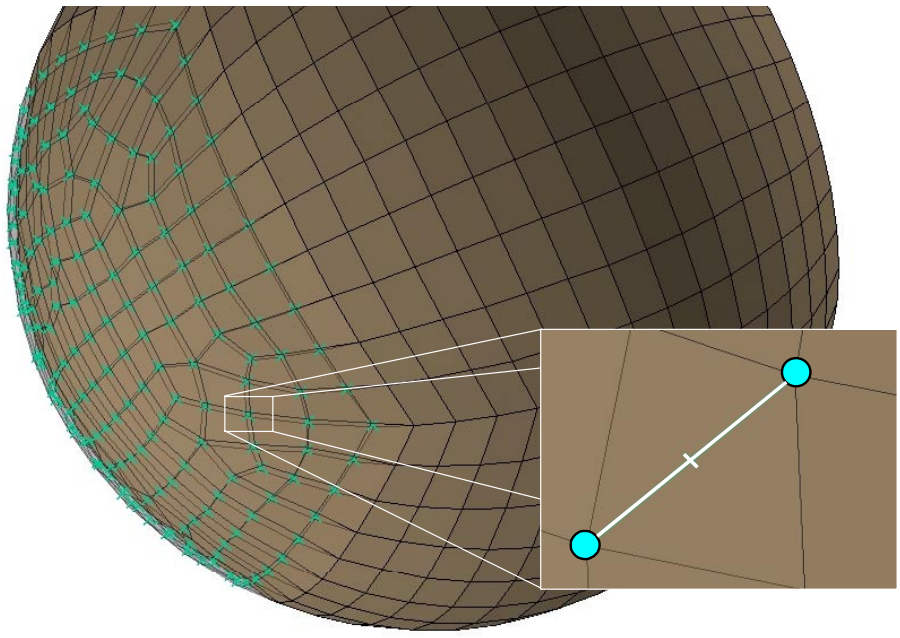

Figure 8.12: Detail of node-node weld implemented in the biomechanical model between the choroid layer (wire-frame) and the retinal layer (shaded-wire-frame).

Contact Interactions

There are three contact interactions specified in the model, depending on the type of simulation. A contact interaction is a relationship between at least two finite element structures where the nodes of one surface interact with the elements of another. Further enhancements to a contact specification can include node-to-edge contacts, self-contacts, and contacting nodes to defined gaps. Gaps are extensions of the element surfaces in the normal direction and help minimize a physical gap between finite element structures. During a given time step, three phases are performed involving a search phase, a detailed search phase, and a force calculation phase (MADYMO, 2004). Ultimately, if a node is penetrating an element or gap of an element, a force is applied to position the node at the surface of the element. The algorithm used for all contacts in this parametric study uses a penalty method (MADYMO):

$$F_c = \left(\frac{K}{V_0}\right) A^2 \psi \left[\min\left(\lambda, MAX\_FORCE\_PAR \cdot t_e\right)\right] \qquad (8.5)$$

Where MAX_FORCE_PAR, a tuning parameter, is equal to 1.0; F_c is the contact force; K is the bulk modulus of the contact segments penetrated; V_0 is the initial volume of the contact segment; A is the area of the contact segment; ψ is the penalty factor (default value is 0.1 and is recommended in MADYMO not to change); λ is the penetration of the contact node; t_e is the penetrated element thickness that is multiplied by the MAX_FORCE_PAR. The fatty tissue utilizes a contact gap to reduce the overall geometrical gap between the eye globe and tissue (Figure 8.13). The contact interactions use the surface elements of the fatty tissue and the nodes of

the cornea and sclera. The tendon-to-sclera contact lowers the penalty factor (ψ) to 0.1 lower the overall force as the nodes of the tendon contact the elements of the sclera shell. This reduced the artificial nodal velocities that resulted due to the contacting algorithm while still providing realistic interactions. No contact gap is specified for the tendon-to-sclera contacts.

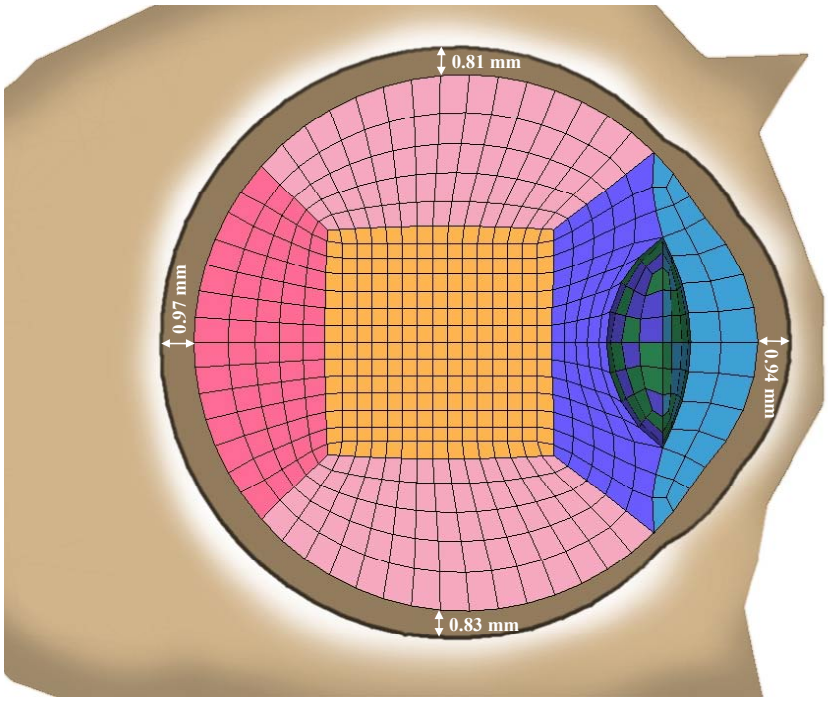

Figure 8.13: Sagittal view of eye model showing the geometrical gap dimensions between the fatty tissue and eye globe.

Finally, the simulations that include retinal detachment need to have a contact interaction specified between the choroid and retina surfaces. In this case the MAX_FORCE_PAR is reduced to 0.1, the same as the tendon-to-sclera contacts. Failure to specify this contact interaction would result in the retina-vitreous exiting

the posterior eye shell when a weld is breached. The welds would also be compromised as the material exists the eye globe due to momentum build-up, and the simulation would therefore be incorrect.

Pure Shaking Motion

In order to model SBS, a motion is modeled such that when a baby is held by the torso and shaken back and forth along the sagittal plane, the motion is similar to harmonic oscillations about the neck pivot (Morison, 2002). The motion is applied directly to the pivot point at the base of the infant's skull location by applying the angular and translational accelerations versus time using Figure 8.14.

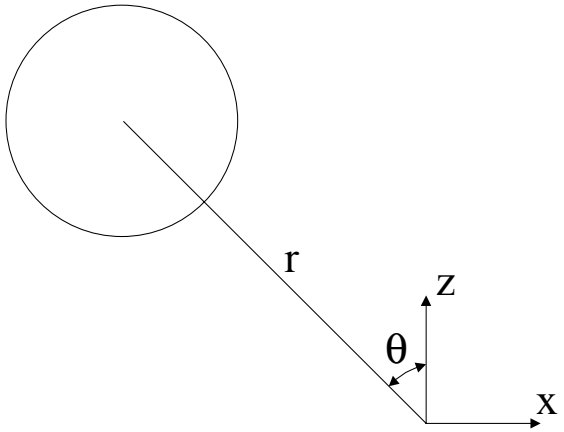

$$\theta = \theta_0 \cos(\omega t) \tag{8.6}$$

$$\dot{\theta} = -\omega\theta_0 \sin(\omega t) \tag{8.7}$$

$$\ddot{\theta} = -\omega^2\theta_0 \cos(\omega t) \tag{8.8}$$

$$\ddot{x} = r\left(\dot{\theta}\sin(\theta) - \ddot{\theta}\cos(\theta)\right) \tag{8.9}$$

$$\ddot{z} = -r\left(\dot{\theta}^2\cos(\theta) + \ddot{\theta}\sin(\theta)\right) \tag{8.10}$$

Figure 8.14: Motion of infant skull adapted from Morison (2002).

In order to incorporate this motion into the eye model, rigid bodies are located to model the locations of the neck pivot location, head cg, and lumped brain mass. The

current simulations do not need the mass properties of the rigid bodies even though they are included as the motion information (8.8, 8.9, 8.10) is used in the prescribed acceleration. The head weight is 820 grams and is the average value reported in Duhaime et al. (1987). The total brain mass is 500 grams from Duhaime et al., while scaling from a 50 percentile[14] gives a mass of 685 grams. The pivot joint is a free joint with angular acceleration about the Y-axis prescribed and translational accelerations in the X and Z-axes prescribed. From Figure 8.14, the moment arm (r) is the distance from the neck pivot to the head center of gravity. A reported neck length of 4.0 cm is used in the moment arm (Duhaime et al.). The frequency of 4 Hz is directly from Duhaime et al. (circular frequency, ω, is 25.13 rad/s). Based on the maximum range of 20 infant heads, the amplitude of motion is measured with a goniometer by Dr. Sunderland (Birmingham Children's Hospital), Morison specifies the amplitude (θ_0) equal to $\pm 60°$. Finally, a gravity field is applied to the eye model in the downward direction. The motion is applied for one second for a total of four complete oscillations starting at -60° for a worst case starting position. Figure 8.15 shows details the overall motion for one half of an oscillation cycle with start position at -60°.

[14] The term 50 percentile refers to the size and weight of an "average" adult male population (MADYMO, 2004).

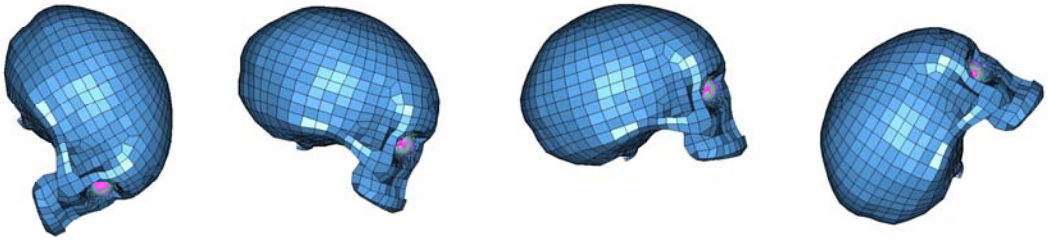

Figure 8.15: Animation sequence of a shake (Figure 8.14) for times 0, 50, 75, and 125 milliseconds.

Impact Pulse

A documented impact scenario (Duhaime et al., 1996) is included for comparison to the pure shaking case. In this case, a father is swinging a 9-month-old baby in a hunched over manner with hands underneath the legs. The arms of the father support the baby's torso as the father swings to-and-fro. Unfortunately, the baby falls backwards through the father's arms whilst the father is gripping the baby's legs. The distance of the fall is approximately 30-45 cm. The infant strikes the back of his head on the floor. At the emergency room, a CT scan reveals blood over the left hemisphere with unilateral hemorrhaging in the retina in the posterior pole of the left eye. After a couple of days, the baby recovers. No description of the impacting surface is given nor the manner of the swing.

Assuming no momentum build up due to the swing is present and only gravity is applied, an impact simulation is created. The contact interaction between the floor and the infant's head is assumed to be rigid. The distance of the fall is interpreted as the distance the father held the baby by the legs to the floor and is set to 45 cm. A TNO P3/4 (MADYMO, 2004) child dummy, representing a 9-month-old child, is positioned in a seated position with a rigid body cylinder underneath the legs

modeling the grip of the father's hands. Applying a gravity field to the dummy results in an impact to the head (Figure 8.16) with measured pulse approximated by a half sine with amplitude 60 G's for duration of 15 milliseconds. This pulse information is directly applied as a field to the eye globe fixing the all the rigid bodies to prevent motion of the skull during the impact. The total simulation duration is 100 milliseconds allowing suitable time for the eye to rebound back to its pre-impact state.

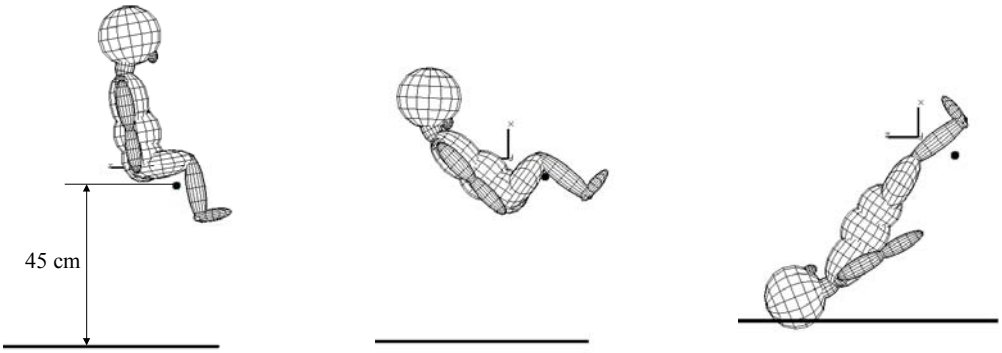

Figure 8.16: Impact sequence of the P3/4 child dummy at times 0, 275, and 475 milliseconds.

Simulation Matrix

Simulations are conducted for the impact and pure shaking inputs (Figure 8.17). A cross comparison is conducted with the type of optic nerve and the material property of the fatty tissue. In addition, an investigation into retinal detachment is considered using the node-node weld syntax in the eye model. The fatty tissue from Samani and Plewes (2004) is extremely compliant and fails in the impact simulations but is very stable in the pure shaking runs. The Verver (2004) is able to complete

every simulation scenario. Retinal detachment is only considered for the pure shaking runs since the impact simulations involve the eye globe depressing into the posterior direction and involves little shear or tension of the retinal-choroid layer. The total simulation time for the pure shaking runs is 1000 milliseconds and includes four cycles. The impact pulse simulation runs are 100 milliseconds in length. The total processing time for the impact runs is just over an hour on a four-processor computer. This time is increased to just over 10 hours for the four-cycle pure shaking simulations.

Table 8.3: Simulation matrix for both the pure shaking and impact runs.

	Optic Nerve Type	Fatty Tissue Type	Welds
Pure Shaking	Analytical nerve	Samani & Plewes, 2004	No
	Analytical nerve	Verver, 2004	No
	Analytical nerve	Samani & Plewes, 2004	Yes
	Analytical nerve	Verver, 2004	Yes
	Sigal et al., 2004	Samani & Plewes, 2004	No
	Sigal et al., 2004	Verver, 2004	No
	Sigal et al., 2004	Samani & Plewes, 2004	Yes
	Sigal et al., 2004	Verver, 2004	Yes
Impact Pulse	Analytical nerve	Verver, 2004	No
	Sigal et al., 2004	Verver, 2004	No

Results and Discussion

A comparison is made with the various runs from the simulation matrix (Table 8.3) regarding the resultant nodal force of the posterior retina. In addition, an

investigation into retinal detachment is presented. In the order of the simulation matrix, screen captures are presented for all pure shaking and impact simulations (Figures B.1 to B.10). Specifically, the figures for the pure shaking simulations are separated into four rows corresponding to each of the cycles during the 1000 millisecond time duration (4 Hz shake). Each of the rows contains five time divisions starting at the beginning and end of the shake cycle. A cycle is the total time it takes for the infant head to traverse the entire amplitude (±60°). Each of the figures is sliced along the sagittal plane of symmetry of the eye exposing the vitreous and other interior components of the eye. The orientation of each figure is in the -60° as the camera view is locked onto the eye globe itself so that the focus remains on the eye. The impact simulation Figures (B.9 and B.10) also show the eye globe from the sagittal plane with six animation views (0, 5, 10, 15, 50, and 100 milliseconds).

A comparison (Figure 8.17) is made between the eye model that utilizes the analytical optic nerve and the two fatty tissue materials (Samani & Plewes, 2004; Verver, 2004). In addition, a limit line is indicated showing the 0.14 N retinal detachment force (Kita & Marmor, 1992). A total of 273 retinal nodes make up the posterior region of the eye. For each node, the output frequency is 10,000 Hz. Accounting for every node for both simulation is an extreme amount of data to process for the resultant nodal forces. However, the only information of interest are the maximum values at each time. Therefore, at a given time step all 273 nodal forces at that time step are evaluated so that only the maximum value is returned. What results is a concise plot showing the same plot information as if all forces are

plotted without the minimum values. This process is continued for all of the nodal force plots.

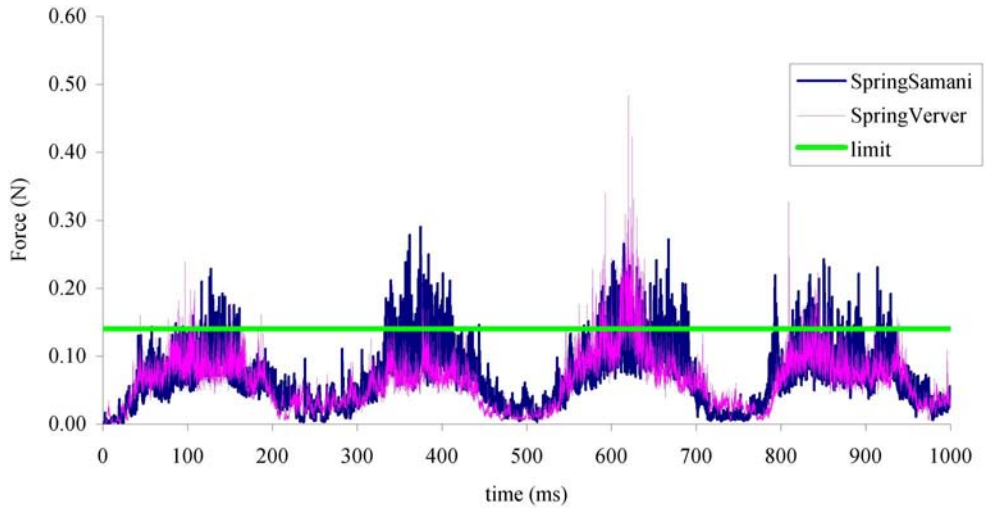

Figure 8.17: Resultant posterior retina nodal forces for shaking only with the analytical optic nerve.

Comparing the two resultant force plots (Figure 8.17), each of the cycles is clearly outlined as nodal forces follow a harmonic pattern. The approximate peak of each cycle occurs when the head is at the +60° amplitude of the shake. Despite the harmonic acceleration being applied to the sagittal plane of the eye, the model is not symmetric due to the off-center optic nerve insert and the asymmetrical muscle tethers (oblique tethers). As a result, each cycle is a little different. The most severe simulation involves the use of the more compliant Samani and Plewes fatty tissue, which results in a larger bandwidth of force at the top of each cycle. The simulation utilizing the Verver fatty tissue shows similar trends but not as extreme until the third

cycle. Comparing the animation time sequence data between the two runs (Figure B.1 and B.2) shows localized pinching of the posterior eye globe as the infant head goes into the +60° limit and then back down again with the eye globe reclaiming the original spherical shape at the -60° limit. This local pinching is attributed to the use of simple constraints (Figure 8.5.C) and the lack of resistance to bending of the ocular shell layers. Otherwise, the animation cycles are almost indistinguishable with the only visible difference being the more severe deflection of the Samani and Plewes tissue (Figure B.1).

A similar comparison is conducted utilizing the Sigal et al. nerve model and the two fatty tissues for the shaking only simulation. Comparing the animation sequences (Figures B.5 and B.6) indicates no localized globe pinching as in the case with the analytical optic nerve. In addition, little deformation of the vitreous body is detected with the exception of the central block swaying about due to the external motion. Comparing the retinal forces (Figure 8.18) shows a similar non-eventful trend. The forces are well below the retinal detachment threshold with the exception of a few spikes in force. The finite element optic nerve is over constraining the eye globe instead of acting as a tether. At the apex connection, the optic nerve is supported by a translational body with negligible mass to allow sliding along the length of the optic nerve and to introduce slack. However, the motion of the shake and the asymmetrical location of the nerve cause localized bending resistance at the ONH interface.

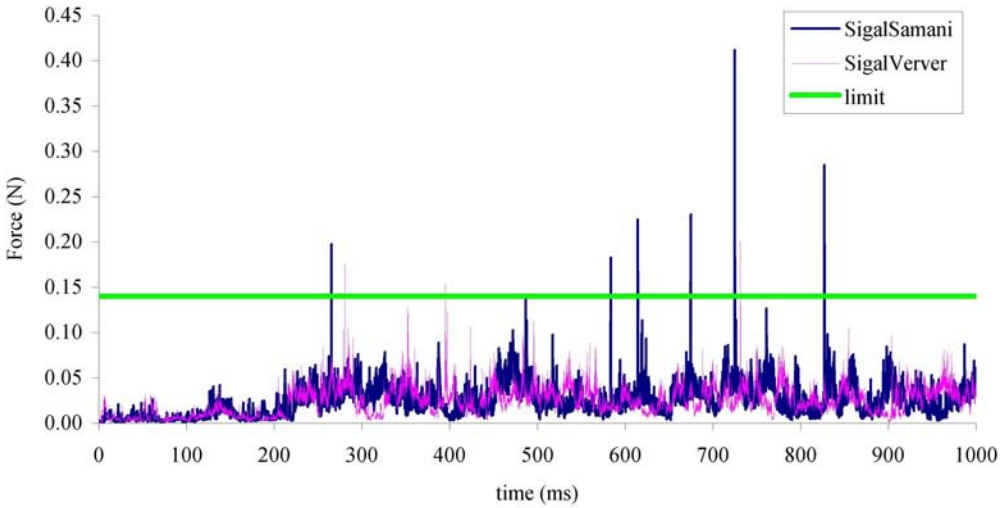

Figure 8.18: Resultant posterior retina nodal forces for shaking only with the finite element optic nerve.

The impact simulations utilize the Verver fatty tissue materials comparing the analytical optic nerve to the finite element optic nerve. The Samani and Plewes material properties are too compliant for the current fatty tissue tetrahedral mesh model and become unstable after about 10 simulation milliseconds. Comparing the animation sequence (Figures B.9 and B.10) shows very little difference between the two nerve choices. The response is visually identical and is perhaps attributed to the support of the finite element nerve allowing free motion along the axis of the nerve and the analytical model axial spring force set to zero for compression. In short, the optic nerve is all but removed from the model due to the application of the pulse. The nodal resultant force of the posterior nodes also is in approximate agreement with each other (Figure 8.19) where comparison shows forces well below the threshold limit.

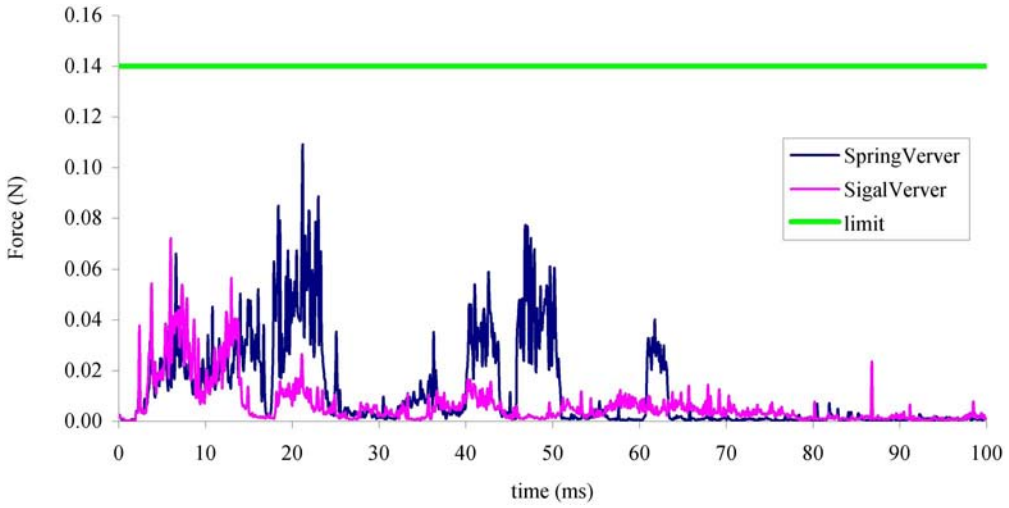

Figure 8.19: Comparison of the posterior retina resultant nodal forces for both optic nerve models with the Verver (2004) fatty tissue.

There are some differences between the two results (Figure 8.19) that are attributed to rebounding of the eye globe and the reaction of the optic nerve. For the first 15 milliseconds, both plots are very similar until after 15 milliseconds to 25 milliseconds when the analytical optic nerve model shows an increase in nodal force before dropping to similar levels around 30 milliseconds. Between 40 and 50 milliseconds the force is again increased due to stretching of the optic nerve causing some localized retinal forces to increase a bit. Again, the analytical nerve shows much greater values than the finite element nerve model.

A comparison is presented for the eye model utilizing the analytical optic nerve and the fatty tissue using the Verver material properties (Figure 8.20).

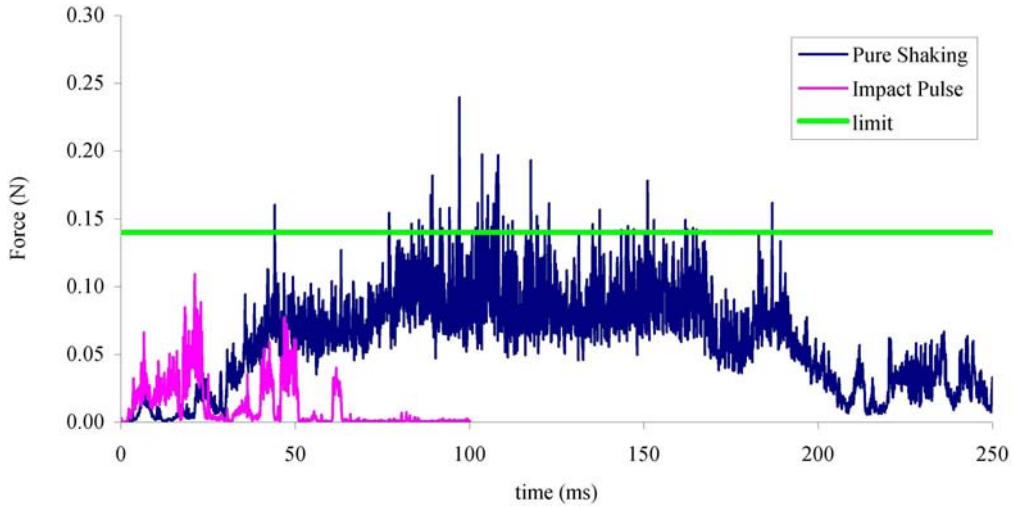

Figure 8.20: Resultant posterior nodal forces for both the shaking and impact simulations using the analytical optic nerve model with the Verver material for the fatty tissue.

In Figure 8.20, the first cycle of the shaking is shown compared to the 100-millisecond duration of the impact simulation. Immediately apparent is the breach of force for the pure shaking, while the impact is well below the limit. This would indicate that forces due to shaking that involve shearing as the eye globe rotates causing stress areas when the nerve and muscles are engaged in full tension.

Retinal weld results are examined (Figures B.3, B.4, B.7, & B.8) for four cases and compared (Figure 8.21). The inclusion of the retinal detachment is extremely experimental, and there are limitations to the model as a result. As seen in Figures B.3 and B.4, the analytical nerve is attached to the ONH using simple constraints. A modeling limitation in MADYMO is that nodes involved in simple constraints or welds cannot be included in other types of welds or simple constraints. Therefore, the retinal attachment point at the ONH head will never separate. This issue does not exist in the model using the finite element optic nerve (Figures B.7 and

B.8), and as a result, the entire posterior retina can separate from the choroid. To interpret Figure 8.21, the total number of welds at the start of the simulation is 100%. As the simulation time increases for the shaking run, the welds start to fail and the time is recorded for each weld failure. The trend of the models using the analytical optic nerve start at 100% but quickly decline (more so for the Samani and Plewes fatty tissue material) to less than 10% total welds left before the first shake cycle is complete. The values for the model using the finite element optic nerve (Sigal nerve) stay at 100% until 200 milliseconds for the Verver fatty tissue material and 250 milliseconds for the Samani and Plewes fatty tissue. While the analytical nerve in the eye model showed similar trends in weld breaks for the different fatty tissue materials, the use of the Sigal nerve is quite different. At 200 milliseconds a significant drop in welds is seen in the SigalVerver eye model (about 75% welds are left). Then a plateau region occurs from 200 to 350 milliseconds, after which, almost all welds are broken and the retina-vitreous completely separates (Figure B.8 at time 437 milliseconds). The SigalSamani run maintains a plateau up to 500 milliseconds with two reductions at 250 milliseconds to 95% and then to 90% at 500 milliseconds. Just before 550 milliseconds a large amount of welds break leaving only 40% left for the rest of the simulation.

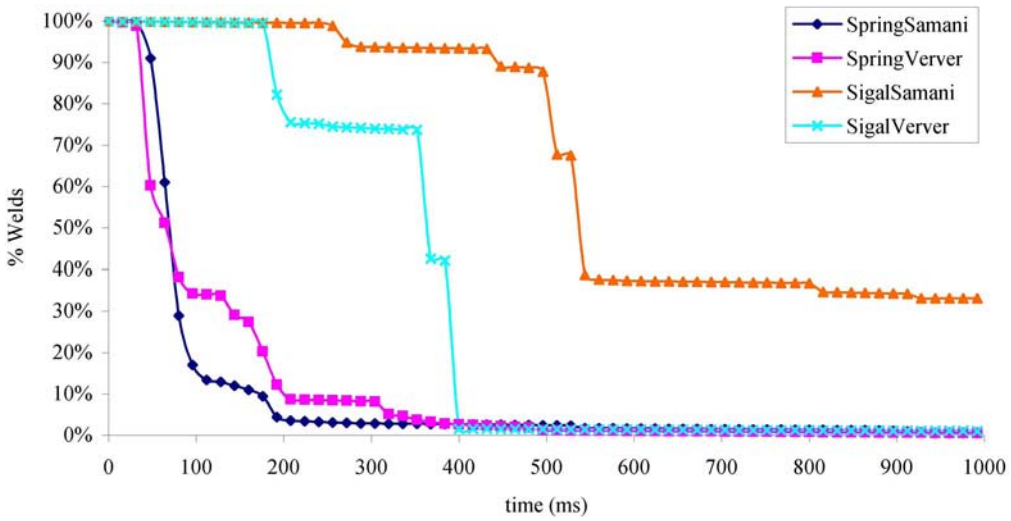

Figure 8.21: Retinal node welds for all eye models in the pure shaking motion runs.

The inclusion of the retina node welds neglects the strain rate characteristics of the applied force (Deguillebon & Zauberman, 1972) and only considers the instantaneous force limit. Indeed, increasing the time delay before a weld breaks to just one-millisecond results in no weld breaks at all. This is not surprising since most of the forces are only short duration peaks (Figure 8.17). Ideally, to model retinal adhesion would be to consider the retina-choroid interface by having the nodes of each structure start at a coincident location until a strain rate or force is applied that would separate the two (Kostopoulos et al., 2002). However, the current limitation of the node-node weld requires a distance greater than zero between the nodes and only allows the input of rupture force, the shape of the rupture, and a time window of rupture (see equation 8.4).

Conclusion

The parametric investigative eye model is the first to address retinal forces as a result of shaken baby syndrome. Although the finite element model is not validated as no experiment has been conducted (and may never be) to validate such a model. The best that can be done is to provide a comprehensive study of all possible materials that exist. In regards to material properties, the infant and infant eye has unique physiological characteristics (Levin, 2000) that specifically predispose them to injury due to shaking. Unfortunately, there are no materials testing of the ocular components of infant eyes currently in existence that can be utilized in a mathematical model. There are several clinical observations and histological studies that describe the geometry and qualitative properties that can be used to influence the finite element model.

Some conclusions can be formulated about the current study. The first consideration looks at the tethering of the eyeball where the passive muscles and slack nerve are firmly attached to the eyeball. Levin coins the term "orbital shaking" where the eyeball rotates and, at the limits of the optic nerve length, causes stresses on the eye. Further, this also explains hemorrhaging in the optic nerve sheath itself. In order to model this in a violent dynamic simulation, two camps of research are considered.

One group (Lehman & Stark, 1979; Robinson, 1981; Lehman & Stark, 1983; Winters & Stark, 1985; Winters & Stark, 1988) models the eye in dynamic simulations with original measurements of the orbital tissue damping and stiffness performed by Collins, Scott, and O'Meara (1969). These models are extensive and

complete and lend themselves to be easily incorporated into the MADYMO software, which allows coupling between rigid body dynamics and finite element method. Another benefit is that these properties are easily scalable to infant dimensions provided that the eye would respond the same for an infant as an adult, which may be an invalid assumption.

The second group of studies focuses efforts on glaucoma studies and the effects of the lamina cribrosa (Dongqi & Zeqin, 1999; Edwards & Good, 2001; Bellezza, Hart, & Burgoyne, 2000; Sigal et al. 2004; Burgoyne et al., 2005). Of these studies, the most applicable for use in the current model is the work from Sigal et al. where static finite element analysis is conducted centered on the strain levels in the lamina cribrosa. The authors provide a literature review of material candidates that are very approximate and averaged. Unfortunately, some of these small, delicate structures have little information on mechanical properties, so substitutes are used. For example, the neural tissue in the optic nerve is approximated by brain and spinal cord tissue. This is perhaps a valid assumption, but only testing can verify this.

Inclusion of these materials into a finite element optic nerve is rather crude to only consider the optic nerve a tether in this case. Simplifying the optic nerve components adversely affects the overall kinematics of the eyeball by stiffening the motion. The optic nerve does not behave totally as a slack tether despite the apex fixation allowing translation along the axis of the nerve. In order to use this model, complexity needs to be introduced into the optic nerve so that the structure is more compliant. This would involve building the dura, cerebral fluid layer, pia layer, arachnoid layer, and optic nerve tissue. Specifically, just posterior the ONH, the

optic nerve is bulbous with a greater amount of fluid between the sheath and nerve tissue (Hayreh, 1984). This would create a more narrow and compliant interface to the eye globe. However, the current model considers the materials and model build up from Sigal et al. with modifications to the outermost pia layer so that it is more representative of the dura. This would also add stiffness to the nerve sheath. Therefore, there is more confidence with the analytical optic nerve model as this was derived from previous dynamic models and previous measurements of the overall response.

The next parameterized material is the fatty tissue. Surprisingly, the eye globe kinematics are more sensitive to the different optic nerve models considered; however, there are higher forces associated with the more compliant Samani and Plewes (2004) material properties for the harmonic shaking. Unfortunately, this same material was too compliant in the impact simulations, so the stiffer Verver (2004) material is also considered.

One of the most important structures to consider is the vitreous body. At birth and early stages of life this vitreous body is very gelatinous and tenaciously attached to the retina (Levin, 2000). Most studies consider this material viscoelastic (Bettelheim & Wang, 1976; Tokita, Fujiya, & Hikichi, 1984; Lee, Litt, & Buchsbaum, 1994; Nickerson et al., 2005); however these studies did not consider finite element analysis with Lagrangian meshes. For gentle eye motions these materials would perform reasonably well but are simply too compliant to use in a violent motion of the eye. In addition, there is debate regarding the inappropriate handling and testing of these delicate structures (Nickerson et al., 2005). The vitreous

determination from Weber and Landwehr (1982) approached the vitreous in a non-invasive manner and postulated the material as "rubber-elastic." No other study since as made such a conclusion; however, the material performance is stable in violent simulations. The only other option would be to model the vitreous using a bulk modulus in a hydrostatic formulation (Uchio et al., 1999; Stitzel et al., 2002). However, the current study only considers the material from Weber and Landwher. One of the pinnacle advancements that could be made to this model is to have material testing on infant vitreous, as this material is physiologically different from adults and would certainly affect the retinal-choroid layer.

Very little information is given about the retina and choroid, and this is the first model to include these structures in a dynamic finite element model. Currently, the model considers the retina and choroid to have uniform thickness with homogenous elastic properties. These assumptions are based on very limited mechanical property studies. Of interest is the retinal adhesion studies which give force values ranging from 0.1 to 0.14 N (Zauberman & deGuillebon, 1972; Kita & Marmor, 1992). These studies are useful for understanding the current retinal forces-assuming that these forces are appropriate for infant retina.

The motion studies for shaken baby syndrome are well quantified (Duhaime et al., 1987; Morison, 2002) and provide a continuation. In fact, the infant brain model from Morison addresses further work in this area would include the eye model for study of retinal hemorrhaging. Therefore, using the same harmonic shaking motion would seem appropriate. Also important to consider are impact studies. As diagnosis of shaken baby syndrome would directly place caretakers as perpetrators of violence,

the most common cover up of shaking would be to say that the infant fell. However, falls less than four feet that cause death are very suspicious (Chadwick et al., 1991).

Accidental injuries such as bilateral retinal hemorrhaging have not been able to show similar patterns as SBS (Elder, Taylor, & Klug, 1991; Johnson & Braun, 1993; Reiber, 1993; Duhaime et al., 1996). Duhaime et al. (1996) provide a unique study where an actual accidental injury is witnessed with clinical examination allowing for the reproduction of the scenario using a TNO P3/4 (MADYMO, 2004) child dummy, representing a 9-month-old child. As the clinical examination states there was indication of retinal hemorrhaging in the left eye with blood over the left hemisphere of the brain.

Considering the retinal forces in the simulation, they are not high enough for retinal detachment in the Kita and Manor study assuming adhesive strength is the same as monkeys; however, the lower bound is 0.1 N for rabbit retina and they do manage to just breach this bound (Figure 8.20). What is quite remarkable is the comparison of the posterior retinal forces for the shake and impact simulations (Figure 8.20). This is no indication that the current study is validated; however, it does provide insight into the mechanisms of possible retinal hemorrhaging and supports clinical observations further bolstering the fact that shaking without impact causes injury in infants.

CHAPTER IX

CONCLUSIONS

Modeling Assumptions

A comparison is presented between various vitreous materials from the literature. From this important review, as presented in chapter 7, another layer of validity is provided for these materials. Although some of the testing approaches the material as mostly a liquid, one cannot deny that the collagen fiber network inside the vitreous should preclude this assumption (especially for the infant vitreous). Serious consideration for likely candidate materials for the shaken baby syndrome and impact pulse simulations presented in chapter 8 is given to material studies that try to maintain this collagen network. Also important, constitutive equations that couple the deviatoric and hydrostatic stress components need to be ruled out as these material behaviors are overruled by the bulk modulus.

The viscoelastic properties of the Nickerson et al. (2005) test is attractive in that the shear modulus is 30 times greater than other viscoelastic studies. However, the sample is compromised by the preparation method. In addition, weeping of fluid from these samples is reported, which would increase the compliancy. The work of Weber and Landwehr (1982) is promising as inserting a steel sphere into the vitreous and controlling the motion via magnetic force maintains the integrity of the sample. In addition, Weber and Landwehr assume the vitreous to behave as a “rubber elastic” material and determine the stiffness and damping constants. Chapter 7 compares this

material with the viscoelastic materials of Nickerson et al., Bettelheim and Wang (1976), and Tokita, Fujiya, and Hikichi (1984). There is a strong resistance to shear that would be transferred to the retinal interface as reported in Levin (2000). This material would be the best fit for modeling the infant vitreous due to this high resistance to shear. Bettelheim and Wang also perform noninvasive methods of measuring the vitreous material assuming viscoelasticity. However, only four data points per sample are given, which would not allow for a reliable curve fit. An issue with all these vitreous materials is assuming the material is homogenous, which it is not. However, this is also an issue with the finite element method and needs to be understood when interpreting results. The viscoelastic materials are sensitive to mesh density as reported by Brands (2002).

Coarseness in the vitreous hexahedral mesh shows a stiffening or resistance to shearing strain for the viscoelastic materials. Comparing the more refined mesh to the courser mesh of the Weber material, in chapter 7, shows that this material is insensitive to the difference in the mesh density of the two mesh models.

Another assumption in the current study is not detailing the anterior chamber of the eye. This is perhaps a minor issue as most of the interest is with the posterior region of the eye and is rather far from the anterior chamber. The vitreous body attachment to the anterior lens and ciliary body is fixed and is consistent for adult (Wolter, 1961) and infant vitreous (Sebag, 1998). A special consideration of the infant eye is that the vitreous is tenaciously attached to the retinal interface (Levin, 2000). This would allow for the assumption that the vitreous and retina share the same boundary so that they both share the same nodes in the model. However,

furthering the assumption, the choroid, sclera, and retina share the same nodes. This assumption is based on peeling rate testing performed (Zauberman & Deguillebon, 1972), where a jerky or quick peeling rate resulted in both the choroid and retina peeling off. Therefore, the bond is considered strong for the current simulation cases presented in chapters 7 and 8.

However, at slower peeling rates the retina removes smoothly from the choroid. Test cases are considered where the retina may detach from the choroid in chapter 8. Using retina adhesion studies (Kita & Marmor, 1992), a possible means of modeling the detachment is accomplished by using a node-node weld method. Unfortunately, this method required moving the retina from the choroid so that the distance between the nodes is greater than zero. A single weld is analogous to a rod attached to one spherical joint (retina node) to another spherical joint (choroid node). This would not be an appropriate way to model the detachment. A better way would be to allow the nodes to be coincident and a force or stress applied that will remove the retina from the choroid- a delamination method.

The retina and choroid also assume a constant thickness and are homogenous elastic materials that act as perfect membranes. These assumptions are carried over from other studies that test the elastic properties of the retina and choroid. The retina and choroid are extremely thin structures, so assuming they act as membranes is a valid assumption. The thickness information and elastic assumptions may cause problems as assuming a thickness in the materials testing changes the modulus. Also in-vitro studies compromise the thickness and stiffness of the material and may not be representative of the actual structures.

The cornea and sclera shell are also considered membranes, although not on the same scale as the retina and choroid. There would be some localized bending resistance, especially in the thicker region of the sclera and cornea shell that should be considered. The current eye model assumes that this layer is a membrane, so there is no resistance to bending at the immediate attachment of the optic nerve. This causes more deformation in the posterior region of the eye during the shaking sequence in chapter 8. Compounding this deformation is the lack of self-contact interactions of the tissue structures. The self-contact is assumed to be minor compared to assuming the shell being a membrane. The cornea-sclera shell does vary in thickness; however, the thickness is defined per element so that a discrete step between the elements exists.

The optic nerve has been measured in-vivo during surgery (Collins, Scott, & O'Meara, 1969) providing stiffness and damping coefficient. Assuming that the optic nerve in this parametric model acts as a simple tether as indicated in Levin (2000) provides a means to include the nerve in the dynamic simulation. Further, confidence in this method is provided as the properties have been used in dynamic horizontal eye movement studies in the past (Winters, 1985). An experimental effort is considered regarding an optic nerve composed of hexahedral elements for the neural tissue and membrane elements for the outer sheath layers. This idea is adapted from Sigal, Flanagan, and Tertinegg (2004), where they considered effects on the laminar cribrosa. Unfortunately, the literature review of the materials used is composed of elastic values with an average modulus value assigned. Further, the current model uses a simplified version of the optic nerve geometry in order to maintain the idea of

a simple tether. However, as a result, the optic nerve using the hexahedral elements results in an over stiffening of the eye globe response and equally resists compression as well as tension. The analytical model based on specifying the stiffness and damping coefficient allows the specification of tension resistance with no resistance to compression that is consistent with allowing slack in the nerve as reported in Levin (2000). In order to use the finite element nerve based on the work of Sigal et al., it would be necessary to introduce complexity into the model so that the bulbous anterior nerve is modeled (Hayreh, 1984) just posterior the sclera shell attachment. This would also have to include a way to model the cerebral fluid between the dura and nerve tissue.

The muscles used in the current model use a Hill-type formulation with variables provided by Winters (1985) for horizontal motion. These values are based on an adult eye and not an infant eye. The assumption is made here that the adult extra-ocular muscles would have the same fiber composition as the infant extra-ocular muscles and are set to be the same. Currently, there exists no study that describes the material properties or Hill-type parameters for the infant eye. In addition, an assumption is made that all six muscles have the same Hill-type parameters. This assumption is acceptable in chapter 7, as all the other muscles are made passive allowing the lateral rectus and medial rectus to move the eye in a saccade. In chapter 8, all the muscles are considered passive as mentioned in Levin (2000) during a shake. These muscles are also made passive for the impact pulse case as well.

Distributing the muscle force are the membrane tendons that are attached to the eye globe. This provides a more realistic method of distributing the force to the sclera shell than applying point attachments. In addition, contact interaction between the tendon and sclera is specified to account for the muscle wrapping the eye during eye rotations. This is realized more in the vitreous studies in chapter 7 where a 20° saccade is induced. This contact interaction may not be as important in the impact case presented in chapter 8. The contact between the tendon and sclera shell would have more influence in the shaking sequence however.

The eye model is completely encased in the fatty tissue and eyelid with material properties compared from tissue samples from various studies presented in chapters 6, 7, and 8. No study has been done that measures the mechanical properties of the orbital fat. However, Luboz et al. (2004) did compare their tissue model with actual globe depression measurements and are able to predict tissue decompression in orbital surgery. A material that is comparable in stiffness to the Luboz et al. study is the work of Verver (2004). Verver determined the hyperelastic coefficients of fatty tissue for buttocks comfort analysis based on an average of reported values in theliterature. These values are used and compared with Samani and Plewes (2004) in chapter 8. The Samani and Plewes study used material properties from breast tissue samples and determined the hyperelastic coefficients. This material is too compliant for the impact simulation in chapter 8 but can be utilized in the shaking sequence. The most reliable material to use for the fatty tissue is the Verver or Luboz material presented in chapter 6, 7, and 8. In this study, the Verver material, which is based on average values of fatty tissue, is chosen.

The orbital fat is directly supported by the ocular cavity as in Luboz et al. and Power (2001). However, during severe simulations this could present a potential problem by either adding falsely to the stiffness of the material or causing element shape deformations that are unrealistic at the ocular cavity wall. Using the hyperelastic material and considering Luboz et al. are able to perform a validation using this support, this study considers the support assumption acceptable for the current motions applied.

The contact interaction is also specified between the fatty tissue and cornea-sclera shell. There is no information regarding the contact and what friction forces would be between the two tissues. However, it is assumed that the friction would be zero, as the fatty tissue would provide a slick surface to the moist eye globe and allow for little resistance during the quick eye movements. This assumption is based more on intuition.

A summary of modeling assumptions with support for the first version infant eye model is discussed. Based on the assumptions, the model that utilizes the analytical optic nerve, Weber vitreous body, and Verver fatty tissue is chosen for the initial modeling effort. Without conducting a parameter study by applying various force conditions and modeling conditions, it would be impossible to choose, with confidence, a preliminary model that can be potentially useful in investigating posterior retinal forces in impact and pure shaking motions.

Conclusions

The motivation of this research is to continue the biomechanical modeling of shaken baby syndrome from the bridging vein studies of Morison (2002) in order to investigate retinal hemorrhages. Several eye models have been investigated in the past and provide a starting point for this research. Unfortunately, these simulations (Uchio et al., 1999; Power et al., 2002; Stitzel et al., 2002) concentrate on direct trauma to the cornea and sclera shells. Assumptions for these types of simulations are quite different than those for runs that deal with indirect trauma through kinematics between the soft ocular tissues and surrounding structures. Assuming only a bulk modulus property or a pressure state for the vitreous may not capture the behavior at the retinal-vitreous boundary, as is the scope of this effort. Immediately apparent is the fact that the vitreous body is an extremely important, prominent, and complex structure of the eye. Modeling this structure that occupies $4/5^{th}$ of the eye globe presents a problem due to materials testing showing the vitreous to have low shear strain moduli with a high bulk modulus. Applying the finite element method using Lagrangian meshes causes severe shape deformation for the viscoelastic materials.

Literature review highlights the highly sensitivity of determining the material properties of this structure. How can one group present values below 1 Pa for the shear modulus (Bettelheim & Wang, 1976) while another reports values in excess of 30 Pa (Nickerson et al., 2005)? One could ascertain that one group mishandled the tissue or improperly conducted the experiment.

Another issue is assuming a constitutive model for the vitreous. Although many maintain the vitreous as viscoelastic, there are variations on the actual

viscoelastic model. Lee, Litt, and Buchbaum (1992) perform creep test and fit the vitreous behavior to a Burger's model while Weber and Landwher (1982) perform oscillatory tests and fit the behavior to an elastic Voigt-Kelvin model. Which is correct? In this case, they both utilize small steel spheres into the vitreous so that the integrity of the complex collagen fiber network is maintained as opposed to Nickerson et al. and Tokita, Fujiya, and Hikichi (1984) who remove the sample and prep for testing. Finally, the infant vitreous is reported to be more viscous (Zimmerman, 1980) than the adult and no group has investigated the material properties of human infant vitreous.

This work leads into the actual force mechanism investigation of shaken baby syndrome and impact dynamics. A full-featured eye model with complete surrounding boundary tissues is presented with harmonic oscillatory shaking applied. The manner of the shake is extremely violent and is derived from Morison (2002) and Duhaime et al. (1996). The investigative study addresses retinal forces to the posterior retina in an infant eye and provides some supportive results to previous clinical studies when compared to a well-documented impact due to a fall. This study provides a reasonable correlation to clinical assessments on shaken baby syndrome in that pure shaking is enough to cause retinal forces that may be consistent with hemorrhaging. Comparing an impact pulse to a pure shake, in chapter 8, illustrates that there are considerably higher retinal forces and a greater bandwidth of these forces in the pure shaking case regardless of knowing the magnitude of force needed for retinal damage.

In addition, this entire work provides parameter studies comparing previously reported values for the optic nerve, fatty tissue, and vitreous body, allowing for an increase in confidence when choosing a particular model. Further, these simulations provide a tool for highlighting possible trouble areas due to invalid assumptions by examining the model behavior under long time durations under physiological or near physiological loading conditions –something that has not been done before.

Further Work

This research effort involves building a preliminary model of the infant eye and surrounding tissues. In order to further the predictive reliability of such a model, material testing needs to be done on infant tissue even though this is controversial. The vitreous body of the infant needs to be tested so that material parameters can be refined to use in the infant eye model. Testing the vitreous body to capture material properties is not an easy process and, as the literature shows, not a consistent process. Perhaps there needs to be a new method of determining the material properties of the vitreous. Certainly, using the method of Weber and Landwehr (1982) for the infant vitreous would be interesting in order to compare it to current published values.

Currently, the optic nerve uses a simple analytical spring model to represent a tether to the eye globe. This is an acceptable assumption until there is a desire to see forces and stresses in the actual optic nerve sheath. Levin (2000) does report hemorrhaging in the optic nerve sheath as well. In order to assess forces in the optic

nerve, material parameters and the cerebral fluid layer need to be included in the model.

The current eye model considers the cornea and sclera to be a membrane. This assumption is maintained through several studies. However, when considering localized stress concentrations and bending, this assumption may not be as valid. The more correct way to model the outer most cornea-sclera shell would be to use solid elements with triaxial stress-strain characteristics included so that there is slight resistance to bending. This triaxial stress-strain characteristic would also better approximate the collagen fiber alignment in the shell (assuming that the fibers are aligned in an orthotropic manner).

Concerning the shaking sequence and impact in chapter 8, the dynamics of an actual cadaver (infant or adult) would be very useful in comparing the behavior of the optic nerve tether with the muscles attached to the eye globe. This could be achieved by tracking the motion of these structures.

Final Thoughts

When building a mathematical model to model a complex biological structure, there are several variables that need to be considered. In addition, complexity introduced into the model needs to be scrutinized, as additions may look more believable but need justification (Morison, 2002). Initial complexity added to the model caused bizarre behavior and needed removal (i.e. adding an eyelid opening caused instability with contact interaction). Each chapter provided in this work is

done in such a way that the reader hopefully understands all the details that went into the model. All aspects are important- from geometrical modeling to mesh creation to the detailed parameter studies of the ocular components. While this research is not a validation study, it does provide some insight into the modeling of the infant eye and supports clinical assessments that pure shaking is more injurious then impact alone. This work provides a continuation from Morison where mention of further refinements into biomechanical modeling of SBS would include eye modeling with retinal hemorrhaging.

BIBLIOGRAPHY

Anderson, D. R. (1995). Glaucoma, Its Terminology and Fundamental Nature. *Optic Nerve in Glaucoma* (pp. 1-14). Amsterdam, New York: Kugler Publications.

Andrews, A. (1996). Ocular Manifestations of Child Abuse. *Penn Med*, *99S*, 71-75.

Ansys. *4.82 PLANE82 2-D 8-Node Structural Solid*. Retrieved July 19, 2005, from http://www.cesup.ufrgs.br/ansys/elem_55/chapter4/ES4-82.htm

Arbogast, K. B., Thibault, K. L., Pinheiro, B. S., Winey, K. I., & Margulies, S. S. (1997). A High-Frequency Shear Device for Testing Soft Biological Tissues. *J Biomechanics*, *30*, 757-9.

Avetisov, E. S., Savitskaya, N. F., Vinetskaya, M. I., & Iomdina, E. N. (1984). A Study of Biochemical and Biomechanical Qualities of Normal and Myopic Eye Sclera in Humans of Different Age Groups. *Metabolic, Pediatric & Systemic Ophthalmology*, *7*, 183-8.

Bain, A. C., & Meaney, D. F. (2000). Tissue-Level Thresholds for Axonal Damage in an Experimental Model of Central Nervous System White Matter Injury. *J Bio Eng*, *122*, 615-622.

Ballantyne, S. A., O'Neill, G., Hamilton, R., & Hollman, A. S. (2002). Observer Variation in the Sonographic Measurement of Optic Nerve Sheath Diameter in Normal Adults. *European Journal of Ultrasound*, *15*, 145-149.

Battaglioli, J. L., & Kamm, R. D. (1984). Measurements of the Compressive Properties of Scleral Tissue. *Invest. Ophthal. & Vis. Sci.*, *25*, 59-65.

Bedell, A. (1955). The importance of ophthalmoscopic photographs in forensic medicine; Kodachromes. *Trans Am Ophthalmol Soc*, *53*, 63-73.

Behr, M., Arnoux, P. J., Serre, T., Bidal, S., Kang, H. S., Thollon, L., Cavallero, C., Kayvantash, K., & Brunet, C. (2003). A Human Model for Road Safety: From Geometrical Acquisition to Model Validation with Radioss. *Comp Meth Biomech Biomed Eng*, *6*, 263-273.

Bellezza, A. J., Hart, R. T., & Burgoyne, C. F. (2000). The Optic Nerve Head as a Biomechanical Structure: Initial Finite Element Modeling. *Invest Ophthal & Vis Sci*, *41*, 2991-3000.

Bellezza, A. J., Rintalan, C. J., Thompson, H. W., Downs, J. C., Hart, R. T., & Burgoyne, C. F. (2003). Deformation of the Lamina Cribrosa and Anterior Scleral Canal Wall in Early Experimental Glaucoma. *Invest Ophthal & Vis Sci*, *44*, 623-637.

Bettelheim, F. A., & Wang, T. J. (1976). Dynamic Viscoelastic Properties of Bovine Vitreous. *Exp Eye Res*, *23*, 435-441.

Bettelheim, F. A., & Zigler, J. S. (2004). Regional Mapping of Molecular Components of Human Liquid Vitreous by Dynamic Light Scattering. *Exp Eye Res*, *79*, 712-718.

Betz, P., Püschel, K., Miltner, E., Lignitz, E., & Eisenmenger, W. (1996). Morphometrical analysis of retinal hemorrhages in the shaken baby syndrome. *Forensic Sci Int*, *78*, 71-80.

Bill, A. (1993). Vascular Physiology of the Optic Nerve. *The Optic nerve in glaucoma* (pp. 37-50). Philadelphia: J.B. Lippincott.

Bilston, L. E., & Thibault, L. E. (1996). The Mechanical Properties of the Human Cervical Spinal Cord In Vitro. *Annals of Bio Eng*, *24*, 67-74.

Bischoff, J. E., Arruda, E. M., & Grosh, K. (2004). A rheological network model for the continuum anisotropic and viscoelastic behavior of soft tissue. *Biomech Model Mechanobiol*, *3*, 56-65.

Brands, D. W. (2002). *Predicting Brain Mechanics During Closed Head Impact. Numerical and Constitutive Aspects.* Unpublished doctoral dissertation, Technische Universiteit Eindhoven, Eindhoven, Netherlands.

Brands, D. W., Bovendeerd, P. H., & Peters, G. W. (2000). Finite Shear Behaviour of Brain Tissue Under Impact Loading. *Proceedings of WAM2000 ASME Symposium on Crashworthiness, Occupant Protection and Biomechanics in Transportation*.

Brands, D. W., Bovendeerd, P. H., & Wismans, J. S. (2002). On the Potential Importance of Non-Linear Viscoelastic Material Modelling for Numerical Prediction of Brain Tissue Response: Test and Application. *Stapp Car Crash Journal*, *46*, 1-19.

Brandt, J. D., Beiser, J. A., Kass, M. A., & Gordon, M. O. (2001). Central Corneal Thickness in the Ocular Hypertension Treatment Study (OHTS). *Am. J. Ophthalmol.*, *108*, 1779-1788.

Brinker, T., Brassel, F., Becker, H., Samii, M., Lüdemann, W., & Rautenfeld, D. B. (1997). Breakdown of the Meningeal Barrier Surrounding the Intraorbital Optic

Nerve After Experimental Subarachnoid Hemorrhage. *Am J Ophthalmol*, *124*, 373-380.

Britton, R. J., Drance, S. M., Schulzer, M., Douglas, G. R., & Mawson, D. K. (1987). The Area of the Neuroretinal Rim of the Optic Nerve in Normal Eyes. *American journal of ophthalmology*, *103*, 597-504.

Buchanan, T. S., Lloyd, D. G., Manal, K., & Besier, T. F. (2005). Estimation of muscle forces and joint moments using a forward-inverse dynamics model. *Med Sci Sports Exerc*, *37*, 1911-6.

Buchsbaum, G., Sternklar, M., Litt, M., Grunwald, J. E., & Riva, C. E. (1984). Dynamics of an Oscillating Viscoelastic Sphere: A Model of the Vitreous Humor of the Eye. *Biorheology*, *21*, 285-296.

Budaev, O. R., Ivanova, M. N., & Damdinov, B. B. (2003). Temperature Dependence of Shear Elasticity of Some Liquids. *Advances in Colloid & Interface Science*, *104*, 307-10.

Budenz, D., & Et Al. (1994). Ocular and optic nerve hemorrhages in abused infants with intracranial injuries. *Ophthalmology*, *101*, 559-565.

Burd, H. J., Judge, S. J., & Cross, J. A. (2002). Numerical Modelling of the Accommodating Lens. *Vis. Res.*, *42*, 2235-2251.

Burd, H. J., Judge, S. J., & Flavell, M. J. (1999). Rapid Communication. Mechanics of Accommodation of the Human Eye. *Vis. Res.*, *39*, 1591-1595.

Burgoyne, C. F., Downs, J. C., Bellezza, A. J., Suh, J. F., & Hart, R. T. (2005). The optic nerve head as a biomechanical structure: a new paradigm for understanding the role of IOP-related stress and strain in the pathophysiology of glaucomatous optic nerve head damage. *Prog Retin Eye Res*, *24*, 39-73.

Buzard, K. A. (1992). Introduction to Biomechanics of the Cornea. *Refractive & Corneal Surgery*, *8*, 127-138.

Caffey, J. (1972). On the theory and practice of shaking infants. Its potential residual effects of permanent brain damage and mental retardation. *Am J Dis Child*, *124*, 161-169.

Caffey, J. (1974). The whiplash shaken infant syndrome: manual shaking by the extremities with whiplash-induced intracranial and intraocular bleedings, linked with residual permanent brain damage and mental retardation. *Pediatrics*, *54*, 396-403.

Caprioli, J., & Miller, J. M. (1988). Videographic Measurements of Optic Nerve Topography in Glaucoma. *Invest Ophthal & Vis Sci*, *29*, 1294-1298.

Carnell, P. H., & Vito, R. P. (1992). A Model for Estimating Corneal Stiffness Using an Indenter. *J Bio Eng*, *114*, 549-551.

Chabanas, M., Luboz, V., & Payan, Y. (2003). Patient Specific Finite Element Model of the Face Soft Tissues for Computer-Assisted Maxillofacial Surgery. *Med. Image Anal.*, *7*, 131-151.

Chadwick, D. L., Chin, S., Salerno, C., Landsverk, J., & Kitchen, L. (1991). Deaths from Falls in Children: How Far is Fatal? *The Journal of Trauma*, *31*, 1353-1355.

Chang, G. L., Hung, T. K., & Feng, W. W. (1988). An In-Vivo Measurement and Analysis of Viscoelastic Properties of the Spinal Cord of Cats. *J Bio Eng*, *110*, 115-122.

Chan, R. W., & Titze, I. R. (2003). Effect of Postmortem Changes and Freezing on the Viscoelastic Properties of Vocal Fold Tissues. *Annals of Bio Eng*, *31*, 482-491.

Charriere, E., Sirey, F., & Zysset, P. K. (2003). A Finite Element Model of the L5-S1 Functional Spinal Unit: Development and Comparison with Biomechanical Tests In Vitro. *Comp Meth Biomech Biomed Eng*, *6*, 249-61.

Chen, C. H., & Wang, Y. C. (1997). An Extended Nonlinear Mechanical Model for Solid-Filled Mooney-Rivlin Rubber Composites. *Polymer*, *38*, 571-6.

Chirila, T. V., Hong, Y., Dalton, P. D., Constable, I. J., & Refojo, M. F. (1998). The Use of Hydrophilic Polymers as Artificial Vitreous. *Prog. Polym. Sci.*, *23*, 475-508.

Christensen, R. M. (1982). *Theory of Viscoelasticity An Introduction* (2nd ed.). New York: Academic Press.

Coleman, D. J., & Lizzi, F. L. (1979). In Vivo Choroidal Thickness Measurement. *Am J Ophthalmol*, *88*, 369-375.

Collins, C. C., Scott, A. B., & O'Meara, D. M. (1969). Elements of the peripheral oculomotor apparatus. *Am. J. Opt. Arch. Acad. Opt.*, *46*, 510-515.

Contact interaction models. *MADYMO v5.4 Theory Manual* (pp. 167-191). (1999). TNO Automotive.

Crandall, J. R., Portier, L., Petit, P., Hall, G. W., Bass, C. R., Klopp, G. S., Hurwitz, S., Pilkey, W. D., Trosseille, X., Tarriere, C., & Lassau, J. P. (1996). Biomechanical Response and Physical Properties of the Leg, Foot, and Ankle. *Stapp Car Crash Conference proceedings*, *40th meeting*, 173-192.

Cubit 10.2 [Computer software]. Sandia Corporation. Retrieved April 2, 2007, from http://cubit.sandia.gov/

Curtin, B. J. (1969). Physiopathological Aspects of Scleral Stress-Strain. *Tr. Am. Ophth. Soc.*, *67*, 417-461.

Dalton, P. D., Chirila, T. V., Hong, Y., & Jefferson, A. (1995). Oscillatory Shear Experiments as Criteria for Potential Vitreous Substitutes. *Polymer Gels & Networks*, *3*, 429-44.

Dana, M. R., Werner, M. S., Viana, M. A., & Shapiro, M. J. (1993). Spontaneous and Traumatic Vitreous Hemorrhage. *Ophthalmology*, *100*, 1377-1383.

David, T., Smye, S., Dabbs, T., & James, T. (1998). A Model for the Fluid Motion of Vitreous Humour of the Human Eye During Saccadic Movement. *Phys Med Biol*, *43*, 1385-99.

Deguillebon, H., & Zauberman, H. (1972). Experimental Retinal Detachment. Biophysical Aspects of Retinal Peeling and Stretching. *Arch Ophthalmol*, *87*, 545-548.

Delp, S. L. (1990). Surgery simulation: A computer graphics system to analyze and design musculoskeletal reconstructions of the lower limb. *Dissertation Abstracts International*. (UMI No. 9108807)

Delp, S. L., Loan, J. P., Hoy, M. G., Zajac, F. E., Topp, E. L., & Rosen, J. M. (1990). An Interactive Graphics-Based Model of the Lower Extremity to Study Orthopaedic Surgical Procedures. *Trans. Biomed. Eng.*, *37*, 757-767.

Deng, Y. C., & Goldsmith, W. (1987). Response of a Human Head/Neck/Upper-Torso Replica to Dynamic Loading-II. Analytical/Numerical Model. *J Biomechanics*, *20*, 487-497.

Deng, Y. C., & Goldsmith, W. (1987). Response of a Human Head/Neck/Upper-Torso Replica to Dynamic Loading-I. Physical Model. *J Biomechanics*, *20*, 471-486.

Dluzewski, P. (2000). Anisotropic Hyperelasticity Based Upon General Strain Measures. *J Elasticity*, *60*, 119-129.

Dong, F., Clapworthy, G. J., Krokos, M. A., & Yao, J. (2002). An Anatomy-Based Approach to Human Muscle Modeling and Deformation. *Trans. Vis. Comp. Graph.*, *8*, 154-170.

Dongqi, H., & Zeqin, R. (1999). A biomathematical model for pressure-dependent lamina cribrosa behavior. *J Biomechanics*, *32*, 579-584.

Downs, J. C., Blidner, R. A., Bellezza, A. J., Thompson, H. W., Hart, R. T., & Burgoyne, C. F. (2002). Peripapillary Sclera Thickness in Perfusion-Fixed Normal Monkey Eyes. *Invest. Ophthal. & Vis. Sci.*, *43*, 2229-2235.

Downs, J. C., Burgoyne, C. F., Thomas, K. A., Thompson, H. W., & Hart, R. T. (1999). Effects of Strain Rate on the Mechanical Properties of Posterior Rabbit Sclera. *Proceedings of the First Joint BMES/EMBS Conference*, 1310.

Downs, J. C., Suh, J. F., Thomas, K. A., Bellezza, A. J., Burgoyne, C. F., & Hart, R. T. (2003). Viscoelastic Characterization of Peripapillary Sclera: Material Properties by Quadrant in Rabbit and Monkey Eyes. *J Bio Eng*, *125*, 124-131.

Drozdov, A. (1998). *Viscoelastic Structures: Mechanics of Growth and Aging*. San Diego: Academic Press.

Duck, F. A. (1990). *Physical Properties of Tissue. A Comprehensive Reference Book*. Bath, England: Academic Press.

Duckman, R. H., & Fitzgerald, D. E. (1992). Evaluation of Intraocular Pressure in a Pediatric Population. *Opt. Vis. Sci.*, *69*, 705-9.

Duhaime, A. C., Christian, C., Armonda, R., Hunter, J., & Hertle, R. (1996). Disappearing Subdural Hematomas. *Pediatr. Neurosurg*, *25*, 116-122.

Duhaime, A. C., Gennarelli, T. A., Thibault, L. E., Bruce, D. A., Margulies, S. S., & Wiser, R. (1987). The Shaken Baby Syndrome: A clinical, pathological, and biomechanical study. *J Neurosurg*, *66*, 409-415.

Durfee, W. K., & Palmer, K. I. (1994). Estimation of Force-Activation, Force-Length, and Force-Velocity Properties in Isolated, Electrically Stimulated Muscles. *Trans. Biomed. Eng.*, *41*, 205-216.

EasiCrash Mad [Computer software]. Retrieved April 3, 2007, from http://www.esi-group.com/SimulationSoftware/EASI-CRASHMAD

Edwards, M. E., & Good, T. A. (2001). Use of a mathematical model to estimate stress and strain during elevated pressure induced lamina cribrosa deformation. *Cur Eye Res*, *23*, 215-225.

Einstein, D. R., Reinhall, P., Nicosia, M., Cochran, R. P., & Kunzelman, K. (2003). Dynamic Finite Element Implementation of Nonlinear, Anisotropic Hyperelastic Biological Membranes. *Computer methods in biomechanics and biomedical engineering, 2003 Aug, 6(4):263-73*, *6*, 33-44.

Elder, J. E., Taylor, R. G., & Klug, G. L. (1991). Retinal haemorrhage in accidental head trauma in childhood. *J Paediatr. Child Health*, *27*, 286-289.

Elliott, J. D., & Elliott, G. B. (1973). The Hyaloid Vessel and Physiologic Optic Cup. *Microvascular Res.*, *6*, 93-8.

Ellis, E. F., McKinney, J. S., Willoughby, K. A., Liang, S., & Povlishock, J. T. (1995). A New Model for Rapid Stretch-Induced Injury of Cells in Culture: Characterization of the Model Using Astrocytes. *J Neurotrauma*, *12*, 325-339.

Elner, S. G., Elner, V. M., Arnall, M., & Albert, D. M. (1990). Ocular and Associated Systemic Findings in Suspected Child Abuse: A Necropsy Study. *Arch Ophthalmol*, *108*, 1094-1101.

Endo, E. G., Yao, X. Y., & Marmor, M. F. (1988). Pigment Adherence as a Measure of Retinal Adhesion: Dependence on Temperature. *Invest. Ophthal. & Vis. Sci.*, *29*, 1390-1396.

Ethier, C. R., Tertinegg, I., Pathmanathan, T., Yan, D. B., Trope, G. E., & Flanagan, J. G. (1999). A system for studying lamina cribrosa biomechanics in human eyes. *Presented at the First Joint Meeting of Biomedical Engineering Society (BMES) and Engineering in Medicine and Biology Society (EMBS)*, 1312-1313.

Feldman, K. W., Brewer, D. K., & Shaw, D. W. (1995). Evolution of the Cranial Computed Tomography Scan in Child Abuse. *Child Abuse Negl*, *19*, 307-314.

Fernandez, J. W., Mithraratne, P., Thrupp, S. F., Tawhai, M. H., & Hunter, P. J. (2004). Anatomically Based Geometric Modelling of the Musculo-Skeletal System and Other Organs. *Biomech Model Mechanobiol*, *2*, 139-155.

Ferrone, P. J., & De Juan Jr, E. (1994). Vitreous Hemorrhage in Infants. *Arch Ophthalmol*, *112*, 1185-1189.

Fisher, R. F. (1986). The Ciliary Body in Accommodation. *Trans. Ophthalmol. Soc. UK*, *105*, 208-219.

Fisher, R. F. (1987). The Influence of Age on Some Ocular Basement Membranes. *Eye*, *1*, 184-189.

Flügge, W. (1967). *Viscoelasticity*. Waltham, Massachusetts: Blaisdell Publishing Company.

Friberg, T. R., & Lace, J. W. (1988). A Comparison of the Elastic Properties of Human Choroid and Sclera. *Exp Eye Res*, *47*, 429-436.

Gardiner, J. C., & Weiss, J. A. (2001). Simple Shear Testing of Parallel-Fibered Planar Soft Tissues. *J Bio Eng*, *123*, 170-5.

Gibbs, D. A., Merrill, E. W., & Smith, K. A. (1968). Rheology of Hyaluronic Acid. *Biopolymers*, *6*, 777-91.

Gillies, G. T., Ritter, R. C., Broaddus, W. C., Grady, M. S., Howard, M. A., & McNeil, R. G. (1994). Magnetic Manipulation Instrumentation for Medical Physics Research. *Rev. Sci. Instrum.*, *65*, 533-562.

Gilliland, M. G., & Folberg, R. (1996). Shaken Babies-Some Have No Impact Injuries. *J Forensic Sci*, *41*, 114-116.

Gilliland, M. G., Luckenbach, M. W., & Chenier, T. C. (1994). Systemic and ocular findings in 169 prospectively studied child deaths: retinal hemorrhages usually mean child abuse. *Forensic Sci Int*, *68*, 117-132.

Gopalakrishnan, S. (2002). Behaviour of isoparametric quadrilateral family of Lagrangian fluid finite elements. *Int. J. Numer. Meth. Engng*, *54*, 731-761.

Graebel, W. P., & Van Alphen, G. W. (1977). The Elasticity of Sclera and Choroid of the Human Eye, and Its Implications on Scleral Rigidity and Accommodation. *J Bio Eng*, *99*, 203-8.

Green, M. A., Lieberman, G., Milroy, C. M., & Parsons, M. A. (1996). Ocular and cerebral trauma in non-accidental injury in infancy: underlying mechanisms and implications for paediatric practice. *Br J Ophthalmol*, *80*, 282-287.

Gundiah, N., Ratcliffe, M. B., & Pruitt, L. A. (2007). Determination of Strain Energy Function for Arterial Elastin: Experiments Using Histology and Mechanical Tests. *J Biomechanics*, *40*, 586-594.

Guy, J., Ellis, A., Kelley, K., & Hope, G. M. (1989). Spectra of G Ratio, Myelin Sheath Thickness, and Axon and Fiber Diameter in the Guinea Pig Optic Nerve. *J. Comparative Neurology*, *287*, 446-454.

Hadley, M. N., Sonntag, V. K., Rekate, H. L., & Murphy, A. (1989). The Infant Whiplash-Shake Injury Syndrome: A Clinical and Pathological Study. *Neurosurgery*, *24*, 536-540.

Hallquist, J. O. (2006). LS-DYNA Theory Manual [Software manual]. Livermore, CA: Livermore Software Technology Corporation.

Hanna, K. D., Jouve, F. E., & Waring, G. O. (1989). Preliminary Computer Simulation of the Effects of Radial Keratotomy. *Arch Ophthalmol*, *107*, 911-918.

Hansen, G. A., Stitzel, J. D., & Duma, S. M. (2003). Incidence of elderly eye injuries in automobile crashes: the effects of lens stiffness as a function of age. *Annual Proceedings for the Advancement of Automotive Medicine*, *47th*, 147-163.

Hatze, H. (1977). A Complete Set of Control Equations for the Human Musculo-Skeletal System. *J Biomechanics*, *10*, 799-805.

Hayreh, S. S. (1984). The Sheath of the Optic Nerve. *Ophthalmologica*, *189*, 54-63.

Heickell, A. G., Bellezza, A. J., Thompson, H. W., & Burgoyne, C. F. (2001). Optic Disc Surface Compliance Testing Using Confocal Scanning Laser Tomography in the Normal Monkey Eye. *J. Glaucoma*, *10*, 369-382.

He, J. (1988). A feedback control analysis of the neuro-musculo-skeletal system of a cat hindlimb (Doctoral dissertation, University of Maryland College Park, 1988). *Dissertation Abstracts International*.

Hernandez, M. R. (2000). The Optic Nerve Head in Glaucoma: Role of Astrocytes in Tissue Remodeling. *Progress in Retinal & Eye Res*, *19*, 297-321.

Hill, A. V. (1950). The Series Elastic Component of Muscle. *Proceedings of the Royal Society of London. Series B, Biological Sciences*, *137*, 273-280. Retrieved from http://links.jstor.org/sici?sici=0080

Hirokawa, S., & Tsuruno, R. (2000). Three-dimensional deformation and stress distribution in an analytical/computational model of the anterior cruciate ligament. *J Biomechanics*, *33*, 1069-1077.

Hochbaum, D. R., Moskowitz, S. E., & Wirtschafter, J. D. (1977). A Quantitative Analysis of Astigmatism Induced by Pterygium. *Biomechanics*, *10*, 735-746.

Hoeltzel, D. A., Altman, P., Buzard, K., & Choe, K. I. (1992). Strip Extensiometry for Comparison of the Mechanical Response of Bovine, Rabbit, and Human Corneas. *J Bio Eng*, *114*, 202-15.

Hogan, M. J. (1963). The vitreous, its structure, and relation to the ciliary body and retina. *Invest Ophthalmol*, *2*, 418-445.

Hogan, M. J., Alvarado, J. A., & Weddell, J. E. (1971). *Histology of the human eye*. Philadelphia: Saunders.

Hollman, K. W., Emelianov, S. Y., Neiss, J. H., Jotyan, G., Spooner, G. J., Juhasz, T., Kurtz, R. M., & O'Donnell, M. (2002). Strain Imaging of Corneal Tissue With an Ultrasound Elasticity Microscope. *Cornea*, *21*, 68-73.

Hymel, K. P., Rumack, C. M., Hay, T. C., Strain, J. D., & Jenny, C. (1997). Comparison of intracranial computed tomographic (CT) findings in pediatric abusive and accidental head trauma. *Pediatr Radiol*, *27*, 743-747.

Jaafar, M. S., & Kazi, G. A. (1993). Normal Intraocular Pressure in Children: A Comparative Study of the Perkins Applanation Tonometer and the Pneumatonometer. *J Pediatr Opthalmol Strabismus*, *30*, 284-287.

Jack, R. L. (1972). Ultrastructure of the Hyaloid Vascular System. *Arch Ophthalmol*, *87*, 555-567.

Joe, B. (2006). Geompack++ [Software manual]. Surrey, BC, Canada: Zhou Computing Services Inc.

Johansson, T., Meier, P., & Blickhan, R. (2000). A Finite-Element Model for the Mechanical Analysis of Skeletal Muscles. *J Theor Biol*, *206*, 131-149.

Johnson, D. L., & Braun, D. (1993). Accidental Head Trauma and Retinal Hemorrhage. *Neurosurgery*, *33*, 231-235.

Jonas, J. B., & Budde, W. M. (2000). Diagnosis and Pathogenesis of Glaucomatous Optic Neuropathy: Morphological Aspects. *Prog Retin Eye Res*, 1-40.

Jonas, J. B., Berenshtein, E., & Holbach, L. (2003). Anatomic Relationship between Lamina Cribrosa, Intraocular Space, and Cerebrospinal Fluid Space. *Invest Ophthal & Vis Sci*, *44*, 5189-5195.

Jonas, J. B., Gusek, G. C., Holzmann, I. G., & Naumann, G. O. (1988). Size of the optic nerve scleral canal and comparison with intravital determination of optic disc dimensions. *Graefe's Arch Clin Exp Ophthalmol*, *226*, 213-215.

Jonas, J. B., Mardin, C. Y., Schrehardt, U. S., & Naumann, G. O. (1991). Morphometry of the Human Lamina Cribrosa Surface. *Invest Ophthal & Vis Sci*, *32*, 401-405.

Jones, I. L., Warner, M., & Stevens, J. D. (1992). Mathematical Modelling of the Elastic Properties of Retina: A Determination of Young's Modulus. *Eye*, *6*, 556-559.

Judge, S. J., & Burd, H. J. (2002). Modelling the Mechanics of Accommodation and Presbyopia. *Ophthal. Physiol. Opt.*, *22*, 397-400.

Kain, H. L. (1984). A New Model for Examining Chorioretinal Adhesion Experimentally. *Arch. Ophthalmol*, *102*, 608-611.

Kapoor, S., Schiffman, J., Tang, R., Kiang, E., Li, H., & Woodward, J. (1997). The significance of white-centered retinal hemorrhages in the shaken baby syndrome. *Pediatric Emerg Care*, *13*, 183-185.

Kawano, S. I., Honda, Y., & Negi, A. (1982). Effects of Biological Stimuli on the Viscosity of the Vitreous. *Acta Ophthal.*, *60*, 977-991.

Kennedy, E. A., Voorhies, K. D., Herring, I. P., Rath, A. L., & Duma, S. M. (2004). Prediction of Severe Eye Injuries in Automobile Accidents: Static and Dynamic Rupture Pressure of the Eye. *Annual Proceedings for the Advancement of Automotive Medicine*, *48th*, 165-179.

Kirschner, R. H., & Stein, R. J. (1985). The Mistaken Diagnosis of Child Abuse. *AJDC*, *139*, 873-875.

Kisielewicz, L. T., Kodama, N., Ohno, S., & Uchio, E. (1998). Numerical Prediction of Airbag Caused Injuries on Eyeballs After Radial Keratotomy. *International Congress & Exposition*, 1-11.

Kita, M., & Marmor, M. F. (1992). Effects on Retinal Adhesive Force In Vivo of Metabolically Active Agents in the Subretinal Space. *Invest. Ophthal. & Vis. Sci.*, *33*, 1883-1887.

Kita, M., & Marmor, M. F. (1992). Retinal Adhesive Force in Living Rabbit, Cat, and Monkey Eyes. *Invest. Ophthal. & Vis. Sci.*, *33*, 1879-1882.

Kita, M., Negi, A., & Marmor, M. F. (1992). Lowering the Calcium Concentration in the Subretinal Space In Vivo Loosens Retinal Adhesion. *Invest. Ophthal. & Vis. Sci.*, *33*, 23-29.

Kita, M., Negi, A., Kawano, S., & Honda, Y. (1989). A New Method to Evaluate Retinal Adhesive Force in Living Rabbit Eye. *Nippon Ganka Gakkai zasshi*, *93*, 631-635.

Kita, M., Negi, A., Kawano, S., Honda, Y., & Maegawa, S. (1990). Measurement of Retinal Adhesive Force in the In Vivo Rabbit Eye. *Invest Ophthal & Vis Sci*, *31*, 624-628.

Kobayashi, A. S., Woo, L. Y., Lawrence, C., & Schlegel, W. A. (1971). Analysis of the Cornea-Scleral Shell by the Method of Direct Stiffness. *J Biomechanics*, *4*, 323-330.

Kostopoulos, V., Markopoulos, Y. P., Giannopoulos, G., & Vlachos, D. E. (2002). Finite element analysis of impact damage response of composite motorcycle safety helmets. *Composites*, *33*, 99-107.

Krag, S., & Andreassen, T. T. (2003). Mechanical Properties of the Human Posterior Lens Capsule. *Invest. Ophthal. & Vis. Sci.*, *44*, 691-696.

Lambert, S. R., Johnson, T. E., & Hoyt, C. S. (1986). Optic Nerve Sheath and Retinal Hemorrhages Associated With the Shaken Baby Syndrome. *Arch Ophthalmol*, *104*, 1509-1512.

Lam, B. L., Glasier, C. M., & Feuer, W. J. (1997). Subarachoid Fluid of the Optic Nerve in Normal Adults. *Ophthalmology*, *104*, 1629-1633.

Lancon, J. A., Haines, D. E., & Parent, A. D. (1998). Anatomy of the Shaken Baby Syndrome. *Anat Rec*, *253*, 13-18.

Lapeer, R. J., & Prager, R. W. (2001). Fetal head moulding: finite element analysis of a fetal skull subjected to uterine pressures during the first stage of labour. *J Biomechanics*, *34*, 1125-1133.

Lee, B., Litt, M., & Buchsbaum, G. (1992). Rheology of the Vitreous Body. Part I: Viscoelasticity of Human Vitreous. *Biorheology*, *29*, 521-33.

Lee, B., Litt, M., & Buchsbaum, G. (1994). Rheology of the Vitreous Body: Part 2. Viscoelasticity of Bovine and Porcine Vitreous. *Biorheology*, *31*, 339-51.

Lee, B., Litt, M., & Buchsbaum, G. (1994). Rheology of the Vitreous Body: Part 3. Concentration of Electrolytes, Collagen and Hyaluronic Acid. *Biorheology*, *31*, 339-51.

Lehman, S., & Stark, L. (1979). Simulation of Linear and Nonlinear Eye Movement Models: Sensitivity Analyses and Enumeration Studies of Time Optimal Control. *J. Cyb. Info. Sci.*, *2*, 21-43.

Lehman, S. L., & Stark, L. W. (1983). Perturbation Analysis Applied to Eye, Head, and Arm Movement Models. *Trans. Sys. Man Cyber.*, *13*, 972-979.

Levin, A. V. (2000). Retinal haemorrhages and child abuse. *Recent advances in paediatrics* (pp. 151-219). London: Churchill Livingstone.

Levy, N. S., & Crapps, E. E. (1984). Displacement of Optic Nerve Head in Response to Short-term Intraocular Pressure Elevation in Human Eyes. *Arch Ophthalmol*, *102*, 782-786.

Lippert, S. A., Rang, E. M., & Grimm, M. J. (2004). The High Frequency Properties of Brain Tissue. *Biorheology*, *41*, 681-91.

Lockwood-Cooke, P., Martin, C. F., & Schovanec, L. (1999). A Dynamic 3-d Model of Ocular Motion. *Proc. 38th Conf. Decision & Control*, 405-409.

Luboz, V., Pedrono, A., Ambard, D., Boutault, F., Payan, Y., & Swider, P. (2004). Prediction of Tissue Decompression in Orbital Surgery. *Clinical Biomechanics*, *19*, 202-8.

MADYMO v5.4 Theory Manual (pp. 95-148). (1999). TNO Automotive.

MADYMO Model Manual Version 6.2. (2004). Netherlands: TNO MADYMO.

Manzini, G., & Putti, M. (2007). Mesh locking effects in the finite volume solution of 2-D anisotropic diffusion equations. *J Comp Physics*, *220*, 751-771.

Margulies, S. S., & Thibault, K. L. (2000). Infant Skull and Suture Properties: Measurements and Implications for Mechanisms of Pediatric Brain Injury. *J Bio Eng*, *122*, 364-371.

Margulies, S. S., & Thibault, L. E. (1992). A Proposed Tolerance Criterion for Diffuse Axonal Injury in Man. *J Biomechanics*, *25*, 917-923.

Marmor, M. F., Abdul-Rahim, A. S., & Cohen, D. S. (1980). The effect of metabolic inhibitors on retinal adhesion and subretinal fluid resorption. *Invest Ophthal & Vis Sci*, *19*, 893-903.

Massicotte, S., & Et Al. (1991). Vitreoretinal traction and perimacular retinal folds in the eyes of deliberately traumatized children. *Ophthalmology*, *98*, 1124-1127.

Matthews, G. P., & Das, A. (1996). Dense Vitreous Hemorrhages Predict Poor Visual and Neurological Prognosis in Infants With Shaken Baby Syndrome. *J Pediatr Opthalmol Strabismus*, *33*, 260-265.

Mazuchowski, E. L., & Thibault, L. E. (2003). Biomechanical Properties of the Human Spinal Cord and Pia Mater. *Summer Bioengineering Conference*, 1205-6.

Medeiros, F. A., Sample, P. A., Zangwill, L. M., Bowd, C., Aihara, M., & Weinreb, R. N. (2003). Corneal Thickness as a Risk Factor for Visual Field Loss in Patients with Preperimetric Glaucomatous Optic Neuropathy. *Am. J. Ophthalmol.*, *136*, 805-813.

Metz, H., McElhaney, J., & Ommaya, A. K. (1970). A Comparison of the Elasticity of Live, Dead, and Fixed Brain Tissue. *Biomechanics*, *3*, 453-458.

Miller-Young, J. E., Duncan, N. A., & Baroud, G. (2002). Material Properties of the Human Calcaneal Fat Pad in Compression: Experiment and Theory. *J Biomechanics*, *35*, 1523-31.

Miller, K. (1999). Constitutive Model of Brain Tissue Suitable for Finite Element Analysis of Surgical Procedures. *J Biomechanics*, *32*, 531-7.

Miller, K. (2001). How to Test Very Soft Biological Tissues in Extension? *J Biomechanics*, *34*, 651-7.

Molloy, J. A., Ritter, R. C., Grady, M. S., Howard, M. A., Quate, E. G., & Gillies, G. T. (1990). Experimental Determination of the Force Required for Insertion of a Thermoseed Into Deep Brain Tissues. *Annals of Bio Eng*, *18*, 299-313.

Morison, C. N. (2002). *The Dynamics of Shaken Baby Syndrome*. Unpublished doctoral dissertation, The University of Birmingham, West Yorkshire, United Kingdom.

Morrison, J. C. (1995). The Microanatomy of the Optic Nerve. *Optic Nerve in Glaucoma* (pp. 57-78). Amsterdam, New York: Kugler Publications.

Moses, R. A. (1985). Detachment of ciliary body - anatomical and physical considerations. *Invest Ophthalmol*, *4*, 935-941.

Nash, I. S., Greene, P. R., & Foster, C. S. (1982). Comparison of Mechanical Properties of Keratoconus and Normal Corneas. *Exp Eye Res*, *35*, 413-23.

Negi, A., & Marmor, M. F. (1986). Mechanisms of Subretinal Fluid Resorption in the Cat Eye. *Invest. Ophthal. & Vis. Sci.*, *27*, 1560-1563.

Newman, W. D., Hollman, A. S., Dutton, G. N., & Carachi, R. (2002). Measurment of optic nerve sheath diameter by ultrasound: a means of detecting acute raised intracranial pressure in hydrocephalus. *Br. J. Ophthalmol*, *86*, 1109-1113.

Nickerson, C. S., Karageozian, H. L., Park, J., & Kornfield, J. A. (2005). Internal Tension: A Novel Hypothesis Concerning the Mechanical Properties of the Vitreous Humar. *Macromol. Symp.*, *227*, 183-189.

Noulas, A. V., Theocharis, A. D., Feretis, E., Papageoragekopoulou, N., Karamanos, N. K., & Theocharis, D. A. (2002). Pig Vitreous Gel: Macromolecular Composition with Particular Reference to Hyaluronan-Binding Proteoglycans. *Biochimie*, *84*, 295-302.

Numata, T., Constable, I. J., & Whitney, D. E. (1975). Physical properties of experimental vitreous membranes. I. Tensile strength. *Invest Ophthalmol*, *14*, 148-152.

Olsen, T. W., Aaberg, S. Y., Geroski, D. H., & Edelhauser, H. F. (1998). Human Sclera: Thickness and Surface Area. *Am. J. Ophthalmol.*, *125*, 237-241.

Oza, A., Vanderby, R., & Lakes, R. S. (2003). Interrelation of creep and relaxation for nonlinearly viscoelastic materials: application to ligament and metal. *Rheol Acta*, *42*, 557-568.

Ozawa, H., Matsumoto, T., Ohashi, T., Sato, M., & Kokubun, S. (2001). Comparison of Spinal Cord Gray Matter and White Matter Softness: Measurement by Pipette Aspiration Method. *J Neurosurg*, *95*, 221-224.

Paton, L. (1924). Diseases of the nervous system: 1. Ocular symptoms in subarachnoid haemorrhage. *Trans Ophthalmol Soc UK*, 110-124.

Phillips, J. R., & McBrien, N. A. (1995). Form Deprivation Myopia: Elastic Properties of Sclera. *Ophthal. Physiol. Opt.*, *15*, 357-362.

Pounder, D. J. (1997). Shaken Adult Syndrome. *Am J Forensic Med Pathol*, *18*, 321-324.

Power, E. D. (2001). *A Nonlinear Finite Element Model of the Human Eye to Investigate Ocular Injuries From Night Vision Goggles*. Unpublished master's thesis, Virginia Polytechnic Institute, Blacksburg, Virginia.

Power, E. D., Duma, S. M., Stitzel, J. D., Herring, I. P., West, R. L., Bass, C. R., Crowley, J. S., & Brozoski, F. T. (2002). Computer Modeling of Airbag-Induced Ocular Injury in Pilots Wearing Night Vision Goggles. *Aviation, Space & Env Med*, *73*, 1000-1006.

Prange, M. T., & Margulies, S. S. (2001). Tissue Strain Thresholds for Axonal Injury in the Infant Brain. *Proceedings of the 2001 Bioengineering Conference*, 833-834.

Prange, M. T., Coats, B., Duhaime, A. C., & Margulies, S. S. (2003). Anthropomeorphic simulations of falls, shakes, and inflicted impacts in infants. *J Neurosurg*, *99*, 143-150.

Purslow, P. P., & Karwatowski, W. S. (1996). Ocular Elasticity. Is Engineering Stiffness a More Useful Characterization Parameter Than Ocular Rigidity? *Ophthalmology*, *103*, 1686-1692.

Quigley, H. A., & Addicks, E. M. (1981). Regional Differences in the Structure of the Lamina Cribrosa and Their Relation to Glaucomatous Optic Nerve Damage. *Arch Ophthalmol*, *99*, 137-143.

Quigley, H. A. (1995). Overview and Introduction to Session on Connective Tissue of the Optic Nerve in Glaucoma. *Optic Nerve in Glaucoma* (pp. 15-36). Amsterdam, New York: Kugler Publications.

Quigley, H. A., Brown, A. E., Morrison, J. D., & Drance, S. M. (1990). The Size and Shape of the Optic Disc in Normal Human Eyes. *Arch. Ophthalmol*, *108*, 51-57.

Quigley, H. A., Flower, R. W., Addicks, E. M., & McLeod, D. S. (1980). The mechanism of optic nerve damage in experimental acute intraocular pressure elevation. *Invest Ophthal & Vis Sci*, *19*, 505-517.

Raspanti, M., Marchini, M., Pasqua, V. D., Strocchi, R., & Ruggeri, A. (1992). Ultrastructure of the Extracellular Matrix of Bovine Dura Mater, Optic Nerve Sheath and Sclera. *J. Anat.*, *181*, 181-187.

Rath, A. L. (2005). *The Effects of Extraocular Muscles on Eye Biomechanics*. Unpublished master's thesis, Virginia Polytechnic Institute, Blacksburg, Virginia.

Reiber, G. D. (1993). Fatal Falls in Childhood. *Am J Forensic Med Pathol*, *14*, 201-207.

Reichel, E., Miller, D., Blanco, E., & Mastanduno, R. (1989). The Elastic Modulus of Central and Perilimbal Bovine Cornea. *Ann Ophthalmol*, *21*, 205-208.

Rivlin, R. S., & Thomas, A. G. Large Elastic Deformations of Isotropic Materials. VIII. Strain Distribution around a Hole in a Sheet. Retrieved from http://links.jstor.org/sici?sici=0080

RK4 [Computer software]. (2005). Houghton, MI: Tomas Co. Retrieved March 18, 2007, from http://www.chem.mtu.edu/~tbco/cm416/RK4_v3_0.html

Robinson, D. A. (1981). Models of the Mechanics of Eye Movments. *Models of oculomotor behavior and control* (pp. 21-41). Boca Raton, Fla: CRC Press.

Rohrschneider, K., Burk, R. O., & Völcker, H. E. (1993). Reproducibility of topometric data acquisition in normal and glaucomatous optic nerve heads with the laser tomographic scanner. *Graefe's Arch Clin Exp Ophthalmol*, *231*, 457-464.

Ruiz-Moreno, J. M., & Perez-Santonja, J. J. (1998). Dissection of the Posterior Hyaloid. *Arch Ophthalmol*, *116*, 1392-3.

Sahay, K. B., & Kothiyal, K. P. (1984). A Nonlinear Hyperelastic Model of Pressure Volume Function of Cranial Components. *Intern. J. Neuroscience*, *23*, 301-9.

Samani, A., & Plewes, D. (2004). A method to measure the hyperelastic parameters of ex vivo breast tissue samples. *Phys Med Biol*, *49*, 4395-4405.

Samani, A., Bishop, J., Yaffe, M. J., & Plewes, D. B. (2001). Biomechanical 3-D Finite Element Modeling of the Human Breast Using MRI Data. *Trans. Med. Imag.*, *20*, 271-9.

Sarma, P. A., Pidaparti, R. M., Moulik, P. N., & Meiss, R. A. (2003). Non-linear Material Models for Tracheal Smooth Muscle Tissue. *Bio-Med. Mat. Eng.*, *13*, 235-45.

Sauerland, E. K., & Grant, J. (1994). The Head and Neck. *Grant's dissector* (pp. 185-206). Baltimore: Williams & Wilkins.

Schachar, R. A., & Bax, A. J. (2001). Mechanism of Human Accommodation as Analyzed by Nonlinear Finite Element Analysis. *Ann Ophthalmol*, *33*, 103-112.

Schachar, R. A., Huang, T., & Huang, X. (1993). Mathematic Proof of Schachar's Hypothesis of Accommodation. *Ann Ophthalmol*, *25*, 5-9.

Scott, W. R., Lloyd, W. C., Benedict, J. V., & Meredith, R. (2000). Ocular Injuries Due to Projectile Impacts. *44th Annual Proceedings Assoc for the Adv of Auto Med*, 205-217.

Sebag, J. (1991). Age-Related Differences in the Human Vitreoretinal Interface. *Arch Ophthalmol*, *109*, 966-971.

Sebag, J. (1998). Macromolecular Structure of the Corpus Vitreus. *Prog. Polym. Sci.*, *23*, 415-46.

Seshaiyer, P., & Humphrey, J. D. (2003). A Sub-Domain Inverse Finite Element Characterization of Hyperelastic Membranes Including Soft Tissues. *J Bio Eng*, *125*, 363-371.

Shergold, O. A., Fleck, N. A., & Radford, D. (2006). The Uniaxial Stress Versus Strain Response of Pig Skin and Silicone Rubber at Low and High Strain Rates. *International J. Impact Eng.*, *32*, 1384-1402.

Shin, T. J., Vito, R. P., Johnson, L. W., & McCarey, B. E. (1997). The Distribution of Strain in the Human Cornea. *J Biomechanics*, *30*, 497-503.

Shuck, L. Z., Haynes, R. R., & Fogle, J. L. (1970). Determination of Viscoelastic Properties of Human Brain Tissue. *ASME*, *70-BHF-12*, 2-7.

Siegwart, J. T., & Norton, T. T. (1999). Regulation of the Mechanical Properties of Tree Shrew Sclera by the Visual Environment. *Vis. Res.*, *39*, 387-407.

Sigal, I. A., Flanagan, J. G., & Tertinegg, I. (2004). Finite Element Modeling of Optic Nerve Head Biomechanics. *Invest Ophthal & Vis Sci*, *45*, 4378-4387.

Silver, D. M., & Geyer, O. (2000). Pressure-Volume Relation for the Living Human Eye. *Cur Eye Res*, *20*, 115-120.

Smolek, M. (1988). Elasticity of the Bovine Sclera Measured with Real-Time Holographic Interferometry. *Am. J. Opt. Phys. Opt.*, *65*, 653-660.

Spaide, R. F., Swengel, R. M., Scharre, D. W., & Mein, C. E. (1990). Shaken Baby Syndrome. *American Family Physician*, *41*, 1145-1152.

Stark, L., Zangemeister, W. H., Edwards, J., Grinberg, J., Jones, A., Lehman, S., Lubock, P., Narayan, V., & Nystrom, M. (1980). Head Rotation Trajectories Compared with Eye Saccades by Main Sequence Relationships. *Invest. Ophthal. & Vis. Sci.*, *19*, 986-8.

Stevens, J. D., Jones, I. L., Warner, M., Lavin, M. J., & Leaver, P. K. (1992). Mathematical Modelling of Retinal Tear Formation: Implications for the Use of Heavy Liquids. *Eye*, *6*, 69-74.

Stitzel, J. D., Duma, S. M., Cormier, J. M., & Herring, I. P. (2002). A Nonlinear Finite Element Model of the Eye with Experimental Validation for the Prediction of Globe Rupture. *Stapp Car Crash Journal*, *46*, 81-102.

Swindale, N. V., Stjepanovic, G., Chin, A., & Mikelberg, F. S. (2000). Automated Analysis of Normal and Glaucomatous Optic Nerve Head Topography Images. *Invest Ophthal & Vis Sci*, *41*, 1730-1742.

Taber, L. A. (1984). Large Deformation Mechanics of the Enucleated Eyeball. *J Bio Eng*, *106*, 229-234.

Takahashi, T. (1994). *Atlas of the Human Body*. Japan: Kodansha Ltd.

Thijssen, J. M., Mol, H. J., & Timmer, M. R. (1985). Acoustic Parameters of Ocular Tissues. *Ultrasound in Med. & Biol.*, *11*, 157-61.

Todd, B. A., & Thacker, J. G. (1994). Three-dimensional computer model of the human buttocks, in vivo. *J Rehab Res*, *31*, 111-119.

Tokita, M., Fujiya, Y., & Hikichi, K. (1984). Dynamic Viscoelasticity of Bovine Vitreous Body. *Biorheology*, *21*, 751-756.

Tongue, A. (1991). The ophthalmologist's role in diagnosing child abuse. *Ophthalmology*, *98*, 1009-1010.

Torii, H., Takahashi, K., Yoshitomi, F., Miyata, K., Ishii, Y., & Oshika, T. (2001). Mechanical Detachment of the Anterior Hyaloid Membrane from the Posterior Lens Capsule. *Ophthalmology*, *108*, 2182-5.

Tortora, G. J., & Grabowski, S. R. (2001). *Introduction to the human body the essentials of anatomy and physiology* (5th ed.). New York: Wiley.

Uchio, E., Kadonosono, K., Matsuoka, Y., & Goto, S. (2004). Simulation of air-bag impact on an eye with transsclerally fixated posterior chamber intraocular lens using finite element analysis. *J Cataract Refract Surg*, *30*, 483-490.

Uchio, E., Ohno, S., Kudoh, J., Aoki, K., & Kisielewicz, L. T. (1999). Simulation model of an eyeball based on finite element analysis on a supercomputer. *Br J Ophthalmol*, *83*, 1106-1111.

Uchio, E., Ohno, S., Kudoh, K., Kadonosono, K., Andoh, K., & Kisielewicz, L. T. (2001). Simulation of air-bag impact on post-radial keratotomy eye using finite element analysis. *J Cataract Refract Surg*, *27*, 1847-1853.

Uchio, E., Watanabe, Y., Kadonosono, K., Matsuoka, Y., & Goto, S. (2003). Simulation of airbag impact on eyes after photorefractive keratectomy by finite element analysis method. *Graefe's Arch Clin Exp Ophthalmol*, *241*, 497-504.

Van der Horst, M. J. (2002). *Human Head Neck Response in Frontal, Lateral and Rear End Impact Loading*. Unpublished doctoral dissertation, Technische Universiteit Eindhoven, Eindhoven, Netherlands.

Verver, M. M. (2004). *Numerical tools for comfort analyses of automotive seating*. Unpublished doctoral dissertation, Technische Universiteit Eindhoven, Eindhoven, Netherlands.

Vinger, P. F., Duma, S. M., & Crandall, J. (1999). Baseball Hardness as a Risk Factor for Eye Injuries. *Arch Ophthalmol*, *117*, 354-358.

The Visible Human Project. Retrieved March 21, 2007, from http://www.nlm.nih.gov/research/visible/applications.html

Vito, R. P., & Carnell, P. H. (1992). Finite Element Based Mechanical Models of the Cornea for Pressure and Indenter Loading. *Refractive & Corneal Surgery*, *8*, 146-151.

Vito, R. P., Shin, T. J., & McCarey, B. E. (1989). A Mechanical Model of the Cornea: The Effects of Physiological and Surgical Factors on Radial Keratotomy Surgery. *Refractive & Corneal Surgery*, *5*, 82-88.

Walker, W. F., Fernandez, F. J., & Negron, L. A. (2000). A Method of Imaging Viscoelastic Parameters with Acoustic Radiation Force. *Phys Med Biol*, *45*, 1437-47.

Wang, L., Damji, K. F., Munger, R., Jonasson, F., Arnarsson, A., Sasaki, H., & Sasaki, K. (2003). Increased Disk Size in Glaucomatous Eyes vs. Normal Eyes in the Reykjavik Eye Study. *Am. J. Ophthalmol.*, *135*, 226-8.

Weber, H., & Landwehr, G. (1982). A New Method for the Determination of the Mechanical Properites of the Vitreous. *Opthalmic Res*, *14*, 326-334.

Weber, H., Landwehr, G., Kilp, H., & Neubauer, H. (1982). The Mechanical Properties of the Vitreous of Pig and Human Donor Eyes. *Opthalmic Res*, *14*, 335-343.

Weinberg, H. D., & Tunnessen Jr, W. W. (1996). Megacephaly: Heeding the Head. *Contemp Pediatr*, *13*, 169,172,175.

Weissgold, D. J., Budenz, D. L., Hood, I., & Rorke, L. B. (1995). Ruptured Vascular Malformation Masquerading as Battered/Shaken Baby Syndrome: A Nearly Tragic Mistake. *Survey of Ophthalmology*, *39*, 509-512.

Williams, J. G. (1980). *Stress analysis of polymers* (Rev. ed.). New York: Halsted Press.

Winters, J. M., & Stark, L. (1985). Analysis of Fundamental Human Movement Patterns Through the Use of In-Depth Antagonistic Muscle Models. *Bio. Eng.*, *32*, 826-839.

Winters, J. M., & Stark, L. (1988). Estimated Mechanical Properties of Synergistic Muscles Involved in Movements of a Variety of Human Joints. *J Biomechanics*, *21*, 1027-1041.

Winters, J. M. (1985). *Generalized Analysis and Design of ANtagonistic Muscle Models: Effect of Nonlinear Properties on the Control of Human Movement*. Unpublished doctoral dissertation, University of California, Berkeley, California.

Winters, J. M., Nam, M. H., & Stark, L. W. (1984). Modeling Dynamical Interactions between Fast and Slow Movements: Fast Saccadic Eye Movement Behavior in the Presence of the Slower VOR. *Math. Biosci.*, *68*, 159-185.

Woittiez, R. D., Huijing, P. A., & Rozendal, R. H. (1983). Influence of muscle architecture on the length-force diagram. A model and its verification. *Pflu¨gers Archiv : European journal of physiology*, *397*, 73-74.

Woittiez, R. D., Huijing, P. A., & Rozendal, R. H. (1983). Influence of muscle architecture on the length-force diagram of mammalian muscle. *Pflu¨gers Archiv : European journal of physiology*, *399*, 275-279.

Wolfson, D. R., McNally, D. S., Clifford, M. J., & Vloeberghs, M. (2005). Rigid-body modelling of shaken baby syndrome. *Proc. IMechE.*, *219*, 67-70.

Wolter, J. R. (1961). Notes, Cases, Instruments: Adhesions of the Lens Capsule to the Anterior Hyaloid Membrane. *American journal of ophthalmology*, *55*, 511-512.

Woo, S. L., Kobayashi, A. S., Lawrence, C., & Schlegel, W. A. (1972). Mathematical Model of the Cornea-Scleral Shell As Applied to Intraocular Pressure-Volume Relations and Applanation Tonometry. *Annals of Bio Eng*, *1*, 87-98.

Woo, S. L., Kobayashi, A. S., Schlegel, W. A., & Lawrence, C. (1972). Nonlinear Material Properties of Intact Cornea and Sclera. *Exp Eye Res*, *14*, 29-39.

Wu, W., Peters, W. H., & Hammer, M. E. (1987). Basic Mechanical Properties of Retina in Simple Elongation. *J Bio Eng*, *109*, 65-67.

Yan, D. B., Flanagan, J. G., Farra, T., Trope, G. E., & Ethier, C. R. (1998). Study of regional deformation of the optic nerve head using scanning laser tomography. *Cur Eye Res*, *17*, 903-916.

Yao, X. Y., Hageman, G. S., & Marmor, M. F. (1994). Retinal Adhesiveness in the Monkey. *Invest. Ophthal. & Vis. Sci.*, *35*, 744-748.

Young, J. E., Duncan, N. A., & Baroud, G. (2002). Material properties of the human calcaneal fat pad in compression: experiment and theory. *J Biomechanics*, *35*, 1523-1531.

Zajac, F. E. (1989). Muscle and tendon: Properties, models, scaling and application to biomechanics and motor control. *Critical reviews in biomedical engineering*, *17*, 359-441.

Zauberman, H., & Deguillebon, H. (1972). Retinal Traction in Vivo and Postmortem. *Arch Ophthalmol*, *87*, 549-554.

Zauberman, H., Deguillebon, H., & Holly, F. J. (1972). Retinal traction in vitro. *Invest Ophthalmol*, *11*, 46-55.

Zeimer, R. (1995). Biomechanical Properties of the Optic Nerve Head. *Optic Nerve in Glaucoma* (pp. 107-121). Amsterdam, New York: Kugler Publications.

Zhang, Y., & Bajaj, C. (2004). Adaptive and Quality Quadrilateral/ Hexahedral Meshing from Volumetric Imaging Data. *Proceedings of 13th International Meshing Roundtable*, 365-376. Retrieved March/April 03, 2007, from http://www.ices.utexas.edu/~jessica/paper/quadhex/

Zhou, C., Khalil, T. B., & King, A. I. (1996). Viscoelastic Response of the Human Brain to Sagittal and Lateral Rotational Acceleration by Finite Element Analysis. *International IRCOBI Conference on the Biomechanics of Impacts*, 35-48.

Zimmerman, R. L. (1980). In Vivo Measurements of the Viscoelasticity of the Human Vitreous Humor. *Biophys. J.*, *29*, 539-544.

Zobitz, M. E., Luo, Z. P., & An, K. N. (2001). Determination of the Compressive Material Properties of the Supraspinatus Tendon. *J Bio Eng*, *123*, 47-51.

APPENDIX A

ANIMATION SEQUENCE FOR SACCADIC STUDIES

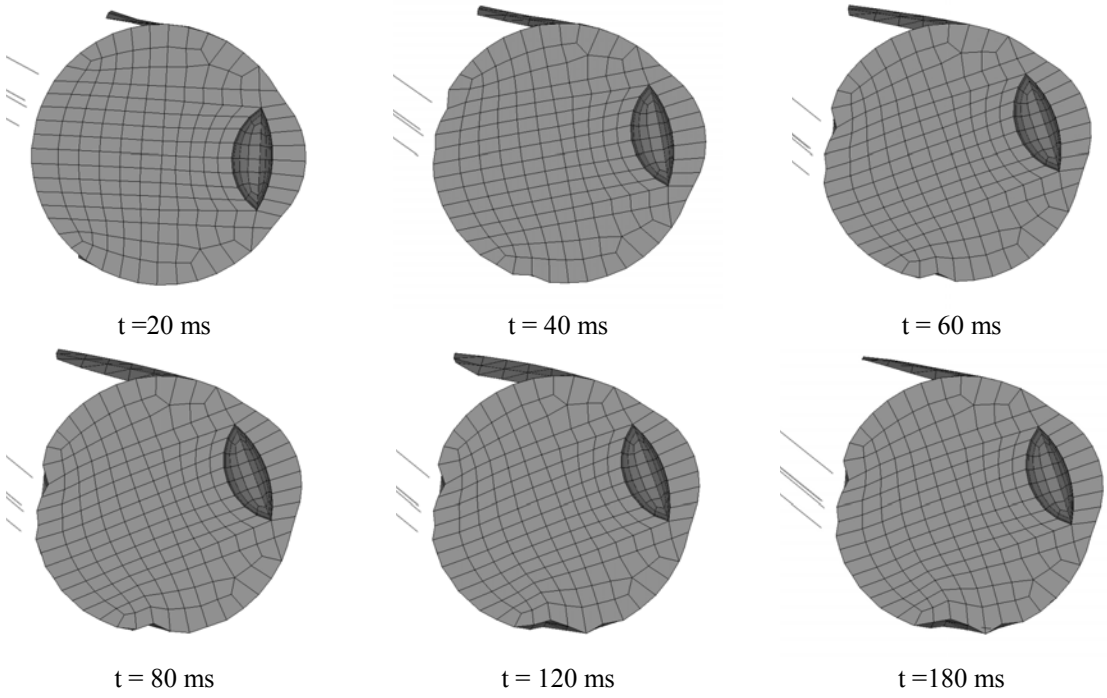

Figure A.1: Sequence of using Weber vitreous material with elastic constitutive model. Eye model is the CUBIT mesh using the analytical spring optic nerve.

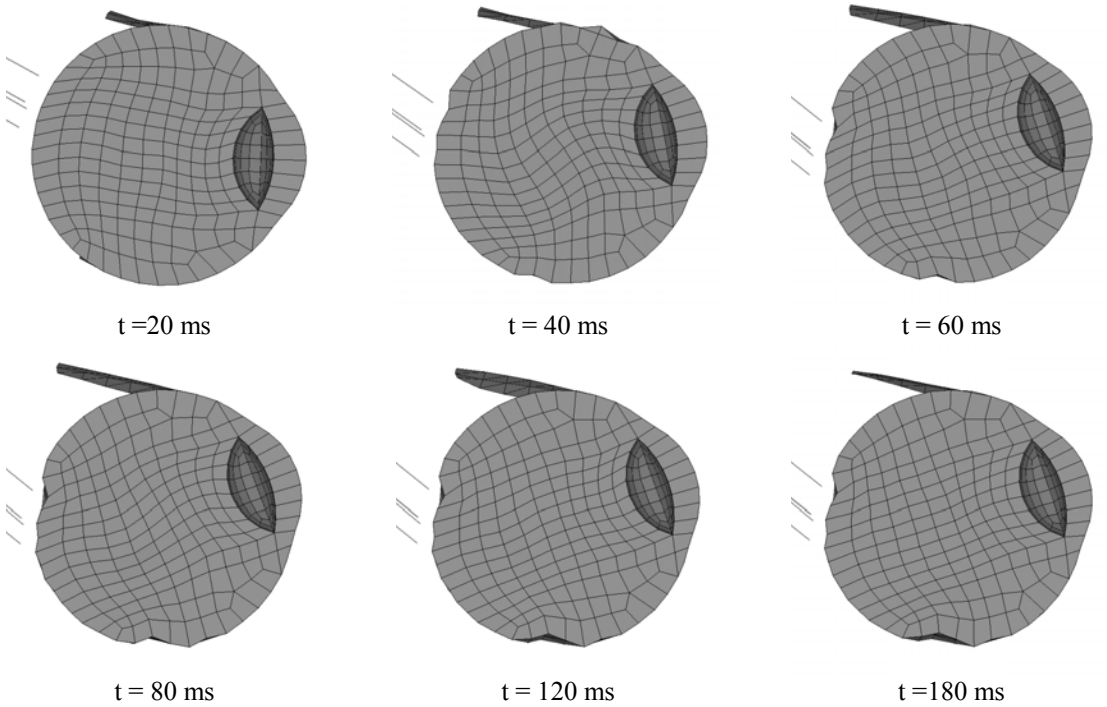

Figure A.2: Sequence of frames using the Nickerson (x5) vitreous with REF constitutive model. Eye model is the CUBIT mesh using the analytical spring optic nerve.

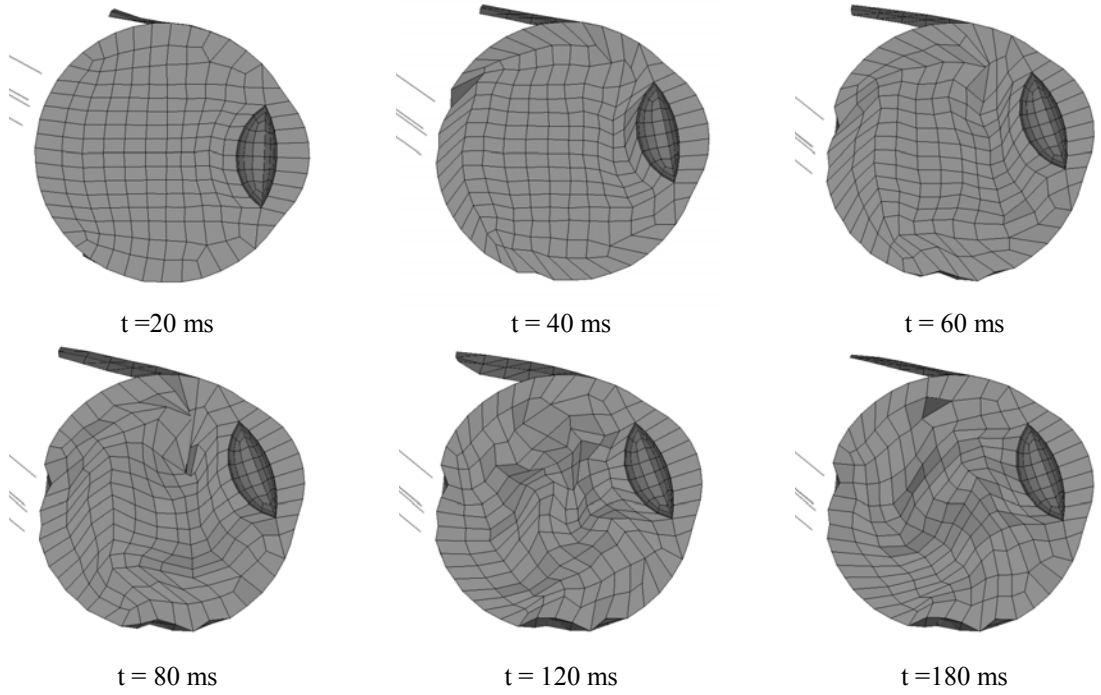

Figure A.3: Sequence of frames using Bettelheim vitreous material with REF constitutive model. Eye model is the CUBIT mesh using the analytical spring optic nerve.

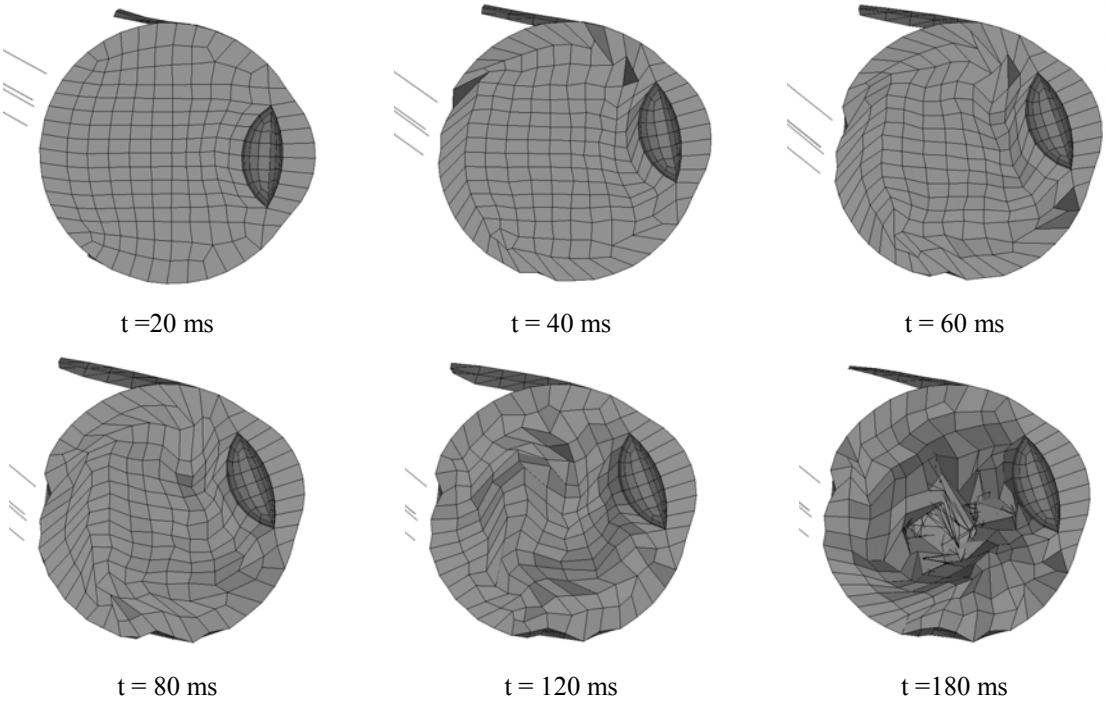

Figure A.4: Sequence of frames using Tokita vitreous material with REF constitutive model. Eye model is the CUBIT mesh using the analytical spring optic nerve.

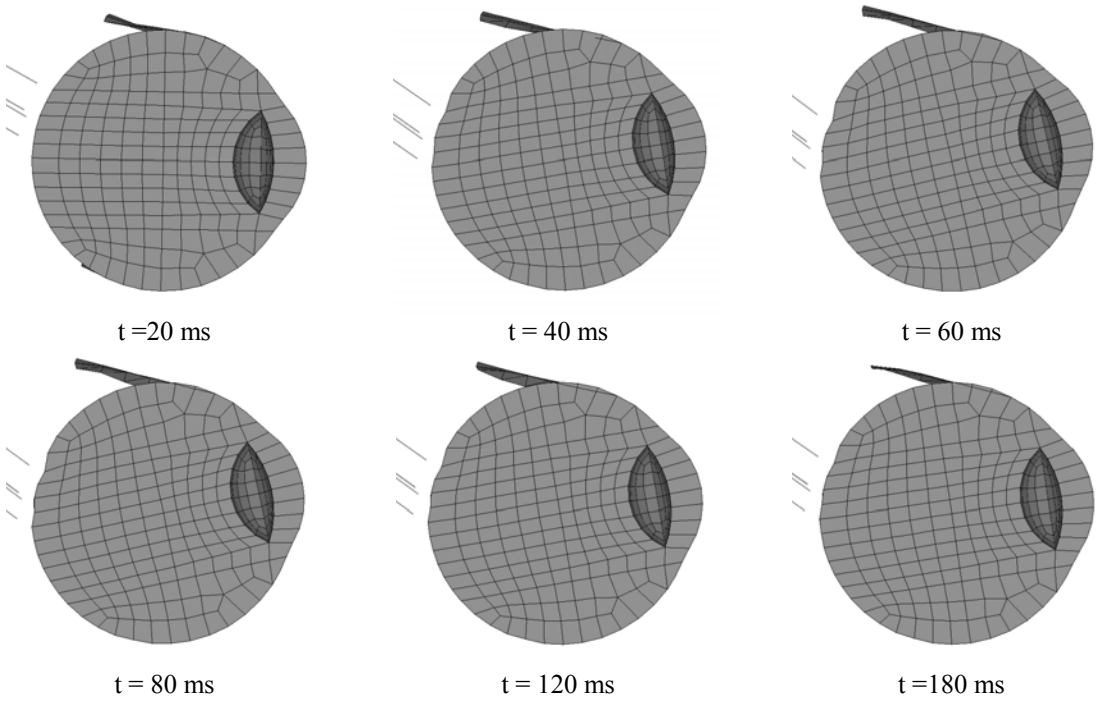

Figure A.5: Sequence of frames using Power vitreous material with REF constitutive model. Eye model is the CUBIT mesh using the analytical spring optic nerve.

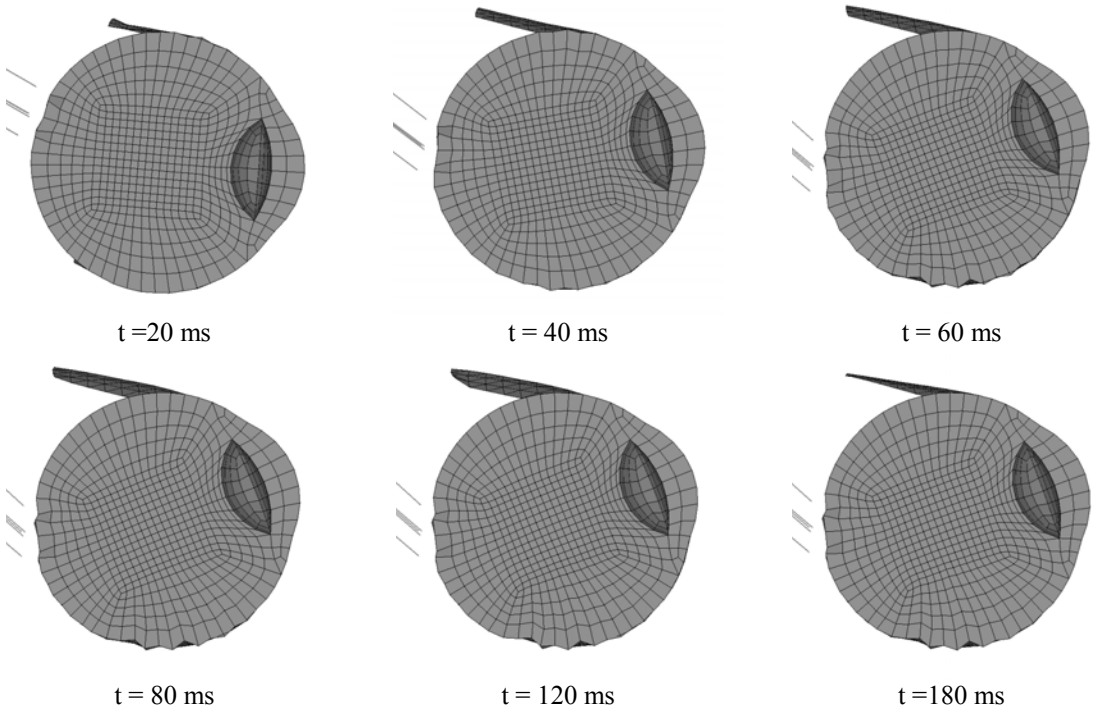

Figure A.6: Sequence of frames using Weber vitreous material with elastic constitutive model. Eye model is the manual mesh using the analytical spring optic nerve.

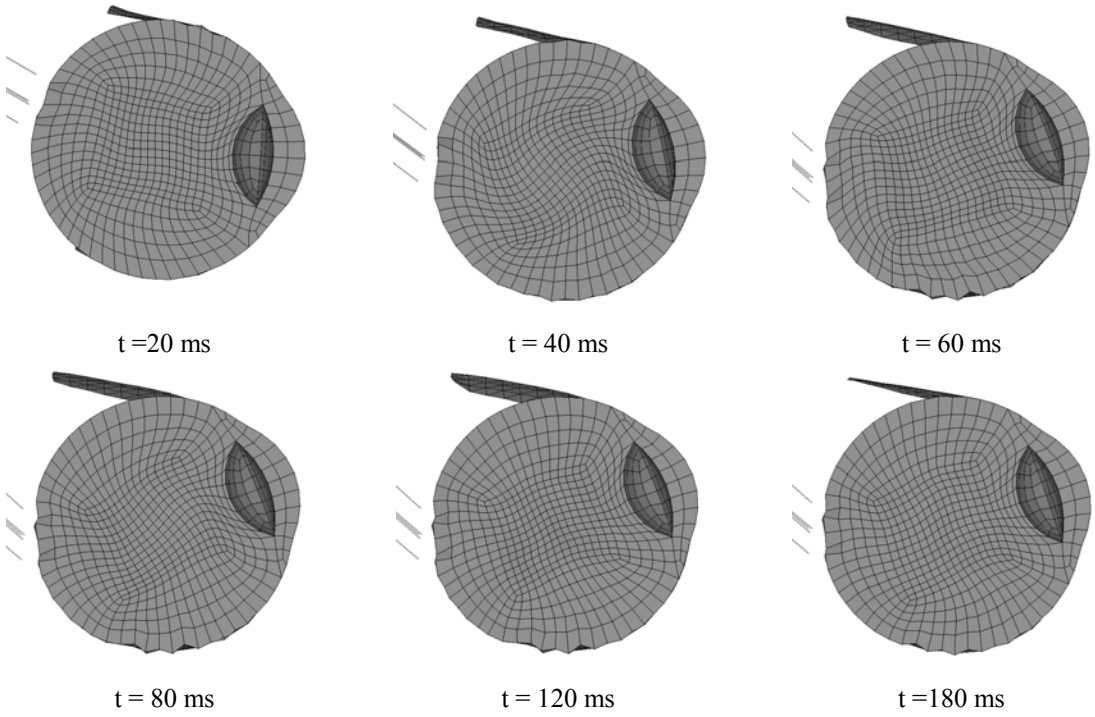

Figure A.7: Sequence of frames using Nickerson (x5) vitreous material with REF constitutive model. Eye model is the manual mesh using the analytical spring optic nerve.

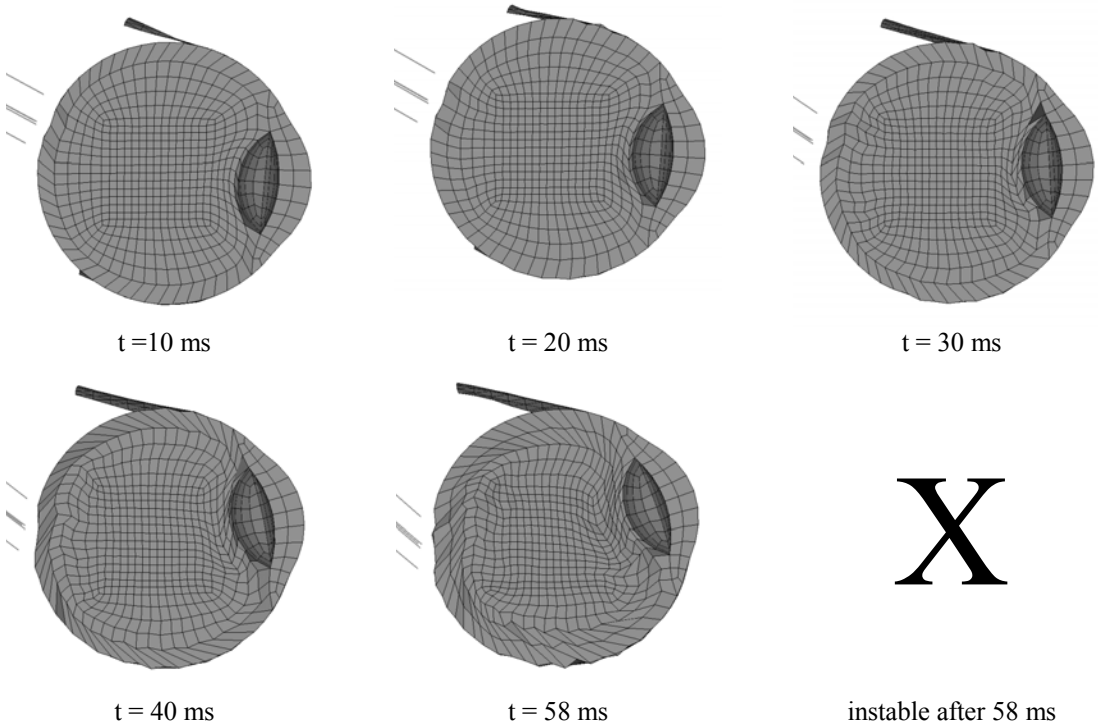

Figure A.8: Sequence of frames using Bettelheim vitreous material with REF constitutive model. Eye model is the manual mesh using the analytical spring optic nerve.

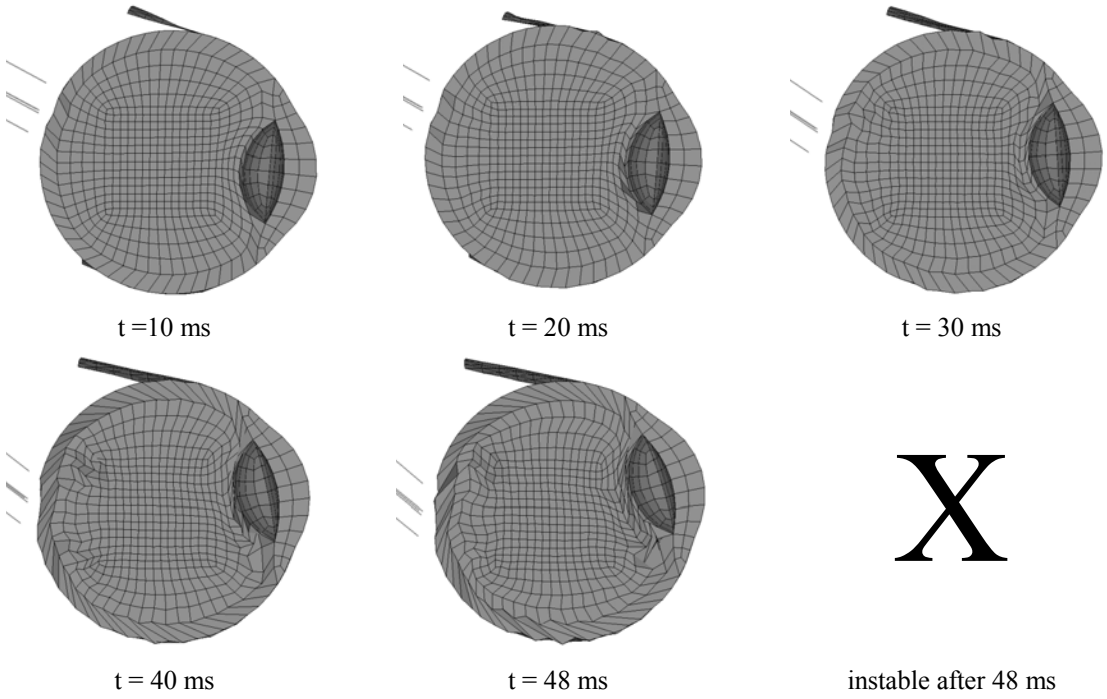

Figure A.9: Sequence of frames using Tokita vitreous material with REF constitutive model. Eye model is the manual mesh using the analytical spring optic nerve.

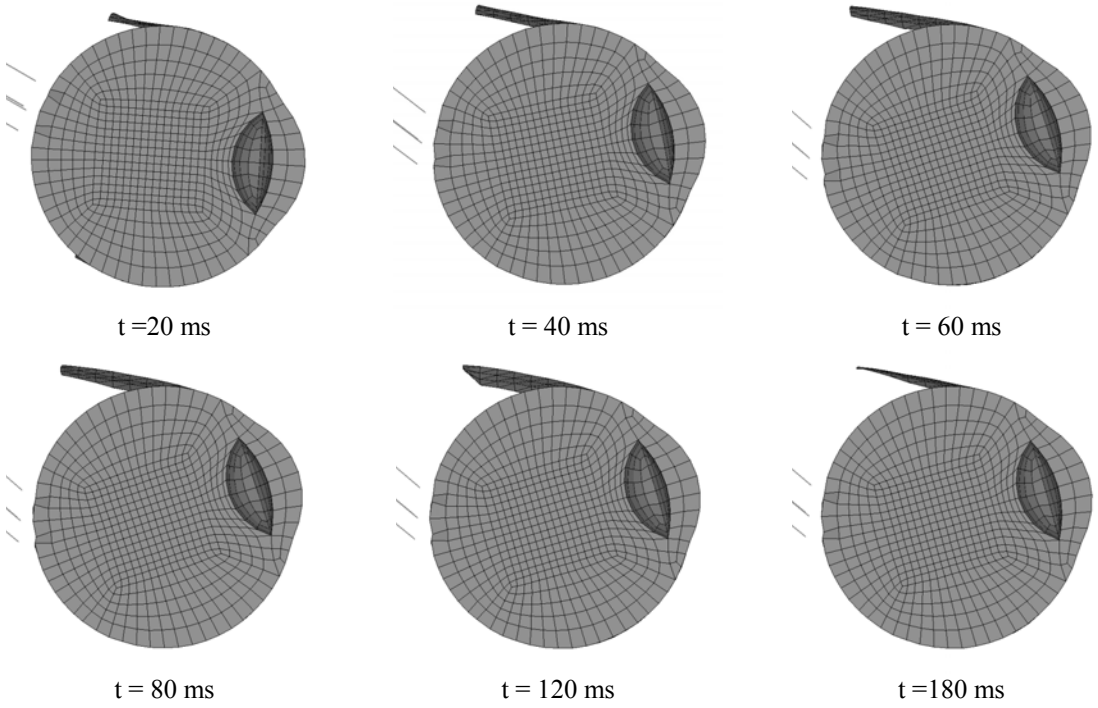

Figure A.10: Sequence of frames using Power vitreous material with REF constitutive model. Eye model is the manual mesh using the analytical spring optic nerve.

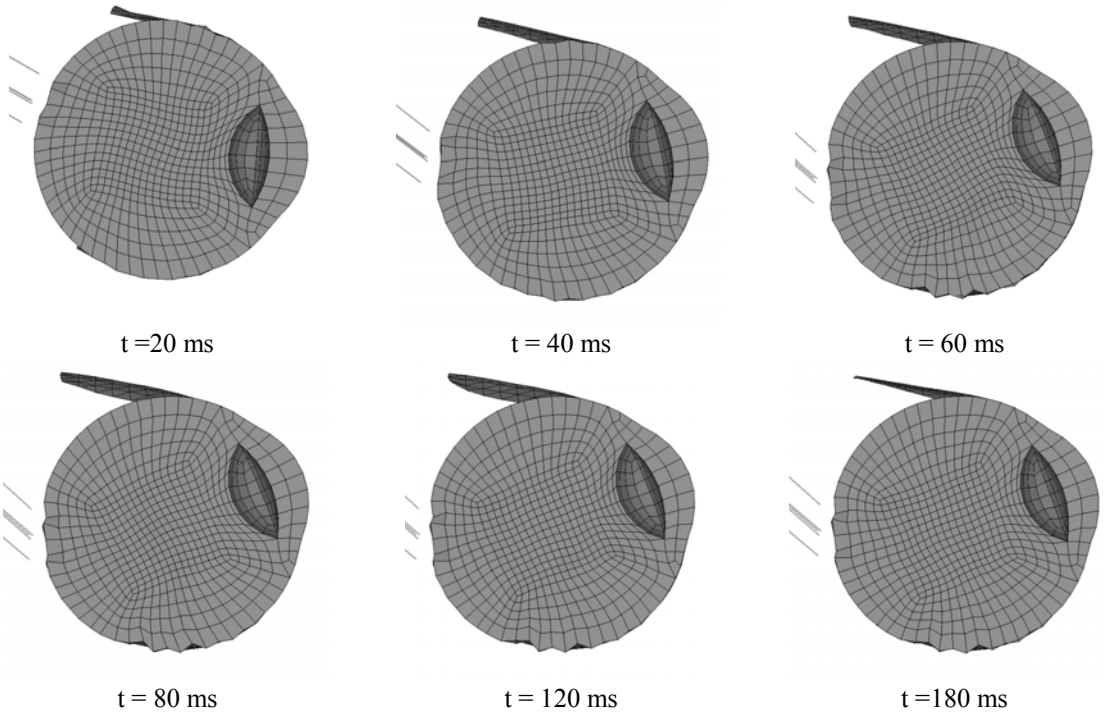

Figure A.11: Sequence of frames using Nickerson (x5) vitreous material with CPL constitutive model. Eye model is the manual mesh using the analytical spring optic nerve.

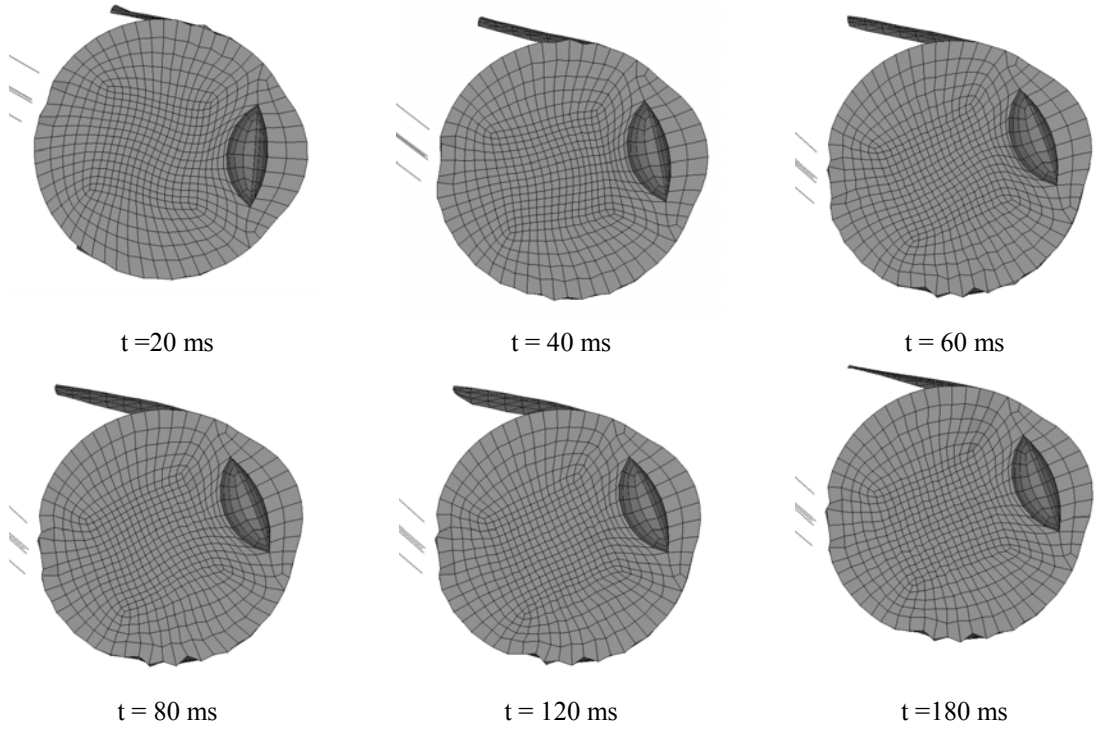

Figure A.12: Sequence of frames using Bettelheim vitreous material with CPL constitutive model. Eye model is the manual mesh using the analytical spring optic nerve.

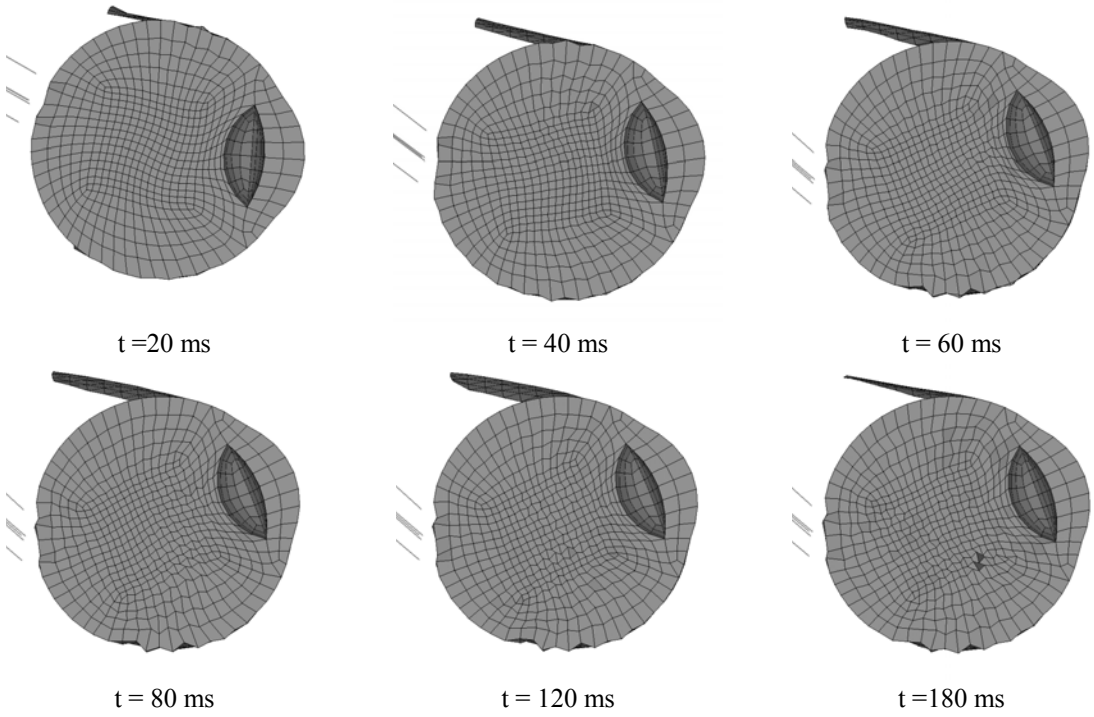

Figure A.13: Sequence of frames using Tokita vitreous material with CPL constitutive model. Eye model is the manual mesh using the analytical spring optic nerve.

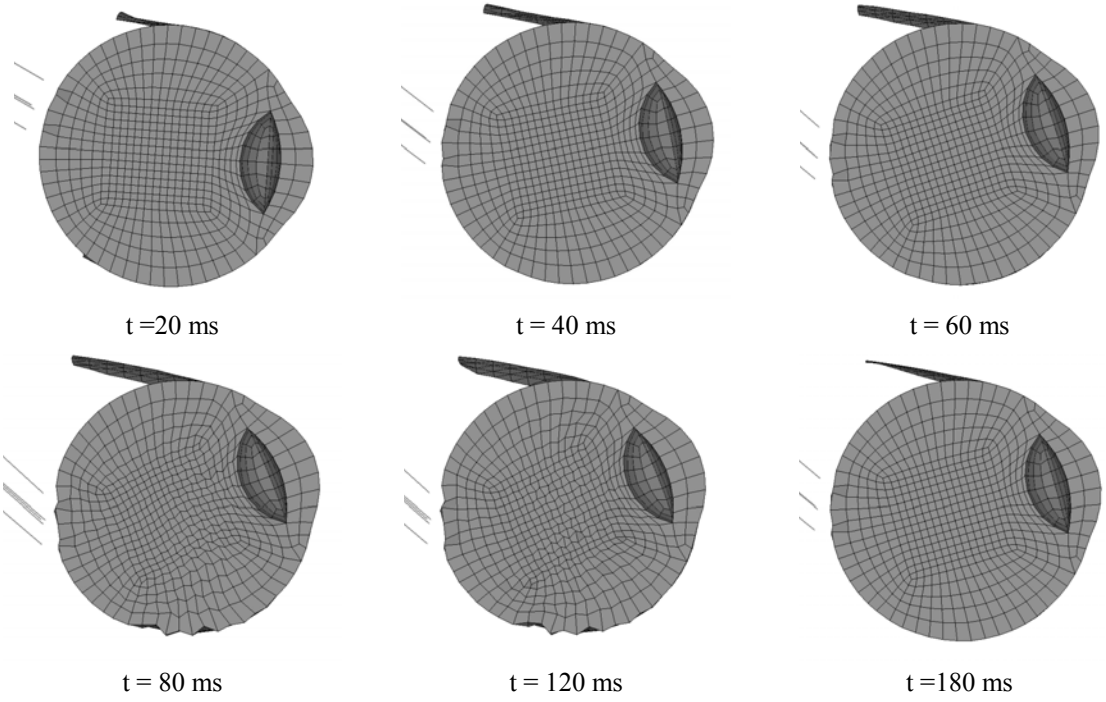

Figure A.14: Sequence of frames using Power vitreous material with CPL constitutive model. Eye model is the manual mesh using the analytical spring optic nerve.

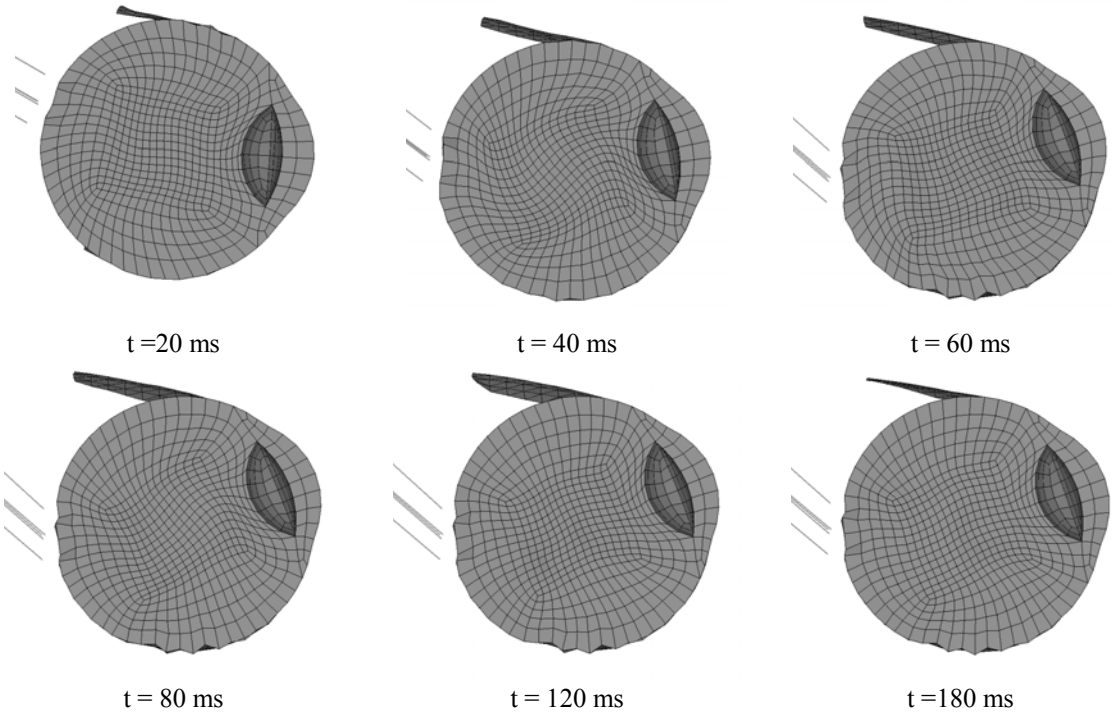

Figure A.15: Sequence of frames using Nickerson (x5) vitreous material with SOF constitutive model (FNLS = 0.01). Eye model is the manual mesh using the analytical spring optic nerve.

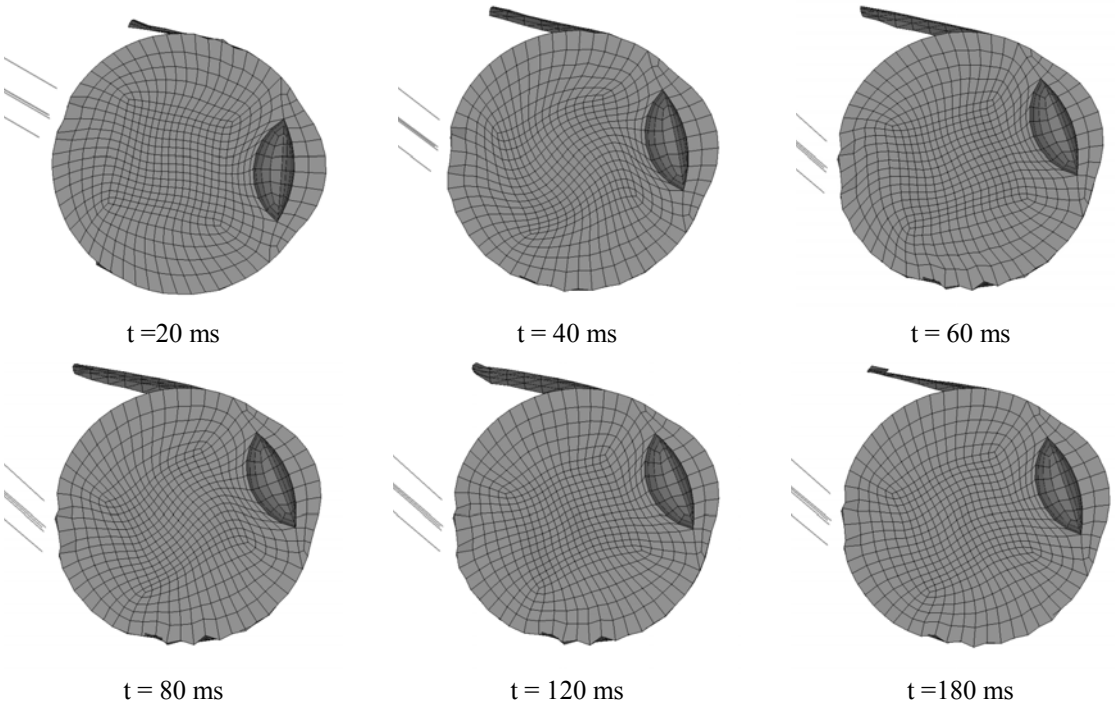

Figure A.16: Sequence of frames using Nickerson (x5) vitreous material with SOF constitutive model (FNLS = 0.1). Eye model is the manual mesh using the analytical spring optic nerve.

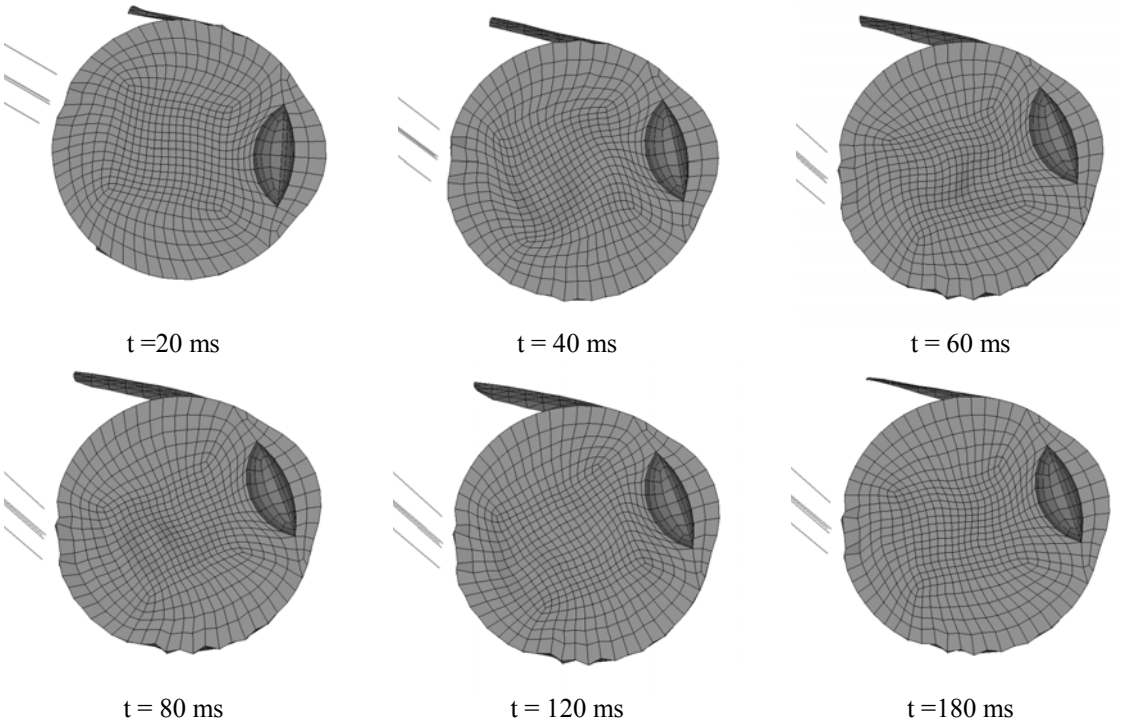

Figure A.17: Sequence of frames using Nickerson (x5) vitreous material with SOF constitutive model (FNLS = 1.0). Eye model is the manual mesh using the analytical spring optic nerve.

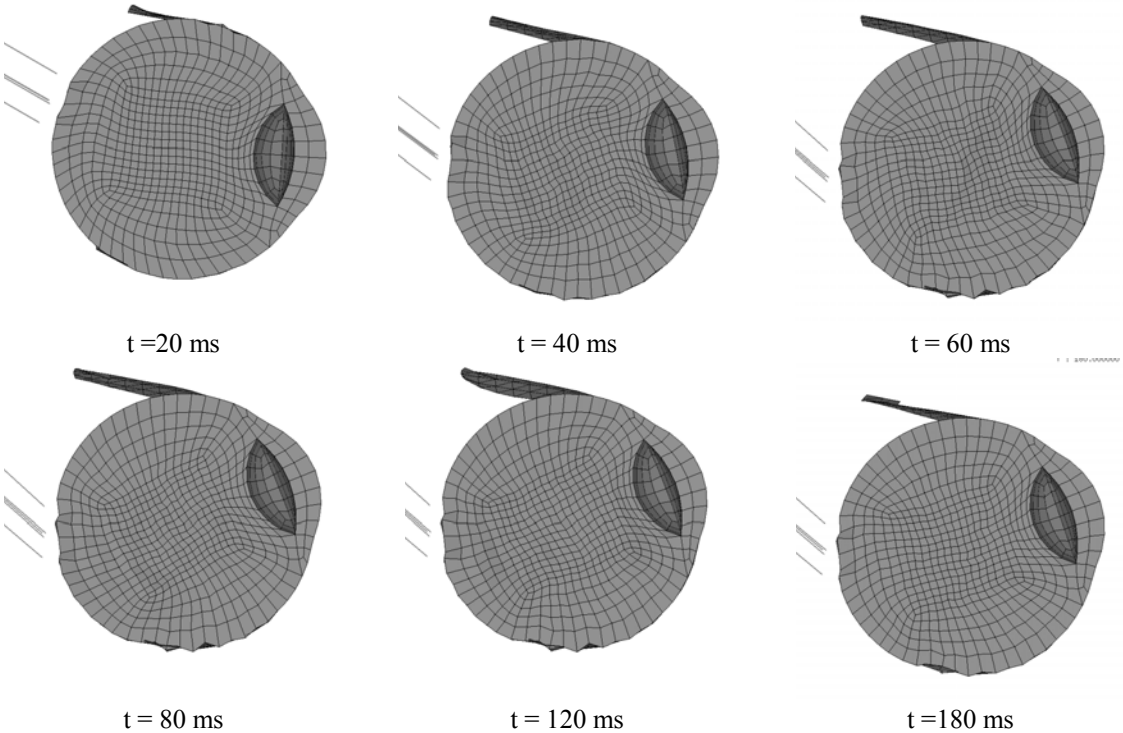

Figure A.18: Sequence of frames using Nickerson (x5) vitreous material with SOF constitutive model (FNLS = 5.0). Eye model is the manual mesh using the analytical spring optic nerve.

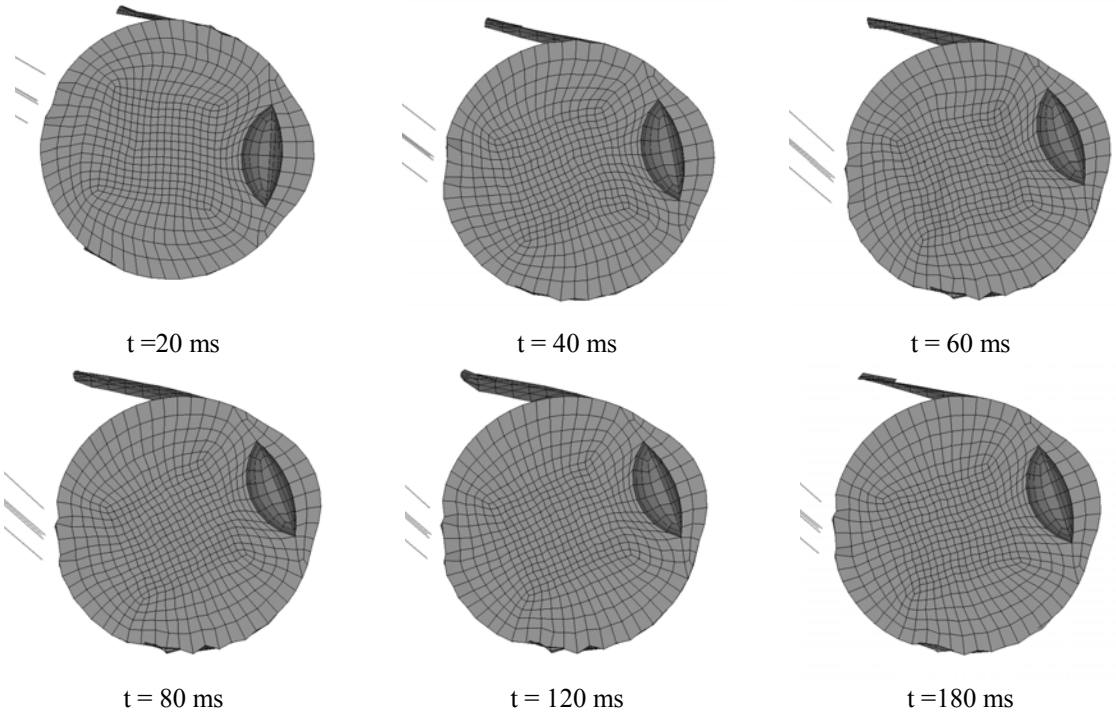

Figure A.19: Sequence of frames using Nickerson (x5) vitreous material with SOF constitutive model (FNLS = 10.0). Eye model is the manual mesh using the analytical spring optic nerve.

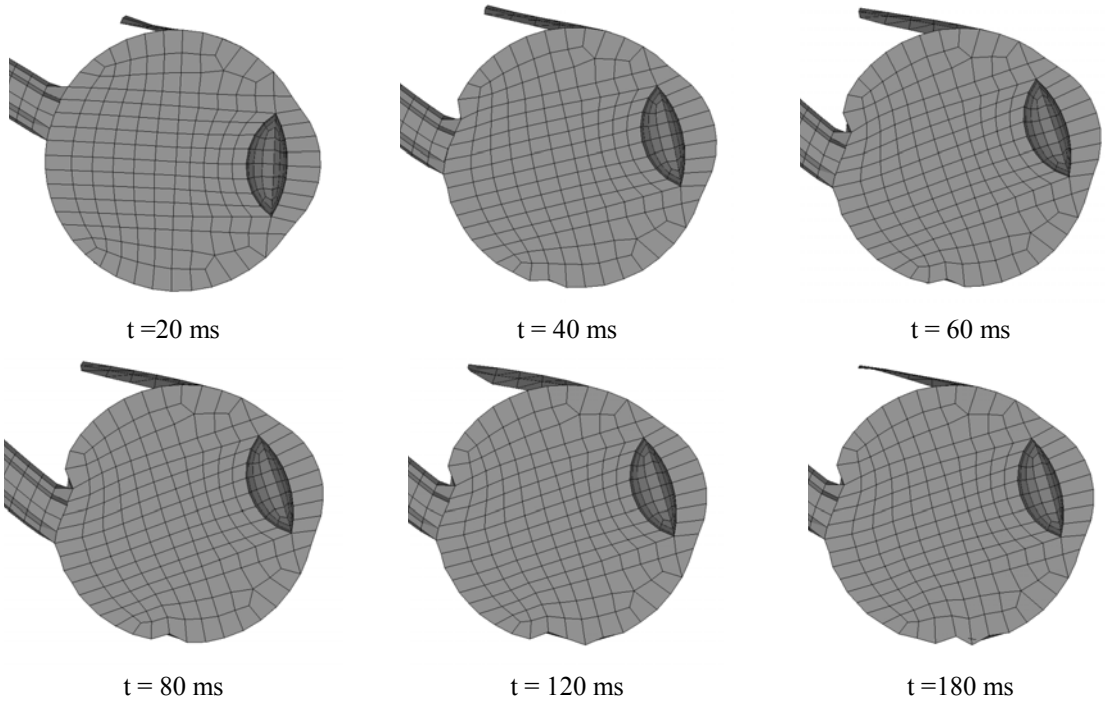

Figure A.20: Sequence of using Weber vitreous material with elastic constitutive model. Eye model is the CUBIT mesh using the FE Sigal optic nerve.

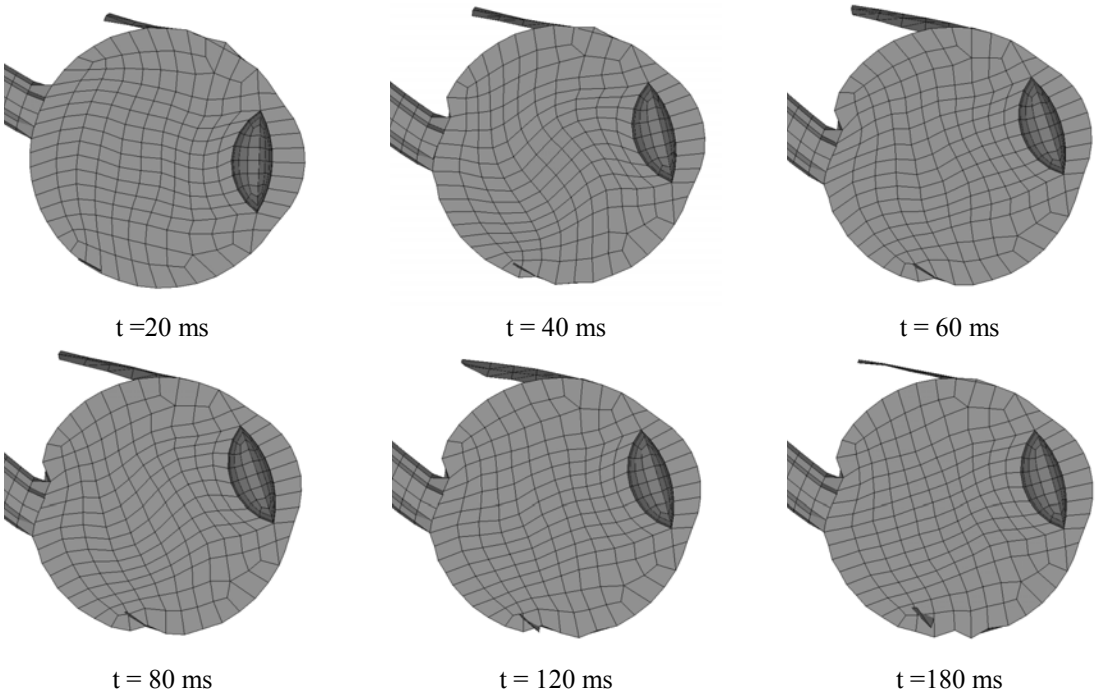

Figure A.21: Sequence of using Nickerson (x5) vitreous material with REF constitutive model. Eye model is the CUBIT mesh using the FE Sigal optic nerve.

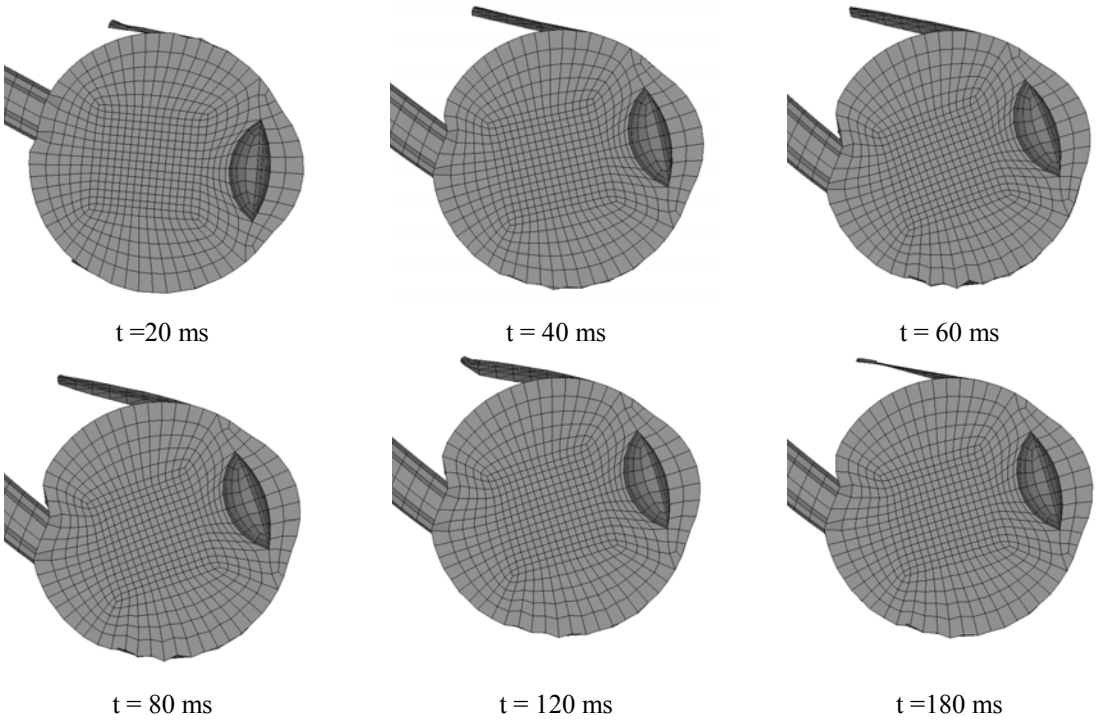

Figure A.22: Sequence of frames using Weber vitreous material with elastic constitutive model. Eye model is the manual mesh using the FE Sigal optic nerve.

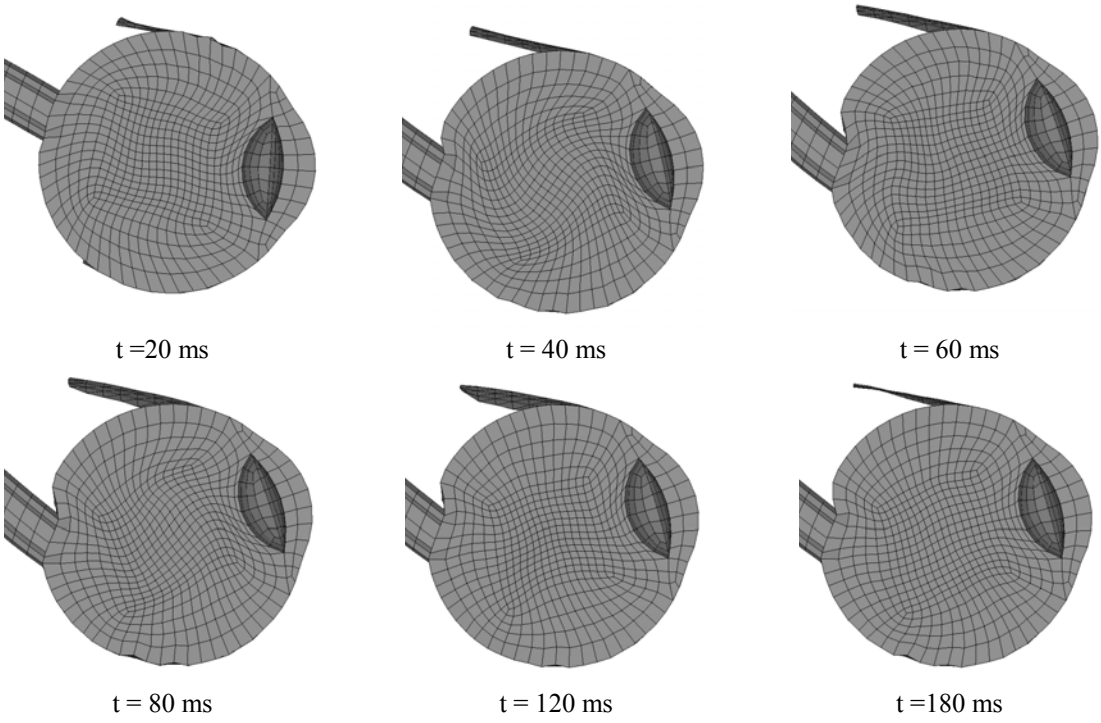

Figure A.23: Sequence of frames using Nickerson (x5) vitreous material with REF constitutive model. Eye model is the manual mesh using the FE Sigal optic nerve.

APPENDIX B

ANIMATION SEQUENCE FOR PURE SHAKING AND IMPACT SIMULATIONS

Figure B.1: Animation sequence of pure shaking simulation using the analytical nerve with the Samani & Plewes (2004) fatty tissue.

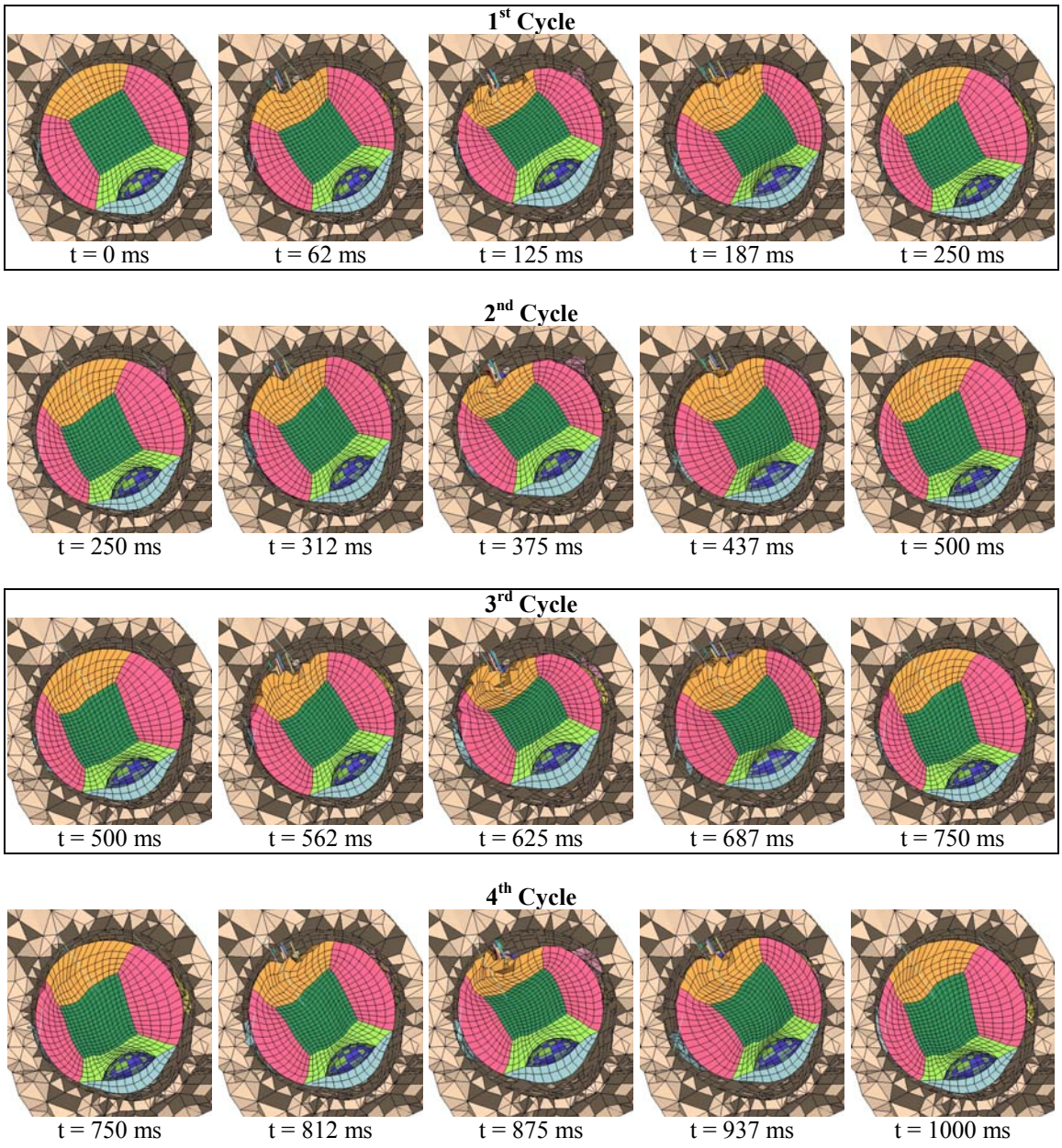

Figure B.2: Animation sequence of pure shaking simulation using the analytical nerve with the Verver (2004) fatty tissue.

Figure B.3: Animation sequence of pure shaking simulation using the analytical nerve with the Samani & Plewes (2004) fatty tissue and retinal welds.

Figure B.4: Animation sequence of pure shaking simulation using the analytical nerve with the Verver (2004) fatty tissue and retinal welds.

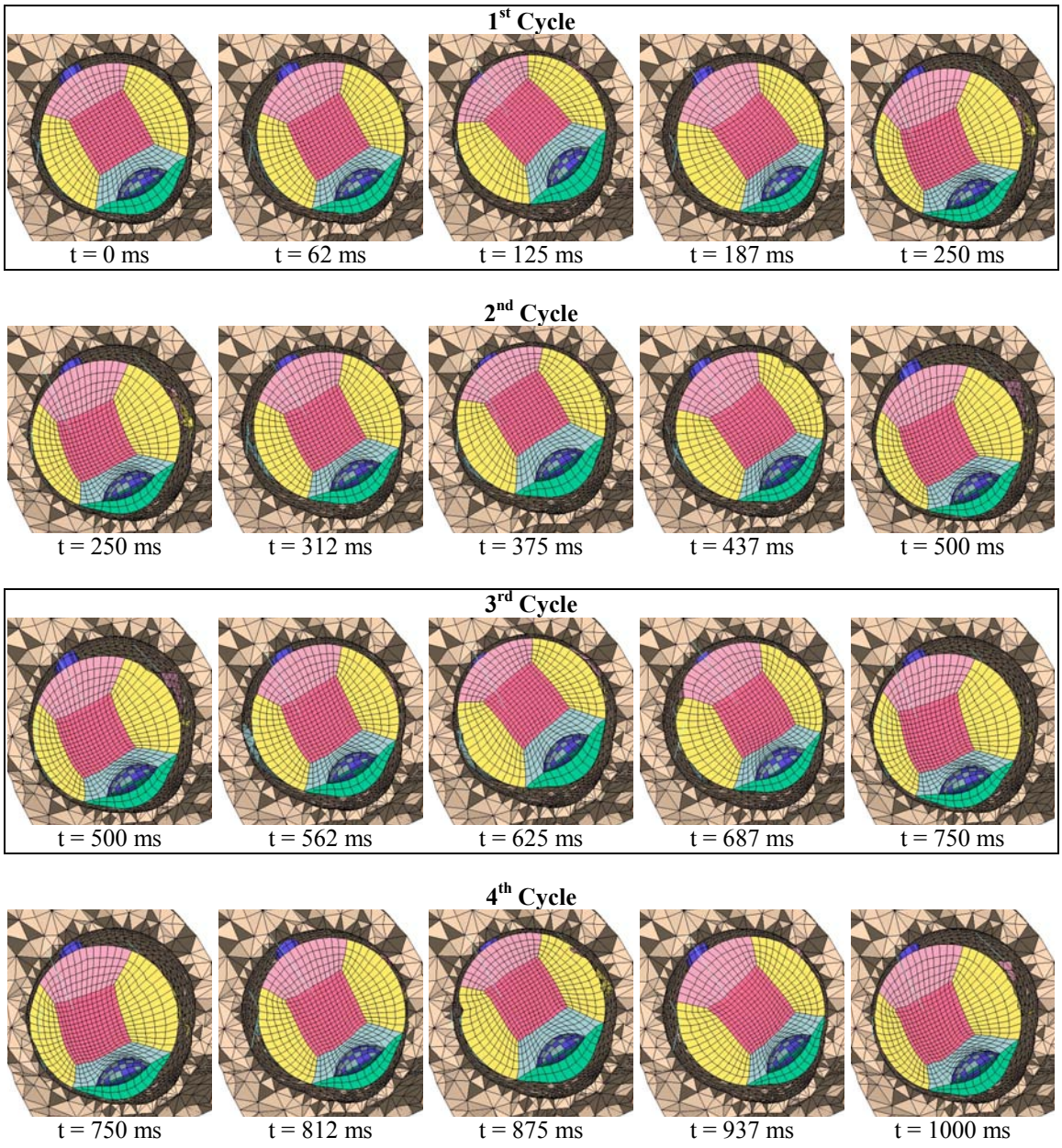

Figure B.5: Animation sequence of pure shaking simulation using the Sigal et al. (2004) nerve with the Samani & Plewes (2004) fatty tissue.

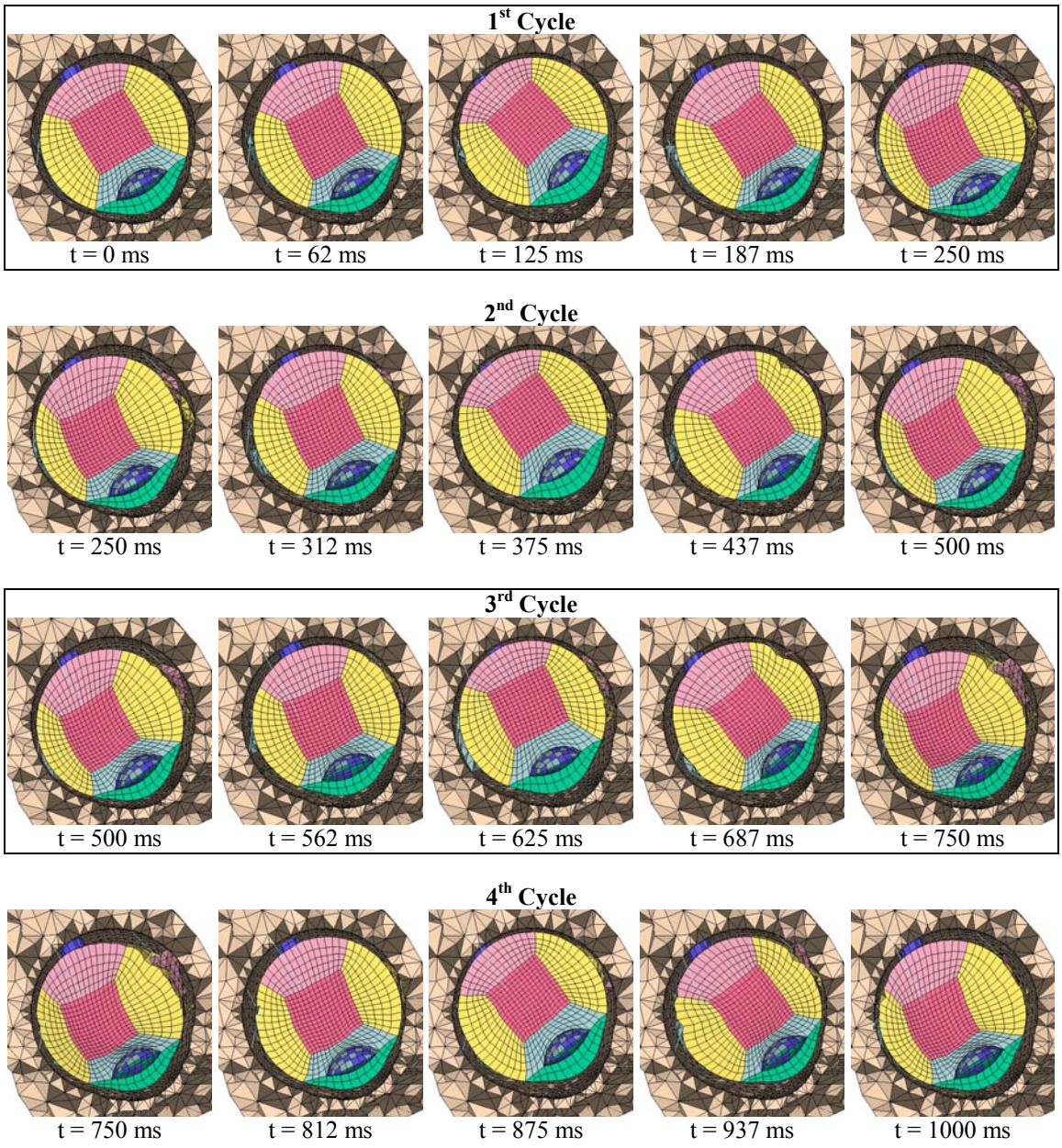

Figure B.6: Animation sequence of pure shaking simulation using the Sigal et al. (2004) nerve with the Verver (2004) fatty tissue.

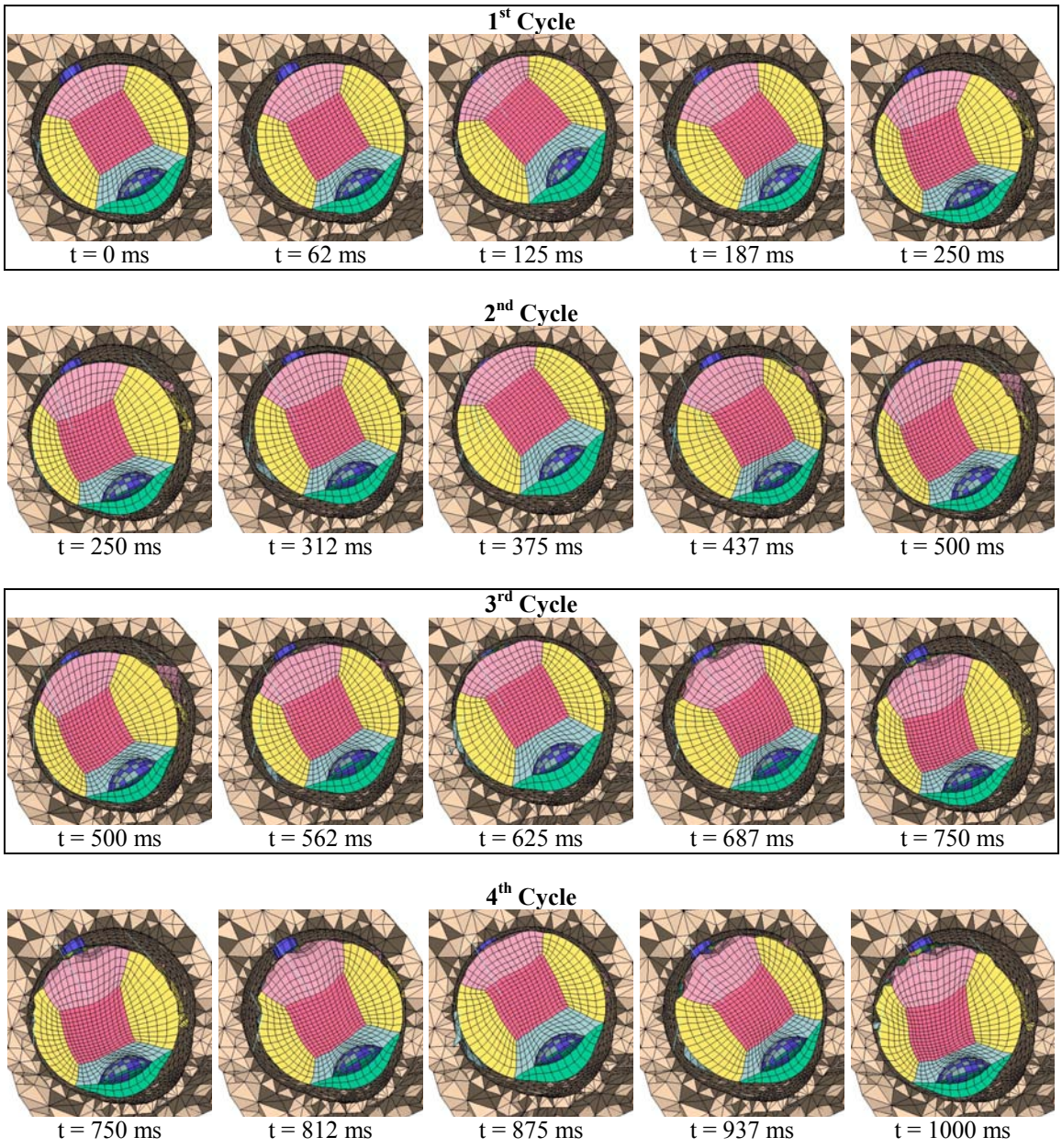

Figure B.7: Animation sequence of pure shaking simulation using the Sigal et al. (2004) nerve with the Samani & Plewes (2004) fatty tissue and retinal welds

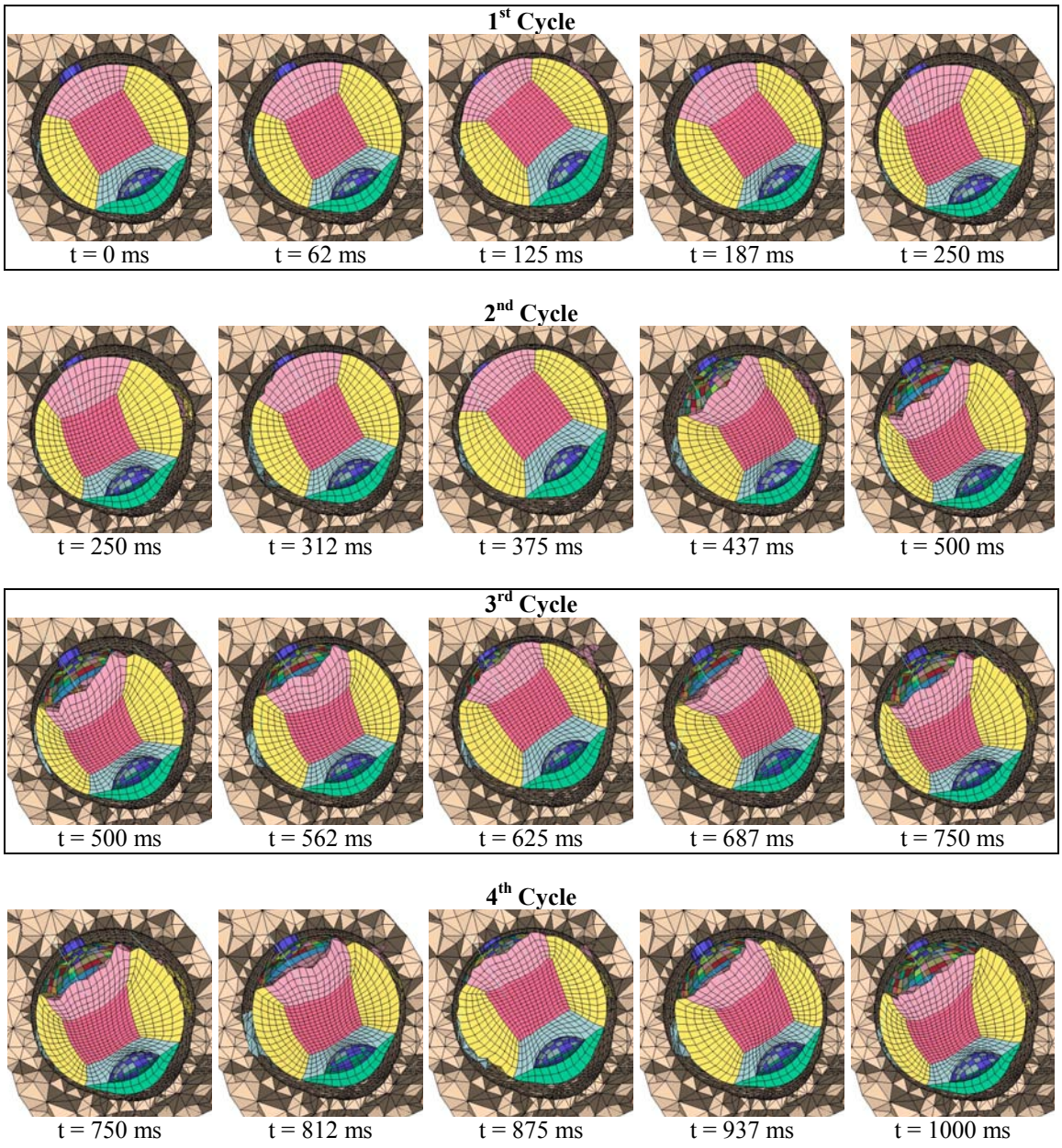

Figure B.8: Animation sequence of pure shaking simulation using the Sigal et al. (2004) nerve with the Verver (2004) fatty tissue and retinal welds

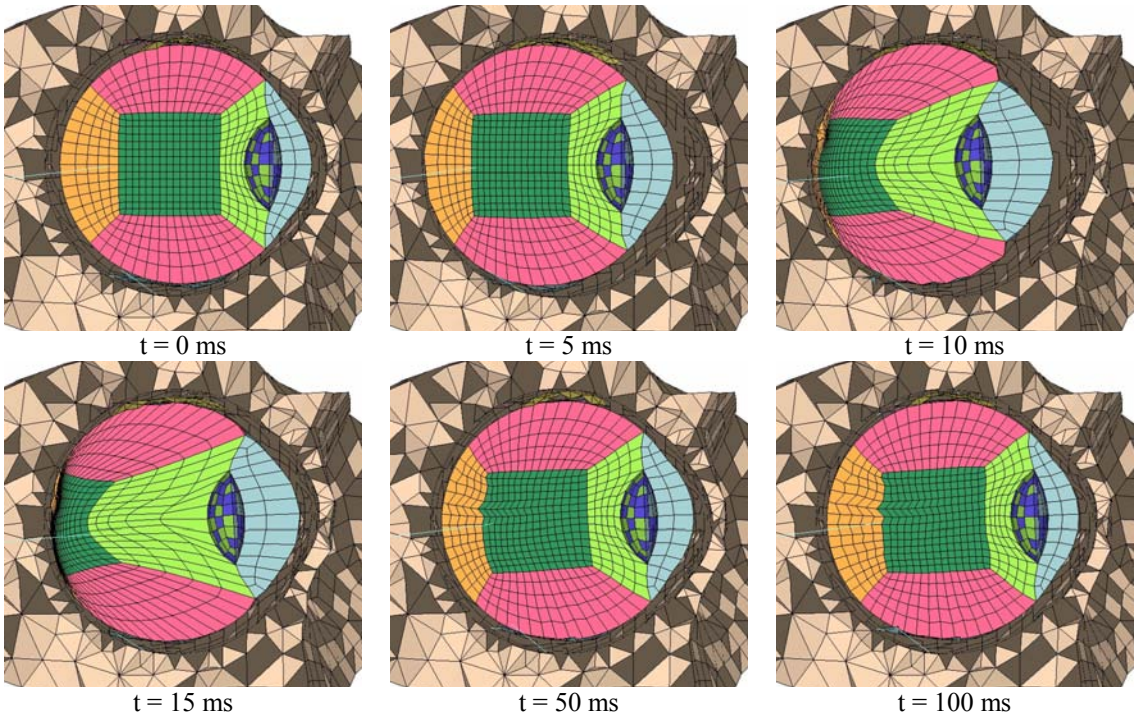

Figure B.9: Animation sequence of impact pulse using the analytical nerve with the Verver (2004) fatty tissue.

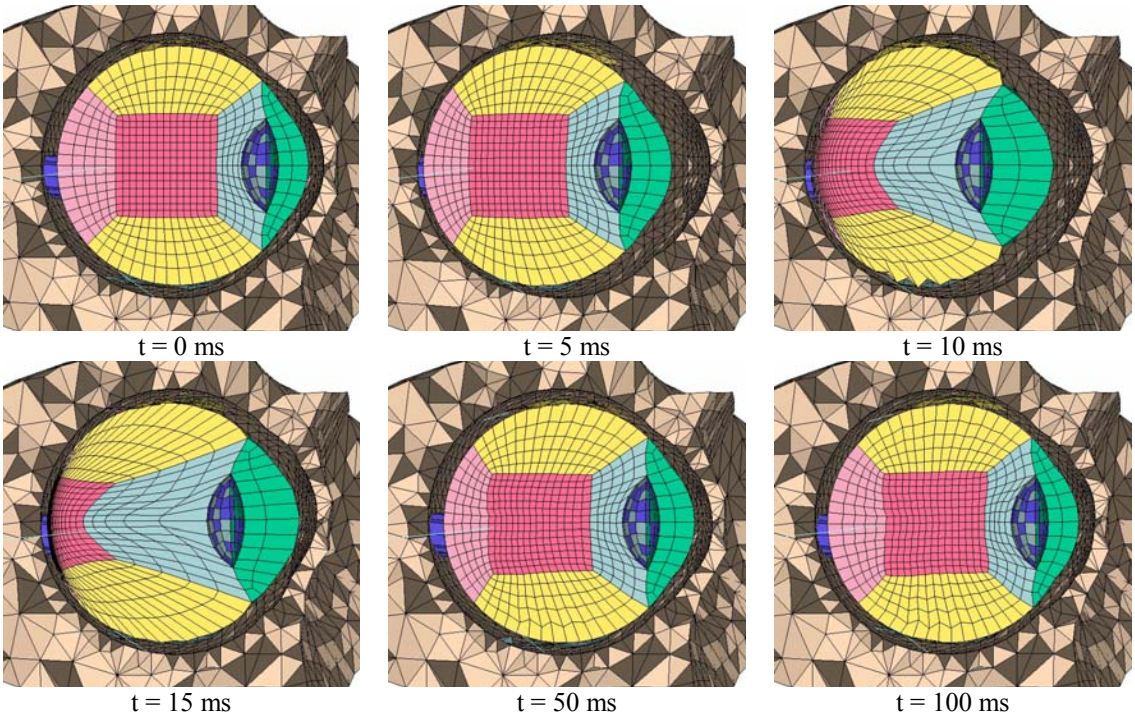

Figure B.10: Animation sequence of impact pulse using the Sigal et al. (2004) nerve with the Verver (2004) fatty tissue.

APPENDIX C

RECONSTRUCTION OF AN EYE MODEL BASED ON PREVIOUS WORK

Finite Element Eye Model and Testing

Currently, studies are conducted on the assembly of an eye model based on Power's (2001) eye model. Fortunately, Power includes the abridged input file (MADYMO, 1999) (mesh data excluded). Using the material properties and thickness information, a reconstruction of a finite element eye is made using the Power thesis as a guide. Power constructed the eye based on geometrical information from Woo et al. (1972). Using the same technique (Figures C.1, C.2, and C.3), an eye mesh is constructed manually by observing screen shots from the Power thesis so that the element placement would be approximately the same. As a check, the number of elements and nodes are compared to the Power tabulated summary to make sure the totals match. Figure C.3 describes the mesh that is comparable to the Power model. The cornea and sclera vary in thickness as seen in the sagittal view (Figure C.1). Therefore, a distribution of thickness is represented (Figure C.3) by the various color variations. Unfortunately, MADYMO only allows a uniform thickness along an element, so there are discrete steps in thickness from one radial mesh strip to the next; this is pointed out as a limitation in the Power model as well. Likewise, the vitreous, aqueous humor, lens, and ciliary body are created using figures from the Power thesis as a visual guide.

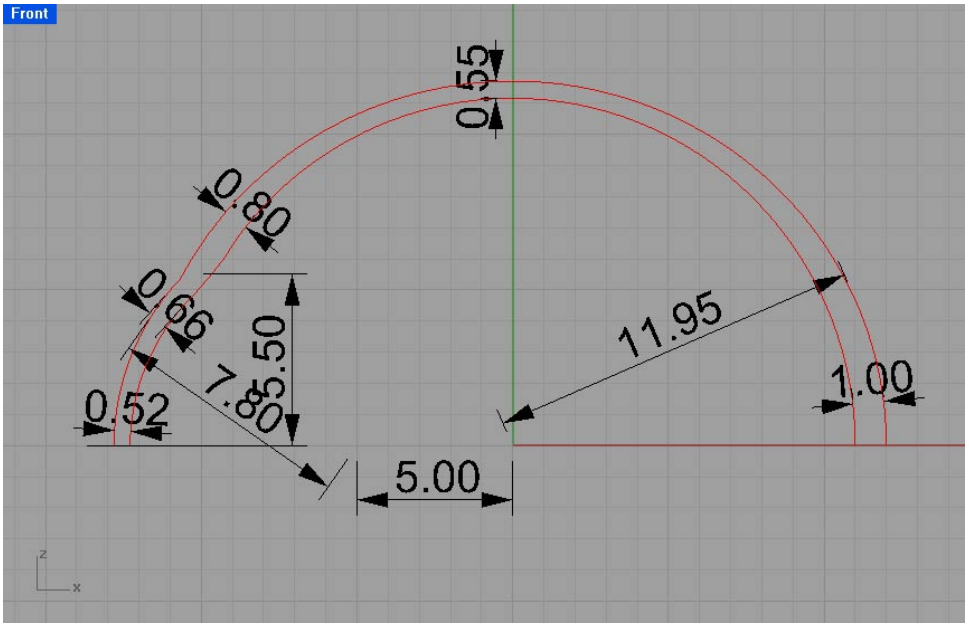

Figure C.1: Construction of cornea and sclera based on Woo et al. (1972).

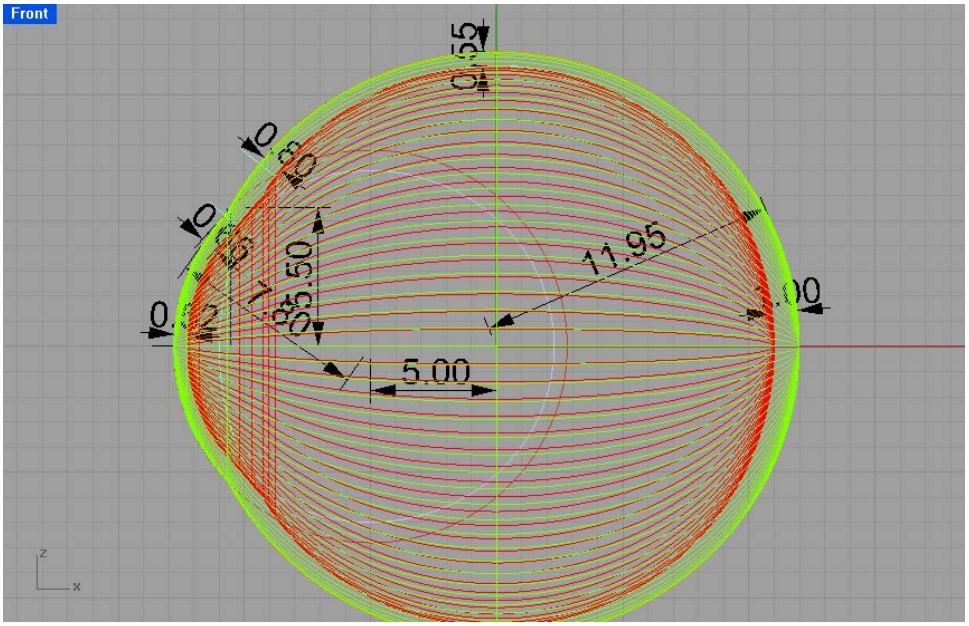

Figure C.2: Surface creation of cornea and sclera creation from the construction curves in Figure C.1.

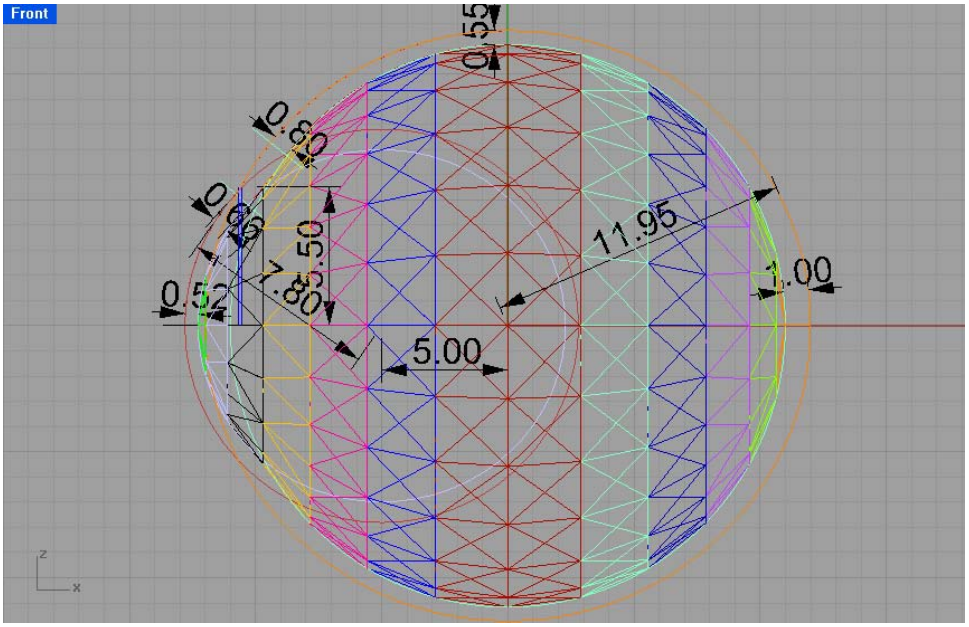

Figure C.3: Manual construction of the mesh data of the cornea and sclera based on Power.

The assembled eye (Figures C.4, C.5 and C.6) is comparable to the Power model and the summary of the finite elements is tabulated (Table C.1) below.

Table C.1: Summary information of the finite element eye mesh matching the Power model.

Component	Element Type	Element Amount	Node Amount
Cornea	Membrane	64	41
Sclera	Membrane	400	193
Lens	Membrane	16	10
Ciliary Body	Membrane	32	32
Aqueous	8-node Solid	72	123
Vitreous	8-node Solid	80	125

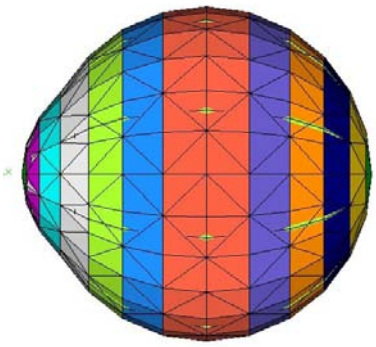

Figure C.4: Completed Eye mesh showing the cornea sclera.

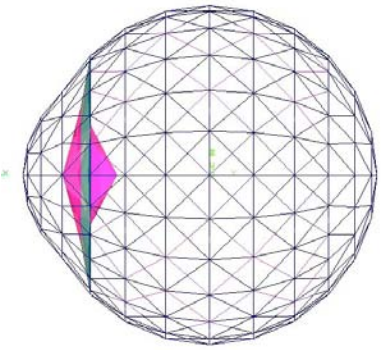

Figure C.5: Inside of the eye structure showing sagittal view of the lens and ciliary body.

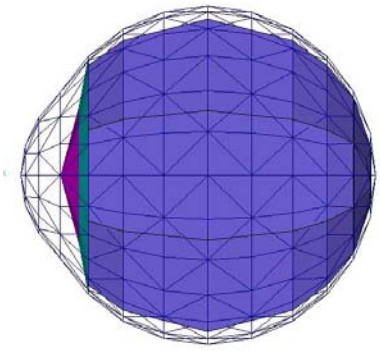

Figure C.6: The vitreous body is shown inside the posterior end of the eye (sagittal view).

Twelve discrete layers of the cornea and sclera structure are assigned thickness to approximate the dimensions in Figure C.4. The thickness for each is tabulated (Table C.2) starting with the apex on the anterior pole and going back to the posterior pole.

Table C.2: Cornea and sclera thickness distribution. The color of each layer is referenced from Figure C.4.

Location	Layer Color	Thickness
Corneal apex	Green	0.52 mm
2nd radial shell strip	Magenta	0.59 mm
3rd radial shell strip	Cyan	0.66 mm
Limbus	White	0.80 mm
5th radial shell strip	Light green	0.72 mm
6th radial shell strip	Blue	0.63 mm
Scleral thinning center strip	Red	0.55 mm
8th radial shell strip	Purple	0.64 mm
9th radial shell strip	Orange	0.73 mm
10th radial shell strip	Dark Blue	0.82 mm
11th radial shell strip	Yellow	0.91 mm
Posterior pole	Green	1.00 mm

The material properties used for the cornea and sclera are adopted from Uchio et al. (1999). Power applied this data to a hysteresis material type to model the non-linear stress-strain relationship. Unfortunately, the limitation of using this type of material property is that the Poisson's ratio cannot be specified (MADYMO, 1999).

The cornea and sclera stress-strain is displayed in Figure C.7. The density is estimated from Power to be between water (999 kg/m^3) and collagen (1800 kg/m^3) and is set to 1400 kg/m^3.

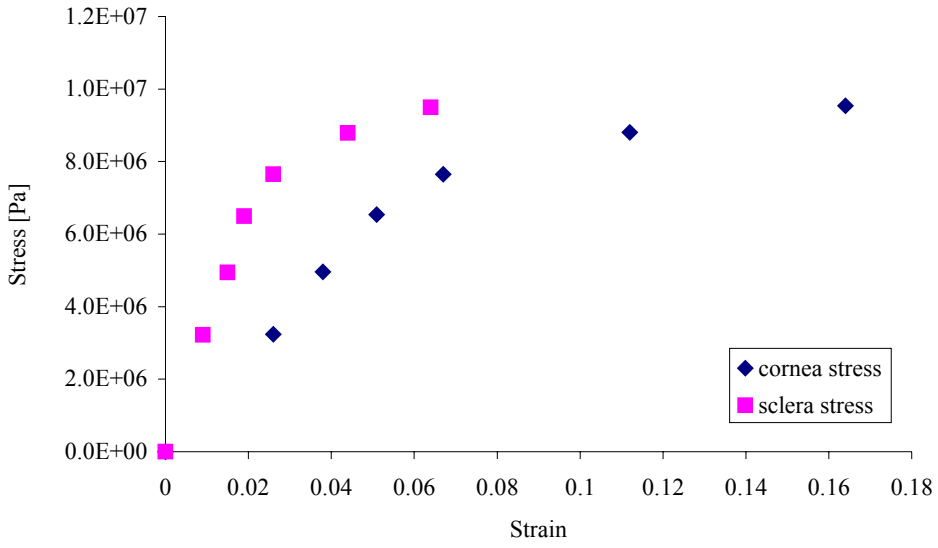

Figure C.7: Cornea and Sclera non-linear stress-strain adapted from Uchio et al. (1999).

The lens is made rigid as Power explains the initial study does not consider deformation of the lens. The ciliary body is specified as a tension only muscle with properties approximated from rat-tail tendon (Power). The values for this isotropic assumption are 5E6 Pa for the modulus of elasticity and 0.4 for the Poisson's ratio and 1600 kg/m^3 for the density.

Power models the fatty tissue of the orbital socket using properties (Todd & Thacker, 1994) that are isotropic and elastic. The values are 0.047E6 Pa for the Young's modules, 0.49 for Poisson's ratio (incompressible material), and the density is set equal to water. This value for the fatty tissue is extrapolated to the aqueous humor and vitreous body. Power approximates the Young's modulus for the aqueous humor to be 0.037E6 Pa or about 21% lower than the fatty tissue. Further, Power approximates the Young's modulus for the vitreous to be 0.042E6 Pa or about 11% lower than the fatty tissue. The aqueous humor is more fluid than the gel-like vitreous (Wolter, 1961), so Power justifies the arbitrary assignments. However, no mention of why the material is made a derivative of the fatty tissue is mentioned.

Contact interactions in the model are made between all the structures. In the model, contact is made with the gel like vitreous and the posterior chamber made up of the sclera and the posterior end of the ciliary body and lens. The aqueous contacts the anterior chamber made up of the cornea and anterior side of the ciliary body and lens.

When testing the simulation of the eye, the vitreous and aqueous would not stay within the defined chambers. In MADYMO version 5.4, nodes of one system contact the element surface of another. Therefore, the aqueous nodes would contact the element surface of the ciliary body. However, if the nodal coordinate information is coincident or located on the edge of an element, the contact is not recognized (MADYMO).

Therefore, deviating from Power, the nodes around the perimeter of the ciliary body that share a common node with the sclera (Figure C.8) had to be changed. The

ciliary body and lens were scaled down by 0.5% and the node that once was shared was duplicated. The new node location is simply constrained to the once common node of the sclera so that the simulation remains the same and allows the node of the aqueous, which is also rotated about the sagittal plane by 0.5 degrees, to have a solid contact with the ciliary element surface (Figure C.9). Similar modifications had to be done to the vitreous as well to ensure good contact. There is no mention of this issue with the Power model.

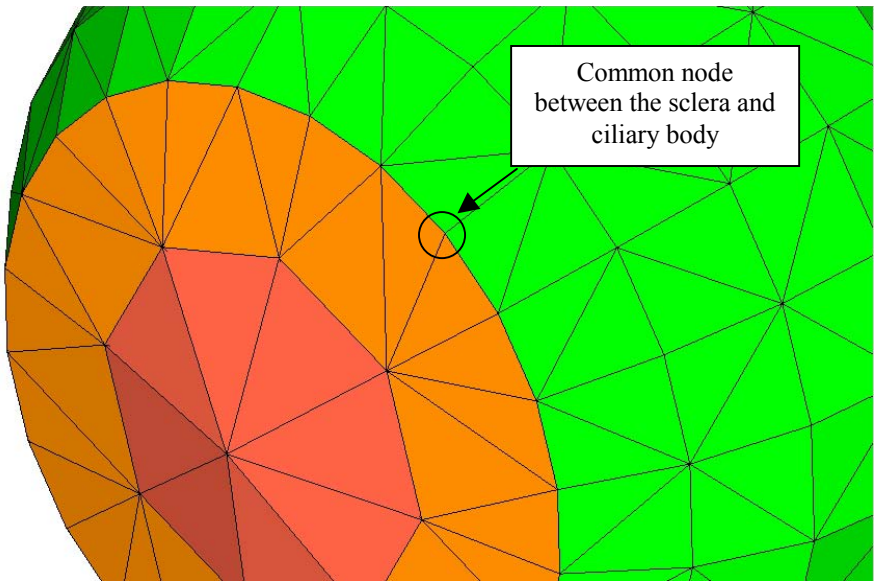

Figure C.8: Before modifying the common node of the ciliary and sclera.

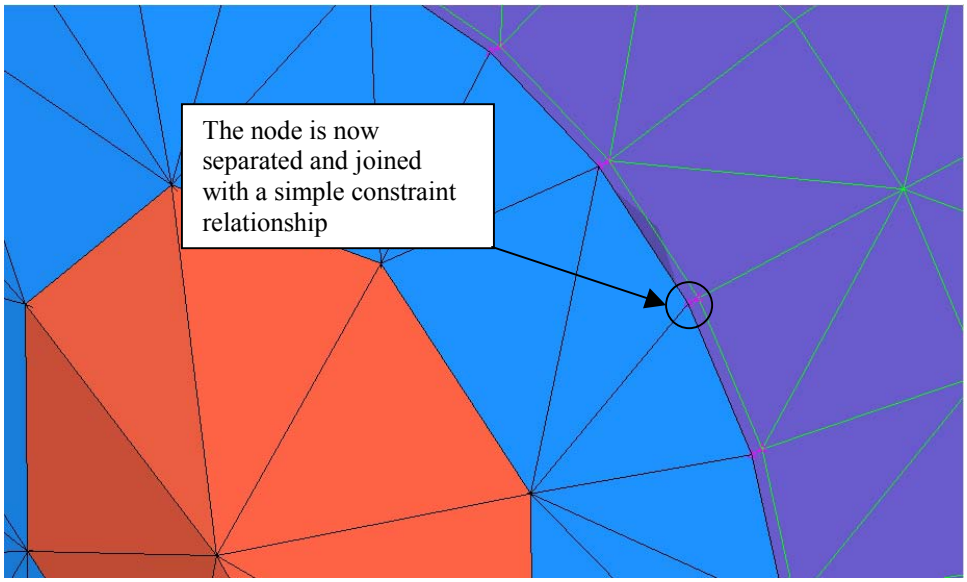

Figure C.9: After modifying, the two separate nodes now are simply constrained.

Power et al. (2002) validate the finite element eye model by impacting the eye with a baseball (Vinger, Duma, & Crandall, 1999) and a steel rod (Scott et al., 2000). The model is able to predict globe rupture with the baseball, but it did not produce rupture with the rod. A similar test is conducted where the fatty tissue from Todd and Thacker is used to hold the eye in place (Vinger et al.). Then a baseball (Figure C.10) with properties determined from Stitzel et al. (2002) is given an initial velocity of 24.7 m/s (mentioned in Power et al.). Unfortunately, major instability occurred after only a few milliseconds of impact. Could this be the failure of the eye that Power et al. is referring to? Further analysis needs to be done with this scenario before assumptions are made to make sure the model is behaving as intended.

Using this same test apparatus (Vinger et al.), a steel rod (Figure C.11), reported by Power et al. to have a diameter of 9.53 mm and mass of 45.5 g (Scott et

al.), is given an initial velocity of 4 m/s and impacts the eye. The simulation is stable until 12 milliseconds into the run. The eye rebounds after nine milliseconds because of the elastic and isotropic property assigned to the fatty tissue. Therefore, the simulation is only valid up to this nine millisecond run. Figures C.12 and C.13 show the animation sequence at various time stamps. Energy is stored in the fatty tissue, and at nine milliseconds the stored energy is released pushing the eye outwards. The von Mises stress is visualized for the same time stamps (Figures C.14 and C.15) with an oblique view (Figures C.12 and C.13) of the eye for clear visualization of the peak stress in the cornea. Since Uchio et al. (1999) measured the non-linear properties of the cornea and sclera up to failure, the results for the rod impacting the eye are in disagreement with the Power et al. assessment.

However, since the simulation for the baseball impact needs to be investigated, the results should be considered preliminary for the steel rod simulation as well. Nevertheless, the values of each of the times reflected in Figures C.14 and C.15 are tabulated below (Table C.3). As can be seen, the cornea limit from Uchio et al. (1999) is 9.54E6 Pa. However, at five milliseconds the peak stress comes very close to this limit until it is breached at 7.01 milliseconds with a value of 1.1E7 Pa (13% higher than the failure value).

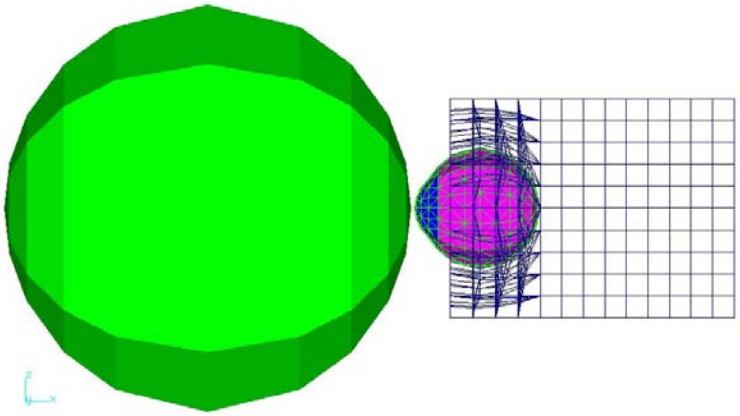

Figure C.10: Baseball testing apparatus (transverse view).

Table C.3: Rod impacting the eye globe von Mises stress results.

Time Stamp	Stress Proximity Location	von Mises Stress Value
0 msec	n/a	0 Pa
1.5 msec	Corneal Apex	1.2E7 Pa
3 msec	Corneal Apex	3.8E6 Pa
5 msec	Cornea close to Limbus	9.4E6 Pa
7.01 msec	Cornea close to Limbus	1.1E7 Pa
9.01 msec	Cornea close to Limbus	6.6E6 Pa

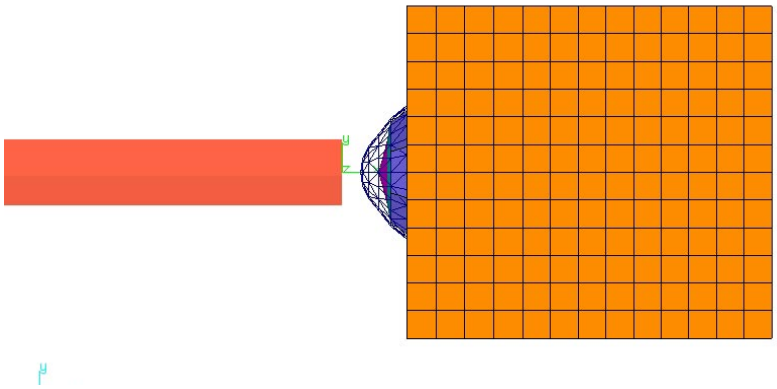

Figure C.11: Cylindrical Rod testing apparatus (transverse view).

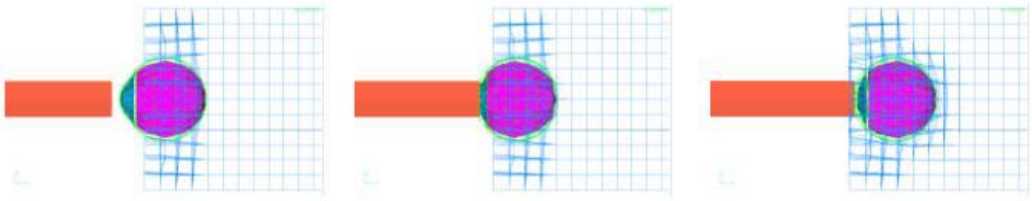

Figure C.12: Animation sequence at times 0, 1.5, & 3 msec (transverse view).

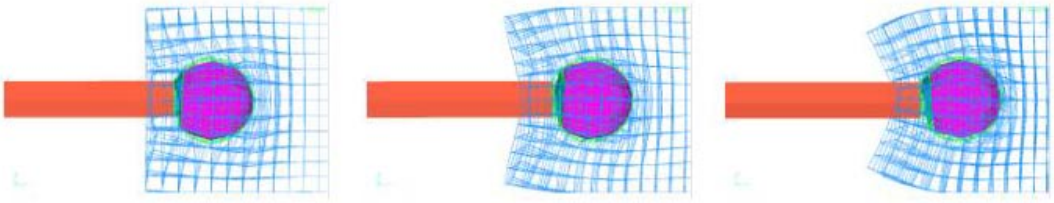

Figure C.13: Animation sequence at times 5, 7.01, & 9.01 msec (transverse view).

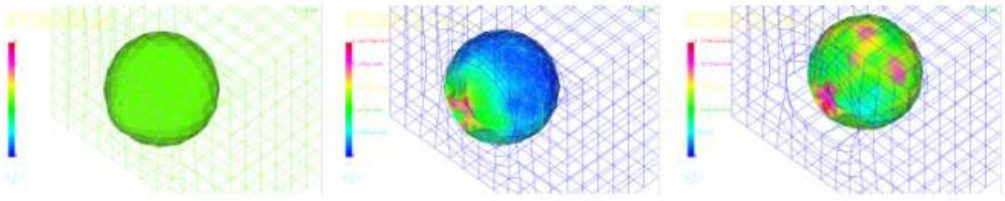

Figure C.14: Animation sequence at times 0, 1.5, & 3 msec (oblique view stress contour).

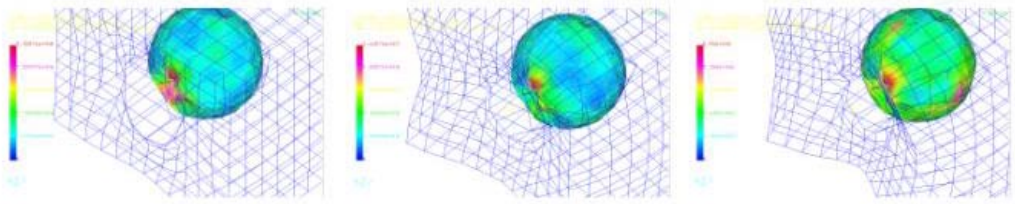

Figure C.15: Animation sequence at times 5, 7.01, & 9.01 msec (oblique view stress contour).

VITA

Name

Steven Alex Hans

Department

Department of Mechanical Engineering
Frank Batten College of Engineering and Technology
Old Dominion University, 241 Kaufman Hall
Norfolk, VA 23529

Education

M.S./Ph. D. (Mechanical Engineering), 2007
Old Dominion University, Norfolk, Virginia

B.S. (Mechanical Engineering), 1998
Old Dominion University, Norfolk, Virginia

Publications

Initial Experience with Parallel Engineering Computation under MPI/FORTRAN and LINUX PCs Computer. S. Hans, S.Y. Bawab, A. Demuren and D.T. Nguyen, Dept. of Civil and Environmental Engineering, Old Dominion University Virginia Academy of Science 78th Annual Meeting Radford University Radford, Virginia May 23-26,2000

Bawab S., S. Hans, T. Mastaglio and M. Woodhouse, "Using Biomechanical Modeling Tools to Support Accident Litigations, Summer Computer Simulation Conference" 2001, pp. 655-660, Society for Computer Simulation, San Diego,CA, July 2001.

J.K. Wilkerson, S.A. Hans, M.L. Woodhouse, S.Y. Bawab, et.al., "The Effects of Occupant and Vehicular Parameters on the Onset and Severity of Whiplash Associated Disorder from Low Speed Rear-End Collisions",SAE 2002-01-0538.

M. P. Venkataramana, S. A. Hans, S.Y. Bawab, et al. "Effects of Initial Seated Position in Low Speed Rear-End Impacts: A Comparison with the TNO Rear Impact Dummy (TRID) Model", Journal of Traffic Injury Prevention, 5:1-9, 2004.

A.M. Hanasoge, S.A. Hans, S. Desetty, et al. "Dynamic Analysis of a Moving Maglev Train", SAE 05B-241 2004.

S.A. Hans, S. Y. Bawab, & M.L. Woodhouse "Simulation of a Vehicular Roof Crush Deformation Using Prescribed Nodal Motion", International Journal of Agile Manufacturing, *In Press.* (2007).